Analysis of tropospheric trace gas amounts from satellite and ship-based DOAS-type measurements: NO$_2$ from biomass burning and other sources

Mag.rer.nat. Ing. Stefan Friedrich Schreier

Dissertation zur Erlangung des Grades *Doktor der Naturwissenschaften* (*Dr.rer.nat.*)

Universität Bremen*

Institut für Umweltphysik

Fachbereich Physik und Elektrotechnik

Universität Bremen

Oktober 2014

1. Gutachter: Prof. Dr. John P. Burrows

2. Gutachter: Prof. Dr. Justus Notholt

Betreuer: Dr. Andreas Richter

Dissertation eingereicht am: 13. Oktober 2014

Datum des Kolloquiums: 11. Dezember 2014

Du kannst dein Leben nicht verlängern und du kannst es auch nicht verbreitern.

Aber du kannst es vertiefen.

Gorch Fock, 1880-1916

Abstract

Nitrogen oxides (NO_x) play key roles in atmospheric chemistry, air pollution, and climate. While the largest fraction of these reactive gases is released by anthropogenic emission sources, a significant amount can be attributed to vegetation fires. Tropospheric nitrogen dioxide (NO_2) amounts can be retrieved from ground-based, ship-based, aircraft-based, and satellite-based remote sensing measurements. The focus of this thesis is to analyze such NO_2 measurements for the characterization of NO_x from open biomass burning and other sources.

In the first part of this thesis, satellite measurements of tropospheric NO_2 from GOME-2 and OMI as well as fire radiative power (FRP) from the MODIS instruments are used to derive seasonally averaged fire emission rates (FERs) of NO_x for different types of vegetation using a simple statistical approach. Monthly means of tropospheric NO_2 vertical columns (TVC NO_2) are analyzed for their temporal correlation with the monthly means of FRP for a multi-year period. The strongest correlation is found to be largely confined to tropical and subtropical regions, which account for more than 80% of yearly burned area, on average, globally. As atmospheric models typically require values for the amount of NO_x being released as a function of time, the retrieved TVC NO_2 is converted into production rates of NO_x from fire (P_f). By separating the monthly means of P_f and FRP according to land cover type, FERs of NO_x could be derived for different biomes and regions. The estimated FERs for the dominating types of vegetation burned are lowest for boreal forest, open shrublands, and savannas (0.25–1.03 g NO_x s^{-1} MW^{-1}) and highest for croplands and woody savannas (0.82–1.56 g NO_x s^{-1} MW^{-1}). This analysis demonstrates that the strong empirical relationship between TVC NO_2 and FRP and the following simplified assumptions are a useful tool for the characterization of NO_x emission rates from vegetation fires in the tropics, subtropics, and in boreal regions. As current fire emission inventories apply emission factors (EFs) of NO_x for the translation of biomass burned into trace gas emissions, the satellite-derived FERs of NO_x are converted into EFs of NO_x. A comparison with NO_x EFs found in the literature shows good agreement for some biomes (e.g. boreal forest, tropical forest, and crop residue).

However, the EFs for savanna and grassland obtained from satellite measurements are lower by a factor of 2.5. This has possible implications for future work in this field, in particular because savanna and grassland is the most frequently burned biome on Earth. As recent satellite-based studies have indicated substantial spatio-temporal variations in NO_x EFs for several biomes, a modified approach is used for the computation of monthly resolved FERs of NO_x. In order to evaluate the impact when such seasonal changes are not included, a case study for the African continent to estimate total NO_x emissions from open biomass burning is performed by applying both seasonally averaged and monthly resolved FERs of NO_x. The results indicate differences between the two tested approaches of up to 90%, in particular on a monthly basis.

In the second part of this thesis, ship-based MAX-DOAS measurements performed within the SHIVA campaign in November 2011 on board RV Sonne in the South China and Sulu Sea are analyzed. Spectral measurements for a total of eleven days are used to retrieve tropospheric slant column densities (SCDs) of NO_2 and sulfur dioxide (SO_2) in the marine environment. An improved NO_2 fit including a cross section for liquid water and an empirical correction spectrum accounting for the effects of liquid water and vibrational Raman scattering and a novel SO_2 fit are applied to the ship-based measurements. The conversion of SCDs into TVC NO_2 is achieved using both a simple geometric approach and the Bremian advanced MAX-DOAS Retrieval Algorithm (BREAM), which is based on the optimal estimation method and accounts for atmospheric radiative transfer. The results show that the geometric approach using the 15° measurements is in good agreement with BREAM, revealing that measurements at 15° elevation angle can be used for retrieving TVC NO_2 in tropical marine environments. As expected, the values of TVC NO_2 are generally low ($< 0.5 \times 10^{15}$ molec cm^{-2}) when no sources of NO_x were in proximity to the RV Sonne. However, increased values of TVC NO_2 ($> 2 \times 10^{15}$ molec cm^{-2}) are observed in the morning when the RV Sonne was heading along the coast of Borneo. This is in good agreement with satellite measurements. Interestingly, elevated tropospheric SO_2 amounts for measurements taken in a busy shipping lane are consistent with the time series of tropospheric NO_2.

Publications

Large parts of this thesis, including text passages, figures, and tables, are based on and/or cited from peer reviewed research articles, oral and poster presentations produced during the thesis. Individual sections that contain such text passages, figures, and tables from published articles, are indicated by an asterisk and appropriate footnotes throughout this thesis.

Articles in peer-reviewed journals

- **Schreier, S. F.**, Richter, A., Kaiser, J. W., and Burrows, J. P.: The empirical relationship between satellite-derived tropospheric NO_2 and fire radiative power and possible implications for fire emission rates of NO_x, Atmospheric Chemistry and Physics, 14, 2014a.

- **Schreier, S. F.,** Richter, A., Schepaschenko, D., Shvidenko, A., Hilboll, A., and Burrows, J. P.: Differences in satellite-derived NO_x emission factors between Eurasian and North American boreal forest fires, Atmospheric Environment (In Press), 2014b.

- Alvarado, L. M. A., Richter, A., Vrekoussis, M., Wittrock, F., Hilboll, A., **Schreier, S. F.**, and Burrows, J. P.: An improved glyoxal retrieval from OMI measurements, Atmospheric Measurement Techniques Discussions, 7, 5559-5599, 2014.

- **Schreier, S. F.**, Peters, E., Richter, A., Lampel, J., Wittrock, F., Burrows, J. P.: Ship-based MAX-DOAS measurements of tropospheric NO_2 and SO_2 in the South China and Sulu Sea, Atmospheric Environment (under review), 2014c.

- **Schreier, S. F.**, Richter, A., and Burrows, J. P.: Estimates of NO_x emission factors from GOME-2 measurements for the major types of open biomass burning, in: Springer Briefs in Earth System Sciences: Towards an interdisciplinary approach in Earth System Science: Advances of a Helmholtz Graduate Research School, edited by Lohmann, G., Meggers, H. , Unnithan, V., Wolf-Gladrow, D., Notholt, J., and Bracher, A., Springer, Heidelberg (under review), 2014d.

Selected oral presentations at conferences and workshops

- **Schreier, S. F.**: Estimates of forest fire NO_x emissions in Russia between 1998 and 2010. Young Scientists Summer Program Workshop, International Institute for Applied Systems Analysis, Laxenburg, Austria, August 2012.

- **Schreier, S. F.**: Vegetation fire emission coefficients derived from MODIS fire radiative power and GOME-2 tropospheric NO_2 measurements. Helmholtz Research School on Earth System Science, Annual Retreat, "Deutsches Auswandererhaus", Germany, November 2012.

- **Schreier, S. F.**: Estimation of NO_x emissions from vegetation fires based on the empirical relationship between tropospheric NO_2 and fire radiative power. AGU Fall Meeting, San Francisco, USA, December 2013.

Selected poster presentations at conferences and workshops

- **Schreier, S. F.**, Richter, A., Schönhardt, A., Burrows J. P.: Relationship between satellite-observed active fires and tropospheric NO_2. EGU General Assembly, Vienna, Austria, April 2012.

- **Schreier, S. F.**, Richter, A., Kaiser, J. W., Burrows J. P.: Biome-specific fire emission rates of NO_x from MODIS fire radiative power and GOME-2/OMI tropospheric NO_2 satellite-derived data sets. EGU General Assembly, Vienna, Austria, April 2013.

- **Schreier, S. F.**, Richter, A., Kaiser, J. W., Burrows J. P.: Using satellite measurements of tropospheric NO_2 and fire radiative power to derive biome-specific fire emission rates of NO_x. Davos Atmosphere and Cryosphere Assembly, Davos, Switzerland, July 2013.

- **Schreier, S. F.**, Richter, A., Schepaschenko, D., Shvidenko, A., Hilboll, A., Burrows, J. P.: Differences in NO_x emission factors between Eurasian and North American boreal forest fires. Helmholtz Research School on Earth System Science, Annual Retreat, "Botanika Bremen", Germany, November 2013.

- **Schreier, S. F.**, Peters, E., Richter, A., Wittrock, F., Burrows, J. P.: Ship-based MAX-DOAS measurements of nitrogen dioxide in the South China and Sulu Sea. EGU General Assembly, Vienna, Austria, April 2014.

- **Schreier, S. F.**, Richter, A., Kaiser, J. W., Schepaschenko, D., Shvidenko, A., Hilboll, A., Burrows, J. P.: NO_x emission factors from GOME-2 measurements for the major types of open biomass burning. EGU General Assembly, Vienna, Austria, April 2014.

- **Schreier, S. F.**, Richter, A., and Burrows, J. P.: Two-parameter approach for estimating biomass burning emissions of NO_x for the African continent. 13th IGAC Science Conference on Atmospheric Chemistry, Natal, Brazil, September 2014.

x

Acknowledgements

Die drei Jahre als Doktorand am Institut für Umweltphysik (IUP) in Bremen waren insgesamt eine durchaus positive Zeit. Ich habe mich in der Arbeitsgruppe sehr wohl gefühlt, und konnte mich für die Thematik stets interessieren. Dass ich die drei Jahre auf hohem professionellem Niveau und zugleich in einem so freundlichen Umfeld an meiner Doktorarbeit schaffen durfte, dafür danke ich besonders Prof. Dr. John P. Burrows. Meine Motivation war über die meiste Zeit erstaunlich hoch, und ist nur in manchen Fällen aufgrund unerwarteter Ereignisse gesunken. Gerade in solchen Situationen haben mir kurze Gespräche am Flur oder bei ihm im Büro wieder den nötigen Antrieb gegeben. Dass ein Professor neben seinen üblichen Verpflichtungen auch noch die Energie und Freude für anderweitige (freiwillige) Aktivitäten aufbringen kann, ist schon sehr beeindruckend.

Vielen Dank an dieser Stelle auch an Prof. Dr. Justus Notholt, der sich dazu bereit erklärte, als Zweitgutachter meine Dissertation zu bewerteten.

Den größten Anteil zum Gelingen meiner Arbeit hat Andreas Richter. Es müssen in den drei Jahren hunderte A4 Seiten gewesen sein, die er von mir gelesen und korrigiert hat. Die Tatsache, dass man solche Dinge in meist kurzer Zeit zurückbekommt, obwohl er so nebenbei noch viele andere Studenten und sonstige Arbeiten zu erledigen hat, ist einfach nur beeindruckend. Ich hatte schon beim Vorstellungsgespräch das Gefühl, dass es eine gute Zusammenarbeit werden würde. Es war damals die richtige Entscheidung, meine Dissertation in der DOAS Gruppe am IUP in Bremen zu beginnen. Ein besseres Umfeld könnte ich mir dafür gar nicht vorstellen. Vielen Dank auch fürs Korrekturlesen meiner Einleitung und die damit verbunden Verbesserungsvorschläge.

Für die finanzielle Unterstützung sowie für die Möglichkeit, mich ständig mit anderen Doktoranden austauschen zu können, danke ich Klaus Grosfeld, Helge Meggers, Stefanie Klebe und allen weiteren Mitgliedern der *Earth System Science Research School* (ESSReS). Ich habe die Flexibilität, die man als interner Doktorand genießen durfte, immer sehr geschätzt. Die Lehrveranstaltungen, Seminare, und vor allem die Exkursionen und Soft-Skill Kurse werden mir noch lange im Gedächtnis bleiben.

Allen anderen Mitgliedern der DOAS Gruppe danke ich für die netten Gruppenmeetings samt der interessanten Vorträge und diversen Kuchenvariationen. Die gemeinsamen Stunden auf dem Weg zur sowie in der Mensa waren immer angenehm. Die kreativen Bastelstunden mit Euch haben auch immer wieder Spaß gemacht. Namentlich hervorheben möchte ich an dieser Stelle Jia Jia und Leonardo Alvarado. Beide haben gleichzeitig mit mir angefangen und mir gezeigt, dass aus Kollegen auch Freunde werden können, ja sogar gute Freunde. Ich danke Euch für die vielen privaten Geschichten, die Ihr mit mir geteilt habt, und die ich mit Euch teilen durfte. In meinem Büro herrschte stets eine nette Atmosphäre. Mein Dank richtet sich an meine Bürokollegen Tim Bösch, Maksym Chirkov, Achim Zien und Mathias Begoin.

Bei allen Doktoranden aus der ESSReS Gruppe bedanke ich mich für die gemeinsamen Stunden in Lehrveranstaltungen, Seminaren, Kursen und Exkursionen. Mit einigen von Euch durfte ich auch außerhalb der Universität so einige Stunden verbringen, und manchmal sogar über andere Themen als die Doktorarbeit reden.

Schließlich möchte ich mich auch bei sämtlichen IUP Mitarbeitern für interessante Seminarvorträge und sonstige gemeinsame Aktivitäten wie Weihnachtsfeier, Chor oder Fußball bedanken.

Glücklicherweise habe ich auch Menschen außerhalb der Universität kennengelernt. Aus einer dieser Bekanntschaften wurde über die Jahre eine sehr gute Freundschaft. Die vielen Samstage bei Dir waren eine willkommene Abwechslung und meist sogar produktiv. Herzlichen Dank, Horst.

Der Umzug nach Bremen hätte ohne die Hilfe meiner besten Freunde nicht annähernd so reibungslos funktioniert. Es war mir auch immer eine Freude, wenn Ihr mich in Bremen besucht habt. „Bowling und Bier", sage ich nur. Aber bestimmt nie wieder am Vorabend Eurer Abreise …

Meinen Eltern, Johanna und Friedrich, aber auch meiner Schwester Sabine danke ich für die vielen Telefonate und die gelegentlichen Besuche in Bremen. Und wenn ich mal ein Wochenende bei Euch zu Hause war, dann durfte ich mich für einige Tage verwöhnen lassen und das Familiengefühl genießen. Danke, dass Ihr immer für mich da seid.

Contents

List of abbreviations

AATSR   Advanced Along Track Scanning Radiometer

AfN   Africa North

AfS   Africa South

AMFs   Air Mass Factors

ANE   Africa North of Equator

AOD   Aerosol Optical Depth

ARCTAS   Arctic Research of the Composition of the Troposphere from Aircraft and Satellites

ASE   Africa South of Equator

ATSR   Along Track Scanning Radiometer

AVHRR   Advanced Very High Resolution Radiometer

B3dCTM   Bremen 3d CTM

BAMFs   Box Air Mass Factors

BREAM   Bremian advanced MAX-DOAS retrieval algorithm

CCD   Charge-Coupled Device

CFC   Chloro-Fluoro-Carbons

CINDI   Cabauw Intercomparison campaign for Nitrogen Dioxide measuring Instruments

CSA   Central South America

CTM   Chemical Transport Model

DOAS   Differential Optical Absorption Spectroscopy

DTM   Digital Terrain Model

ECMWF   European Centre for Medium-range Weather Forecasts

ECs   Emission Coefficients

EFs   Emission Factors

EOS   Earth Observing System

ERS   European Remote Sensing satellite

ESA   European Space Agency

EUMETSAT   EUropean organisation for the exploitation of METeorological SATellites

EUR	Eurasia
FERs	Fire Emission Rates
FRE	Fire Radiative Energy
FRESCO+	Fast REtriveal Scheme for Clouds from the Oxygen A-band
FRP	Fire Radiative Power
FTIR	Fourier Transform Infrared Spectroscopy
GFAS	Global Fire Assimilation System
GFED	Global Fire Emission Database
GLC	Global Land Cover
GOES	Geostationary Operational Environmental Satellite
GOME	Global Ozone Monitoring Experiment
GOME-2	Global Ozone Monitoring Experiment-2
GPW	Gridded Population World
GRUMP	Global Rural-Urban Mapping Project
GWEM	Global Wildland fire Emission Model
HYSPLIT	HYbrid Single-Particle Lagrangian Integrated Trajectory
IBBI	Interdisciplinary Biomass Burning Initiative
IFS	Integrated Forecast System
IR	Infrared
ITCZ	Inter-Tropical Convergence Zone
LPJ-DGVM	Lund-Potsdam-Jena Dynamic Global Vegetation Model
MACC	Monitoring of Atmospheric Composition and Climate
MAX-DOAS	Multi-AXis Differential Optical Absorption Spectroscopy
MetOp	Meteorological Operational satellite
MODIS	MODerate resolution Imaging Spectroradiometer
MOZART	Model for OZone And Related chemical Tracers
MSG	Meteosat Second Generation
NAM	North America
NASA	National Aeronautics and Space Administration

NAU	Northern Australia
NDVI	Normalized Differential Vegetation Index
NIR	Near Infrared
NOAA	National Oceanic and Atmospheric Administration
OMI	Ozone Monitoring Instrument
PEM	Pacific Exploratory Mission
P_f	Production rates of NO_x from fire
PSCs	Polar Stratospheric Clouds
RETRO	REanalysis of the TROpospheric chemical composition
RTM	Radiative Transfer Model
RV	Research Vessel
SAMBBA	South AMerican Biomass Burning Analysis
SCD	Slant Column Density
SCIAMACHY	SCanning Imaging Absorption spectroMeter for Atmospheric CHartographY
SEA	Southeast Asia
SEVIRI	Spinning Enhanced Visible and InfraRed Imager
SHIVA	Stratospheric ozone: Halogen Impacts in a Varying Atmosphere
SPOT	Systeme Pour l'Observation de la Terre
SSA	Single Scattering Albedo
TVC	Tropospheric Vertical Columns
UV	Ultraviolet
VCD	Vertical Column Density
VOCs	Volatile Organic Compounds
VRS	Vibrational Raman Scattering

List of figures

List of tables

Motivation

Some parts of the world burn every year. Australia is one of those places, where fires can break out and spread over large grassland areas. Such wildfires are burning in largely unpopulated regions in Central Australia. The areas in the north comprise eucalyptus woodland and savanna fires. Agricultural fires dominate Asia and Southeast Asia with crop cultivation fires in China, Thailand, and the Punjab region in India. Pastoral maintenance fires and fires that are used to clear the tropical rainforest for agriculture and grazing are found in the Amazon basin of South America. In a more irregular cycle, catastrophic forest fires cover large areas in Russia, where the vegetation takes a long time to recover. Africa is per se the fire continent of the world. As healthy green vegetation dries, these areas are consumed by sweeping waves of fire that move from north to south and from south to north – each season. The fires in Africa are primarily grassland and savanna fires, but there are also management fires associated with agriculture and maintenance. Giglio et al. (2013) have recently estimated the annual averaged global burned area for the first decade of the 21st century at 3.5 million square kilometers – slightly larger than the size of the Indian subcontinent.

Although wildfires are a part of nature, as they play a key role in shaping ecosystems including the stimulation of growth, such fires can have serious impacts on wildlife habitat. Moreover, the rapid oxidation of fuel in the chemical process of combustion is accompanied by the release of various reaction products. The ejection of emission constituents into the atmosphere affects atmospheric chemistry, air quality, and climate. Hence, fires – either ignited by lightning strikes or induced by humans – can have harmful consequences for human health and the environment.

Global totals of fire emissions from open biomass burning for the entire globe have so far been calculated by the aggregation of local statistics. For example, one of the most prominent bottom-up emission inventories – the Global Fire Emission Database (GFED) – is based on four parameters including burned area and emission factors (van der Werf et al., 2010). While burned area is obtained from satellite measurements, the parameters fuel load and combustion completeness are derived from model simulations.

Due to the uncertainties associated with these parameters, the estimation of total biomass burned within a specific region or even on the entire globe is still a challenging task. A more recently developed approach for the global estimation of open biomass burning emissions is the Global Fire Assimilation System (GFAS). In comparison to GFED, the number of input parameters is reduced as the satellite-derived fire radiative energy used in GFAS substitutes burned area, fuel load, and combustion completeness (Kaiser et al., 2010). This is precisely where the advantage lies, and where the intensive research in this field is already making sense. Although fire radiative energy provides detailed information about the amount and rate of biomass consumption over large areas, the approach to compute this parameter for the entire globe is still at an immature stage, given the coarse temporal resolution of polar-orbiting satellites and the lack of validation. The translation of biomass consumption into trace gas emissions is inevitably based on emission factors, which are predominantly and extensively investigated under controlled laboratory conditions and/or estimated from measurements by in-situ instruments in the field. While the advantage of investigations performed in the laboratory is the reliability and precision of measurements and the control over boundary conditions, natural wildfire conditions are difficult to reproduce. In contrast, in-situ measurements in the field are performed under natural wildfire conditions. However, such observations are sparse and cover only small areas on the ground level (Andreae and Merlet, 2001).

Aircraft-based in-situ measurement campaigns such as the ARCTAS (Arctic Research of the Composition of the Troposphere from Aircraft and Satellites) and the more recently conducted SAMBBA (South AMerican Biomass Burning Analysis) campaign aimed at investigating the properties of biomass burning pollution over boreal and tropical forest fires, respectively (Jacob et al., 2010; Morgan et al., 2013). While such aircraft-based observations provide detailed vertical information about the chemical composition of smoke from individual fires, they can only produce 'snapshots' both in a spatial and temporal sense.

Since the launch of the Global Ozone Monitoring Experiment (GOME) on board ESA's polar-orbiting ERS-2 satellite in 1995 (Burrows et al., 1999), NO_2 total and tropospheric vertical columns have been retrieved from nadir measurements. The retrieval of

tropospheric NO_2 amounts is based on the analysis of electromagnetic radiation as produced by the Sun and passing through the Earth's atmosphere, being reflected at the Earth's surface and scattered in the atmosphere, and travelling back to the space-based instrument. More specifically, the Differential Optical Absorption Spectroscopy (DOAS), which utilizes Beer-Lambert's law, is applied for these space-based retrievals. The GOME sensor and subsequent satellite missions including the spectrometers SCIAMACHY (SCanning Imaging Absorption spectroMeter for Atmospheric CHartographY) on board ESA's ENVISAT (Burrows et al., 1995), the Ozone Monitoring Instrument (OMI) on board NASA's Aura satellite (Levelt et al., 2006), and the second Global Ozone Monitoring Experiment (GOME-2) on board EUMETSAT's MetOp satellite platforms (Munro et al., 2000) enable the global view of tropospheric NO_2 and gather long-term data sets. Although these polar-orbiting satellites are limited to a maximum of one overpass per day in non-polar latitudes, weekly, seasonal, and interannual variability can be obtained.

In the industrialized parts of the world, anthropogenic emissions are the main source of NO_x in the troposphere. However, biomass burning including wildfires and intentional fires can be a large source locally, in particular in tropical and subtropical regions of Africa, Asia, and South America. While anthropogenic NO_x emissions have been the focus of many studies using satellite NO_2 observations (Richter et al., 2005; van der A et al., 2008; Beirle et al., 2011; Hilboll et al., 2013b), biomass burning has received much less attention. Only recently, the existing long-term data sets of satellite-derived tropospheric NO_2 from the various sensors have opened up completely new strategies for the characterization of NO_x from wildfires. Given their good spatial coverage, these measurements can capture wildfires in different biomes and regions.

The first and major part of this thesis is motivated by the lack of such satellite-based studies. The major objective was to elaborate on this topic by analyzing existing satellite measurements of tropospheric NO_2, fire radiative power, and other useful data sets for the characterization of NO_x emissions from open biomass burning. A simple strategy for the separation of different NO_x sources based on the empirical relationship between tropospheric NO_2 and fire radiative power is developed and fire emission rates of NO_x for different biomes and regions are estimated. For a better comparison with values

found in the literature and used in recent fire emission inventories, fire emission rates are converted into emission factors of NO_x. This thesis also intends to determine the extent of possible uncertainties arising from the use of constant emission factors instead of monthly resolved values in fire emission inventories – for the African continent.

Although satellite instruments can provide the global view of tropospheric NO_2, they are less sensitive to NO_2, and even less so for SO_2, in the lowermost layer of the troposphere close to the surface. For example, satellite-based observations of SO_2 emissions from international shipping still remain challenging. On the other hand, there has been much progress in monitoring tropospheric NO_2 and SO_2 from ground-based remote sensing techniques such as Multi AXis (MAX)-DOAS, which operates at different viewing and elevation angles. Most such existing measurement sites are located on land to observe either background levels in remote areas or pollution levels in large agglomerations and provide unique information for the comparison with satellite measurements. For tropical marine environments, for example, such data is sparse (Peters et al., 2012).

In the second part of this thesis, the focus is on the analysis and interpretation of unique ship-based MAX-DOAS measurements in order to gain new insights into tropospheric pollution levels in the coastal and open waters of the South China and Sulu Sea. These measurements, which were performed during the SHIVA ship campaign in November 2011, are used to analyze tropospheric NO_2 and SO_2 amounts by improved DOAS retrieval settings. The original motivation behind this analysis was the detection of biomass burning plumes, however, as it turned out, other interesting sources are more relevant.

This thesis is divided into seven parts. In the following Sect. 1, scientific background information about vegetation fires in the Earth system and methods behind the determination of emissions from such fires as well as their effects on human health and the environment are given. A brief overview of the Earth's atmosphere, the sources of NO_x and its relevance in terms of atmospheric chemistry is presented. Physics of the atmosphere comprising atmospheric radiative transfer are summarized and current remote sensing techniques including the DOAS technique and respective instruments

used for this thesis are described. A novel satellite-based approach for estimating fire emission rates of NO_x for various tropical and subtropical regions is presented in Sect. 2. The approach is modified and extended to include the boreal latitudes in Sect. 3. A simple conversion of fire emission rates into emission factors of NO_x and the provision of such values for the major types of open biomass burning can be found in Sect. 4. Possible uncertainties arising from the use of seasonally averaged instead of monthly resolved emission rates of NO_x for the estimation of annual biomass burning emissions for the African continent are evaluated in Sect. 5. Ship-based MAX-DOAS measurements taken during the SHIVA campaign are analyzed for tropospheric NO_2 and SO_2 in a tropical marine environment in Sect. 6. Finally, the major findings of this thesis are summarized, conclusions are drawn, and recommendations for further research work in this field are listed in Sects. 7 and 8.

Chapter 1

Scientific background

1.1. Fire in the Earth System

Fire is a part of the Earth system and plays a major role in the individual components such as the biosphere and atmosphere. For example, fire influences the biogeochemical cycles (e.g. carbon and nitrogen), atmospheric composition (e.g. carbon dioxide, carbon monoxide, nitrogen oxides), and the radiation balance of the Earth. With growing populations and increasing demand for food, fire became a necessary tool for several agro-economical systems. Besides the human-induced fires, uncontrolled wildfires ignited by lightning or volcanoes can spread over large areas, affecting ecosystems and biodiversity (Bowman et al., 2009).

The occurrence of vegetation fires is linked to a carbon-rich vegetation, seasonally dry climates, atmospheric oxygen, and ignition either by lightning, volcanoes, or by humans (Bowman et al., 2009). The global annual area burned was estimated at about 350 million hectares on average for the first decade of the 21st century (Giglio et al., 2013), with distinct and characteristic diurnal cycles, strong seasonality, and very large interannual variability at the regional scale (Giglio et al., 2010). Due to differences in intensity and frequency of fires and their associated wide variety of ecological effects, the term *fire regime* was established. Fire regimes are based on fuel type (ground, surface, and crown), spatio-temporal patterns (size, patchiness, rate of spread, seasonality, and frequency), and consequences such as impacts on vegetation and soils (Bond and Keeley, 2005).

Many topics have been the focus of recent efforts towards a better understanding of the influence of fire on atmospheric chemistry and climate. The Interdisciplinary Biomass Burning Initiative (IBBI) was recently initiated to better quantify the present and future impact of biomass burning emissions on the composition and chemistry of the Earth's atmosphere. Satellite observations of fires and emitted trace species, measurements of emission factors, and the development of dynamic emission factors are some of the

current topics being investigated to reduce uncertainties in estimated emissions from biomass burning (http://www.igacproject.org/BiomassBurning).

The term *biomass burning* denotes the burning of living and dead vegetation and includes lightning-induced wildfires and human-initiated burning of vegetation for land clearing and land-use change.

1.1.1. Fire in Earth's history

About 420 million years ago, and soon after the appearance of terrestrial plants, wildfires began to spread over large parts of the globe. Fire activity is always linked to atmospheric oxygen (O_2) levels, and combustion of dried-out vegetation occurs when these levels exceed 13%. Nowadays, O_2 levels are above 20% which favors the occurrence of fires. However, many Permian coals containing large amounts of charcoal indicate that in the past, O_2 amounts of up to 30% made even wet vegetation flammable (Scott and Glasspool, 2006).

The highly flammable savanna biomes have simultaneously spread in tropical and subtropical regions of Africa, America, and Asia. Warm temperatures and high light conditions lead to the expansion of C_4 plants that produce a 4-carbon molecule, whilst the first product of carbon fixation in cool season C_3 plants involves a 3-carbon molecule. Rapid growth of these C_4 plants in tropical and subtropical savannas and the linked production of fine fuels (e.g. grass) enhanced the occurrence of annual fires (Keeley and Rundel, 2005). Today, the largest area burned is found in savannas, which are moreover the greatest emission source among the individual biomes (van der Werf et al., 2010).

As soon as the oxygen level had stabilized around 10 million years ago and when humans first occupied Earth, fires were not exclusively a natural phenomenon anymore. The expansion of modern humans across the Earth later in time ultimately affected the global fire activity (see Fig. 1.1).
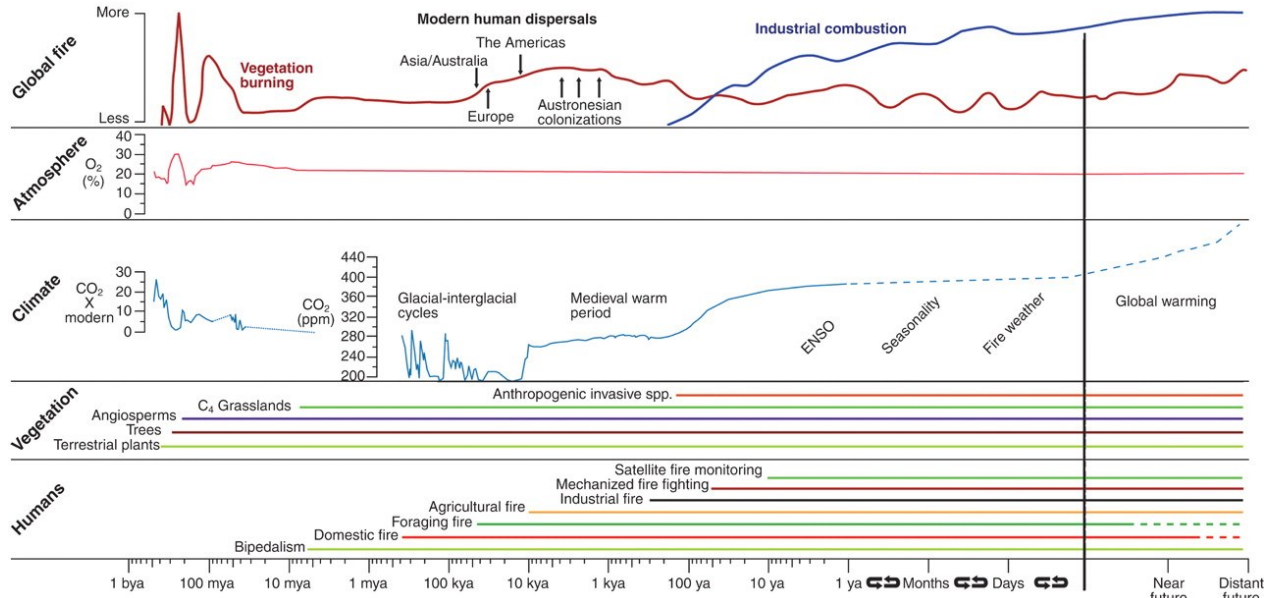
Fig. 1.1: Global fire activity in the past, present, and future. The schematic overview is based on distributions of charcoal, charcoal records, and modern satellite observations. Additional information is given about atmospheric O_2 and CO_2 amounts, vegetation, and the role of humans (from Bowman et al., 2009).

Although fire has been a natural part of the Earth system for many million years, human beings have provided a new source of ignition other than from lightning or volcanoes. Nowadays, fires in all ecosystems are mainly started by humans, either intentionally or by accident (Archibald et al., 2012).

1.1.2. The role of humans

Early hominids originated from highly flammable savanna ecosystems, where they had to adapt to the fire regime and learned how to use and manage fire (Ségalen et al., 2007). Strong signals in fossil records such as smaller teeth and stronger female body mass linked to reduced digestive efforts and increased supply of food energy, respectively, indicate that cooked food might have appeared about 1.9 million years ago (Wrangham et al., 1999). Reliable evidence for controlled fires only appears in archeological records within the last 400,000 years. For example, habitual use of fire by middle Pleistocene hominids was evidenced by burnt remains found in Paleolithic layers

of a cave in Israel (Karkanas et al., 2007). Around 50,000 to 100,000 years ago, the domestic use of fire has begun (Bar-Yosef, 2002) and is still practiced in large parts of the world, especially in developing countries throughout the tropics and subtropics (Sundell, 2004).

1.1.3. Recent and future changes in fire regime

Although fire is episodic in nature, there is clear evidence that climate is the major driver of larger fires. While exceptionally wet periods can create substantial amounts of fuel, the severity or size of a fire is largely determined by drought conditions during the dry season (Westerling et al., 2006). The link between climate and fire activity has also been observed on longer time-scales, such as interannual- and decadal-scale climate oscillations. For example, exceptionally strong rainfalls during the La Niña event in 2010-2011 created higher amounts of fuel in large parts of northern Australia (Letnic et al., 2013), which were then consumed by wildfires later in 2011, causing unusual high levels of tropospheric NO_2 (Schreier et al., 2014a).

During the recent decades, large changes in fire regimes have been observed. In some tropical regions, deforestation has led to the transition of tropical forests into crop and pasture lands for increasing food production. However, deforestation has a negative effect on biodiversity and is responsible for more than 10% of the global increase in carbon dioxide (CO_2) (van der Werf et al., 2010). In the boreal zone, forest fires occur more frequently in regions with increasing percentage area affected by extreme droughts and less frequently in regions with increasing summer moisture (Girardin et al., 2009). However, longer than decadal-scale climate oscillations are difficult to analyze, as the global view of fires from satellite-based platforms only began in the 1980s (Langmann et al., 2009).

The observed historical and present changes in vegetation, fuels, and human activities can be used to identify possible future impacts of climate change on fire regimes. Hessl (2011) proposed three possible pathways of how climate change might alter fire regimes in the future:

- *Alteration of fuel condition* where ignition sources are frequent, the amount of fuel is massive, but the fuel moisture is high. Possible factors that could alter fuel conditions in moist temperate and boreal forests are changes in the length of the fire season, a shift in the fire season, higher frequency and longer duration of drought events, and/or changes in frequency of fire weather.
- *Changes in fuel loading* through increases in fuel loading due to other disturbances (e.g. insect outbreaks) or changes in density of fuels due to warmer and/or wetter conditions. Whether fire activity might decrease or increase due to changes in fuel loading largely depends on the type of biome. For example, reduced fire activity might occur in ecosystems where fuel continuity is already limited and future aridity is likely to reduce productivity. In contrast, future projections of increased precipitation might lead to higher fuel loads in semi-arid forests and thus, it is likely that both fire severity and emissions might increase.
- *Changes in ignitions* are expected in regions such as semi-arid forest environments, where convective and lightning activity is altered by climate change.

Current model predictions of future fire regimes in the boreal zone, for example, suppose (i) a doubling of the number of wildfires by the end of the 21st century, (ii) increases in the occurrence of catastrophic fires and fires that escape from control, (iii) substantial increases of burning severity, and (iv) changes in intensity and gas composition of fire emissions caused by increased soil burning (Flannigan et al. 2009). Linkage between catastrophic fires and large scale atmospheric anomalies becomes more clear (e.g. fire in the Russian Far East and flooding in China in 2003, fires in European Russia and flooding in Pakistan and India in 2010). Very likely, thawing permafrost and following aridization of typical landscapes in higher latitudes will lead to degradation and death of forests and explosive alteration of catastrophic fires (Shvidenko et al., 2012).

The already observed on-going changes in frequency and size of forest fires in Russia in the 21st century as a consequence of climate change is becoming quite evident (Shvidenko and Schepaschenko, 2013). Therefore, an exact knowledge of the impact of such fires on the nutrient budgets in terms of carbon/nitrogen being transferred from the

land to the atmosphere is desirable. As the effect of fire on the nutrient budgets is known to be crucial also in other regions, different methods for estimating fire emissions on the global scale have been developed.

1.1.4. Determination of fire emissions

Despite the large extent of vegetation fires and their environmental and human health related problems, the spatial extent and the seasonal variation of these fires were not fully perceived until the late 1970s. This can be explained by the sparse information about fires in many remote areas in the tropics and subtropics which are however, the main contributors to the global emissions produced by the combustion of biomass (Langmann et al., 2009).

The estimation of emissions for large areas and long-term periods has to be carried out in a simplified way as the whole combustion process is very complex. Seiler and Crutzen (1980) have introduced a general bottom-up approach (aggregation of disparate local statistics) for estimating the total amount of biomass burned, defined as the product of land area burned annually [km^2 yr^{-1}], the average organic matter or dry matter per unit area in the individual biomes [kg m^{-2}], the fraction of the average above-ground biomass relative to the total average biomass, and the burning efficiency of the above-ground biomass. Emission factors (see Sect. 1.1.4.3) for different trace gas and aerosol species can be used for the translation of total biomass burned into trace gas and aerosol emissions.

Although some problems of this simple formulation have become clear, for example the non-consideration of below-ground biomass such as peat, this general bottom-up approach is still in use in a modified way for estimating global fire emissions (Hoelzemann et al., 2004; Schultz et al., 2008; Thonicke et al., 2010; van der Werf et al., 2010; Kaiser et al., 2012). In a recent review by Langmann et al. (2009), the bottom-up equation can be found in the following formulation:

$$E_{(i)} = A * FL * CC * EF_{(i)},$$ (Eq. 1.1)

where the emissions (E) for a specific species (i) are calculated as the product of burned area (A), fuel load (FL), combustion completeness (CC), and emission factor (EF) for a specific species (i). Here, the average organic matter per unit area was replaced by fuel load which is not equal in that sense. For example, savanna vegetation consists of grasslands, bushes, and single trees, which are far apart from each other. These trees are protected from the rapidly moving grassland fires through their thick bark (Langmann et al., 2009). Only a fractional amount of the average organic matter per unit area is burned and thus, termed as fuel load.

A summary of the progress made in retrieving the individual parameters used for Eq. 1.1 to estimate biomass burning emissions is given in the following Sects. 1.1.4.1., 1.1.4.2., and 1.1.4.3. Global fire emission estimates of NO_x based on the bottom-up approach are given in Sect. 1.1.4.5.

1.1.4.1. Active fire and burned area

The detection of active fires from space, which demonstrated the global extent of fires for the first time, emerged with the availability of different satellite instruments such as the Advanced Very High Resolution Radiometer (AVHRR) on board the NOAA-series (Dozier, 1981; Matson and Dozier, 1981; Matson et al., 1984), the MODerate resolution Imaging Spectroradiometer (MODIS) on board Terra and Aqua (Kaufman et al., 1998; Justice et al., 2002), the Along Track Scanning Radiometer (ATSR) on board the ERS-2 satellite (Arino et al., 1999), and the Advanced ATSR (AATSR), which is a follow-up of ATSR on board of ENVISAT (Le Page et al., 2008).

The algorithm for detecting active fires from satellite instruments uses brightness temperatures derived from different channels (e.g. 4 and 11 µm). In general, such active fire detection is based on temperature threshold values for daytime and nighttime. Once the temperature of a pixel exceeds the given threshold value, the pixel is classified as a fire pixel. Water bodies, clouds, and sunglint are identified with external water and cloud masks, and reflectance in near-infrared channels, respectively (Justice et al., 2002).

The analysis of AVHRR images was based on active fire detection in specific regions and for shorter time periods (Cooke et al., 1996; Olson et al., 1999; Soja et al., 2004). However, attempts to use AVHRR in combination with the Normalized Differential Vegetation Index (NDVI) have shown that AVHRR is not best suited for the detection of burned area (Pereira, 1999).

Global fire activity patterns were first derived from ATSR and MODIS sensors for the nighttime and daytime, respectively (Arino and Plummer, 2001; Justice et al., 2002). First analysis of MODIS data showed that July, August, and September are the months with the highest global number of active fires, whereas in February least fires are detected. Indeed, fire activity is found for every month on our planet (Giglio et al., 2006b). While savannas are the dominant biomes burned globally, agricultural fires account for ~10% of annual global fire activity. Cropland burning in the Russian Federation, Ukraine, India, and China was found to contribute ~40% of global agricultural fires (Korontzi et. 2006). The most significant burning regions are located in Africa north and south of the Equator, Brazil, and Southeast Asia (Duncan et al., 2003).

Although an area can be easily detected by eye after the burning of vegetation due to its dark appearance, the detection of burned area from space is still a difficult task. However, such burned area products are more representative than active fires as the influence of cloudiness is less strong (Langmann et al., 2009).

Zhang et al. (2003) have mapped 2,764 fires with a total area of 41,792 km^2 during the Russian fire season in the year 2001 using data from Systeme Pour l'Observation de la Terre (SPOT) VEGETATION (VGT). The largest fire was found to spread over an area of 4,063 km^2 and the longest-lasting fire was burning for 3 months.

Tansey et al. (2004) presented a global inventory of monthly burned area from the SPOT-VGT at 1 km spatial resolution for the year 2000. Global burned area detection was also performed using ATSR-2 observations (Simon et al., 2004). However, first attempts towards estimating global burned area on a multi-year basis were based on the use of combined MODIS active fire observations and vegetation cover information. The global annual burned area was estimated between 2.97 x 10^6 and 3.74 x 10^6 km^2 for the years 2001-2004, with ~80% of burned area observed in Africa and Australia (Giglio et

al., 2006a). Giglio et al. (2010) combined active fire and burned area products from different satellite sensors in order to provide a high quality global and monthly burned area product for long-term trend analysis. It was shown that the total global annual burned area varied within 3.3 x 10^6 and 4.31 x 10^6 km^2 for the years 1997 to 2008 with maximum and minimum observed in 1998 and 2008, respectively. Daily, monthly, and annual global burned area estimation based on different satellite sensors was recently performed at 0.25° x 0.25° spatial resolution for the period 1995 to 2013 (Giglio et al., 2013). The global annual burned area varied within 3.01 x 10^6 and 3.77 x 10^6 km^2 for the years 1997 to 2011, with a net decreasing trend from 2000 to 2012 of 0.43 x 10^6 km^2 yr^{-1} (-1.2% yr^{-1}).

The global long-term average of burned area from the Global Fire Emission Database (GFED4) is presented as a fraction of grid cell in Fig. 1.2. As already outlined earlier, the largest areas burned are found in tropical and subtropical regions, in particular in Africa and Australia.
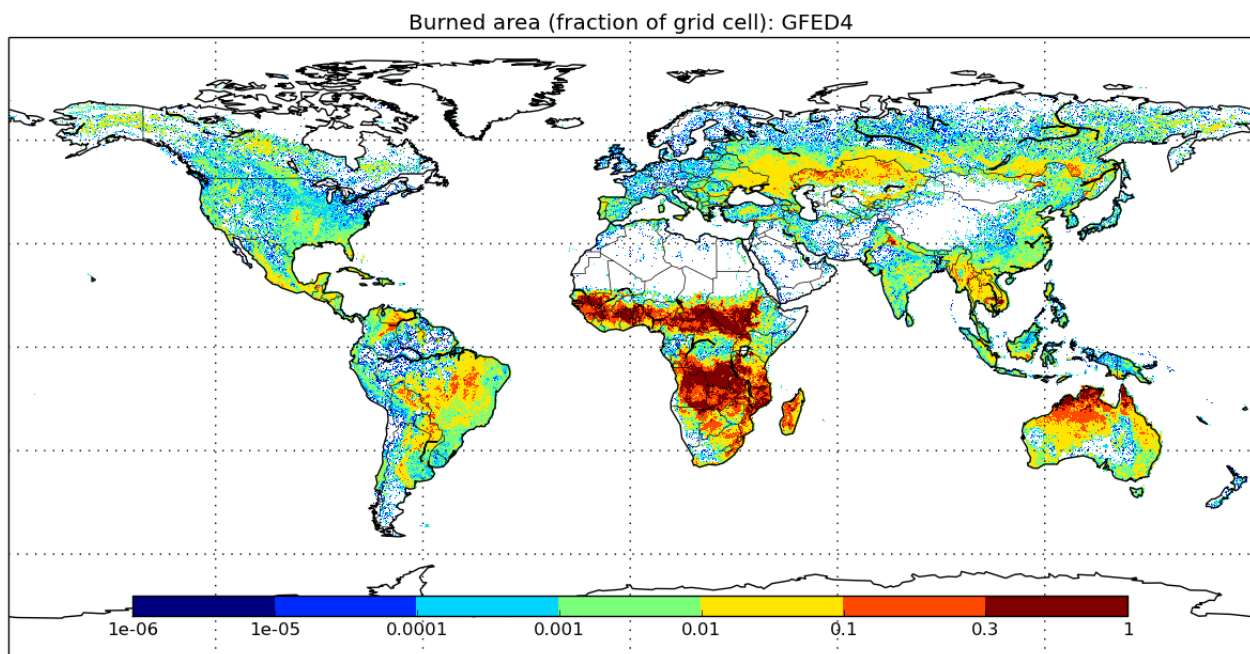
Fig. 1.2: Global distribution of burned area (fraction of grid cell) from GFED4 (from http://www.globalfiredata.org/index.html).

The detection of active fires and burned areas for providing information about the location and spatial extent of vegetation fires, respectively, is a prerequisite for modeling trace gas and aerosol emissions from biomass burning within the bottom-up approach. However, the type, composition and density, and moisture content of vegetation fluctuate on the spatio-temporal scale. Therefore, the inclusion of fuel load, combustion completeness, and emission factors as highlighted in Eq. 1.1 is essential for estimating trace gas and aerosol emissions from biomass burning.

1.1.4.2. Fuel load and combustion completeness

Fuel load depends on various factors including vegetation type, climate, soil type, recreation time after last disturbance (e.g. fire), and competing processes (Langmann et al., 2009).

Trollope et al. (1996) found that the experimental data of grass fuel loads from Southern Africa can be used for the extrapolation to similar savanna fires on the African subcontinent. For example, the fuel load in semi-arid savannas in Southern Africa was 4,295 kg ha^{-1} at sites that have been burned within every 4 years. In contrast, the fuel load was 5,772 kg ha^{-1} and 7,350 kg ha^{-1} for moist woodland and a similar site but slashed 4 years before, respectively. The higher value of the latter one arises due to additional woody debris from the earlier slashed woodland (Shea et al., 1996). Early studies have estimated the fuel load for each vegetation type by using production models driven by monthly rainfall data (Scholes et al., 1996). Besides the amount of rainfall, fuel load largely depends on the time since the last fire. Consequently, mean fuel loads in savanna increased with both increase in rainfall in the previous years and increase in post-fire age (Govender et al., 2006).

For some regions in Australia, it was found that rehabilitated mine sites can add up to some 17 t ha^{-1} fuel load after 17 years (Chaffey and Grant, 2000). For example, bauxite mines that have been restored to forest accumulated fuel loads of up to 30 t ha^{-1} after 8 years. The fire behavior in this region is mainly influenced by the high variability of available fuel (2-60 t ha^{-1}) (Smith et al., 2004). Interestingly, a study by Werner (2005) has pointed out the influence of buffalo grazing on fuel load. It was demonstrated that

buffalo grazing may reduce fuel load from 5-8 t ha^{-1} (without grazing) to 2-3 t ha^{-1} and thus, influences the fire intensity. In addition, burning followed by grazing is known to reduce available fuel loads to a higher degree than either burning or grazing alone (Kirkpatrick et al., 2011). Invasive grasses in semi-arid regions may also influence the fire regimes due to increasing fuel loads (Clarke et al., 2005). Occasionally, such invasive perennial grass types may even accumulate the available fuel load in arid regions which are actually fire-free (Rahlao et al., 2009).

In comparison to savanna vegetation, higher fuel loads in the range of 30-40 t ha^{-1} are observed in tropical moist mixed secondary deciduous forests. It was shown that fuel loads of different vegetation classes in southeastern India significantly affect the combustion process (Prasad et al., 2001).

The combustion efficiency or combustion completeness, which largely depends on moisture content, fire, and fuel type, is nowadays derived from biogeochemical models and defined as the fraction of the available fuel that is combusted during a vegetation fire (Langmann et al., 2009).

It was shown that the state of vegetation prior to the fire event determines both the intensity and completeness of combustion. In general, fragmented burned areas are characterized by lower combustion completeness (Lambin et al., 2003).

The product of burned area [km^2], fuel load [kg km^{-2}], and combustion completeness is used to estimate the total biomass burned [kg], either for a specific region or at the global scale. However, the estimation of trace gas emissions from the total biomass burned via the bottom-up method still relies on emission factors.

1.1.4.3. Emission factors

Emission factors (EFs) are used for the translation of biomass burned [kg] into trace species emissions [g kg^{-1}] and are thus expressed as the mass of a specific trace species emitted per mass of biomass burned.

EFs have so far been mainly derived from in-situ measurements of smoke, either in the laboratory or in the field. While in-situ measurements (e.g. from aircraft-based platforms) are precise for individual wildfires, they can only provide information about a rather small number of fires. On the other hand, measurements under controlled laboratory conditions do not sufficiently reproduce natural wildfire conditions including the size of the fire and fuel moisture (Andreae and Merlet, 2001; Yokelson et al., 2008). In the case of NO_x, EFs largely depend on the fire conditions (flaming vs. smoldering), which can vary greatly in space and time. High-temperature flaming combustion, for example, oxidizes nitrogen (N) more efficiently. Moreover, higher amounts of N in the fuel provide a source of N for the oxidation when temperatures are large enough (Andreae and Merlet, 2001).

Ortiz de Zárate et al. (2000) have carried out a field burning experiment in Spain to estimate EFs for cereal waste and suggested a value of 2.8 ± 0.2 g NO_x kg^{-1}. However, the mass of NO_x emitted during flaming combustion was three times higher than during smoldering combustion. Moreover, the fuel N content greatly affected the NO_x emissions. Ferek et al. (1998) obtained EFs from aircraft-based measurements for various vegetation fires such as forest, cerrado, and pasture fires in Brazil. They also found higher EFs of NO_x when the ratio of flaming to smoldering was increased. The production of NO_x was associated with flaming combustion and higher temperatures rather than combustion completeness. Soares Neto et al. (2011) reported average emission factors of 2.74 ± 0.75 g NO_x kg^{-1} for Amazon forest species burned in laboratory experiments. Interestingly, the NO_x emission factors for Indonesian fuels are lower than for African fuels, which could limit the ozone production within the smoke plumes (Christian et al., 2003).

Andreae and Merlet (2001) have summarized EFs for more than 100 trace species for savanna and grassland, tropical forests, extratropical forests, and agricultural residues, based on a large number of in-situ measurements. They have, however, not taken into account peat vegetation which is still a highly uncertain source of specific trace species emissions as the exact depth of burning into the soil is difficult to obtain. However, it is well known that such peat fires emit large quantities of carbon monoxide (CO) into the atmosphere, while the amount of NO_x is relatively low. An updated emission factor

compilation additionally provides EFs for pasture maintenance and subdivides extratropical forests into temperate and boreal forest (Akagi et al., 2011).

Current bottom-up fire emission inventories (Hoelzemann et al., 2004; Schultz et al., 2008; Thonicke et al., 2010; van der Werf et al., 2010), which are almost solely based on Eq. 1.1, depend on EFs for only few different land cover types. Moreover, the reported uncertainties of these NO_x EFs are in the range of ±50% (Andreae and Merlet, 2001; Akagi et al., 2011).

Table 1.1: Emission factors (EFs) of NO_x (in g kg^{-1}) as reported in emission factor compilations and applied in bottom-up fire emission inventories

	savanna and grassland	tropical forest	extratropical forest	agricultural residue	peat burning
Andreae and Merlet (2001)[a]	3.9±2.4	1.6±0.7	3.0±1.4	2.5±1.0	-
Hoelzemann et al. (2004)[b]	2.3	1.9	3.0	-	-
van der Werf et al. (2010)[b]	2.1	2.1	2.2	2.3	1.0
Akagi et al. (2011)[c]	3.9(0.8)	2.6(1.4)	1.12(0.69)	3.1(1.57)	-
Kaiser et al. (2012)[b]	2.3	3.4	3.4	2.3	2.3

[a] emission factor compilation by Andreae and Merlet (2011). Additional values show one standard deviation of the mean.

[b] bottom-up fire emission inventory

[c] emission factor compilation by Akagi et al. (2011). Values in parenthesis give an estimate of the natural variation.

For example, Hoelzemann et al. (2004) utilized emission factors of 2.32, 1.85 and 3.0 g NO_x kg^{-1} for savanna and grassland, tropical forests, and extratropical forests, respectively (see Table 1.1). More recent bottom-up fire emission inventories have used emission factors of 2.12, 2.1, and 2.19 g NO_x kg^{-1} (van der Werf et al., 2010) and 2.3, 3.41, and 3.4 g NO_x kg^{-1} (Kaiser et al., 2012), for savanna and grassland, tropical forests, and extratropical forests, respectively. The latter two studies have additionally included EFs for agricultural residue (2.3 g NO_x kg^{-1}) and peat burning (1 and 2.26 g NO_x kg^{-1}). The large discrepancy between the EFs used for peat burning can be explained by the difficulty in distinguishing between flaming and smoldering combustion in peat soils.

1.1.4.4. Fire radiative power *

Fire radiative power (FRP) is a parameter describing the radiant component of energy release from the fire and is quantified in the infrared (IR) spectral range (Kaufman et al., 1998). First analyses of satellite-based FRP measurements have indicated clear spatio-temporal differences in the energy radiated by active fires (Wooster and Zhang, 2004).
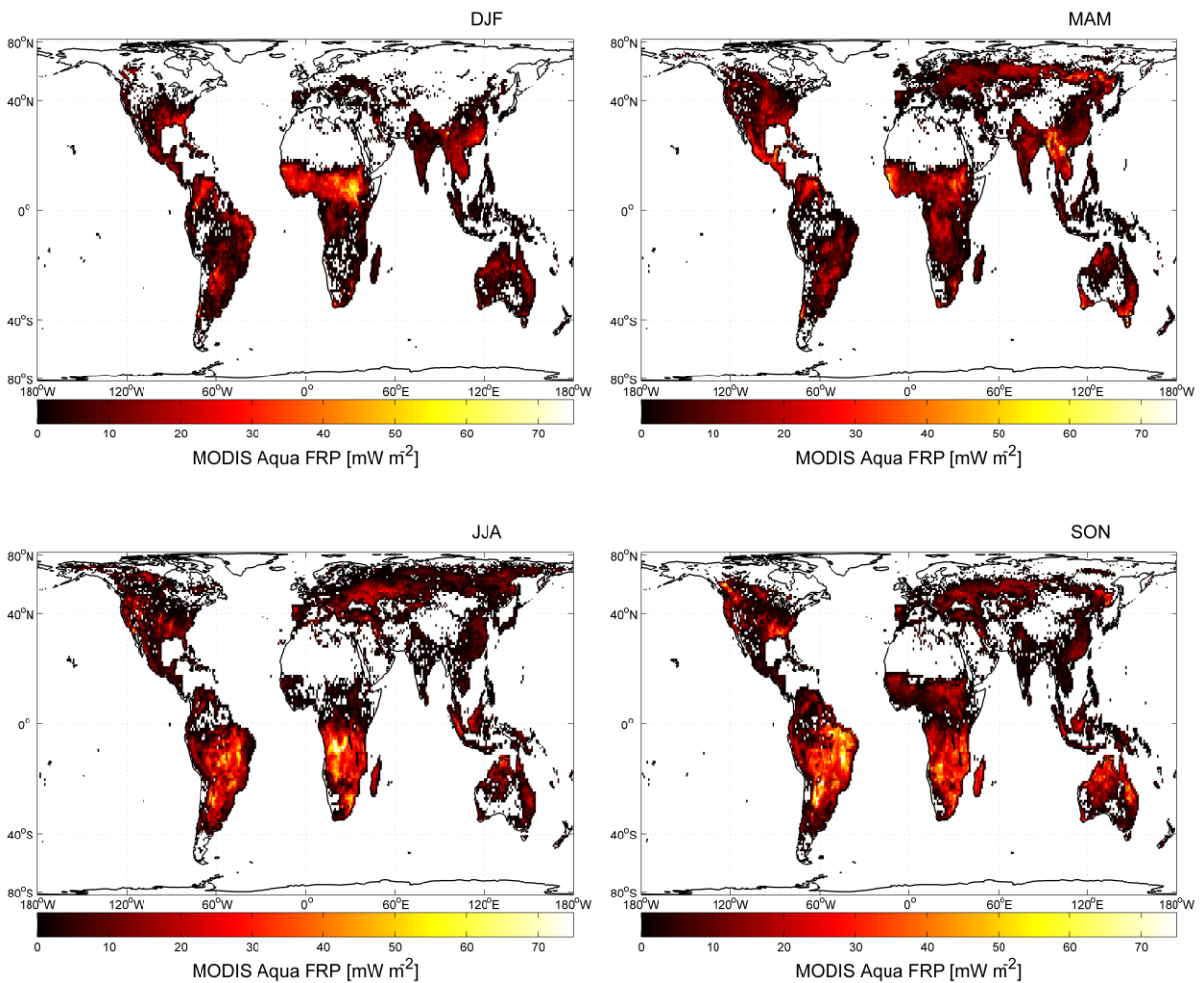
Fig. 1.3: Seasonal patterns of fire radiative power (FRP) from MODIS Aqua satellite for December, January, and February (DJF), March, April, and May (MAM), June, July, and August (JJA), and September, October, November (SON) averaged over the period 2007-2012 (data from ftp://fuoco.geog.umd.edu/modis/C4/cmg/monthly/hdf/).

* This subsection has been previously published as part of Schreier et al. (2014a).

The seasonal pattern of FRP as derived from MODIS on board Aqua is shown in Fig. 1.3. There are distinct spatio-temporal differences in FRP in the main biomass burning regions such as Africa north and south of the Equator. With diminishing rainfalls towards the dry season, vegetation gets drier and ignition frequency increases. Both fire intensity and number of fires reach their peaks with the summit of the dry season.

Wooster et al. (2005) have found proportionality between FRP and the combustion rate (the amount of a material that undergoes combustion over a period of time) and thus, proposed a universal conversion factor of 0.368 kg MJ^{-1}, which quantitatively links FRP to dry matter combustion rate. This approach, which substitutes burned area, fuel load, and combustion completeness, and moreover better accounts for the spatio-temporal variability of fires, was taken up again and implemented into the Global Fire Assimilation System (GFASv1.0). GFASv1.0 makes use of biome-specific conversion factors and assimilates daytime and nighttime FRP data for the calculation of the total biomass burned (Kaiser et al., 2012).

Ichoku and Kaufman (2005) have established a FRP-based method to derive smoke emission rates by using FRP measurements from MODIS on board the polar-orbiting satellites Terra and Aqua. They found differences in the emission strength among different regions and biomes. However, they also pointed out that the derived emission rates are most likely overestimated.

Geostationary FRP observations from the Spinning Enhanced Visible and Infrared Imager (SEVIRI) on board the Meteosat-8 satellite have been used to investigate the annual and diurnal cycle of open biomass burning in Africa. It was shown that the diurnal cycles differ markedly among the selected land cover types, but are very similar in both hemispheres. The typical diurnal cycle of FRP in African biomes is characterized by low fire intensity between 00:00 LT and 07:00 LT, followed by a sharp increase, peaking around 14:00 LT (Roberts et al., 2009).

Roberts and Wooster (2008) compared temporally coincident FRP measurements from MODIS and SEVIRI and found strong agreement when both sensors detected a fire successfully. Due to the coarser spatial resolution of SEVIRI, however, the summed FRP is underestimated as the lowest FRP fires are not detected. While MODIS benefits

from a higher spatial resolution, it measures only a few times per day and thus, the temporal integration of FRP is challenging. Freeborn et al. (2011) elaborated on this and combined SEVIRI and MODIS measurements to derive the fire radiative energy (FRE) for the African continent. At the continental scale, FRE estimated by MODIS observations is ~30% less than FRE estimated by MODIS coupled with SEVIRI measurements, taking into account low spatial resolution detection biases. They found that this underestimation can be attributed to the MODIS scan geometry and the typical calculation of the sum of FRP.

More details about FRP measurements are given in Sect. 2.2.2.

1.1.4.5. Estimating fire emissions

The most common approaches for estimating fire emissions of NO_x (reported as NO) on the global scale are based on Eq. 1.1. For example, global fire emissions have been estimated at 8.08 g NO_x for the year 2000 by implementing GLOBSCAR burned area and simulated data from the Lund-Potsdam-Jena Dynamic Global Vegetation Model (LPJ-DGVM) into a Global Wildland Fire Emission Model (GWEM) (Hoelzemann et al., 2004). Fire emissions constructed for the REanalysis of the TROpospheric chemical composition over the last 40 years (RETRO) are reported at 4.6 Tg NO_x yr^{-1} on average for the period 1960 to 2000 (Schultz et al., 2008). Another approach, which uses a process-based fire regime model (SPITFIRE) and is coupled with LPJ-DGVM, reports an average release of 15 Tg NO_x yr^{-1} from biomass burning during the 1980s and 1990s (Thonicke et al., 2010).

Annual average global fire emissions presented in the Global Fire Emission Database (GFEDv3) are 9.5 Tg NO_x yr^{-1} on average for the period 1997-2009 (van der Werf et al., 2010). Kaiser et al. (2012) reported annual average global fire emissions of NO_x in the same order of magnitude as van der Werf et al. (2010). However, both approaches are based on MODIS fire products and use similar values for savanna and grassland, which is the dominant type of open biomass burning. A summary of average annual emissions of NO_x from open biomass burning is presented in Table 1.2.

Table 1.2: Average annual emissions of NO$_x$ from open biomass burning (in Tg NO$_x$, as NO) for the globe and specific regions. Emission estimates are taken from van der Werf et al. (2010) and Kaiser et al. (2012).

	global	NAme	CAme	SAme	Euro	NHAf	SHAf	NAsi	SAsi	TAsi	Aust	EoMo
van der Werf et al. (2010)	9.431	0.505	0.203	1.428	0.084	2.058	2.700	0.837	0.517	0.517	0.582	0.017
Kaiser et al. (2012)	9.529	0.632	0.308	1.589	0.159	1.891	2.293	1.179	0.607	0.272	0.594	0.025
percent difference	1.03	22.34	41.1	10.67	61.73	8.46	16.3	33.93	16.01	62.1	2.04	38.1

NAme (North America; 30°N - 75°N, 170°W - 30°W), CAme (Central America; 0° - 30°N, 170°W - 30°W), SAme (South America; 60°S - 0°, 170°W - 30°W), Euro (Europe; 30°N - 75°N, 30°W - 60°E), NHAf (North Africa; 0° - 30°N, 30°W - 60°E), SHAf (South Africa; 35°S - 0°, 30°W - 60°E), NAsi (North Asia; 30°N - 75°N, 60°E - 170°W), SAsi (South Asia; 10°N - 30°N, 60°E - 170°W), TAsi (Tropical Asia; 10°S - 10°N, 60°E - 170°W), Aust (Australia; 50°S - 10°S, 60°E - 170°W), and EoMo (East of Moscow; 50°N - 60°N, 35°E - 55°E).

Due to the uncertainties in the individual parameters, there still exist large differences of up to 80% between the individual approaches (Granier et al., 2011). It is expected that inventories based on the bottom-up method are limited even in the near future due to large uncertainties in the emission factors, the depth of burning into the soil (e.g. peat fires), the variability in fuel load and the limited spatial resolution and geo-location issues of burned area. However, recent efforts towards the use of fire radiative power for estimating emissions may reduce these uncertainties considerably (Kaiser et al., 2012). Other efforts are directed towards gaining information about the spatio-temporal variability of EFs using satellite-based measurements (Mebust and Cohen, 2013; Castellanos et al., 2014; Schreier et al., 2014a).

1.1.5. Impacts on the environment and human health

The majority of outdoor biomass burning occurs in developing countries throughout the tropics and subtropics. Clearing land for shifting cultivations, conversion of forests to agricultural or pastoral land, and removing dry vegetation for promoting agricultural productivity are the dominant intentions for the burning of vegetation. In such cases, the

local water and soil resources as well as air quality are affected on the short-term and in some cases even on the long-term scale.

The emissions of aerosols can largely decrease the visibility and thus, directly affect main infrastructures. For example, smoke plumes from fires in Indonesia can reduce the visibility in nearby cities such as Singapore to less than 1 km. Consequently, irregularities in the operation of infrastructures such as airports, highways, and hospitals may arise (Goldammer, 2008). Heavy metals, which can be contained in large amounts in ash of fires, can affect the environment when released to soil and water resources. Such excessive amounts of heavy metals can have coercive effects on human health (Pereira and Úbeda, 2010).

The smoke plumes of vegetation fires generally consist of water vapor, reactive (including nitrogen oxides (NO_x)) and non-reactive gases (including carbon dioxide (CO_2)), volatile organic compounds (VOCs), semi-volatile compounds, particulates, and many other compounds. Smoke plumes may contain toxic compounds such as respiratory irritants (including NO_2, ozone (O_3), and ammonia (NH_3)), asphyxiants (including CO_2), carcinogens (including formaldehyde (HCHO) and benzene (C_6H_6)) and mutagens (including toluene (C_7H_8)). These toxic compounds endanger human health to a large extent (Goldammer et al., 2008). A recent satellite-based study detected 14 rare gases in a pyrocumulus cloud, which originated from Australian bush fires in the year 2009 (Clarisse et al., 2011).

Short-term or chronic exposure to elevated trace gas concentrations and to aerosols released from biomass burning can cause adverse human health effects (Goldammer, 2008). The population of specific regions in Brazil with frequent sugar cane burning during the dry season, for example, is exposed to high pollution levels with the health effects greatly depending on exposure time (Cancado et al., 2006).

In contrast to urban air pollution studies, which are commonly carried out over a time period of several years (Zemp et al., 1999), the examination of vegetation fire emissions affecting human health is more complicated due to the shorter duration of these fires. Consequently, there is a lack of studies analyzing the effect of biomass burning emissions on mortality but also on long-term health effects as they are difficult to detect

(Dennekamp and Abramson, 2011). However, many of these urban air pollution studies with chemical mixtures similar to biomass smoke found evidence for the relationship between air pollution and mortality. Therefore, the exposure to biomass burning emissions appears to increase the risk of mortality (Frankenberg et al., 2005). In general, children are more affected than adults as the amount of particulates inhaled is higher relative to their body size (Sastry, 2002). In a recent study, it was shown that the population may even be affected by far-away wildfires as a result of long-range transport of smoke plumes (Hänninen et al., 2010).

Appropriately targeted measures to reduce the extent of vegetation fires should receive more attention as many humans are affected by smoke. Currently, the opposite is taking place as the frequency of both accidental and intentional fires increased during the last decades, especially in higher latitudes (Mollicone et al., 2006; Bell and Adams, 2008).

1.2. The Earth's atmosphere

About 4.6 billion years ago, the solar system was formed through condensation of an interstellar cloud of gas and dust. As a result of trapped volatile compounds from the planet itself, the atmosphere of the Earth has been formed. The original Earth's atmosphere was composed of carbon dioxide (CO_2), nitrogen (N_2), and water vapor (H_2O), with little amounts of hydrogen (H_2). These compounds are emitted from present-day volcanoes and thus, it is believed that the early atmosphere was produced by outgassing from the Earth's surface and volcanic eruptions (Seinfeld and Pandis, 2006).

While most of the water vapor condensed out of the atmosphere to form oceans and due to the fact that large amounts of atmospheric CO_2 formed sedimentary carbonate rocks after dissolution in the oceans, the chemically inert, non-water-soluble, and non-condensable N_2 accumulated over geologic time to become the most abundant constituent of the present atmosphere (Seinfeld and Pandis, 2006).

With strongly increasing amounts of oxygen (O_2) produced by bacteria, beginning about 2.3 billion years ago, the atmosphere became more and more oxidizing. In contrast to the original and slightly reduced atmosphere, the present one is strongly oxidizing. The

balance between production from photosynthesis and the removal through respiration maintains the present atmospheric O_2 levels (Seinfeld and Pandis, 2006).

Today's atmosphere is a gaseous layer, which is mainly composed of N_2 (78%), O_2 (21%), and Argon (Ar) (0.93%), surrounds our planet and is retained from Earth's gravity, separating the Earth's surface from space. While the concentrations of these main compounds are rather constant, concentrations of the next most abundant constituent – H_2O – is highly variable (Seinfeld and Pandis, 2006).

The remaining gaseous constituents represent less than 1% of the atmosphere and thus, they are referred to as *trace gases*. In terms of radiative forcing (e.g. the difference between insolation absorbed by the Earth and energy radiated back to space), these trace gases play a crucial role because they act as atmospheric thermal insulators. The concentrations of these so-called *greenhouse gases*, including CO_2, methane (CH_4), and nitrous oxide (N_2O), have increased dramatically throughout the past two hundred years (IPCC, 2013).

Moreover, trace gases can affect the chemical properties of the atmosphere. For example, the emissions of halogenated trace gases generated by human activities caused a thinning of the stratospheric ozone (O_3) layer, which protects the biosphere from harmful ultraviolet (UV) radiation from the sun. Observations have shown that the ozone layer has even disappeared in the Antarctic stratosphere during the austral spring. This well-known example of human impact on the composition of the atmosphere has been termed the *Antarctic ozone hole* (Seinfeld and Pandis, 2006).

Without the present mixture of gases in the atmosphere, life on Earth as we know would not exist. The atmosphere provides us with oxygen to breath, distributes water and heat, and removes harmful gases. Although the 'natural' state of the atmosphere is essential for supporting life of plants, animals, and humans on Earth, human activity has strongly affected the composition of the atmosphere – in particular trace gas abundances – with the beginning of industrialization in the 18th century (IPCC, 2013).

1.2.1. Structure and composition of the Earth's atmosphere

The mean pressure at sea-level is 1013.25 hPa and air temperature reaches about 15°C on average at the Earth's surface. While the pressure decreases monotonically with increasing altitude, there are distinct variations in temperature between the Earth's surface and the top of the atmosphere (see Fig. 1.4). According to the variation of the average temperature profile with altitude, the atmosphere can be divided into five layers (Seinfeld and Pandis, 2006).
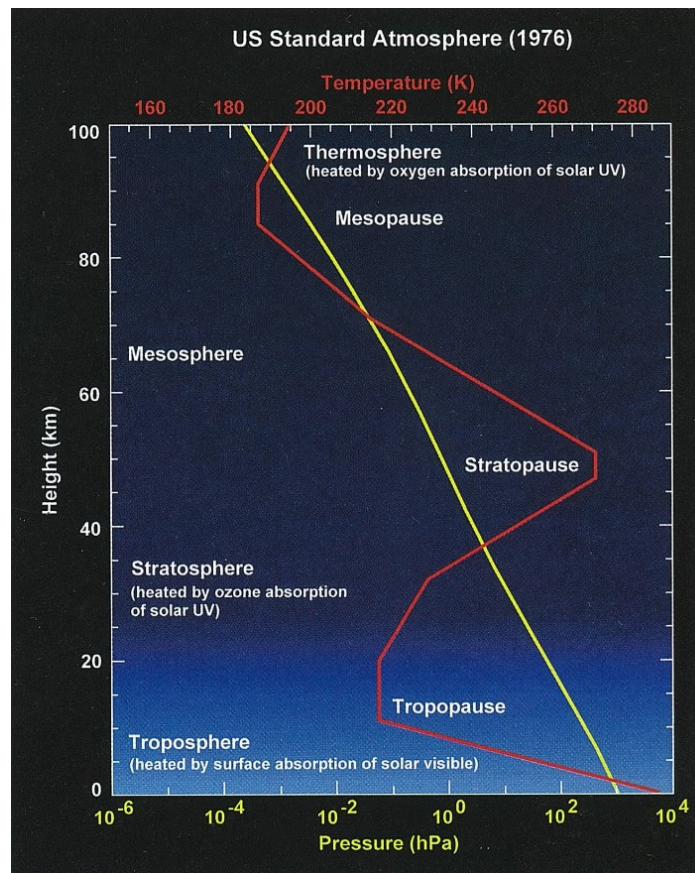
Fig. 1.4: Vertical profiles of atmospheric pressure (yellow) and temperature (red) based on US Standard Atmosphere for mid-latitudes (from Gottwald and Bovensmann, 2011)

- The lowermost layer of the atmosphere is the well-mixed troposphere that extends from the surface to about 8 and 18 km at the poles and at the Equator, respectively. However, the altitude of the tropopause can change with latitude and time of year. The troposphere can be further subdivided into the planetary

boundary layer and the free troposphere. A decreasing temperature with height and rapid vertical mixing (see Sect. 1.4.1) are the main characteristics of the troposphere. In spite of the relatively low height (compared to the total height of the atmosphere), the troposphere contains about 80% of the atmospheric total mass.

- The poorly mixed stratosphere is the layer above the troposphere and reaches up to about 50 km altitude. In contrast to the troposphere, the temperature increases with altitude (from 20 to 50 km) and vertical mixing is slow. The increase in temperature with increasing height is a result of absorption of solar ultraviolet radiation by O_3.

- The mesosphere, which is characterized by a decrease of temperature with altitude and rapid mixing, extends from the stratopause (~45 to 55 km) to the mesopause (~80 to 90 km).

- In the thermosphere, temperatures increase again with increasing altitude due to absorption of short-wavelength radiation by N_2 and O_2.

- The outermost layer of the Earth's atmosphere is referred to as exosphere. In this region, planetary atmospheric gases with sufficient energy can escape to outer space.

As already outlined in Sect. 1.2, the Earth's atmosphere is mainly composed of naturally occurring gaseous compounds such as N_2 (78%), O_2 (21%), and Ar (0.93%) (Table 1.3). In addition, the atmosphere contains a large number of other gases referred to as trace gases – due to their relatively small concentrations – such as CO_2, CH_4, and N_2O. In contrast to these rather well-mixed greenhouse gases, reactive gases such as nitrogen dioxide (NO_2), sulphur dioxide (SO_2), and O_3 are highly variable in space and time. Another important species in the atmosphere are non-gaseous small liquid and solid particles suspended in air, referred to as *aerosols*. These trace species and aerosols are released and produced both naturally and anthropogenically and have only relatively low concentrations. However, they play a significant role in atmospheric chemistry, air pollution, and climate change, in particular in urban environments (WHO, 2003; IPCC, 2013), and moreover affect the retrieval of tropospheric NO_2 vertical columns (see Sect. 2.2.1).

Table 1.3: The main gaseous constituents of the unpolluted and dry atmosphere (from Platt and Stutz, 2008)

Gas and chemical formula	Mixing ratio by volume
Nitrogen (N_2)	0.7808
Oxygen (O_2)	0.2095
Argon (Ar)	9.3×10^{-3}
Carbon dioxide (CO_2)	0.37×10^{-3}
Neon (Ne)	18×10^{-6}
Helium (He)	5.2×10^{-6}
Methan (CH_4)	1.7×10^{-6}
Krypton (Kr)	1.1×10^{-6}
Xenon (Xe)	0.9×10^{-6}
Hydrogen (H_2)	0.5×10^{-6}
Dinitrogen oxide (N_2O)	0.3×10^{-6}

While the greenhouse gases CO_2, CH_4, and N_2O have a very noticeable impact on the climate system (see Sect. 1.2), reactive gases such as NO_2, SO_2, and O_3 significantly affect tropospheric chemistry, air pollution, and human health (IPCC, 2013).

1.2.2. Sources of nitrogen oxides (NO_x) in the troposphere *

Nitric oxide (NO) and nitrogen dioxide (NO_2) are coupled in the atmosphere as NO_2 is photolyzed to produce NO and an oxygen atom (O), which then reacts with molecular oxygen (O_2) to produce ozone (O_3). Major sources of NO_x are anthropogenic activities (e.g. high temperature combustion processes), biomass burning (intentional and accidental), soil microbial production from the oxidation of ammonium ions (NH_4^+) and the reduction of nitrate ions (NO_3^-), and lightning strikes (Lee et al., 1997). Minor tropospheric sources of NO_x include transport of from the stratosphere, oxidation of ammonia (NH_3), and the reaction of $O(^1D)$, which is produced by the photolysis of O_3 in the UVB (280–320 nm) and to a minor extent in the UVA (320–400 nm) with nitrous oxide (N_2O) (Olivier et al., 1994).

---

* This subsection has been previously published as part of Schreier et al. (2014a).
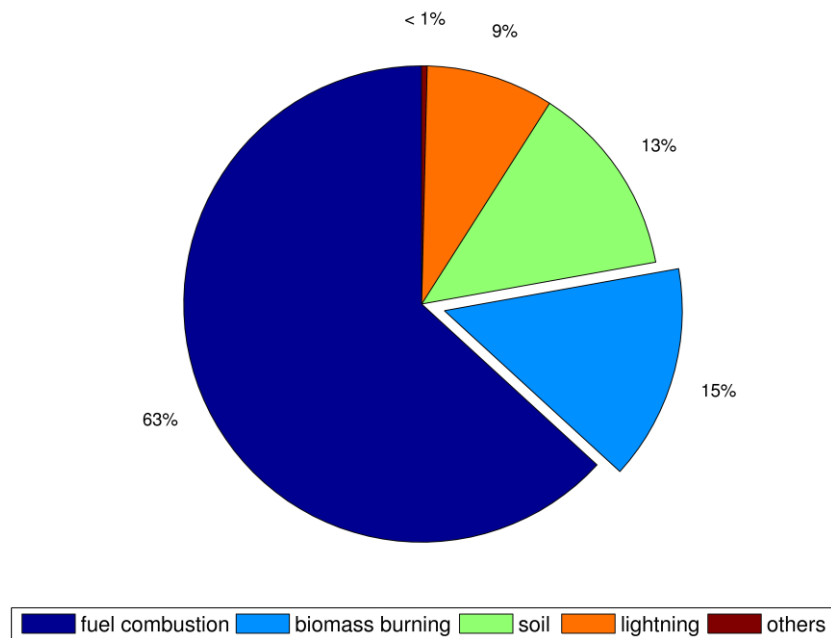
Fig. 1.5: Sources of NO$_x$ with their relative contribution to the global total. The values are taken from Jaeglé et al. (2005).

Total global NO$_x$ emissions have been estimated with bottom-up emission inventories and top-down approaches (using atmospheric understanding to quantify emissions) at about 40-45 Tg N yr^{-1} (Lee et al., 1997; Jaeglé et al., 2005; Miyazaki et al., 2012). The relative contribution of different NO$_x$ sources to the global total is presented in Fig. 1.5, based on values reported in Jaeglé et al. (2005). Although emission inventories are still affected by large uncertainties, NO$_x$ from fossil fuel combustion is estimated to contribute more than 50% to the total global NO$_x$ emissions (Lee et al., 1997; Miyazaki et al., 2012), with an annual release of 21–28 Tg N yr^{-1} (IPCC, 2007). Uncertainties of global NO$_x$ emission estimates are even larger for the natural sources of NO$_x$. Global emission estimates for soil emissions, biomass burning, and lightning, are in the range of 5–8 Tg N yr^{-1}, 6–12 Tg N yr^{-1}, and 3–7 Tg N yr^{-1}, respectively (IPCC, 2007).

1.2.2.1. Fossil fuel combustion

With the onset of a gradually increasing industrialization more than 150 years ago, atmospheric composition including NO_x has dramatically changed. Contemporaneously with the industrial revolution, a shift of rural communities to urban agglomerations together with growing populations have led to the formation of urban agglomerations of more than 10 million inhabitants, or so-called *megacities*. Increases in the combustion of fossil fuels for industrial production, traffic, and energy use and thus, increases in emitted NO_x and other air pollutants resulted in a degradation of air quality in these areas (Atkinson et al., 2000; Molina and Molina, 2004).

While satellite measurements indicated substantial reductions in NO_2 over populated areas in Europe and the USA during the period 1996 to 2004, increases were found over industrialized regions in China during the same period (Richter et al., 2005). Van der A et al. (2008) suggested a linear increase in NO_2 columns of 20% ±6% and 10% ±4% yr^{-1} (reference year 1996) for Shanghai and Beijing, respectively. A more recent study by Hilboll et al. (2013b), which is based on measurements from multiple satellite instruments for the period 1996 to 2011, highlighted the ongoing trends of tropospheric NO_2 over megacities. While the results of that study show decreasing trends of up to -6% yr^{-1} over industrialized countries, strong increases of tropospheric NO_2 of up to +20% were found over megacities in China and India.

1.2.2.2. Biomass burning

The emissions of trace gases and aerosols resulting from the combustion of biomass alter the atmospheric composition, air quality, and human health (see Sects. 1.1.5 and 1.3.2). Biomass burning as a dominant NO_x emission source in tropical regions was already mentioned by Cahoon et al. (1992). Moreover, the seasonal variation of NO_2 for African biomass burning regions, usually peaking during the dry season, was pointed out by van der A et al. (2008).

1.2.2.3. Microbial activity from soil

Another important source of NO_x emissions is related to bacteria in soils. NO is released as a by-product of microbial nitrification and denitrification in soils to produce NO_x emissions (Firestone and Davidson, 1989; Conrad, 1996). Soil emissions of NO_x largely depend on temperature, soil moisture, and soil N content (Stehfest and Bouwman, 2006). Large pulses of biogenic NO emissions occur during the onset of rains after a dry period (Davidson, 1992). Such pulsing events are associated with water-stressed nitrifying bacteria, which are activated by the rain and metabolize inorganic N in the soil. In comparison to background levels, pulsing events lasting for about 1-2 days can be 100 times as large (Yienger and Levy, 1995; Hudman et al., 2012). It was estimated that about 70% of global soil emissions take place in the tropics (Yienger and Levy, 1995).

1.2.2.4. Lightning

Lightning-produced NO_x mainly consists of NO (75-95%) and barely of NO_2 (Franzblau, 1991). O_2 and N_2 are partly dissociated to O and N in and close to the hot lightning channel. The formation of NO is then driven by the reaction between O and N_2 or N and O_2 (Goldenbaum and Dickerson, 1993). After rapid cooling of the lightning channel, large amounts of the formed NO are 'frozen-in' (Hill et al., 1980). Due to the rapid reaction of NO with O_3 to form NO_2, a photochemical balance between NO and NO_2 is reached during daytime (Levine et al., 1981). NO_x from lightning is mostly found in the tropics and certainly is the largest source of NO_x in the upper troposphere (WMO, 1995).

Beirle et al. (2004a) have related satellite measurements of lightning frequency and tropospheric NO_2 columns and estimated the globally produced lightning NO_x at 2.8 (0.8-14) Tg N yr^{-1}. A more recent study by Miyazaki et al. (2014) comprised an assimilation of multiple satellite data sets to estimate the global production of NO_x from lightning. Their estimated value (6.3 Tg N yr^{-1}) is more than two times larger than the estimate by Beirle et al. (2004a).

1.3. Chemistry of the Earth's atmosphere

The bulk of atmospheric species and about 90% of the total atmospheric mass reside in the troposphere. While some species are released from geological sources such as volcanic eruptions, some are generated in thunderstorms. However, many species are released from living organisms, whereby human activities play an increasing role (see Sect. 1.2.2.1). For some of the emitted species, the hydrosphere, cryosphere, and biosphere can act as a sink.

Tropospheric processes are largely influenced by meteorology as well as diurnal and seasonal variations in both the emission sources and solar illumination. As some compounds tend to contain elements in their lower oxidation states, tropospheric chemical change involves oxidation steps, before the compounds are highly soluble when fully oxidized. After the transformation of trace species into acids and other soluble compounds, they are removed from the atmosphere via wet (precipitation) and dry (aerosols) deposition.

In terms of NO_x removal in the troposphere, the following principal removal paths take place:

- During daytime, hydroxyl radicals (OH) react with NO_2 to form nitric acid (HNO_3).
- During nighttime, the nitrate radical (NO_3) reacts with NO_2 to produce dinitrogenpentoxide (N_2O_5) (see Sect. 1.3.2).

1.3.1. NO_x in the stratosphere

The role of NO_x in stratospheric chemistry was revealed by Crutzen (1970) and Johnston (1971) in the early 1970s. Their findings provided an important basis for understanding the stratospheric ozone chemistry (Seinfeld and Pandis, 2006).

The natural source of NO_x in the stratosphere is N_2O, which is produced by soil microbial activity and the ocean. Due to the fact that N_2O does not undergo reactions in the troposphere, it can slowly advect upward into the stratosphere. The main influx of

N$_2$O into the stratosphere occurs in the tropics. While about 90% of N$_2$O in the stratosphere is destroyed by photolysis (R 1),

$$N_2O + hv \rightarrow N_2 + O(^1D) \tag{R 1}$$

the remainder (10%) reacts with O(^{1}D) to produce NO, N$_2$, and O$_2$ (R 2-R 3).

$$N_2O + O(^1D) \rightarrow NO + NO \qquad\qquad (\sim58\%) \tag{R 2}$$

$$N_2O + O(^1D) \rightarrow N_2 + O_2 \qquad\qquad (\sim42\%) \tag{R 3}$$
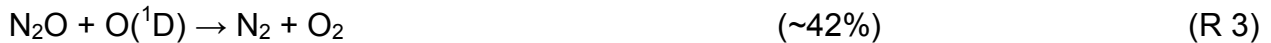
In the stratosphere, NO$_x$ directly controls O$_3$ amounts through the destruction of O$_3$ within the catalytic NO$_x$ cycle (R 4).

$$NO + O_3 \rightarrow NO_2 + O_2 \tag{R 4}$$

$$NO_2 + O \rightarrow NO + O_2 \tag{R 5}$$

When the concentrations of single O atoms are high enough, photodissociation of NO$_2$ to produce NO and O$_2$ will occur (R 5). Moreover, NO$_2$ photolysis (R6)

$$NO_2 + hv \rightarrow NO + O \tag{R 6}$$

is followed by:

$$O + O_2 + M \rightarrow O_3 + M \tag{R 7}$$

The reactions (R 4-R 7) are rapid enough that a steady state can be assumed.

Besides the NO$_x$ cycles as described above, hydrogen oxides (HO$_x$), chlorine oxides (ClO$_x$), and bromine oxides (BrO$_x$) cycles play key roles in stratospheric chemistry. These cycles are interrupted when reactive species OH, NO$_2$, Cl, and ClO are tied up in stable species, which are then not available for acting as catalysts in the cycles. The removal of these species can be permanent if the (relatively stable) product (e.g. nitric acid (HNO$_3$) or hydrogen chloride (HCl)) migrates back to the troposphere, where it is removed by precipitation. On the other hand, a reactive species (e.g. chlorine nitrate (ClONO$_2$)) can also be temporarily removed from the cycles and stored in reservoirs. As the NO$_x$ and ClO$_x$ cycles, for example, are coupled by the reservoir species ClONO$_2$,

ozone depletion by the NO_x and ClO_x cycles can be triggered by increased emissions of N_2O and chloro-fluoro-carbons (CFC), respectively (Seinfeld and Pandis, 2006).

In 1985, annual decreases of stratospheric ozone over Antarctica were reported by Farman et al. (1985). Due to the massive loss of ozone, this event has been termed the *ozone hole*. Besides the magnitude, also the location of the ozone hole was surprising at that time. Due to the fact that the catalytic cycles were not able to describe the massive loss of ozone, and CFCs would be more effective at higher altitudes, Molina and Molina (1987) proposed a mechanism involving the ClO dimer (Cl_2O_2), which could explain the massive ozone loss. However, as it turned out, gas-phase chemistry alone is not able to produce high enough concentrations of ClO and BrO, which are needed to sustain their proposed mechanism.

Therefore, polar stratospheric clouds (PSCs) were considered to be involved in O_3 depletion. These wispy pinky or green clouds are formed during the long polar night at heights of 15-20 km, where temperatures can be as low as 183 K (-90°C). Once it was realized that PSCs provide the surfaces on which halogen-containing reservoirs species are converted to active catalytic species, the Antarctic ozone hole was fully explained. The two prerequisites for this mechanism of ozone destruction are cold temperatures and sunlight. While the cold temperatures are required for the formation of PSCs, on which heterogeneous reactions take place, sunlight is needed for the photolysis of gases produced from these reactions (Seinfeld and Pandis, 2006).

1.3.2. NO_x in the troposphere

In the troposphere, NO_2 leads to oxidation of reactive trace gases and to the (photochemical) formation of ozone (O_3) (R 8-R 9). Thus, tropospheric O_3 is not only transported from the stratosphere into the troposphere (as initially believed), but also formed in the troposphere via photochemical processes including reactions with NO_x and volatile organic compounds (VOCs) in the presence of sunlight.

The mechanism of tropospheric ozone formation became clear in the early 1950s. Large amounts of tropospheric ozone are especially formed when reactive gases such as NO_x

and VOCs are exposed to solar UV radiation. The exact mechanism was not fully understood until the late 1960s and early 1970s. The dominant emission species of NO_x is NO, which however reacts rapidly with O_3 to form NO_2. Besides NO and NO_2, nitrous oxide (N_2O) is also emitted into the atmosphere, but plays no role for the following chemical processes because it is a very inert species (Platt and Stutz, 2008).

$$NO_2 + hv \rightarrow NO + O(^3P) \qquad (\lambda \leq 420\ nm) \qquad \text{(R 8)}$$

$$O(^3P) + O_2 + M \rightarrow O_3 + M \qquad (M = air) \qquad \text{(R 9)}$$

Due to the rapid reaction of O_3 with NO (R 10), the formation of O_3 is reversible and thus, a photoequilibrium between NO, NO_2, and O_3 without any net formation or net loss of O_3 exists in the absence of VOCs (Atkinson, 2000). For calculations of the photo-stationary state, which are useful for the estimation of tropospheric O_3 production, photolysis rate coefficients are necessary.

$$NO + O_3 \rightarrow NO_2 + O_2 \qquad \text{(R 10)}$$

These reactions (R 8-R 10), which lead to a photo-stationary state between NO, NO_2, and O_3, can be expressed as the *Leighton relationship* (Leighton, 1961).

NO from natural and anthropogenic sources reacts with O_3 (R 10) to form NO_2, which than reacts with O_3 to form NO_3 (R 11).

$$NO_2 + O_3 \rightarrow NO_3 + O_2 \qquad \text{(R 11)}$$

The concentration and lifetime (~5s) of NO_3 remain low during daytime due to its fast photolysis and reaction with NO, but can increase to large amounts during nighttime when it becomes one of the most important radicals as hydroxyl radical (OH) concentrations are very low.

$$NO_3 + hv \rightarrow NO + O_2 \qquad (\sim 10\%) \qquad \text{(R 12)}$$

$$NO_3 + hv \rightarrow NO_2 + O(^3P) \qquad (\sim 90\%) \qquad \text{(R 13)}$$
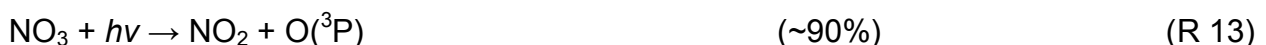
The OH radical, which reacts with all organic compounds, is the key reactive species in the troposphere (Logan et al., 1981). The prerequisite for the formation of OH is a

relatively low amount of tropospheric O_3, which is photolyzed by sunlight to produce $O(^1D)$ (R 14).

$$O_3 + h\nu \rightarrow O_2 + O(^1D) \qquad\qquad (\lambda \leq 335 \text{ nm}) \qquad\qquad \text{(R 14)}$$

The OH radical concentration in the 'clean' troposphere decreases when reacting with methane (CH_4) and CO and thus, an increase in CH_4 in the troposphere will reduce the OH radical concentration. On the other hand, simulations of a coupled chemistry-aerosol-climate model have shown that reductions of NO_x would increase global warming via induced CH_4 increases (Shindell et al., 2005).

$$\dot{R}O_2 + NO \rightarrow \dot{R}O + NO_2 \qquad\qquad\qquad\qquad \text{(R 15)}$$

In the presence of VOCs (biogenic and/or anthropogenic VOCs), the degradation reactions of VOCs lead to the non-photochemical formation of hydroperoxyl (HO_2) and peroxy ($\dot{R}O_2$) radicals, which react with NO to form NO_2 (R 15). The presence of VOCs results in a net formation of tropospheric O_3 as they bypass the removal of ozone (R 10) via reaction (R 15). However, reactions of O_3 with OH and HO_2 radicals result in a net loss of tropospheric O_3 (R 16-R 17) when NO concentrations are very low.

$$OH + O_3 \rightarrow HO_2 + O_2 \qquad\qquad\qquad\qquad \text{(R 16)}$$

$$HO_2 + O_3 \rightarrow OH + 2O_2 \qquad\qquad\qquad\qquad \text{(R 17)}$$

Whether net formation or net loss of tropospheric O_3 is dominating, depends on the NO amounts (threshold mixing ratio of NO ~10-30 x 10^{-12}) and the rate of the reaction of HO_2 and $\dot{R}O_2$ radicals with NO (Logan, 1985). NO_2 reacts with NO_3 to form N_2O_5 in a reversible process (R 18).

$$NO_3 + NO_2 + M \leftrightarrow N_2O_5 + M \qquad\qquad\qquad\qquad \text{(R 18)}$$

The uptake of N_2O_5 by aerosol during nighttime and subsequent deposition is a major atmospheric sink of NO_x (Jacob, 2000). It was shown that the ability of NO_3 and N_2O_5 to serve either as a reservoir or a sink of NO_x may depend on the season and location (Brown et al., 2004). Gas-phase reactions of OH radicals with NO and NO_2 are significant sinks of NO_x during daytime (R 19-R 20). Typical values for the lifetime of

tropospheric NO_x during daytime are in the range of 4-8 hours for megacities (Beirle et al., 2011) and 2.5-7 hours for biomass burning plumes (Takegawa et al., 2003).

$$OH + NO + M \rightarrow HONO + M \qquad (R\ 19)$$

$$OH + NO_2 + M \rightarrow HNO_3 + M \qquad (R\ 20)$$

The reaction of OH with NO_2 is the major loss process for NO_x during daytime and an important loss process also for OH radicals at regions with elevated NO_2 levels.

Large wildfires emit large amounts of trace species into the atmosphere, among them NO_x.
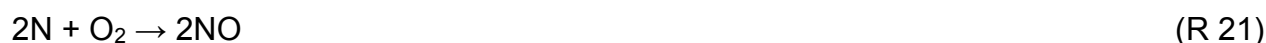
$$2N + O_2 \rightarrow 2NO \qquad (R\ 21)$$

$$O_2 \leftrightarrow 2O \qquad (R\ 22)$$

$$O + N_2 \leftrightarrow NO + N \qquad (R\ 23)$$

$$N + O_2 \leftrightarrow NO + O \qquad (R\ 24)$$

The nitrogen bound in the fuel is converted in part into oxides and N present in amino acids is converted to NO during the burning process. However, NO_x may also result from the reaction of atmospheric nitrogen (N_2) with O (R 23) at very high temperatures (Andreae and Merlet, 2001). While the higher thermal energy during the flaming stage leads to the break-up of plant materials into simpler N molecules enabling a full oxidation to NO_x, smoldering fires are rather incomplete.

There has been much discussion about the leading cause of NO_x emissions from wildfires. Andreae and Merlet (2001) suggest that temperatures in typical wildfires are not high enough to produce large amounts of NO_x via the oxidation of N_2. However, the production of NO_x is more efficient during the flaming combustion. The fraction of volatilized fuel nitrogen emitted as reactive nitrogen accounts for 25-50%, with NO_x and NH_3 being the dominant reactive nitrogen species during flaming and smoldering combustion, respectively (Goode et al., 2000; Yokelson et al., 2008). In comparison, up to 50% of the fuel nitrogen might be converted into N_2 (Lobert et al., 1990). However, the

exact mechanism of N_2 formation remains unclear as the detection of N_2 from open fires is influenced by the large N_2 fraction of the ambient air.

1.4. Physics of the Earth's atmosphere

Atmospheric chemistry and composition can influence physical parameters such as pressure and temperature. Moreover, atmospheric motions can transport chemical compounds vertically and horizontally (longitudinally and latitudinally). As the translational kinetic energy of gaseous compounds competes with sedimentation forces, the particles do not settle down. The density of the gas, which decreases with increasing altitude, can be determined from the Boltzmann equation by assuming constant values for the temperature and the acceleration due to gravity,

$$p(z) = p_0 \, exp\left(-\frac{mgz}{kT}\right),$$
(Eq. 1.2)

where T is the temperature, p_0 is the surface pressure, $p(z)$ the pressure at altitude z, g the acceleration due to gravity, m the molecular mass of the gas, and k denotes the Boltzmann's constant (Holloway and Wayne, 2010).

The amount of a specific trace gas in the atmosphere can be described as the concentration of the trace gas.

$$c = \frac{amount \; of \; trace \; gas}{volume \; of \; air}$$
(Eq. 1.3)

In this case, the term c might refer to either mass (c_m), number of molecules (c_n), or number of moles (c_M). The column density, expressed in units of molecules per cm^{-2}, is the integral of c_n along a certain light path in the atmosphere. For Differential Optical Absorption Spectroscopy (DOAS)-type measurements (see Sects. 1.5.2 and 1.5.3) of trace gases (e.g. NO_2), the amount or concentration is usually expressed in terms of integrated c_n (Platt and Stutz, 2008).

The term *mixing ratio* is another frequently used term for expressing trace gas amounts in the atmosphere.

$$x = \frac{amount\ of\ trace\ gas}{amount\ of\ air + trace\ gas}$$ (Eq. 1.4)

The trace gas amount can either be described in volume (x_V), number of moles (x_M), number of molecules, or mass, with the latter two being rarely used (Platt and Stutz, 2008).

The conversion of the number density c_n (in molecules per cm^{-3}), for example, into a volume mixing ratio x_V is given by:

$$x_V = \frac{c_n V_0}{N_A}$$ (Eq. 1.5)

N_A denotes Avogadro's number (N_A = 6.0221420 x 10^{23} molecules $mole^{-1}$), and V_0 is the molar volume in cm^3. The molar volume V_0 = 22414.00 cm^3 $mole^{-1}$ for standard conditions (p_0 = 1013.25 hPa and T = 273.15 K). While mixing ratios (e.g. x_V) are independent of pressure and temperature, concentrations (e.g. c_n) depend on both parameters, which can change horizontally and vertically when air is transported (Platt and Stutz, 2008).

1.4.1. Horizontal and vertical transport of NO_x

As already outlined in Sect. 1.4, atmospheric compounds can be mixed and redistributed by the movement of air and thus, such motions in vertical, longitudinal, and latitudinal direction can affect atmospheric chemistry.

Horizontal transport of chemical compounds is largely driven by wind systems. While winds near ground level are turbulent and variable due to friction, winds at higher altitudes are more regular. In general, winds are caused by differences in pressure and temperature between two distinct locations. Global circulation patterns in both hemispheres are driven by the rise of hot air near the Equator and the subsequent drop of cold air at higher latitudes. The so-called *Hadley cell* converges near the Equator with the inter-tropical convergence zone (ITCZ), which migrates with the Sun causing strong upward motion and heavy rainfall in northern and southern summer. When the ITCZ is located in the north of the Equator, the dry season period occurs south of the Equator,

and vice versa. As for the Hadley cells, atmospheric oscillations such as Rossby and planetary waves can also cause mass transport through oscillating air parcels (Holloway and Wayne, 2010).

In general, transport of atmospheric pollution involves long-lived species (e.g CO and O_3). In certain cases, however, short-lived species such as NO_2 can be transported over longer distances. Such long range transport events are often linked to cyclones passing over emission regions (Zien et al., 2014). However, under clear-sky conditions and at lower altitudes, the horizontal transport of NO_x is limited due to its chemical removal.

Turbulence in the troposphere ensures vertical mixing and redistribution of atmospheric compounds. In an inhomogeneous atmosphere, in particular at higher altitudes, molecular diffusion represents another type of vertical mixing. In this case, molecules are moving in response to a concentration gradient. Thermal diffusion is a process, which distributes matter by thermal conduction. While turbulence controls vertical mixing of atmospheric compounds in the troposphere, molecular and thermal diffusion dominate in the upper atmosphere. The upward and downward transfer of chemical compounds across the tropopause is of great importance with respect to the stratospheric ozone budget. At middle and high latitudes, exchange of stratospheric and tropospheric air is the result of tropopause folding, which is a mechanism for pumping stratospheric air into the turbulent troposphere (Holloway and Wayne, 2010).

1.4.2. Atmospheric radiative transfer

There are two main processes that take place when incoming and outgoing electromagnetic radiation interacts with the atmosphere: light scattering and light absorption. While greenhouse gases such as CO_2, CH_4, N_2O, and water vapor absorb a wide range of infrared radiation in rather broad bands, other trace gases such as O_3, NO_2, and HCHO have distinct narrow band absorption structures in the UV and visible range (Gottwald and Bovensmann, 2012).

Besides the importance of atmospheric radiative transport for the greenhouse effect (climate change) and for the determination of the efficiency of photochemical reactions

in the atmosphere, accurate knowledge of atmospheric radiative transport is essential for the retrieval of trace gases, aerosols, and cloud parameters from remote sensing data (Burrows et al., 2011).

The usual input parameters used for the computation of radiative transfer are the solar spectral input, extinction optical depth (the sum of the layer optical depths due to molecular absorption, Mie and Rayleigh scattering), single-scattering albedo, and phase function of scattered radiation (Ricchiazzi et al., 1998).

1.4.2.1. The solar spectrum

All energy used for physical and biological processes within the atmosphere and biosphere comes from the Sun. Hydrogen is converted to helium inside the Sun by nuclear fusion under enormous pressure and high temperatures. Large quantities of heat are transported by convection to the Sun's surface. The superheated gas on the Sun's surface emits electromagnetic radiation, which travels through space to the top of the Earth's atmosphere within about 8.5 minutes.
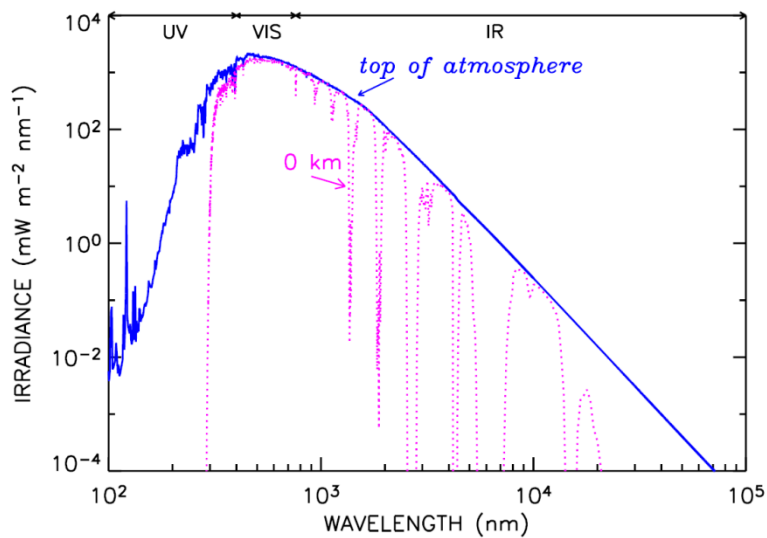
Fig. 1.6: The Sun's spectral irradiance (in terms of power of the Sun's electromagnetic radiation received per unit area) at the top of the atmosphere (solid blue) and at the surface (dotted magenta) (from Fröhlich and Lean, 2004)

The radiative output of the Sun was initially believed to be constant and thus, expressed as the *solar constant*. However, long-term observations from space beginning in the late 1970s have shown that the radiative output of the Sun changes in time, from minutes to decades (Fröhlich and Lean, 2004).

One quantity commonly related to radiation transfer is the irradiance, which is the radiant flux (defined as the radiated energy per time) received per unit area, expressed in units of $W\ m^{-2}$ (Platt and Stutz, 2008).

In the simplest case, full transmission of the solar irradiance without any absorption and/or scattering processes would take place in the absence of an atmosphere. A surface albedo of one (perfect reflection of a white surface) would mean that no loss of the incoming irradiance due to absorption occurs, and all of the light is reflected back to space. Assuming this to be the case, the solid blue line (the incoming irradiance at the top of atmosphere) in Fig. 1.6 would not change. In reality, both the composition of the atmosphere and the fact that the Earth's surface is not a perfect reflector, lead to a decreased solar irradiance when reaching the Earth's surface (dotted magenta line).

1.4.2.2. Scattering, absorption, and emission of photons

As soon as the amount of energy (in the form of radiation) emitted by the Sun reaches the top of the atmosphere and enters the atmosphere, many interaction processes between radiation and atmosphere occur (Platt and Stutz, 2008; Burrows et al., 2011).

- Scattering processes in the Earth's atmosphere can be subdivided into elastic (*Rayleigh* and *Mie* scattering) and inelastic scattering (*Raman* scattering). While Rayleigh scattering due to air molecules is simply demonstrated by the blue color of cloud free skies, Mie scattering due to aerosol particles leads to the white and grey color of cloudy skies. Both Rayleigh and Mie scattering are elastic scattering processes without any changes in photon energy. In contrast, the inelastic Raman scattering occurs when the scattering molecule changes its state of excitation during the scattering process. The transfer of the photon's energy to the molecule produces vibration and/or rotation of the molecule.

- Because of the strong interaction with absorbers at particular wavelength intervals (see Fig. 1.6), radiation is removed from the radiation field and converted into some other form of energy (e.g. heat). While the absorption of solar UV radiation is an important prerequisite for life on land, the absorption of IR radiation is a key process in the climate system. The absorption processes in the atmosphere are used for the detection of trace gases by remote sensing techniques (see Sect. 1.5). Although the absorption of solar radiation is relatively low in the visible part of the electromagnetic spectrum (see Fig. 1.6), the narrow band absorption structures of NO_2 can be used for retrieval of tropospheric NO_2 amounts (Richter, 2006).

- Thermal emission of air molecules or aerosol particles, which cannot exceed the emission from a black body for the temperature of the atmosphere, takes place at infrared wavelengths. However, it can be neglected in the visible part of the electromagnetic spectrum and thus, the observed spectral signatures can be directly related to absorption spectra of atmospheric constituents (Burrows et al., 2011).

For the retrieval of trace gases from remote sensing techniques, the effective light path within the atmosphere is simulated by radiative transfer models, which is usually achieved by invoking so called *airmass factors* (AMFs). The light path is determined by the geometry (e.g. viewing angle of the instrument and solar zenith angle), surface reflection, and scattering from air molecules, aerosol particles, and clouds. For weak absorbers, it is assumed that the effective light path is independent of the amount and vertical distribution of the absorber itself.

As the vertically integrated trace gas concentration or vertical column density (VCD) is the more typical quantity, the AMF is applied to convert the slant column density (SCD):

$$AMF = \frac{SCD}{VCD}$$

(Eq. 1.6)

1.4.2.3. The radiative transfer model SCIATRAN

The radiative transfer model (RTM) GOMETRAN was developed within the scope of the Global Ozone Monitoring Instrument (GOME) project for the simulation of backscattered radiation from the atmosphere and reflected radiation from the Earth's surface in the spectral range 240-800 nm (Rozanov et al., 1997; Burrows et al., 1999). With the objective of the Scanning Imaging Absorption spectroMeter for Atmospheric CHartographY (SCIAMACHY) instrument to detect additional trace gases, the successor RTM SCIATRAN was extended to allow simulations in the larger spectral window and in limb viewing direction (the instrument looks at the edge of the atmosphere) (Rozanov et al., 2005). Besides a number of new capabilities, SCIATRAN also allows for the calculation of AMFs for ground-based and satellite-based measurements, which are used for the retrieval of tropospheric trace gas columns (see Sects. 2.2.1, 3.2.1, and 6.3.1.5).

1.4.3. Vertical profiles of NO_x and aerosols

As the lifetime of NO_x is relatively short, tropospheric NO_2 amounts are highly variable in space and time. NO_x released from the major emission sources (see Sect. 1.2.2.) is generally distributed within the lowermost layers of the troposphere. While NO_x from anthropogenic and soil emission sources remain within the boundary layer in most cases, NO_x from lightning is an exceptional case as it is emitted into the upper troposphere (WMO, 1995). Occasionally, intensive wildfires can inject emissions into the free troposphere as well (Labonne et al., 2007).

Besides the aerosol type, albedo, ground level, and solar zenith angle, the NO_2 profile is an important input parameter used for the computation of AMFs, which are required for obtaining tropospheric vertical NO_2 columns (see Sects. 2.2.1 and 3.2.1). Such profiles are usually computed by Chemical Transport Models (CTMs) and show different spatio-temporal patterns. Over polluted regions, for example, NO_2 mixing ratios gradually decrease from the surface to the top of the boundary layer by a factor of 2-3. In comparison to NO_2 profiles over anthropogenic regions, NO_2 mixing ratios over biomass burning regions decrease slower with altitude (Nüß, 2005).

1.5. Remote sensing of nitrogen dioxide (NO$_2$) and other trace gases

Remote sensing techniques make use of the interaction of electromagnetic radiation with matter. With increasing knowledge about the processes involved in the interaction between light and matter, remote sensing products are gaining accuracy (Burrows et al., 2011).

Atmospheric trace species can be measured by the use of various remote sensing techniques in the ultraviolet (UV)/visible, near infrared (NIR), infrared (IR), and microwave parts of the electromagnetic spectrum. The selection of the most adequate technique essentially depends on the trace species itself, but also on the required accuracy and spatio-temporal resolution. The Fourier Transform Infrared Spectroscopy (FTIR), for example, is used for the detection of specific trace species (e.g. O$_3$, NO$_2$, CO, and CH$_4$) by obtaining absorption signatures in the IR. However, this observation technique is limited by the need to observe the solar disc directly and thus, is limited to clear sky conditions.

The use of scattered sunlight as the light source (e.g. Differential Optical Absorption Spectroscopy) enables measurements also during cloudy conditions and thus, a high degree of automation is obtained. As this technique is used for this work, it is explained in more detail in the following Sect. 1.5.1.

1.5.1. Differential Optical Absorption Spectroscopy (DOAS)

Once the energy from the Sun in form of electromagnetic radiation (short-wave solar radiation) penetrates into the atmosphere, it is partly scattered by molecules, particles, and cloud droplets (see Sect. 1.4.2.), before it reaches the Earth's surface and the ground-based instrument. In the case of satellite-based instruments, the sunlight reaching the Earth's surface is reflected and travels back through the atmosphere towards the observing space-based instrument. As some part of the light is absorbed by specific trace species within the atmosphere, the reduction of light intensity can be used for determining the amount of trace species present within the light path. Therefore, the

retrieval of atmospheric trace gases from UV/visible measurements is based on Beer-Lambert's law (see Eq. 1.7),

$$dI(\lambda) = -I(\lambda)\sigma(\lambda)\rho(s)ds \qquad \text{(Eq. 1.7)}$$

which describes the change in intensity (dI) at a given wavelength (λ) proportional to the initial intensity (I), the absorber cross-section (σ), the absorber number density (ρ), and the light path length (s).

The general idea of DOAS is the separation of wavelength dependent absorption signals and particularly, DOAS can be explained as a technique that quantifies atmospheric trace gases with narrow band absorption structures (e.g. NO_2) in the UV and visible part of the electromagnetic spectrum. There exist two general approaches for DOAS measurements: active and passive observations. The basic distinction is made between artificial (e.g. laser) and natural (e.g. solar, lunar, or stars) for active and passive observations, respectively. The passive DOAS application is further subdivided into direct and scattered light measurements (Platt and Stutz, 2008).

The main passive DOAS principle consists of a spectral broadband light source (e.g. the Sun) that emits light with the initial intensity $I_0(\lambda)$, which then passes through a volume with absorbers (e.g. the atmosphere). Besides scattering by air molecules (Rayleigh) and aerosols (Mie), $I_0(\lambda)$ is reduced due to absorption of specific trace gases (e.g. NO_2) when travelling through the atmosphere (Eq. 1.7). This wavelength dependent absorption signal is then separated into a low frequency and a high frequency part with the latter one being used for the retrieval of atmospheric absorptions (Platt and Stutz, 2008; Burrows et al., 2011).

$$I(\lambda) = cI_0(\lambda)exp\{-\Sigma\sigma_i'(\lambda)SCD_i - \Sigma\sigma_i^*(\lambda)SCD_i - \sigma_{Ray}(\lambda)SCD_{Ray} - \sigma_{Mie}(\lambda)SCD_{Mie}\} \qquad \text{(Eq. 1.8)}$$

Briefly, $I_0(\lambda)$ decreases exponentially when passing through the atmosphere resulting in a reduced light intensity $I(\lambda)$, depending on the cross-sections of the trace gas absorber, Rayleigh and Mie scattering and their slant column densities (SCD). The SCD is defined as the trace gas concentration $\rho(s)$ of the absorber integrated along the light path s. In Eq. 1.8, the term c is defined as the efficiency factor accounting for the fact that scattered light is being measured, and $\sigma'(\lambda)$ and $\sigma^*(\lambda)$ are the differential and slowly

varying contributions to the signal, respectively. The cross-sections of Rayleigh $\sigma_{Ray}(\lambda)$ and Mie $\sigma_{Mie}(\lambda)$ scattering can be approximated by a polynomial in wavelength and cause a general slope, which varies slowly. The slow varying cross-sections of Rayleigh and Mie scattering are combined with the slow varying parts of the absorption cross-sections of the trace species of interest (Eq. 1.9).

$$I(\lambda) = cI_0(\lambda)exp\left\{-\Sigma\sigma_i'(\lambda)SCD_i - \Sigma\sigma_i^*(\lambda)a_p\lambda^p\right\}$$ (Eq. 1.9)

Finally, the DOAS equation can be written as a function of the optical depth $ln(I_0/I)$.

$$ln\frac{I_0(\lambda)}{I(\lambda)} = \Sigma\sigma_i'(\lambda)SCD_i + \Sigma c_p\lambda^p$$ (Eq. 1.10)

The prerequisite for precise DOAS retrievals of NO_2 is an accurate set of NO_2 cross-sections, which is achieved by laboratory measurements using, for example, a Fourier transform spectrometer (Vandaele et al., 1996). Harder et al. (1997) and Burrows et al. (1998) reported on a small temperature dependence of the average cross-section of NO_2. However, NO_2 concentrations are also of interest at higher altitudes in the atmosphere and thus, additional laboratory measurements were performed at lower temperatures (Merienne et al., 1995). For the determination of atmospheric NO_2 concentrations, it is therefore of central significance to use well resolved and calibrated data that take into account the effect of temperature (Coquart et al., 1995).

One of the main advantages of the DOAS principle over other measurement techniques is that it requires no calibration of the optical properties or their change with time as the instruments typically show broad spectral characteristics. This fact saves time and keeps the measurements as simple as possible. However, there exist errors that influence both the precision and accuracy of DOAS applications. Both the precision and accuracy of passive scattered light DOAS are influenced by random noise, removal of Fraunhofer lines (dark lines in the solar spectrum that are caused by absorption by chemical elements in the Solar atmosphere), temperature dependent absorption cross-sections, and uncertainties in the path length.

The Fraunhofer lines are well known and created within the solar atmosphere due to absorption by molecules and ions. As they are rather constant over longer time periods

and affect both I and I_0, their effect cancels out (see Eq. 1.10). However, if I and I_0 are measured under different conditions, this effect has to be corrected afterwards.

Another feature is the so-called *Ring effect* that needs special consideration in the DOAS retrieval. The Ring effect became clear when observations of direct and scattered light showed differences in the depth of Fraunhofer lines. The reason is the inelastic rotational Raman scattering on air molecules, which distributes the intensity of scattered photons over several nanometers, resulting in a smaller depth of Fraunhofer lines in the scattered light. Further details on possible factors affecting the DOAS retrieval can be found in Platt and Stutz (2008), Burrows et al. (2011), and Gottwald and Bovensmann (2011).

In the case of satellite DOAS-type measurements, photons travel two times through the atmosphere, before they are detected by the instrument. In contrast, photons have travelled through the atmosphere only once, before they enter ground-based or ship-based DOAS-type instruments. In order to retrieve tropospheric NO_2 vertical columns, a stratospheric correction and air mass factors are applied for the conversion of SCDs into VCDs (see Sects. 2.2.1, 3.2.1, and 6.3.1.5).

The ground-based (on board a Research Vessel) and satellite-based DOAS-type instruments that have been used for this thesis to retrieve tropospheric NO_2 vertical columns, are briefly described in the following Sects. 1.5.2. and 1.5.3.

1.5.2. MAX-DOAS instrument *

The Multi AXis (MAX)-DOAS instrument is an advancement of the zenith scattered light DOAS (Noxon, 1975) and Off-Axis DOAS (Sanders et al., 1993) that allows for measurements at different viewing directions (Hönninger et al., 2004; Wittrock et al., 2004) to obtain tropospheric trace gas amounts.

Briefly, the IUP-Bremen MAX-DOAS system consists of a telescope unit, an optical fibre bundle, and a grating spectrometer. The telescope unit of the MAX-DOAS system collects scattered sunlight at selected viewing and azimuthal directions. Once the photons enter the entrance window of the telescope, they are focused by a lens to limit

the field of view, before they move through an optical fibre bundle and reach a grating spectrometer equipped with a charge-coupled device (CCD) detector (Peters, 2013).

1.5.3. Satellite-based DOAS-type instruments *

Since the launch of the Global Ozone Monitoring Experiment (GOME) on board the European Space Agency's (ESA) European Remote Sensing (ERS)-2 satellite (Burrows et al., 1999) and the SCanning Imaging Absorption spectroMeter for Atmospheric CHartographY (SCIAMACHY) on board ENVISAT (Burrows et al., 1995; Bovensmann et al., 1999), NO_2 total and tropospheric vertical columns have been retrieved from nadir measurements (the atmospheric volume directly under the instrument).

In this work, spectral measurements from the OMI and from GOME-2, which is the improved version of GOME, are used for the retrieval of tropospheric NO_2. A detailed description of the two instruments is given in the following Sects. 1.5.3.1 and 1.5.3.2.

1.5.3.1. GOME-2 instrument *

The second Global Ozone Monitoring Experiment (GOME-2) located on board the MetOp-A satellite was launched in October 2006. GOME-2 is the first of a series of three identical instruments which will provide more than 15 years of space-borne UV/visible observations of the atmosphere (Munro et al., 2000). The GOME-like nadir-viewing spectrometer covers the spectral range between 240 and 790 nm at 0.2–0.4 nm resolution, has a ground pixel size of 80 x 40 km^2, and overpasses the Equator at 09:30 local time (LT) in the descending node (Callies et al., 2004). With its large swath of 1920 km, GOME-2 provides near global coverage every day.

* This subsection has been previously published as part of Schreier et al. (2014a).

1.5.3.2. OMI instrument *

The Ozone Monitoring Instrument (OMI) on board NASA's EOS-Aura satellite was launched in July 2004. OMI performs spectral measurements in the range of 270–500 nm at a spectral resolution of 0.63 nm (Levelt et al., 2006). In nadir geometry, the instrument overpasses the Equator in the ascending node at 13:30 LT with the pixel size being 13 x 24 km^2 at nadir and larger toward the edges of the scan. The OMI instrument provides global coverage of spectral measurements every day.

While OMI measurements have a higher spatial resolution, GOME-2 performs measurements at a higher spectral resolution. Indeed, the main difference between the two instruments is the overpass time of the respective satellite.

Chapter 2

The empirical relationship between satellite-derived tropospheric NO$_2$ and fire radiative power and possible implications for fire emission rates of NO$_x$ *

2.1. Introduction *

In this study, the potential of using satellite-observed TVC NO$_2$ for the quantification of NO$_x$ emissions from outdoor biomass burning using a simple statistical approach is evaluated. The temporal correlation of TVC NO$_2$ and FRP is studied globally and for selected regions. Fire emission rates (FERs) of NO$_x$ (reported as NO) for typical tropical and subtropical biomes are derived for the morning (early afternoon) by making use of the linear relationship between TVC NO$_2$ from GOME-2 (OMI) and FRP from MODIS on board Terra (Aqua). A similar method to derive smoke emissions rates from FRP measurements was already established by Ichoku and Kaufman (2005), but for aerosols. In this study, their concept is used and FERs of NO$_x$ for selected tropical and subtropical biomes and regions are presented. Possible factors affecting the observed biome-specific, diurnal, and regional discrepancies are discussed. The retrieval of TVC NO$_2$ from the GOME-2 and OMI instruments, additional data sets used, and the method developed for the estimation of FERs of NO$_x$ are described in the following Sect. 2.2. The results of this study are presented and discussed in Sect. 2.3, followed by the summary and conclusions (see Sect. 2.4).

2.2. Instruments and data retrieval *

2.2.1. Satellite measurements of tropospheric NO$_2$ *

Brief descriptions of the GOME-2 and OMI instruments, which are used for the retrieval of TVC NO$_2$ in this study, are given in Sects. 1.5.3.1 and 1.5.3.2, respectively.

---

* This subsection has been previously published as part of Schreier et al. (2014a).

The retrieval of tropospheric NO_2 vertical columns (TVC NO_2) from the GOME-2 (morning) and OMI (early afternoon) measurements is achieved in four main steps. In the first step, the trace gas concentration integrated along the light path (slant column density or SCD) is determined by applying the differential optical absorption spectroscopy (DOAS) method, based on Beer–Lambert's law (see Sect. 1.5.1). The DOAS retrieval uses the logarithm of the ratio between sun- and earthshine to determine the optical thickness. The differential optical thickness is then obtained by the subtraction of a suitable polynomial, and a linear fit of the differential absorption cross-sections of all absorbers relevant in the spectral region of interest is performed to determine the SCDs. For the GOME-2 instrument, Richter et al. (2011) have developed an improved NO_2 retrieval including more spectral points and an explicit spike removal algorithm by using a larger fitting window (425–497 nm) than used for GOME and SCIAMACHY (425–450 nm). Here, the SCDs from this retrieval are used for further analysis. The NO_2 SCDs from OMI were downloaded from the NASA website (http://disc.sci.gsfc.nasa.gov/Aura/data-holdings/OMI/omno2_v003.shtml). Details about the DOAS retrieval for the determination of NO_2 SCDs from OMI, which slightly differs with respect to the fitting characteristics, can be found in Bucsela et al. (2006). In the second step, the reference sector method (Richter and Burrows, 2002) is used for removing the stratospheric part from the NO_2 SCDs. The reference sector method selects a region over the Pacific (180–220° longitude), which is assumed to have negligible sources of tropospheric NO_x, and thus only reflects the stratospheric amount. The stratospheric columns, varying with latitude, are then subtracted from the total columns determined by the DOAS method. For some regions, the subtraction leads to negative values of the tropospheric slant column. This may arise due to zonal inhomogeneities in the stratospheric NO_2 distribution or transport of tropospheric NO_2 into the reference sector, leading to higher values, which are then subtracted in remote regions, and thus result in negative values. While at mid- and high latitudes the assumption that there is negligible NO_2 in a scene and used in the reference sector method introduces significant errors into the tropospheric NO_2 data products (see Hilboll et al., 2013a), it is not a concern for the tropical and subtropical regions, which are the focus of this study. Thirdly, measurements with cloud fraction greater than 0.2 are removed via cloud screening by using the improved version of the Fast REtrieval

Scheme for Clouds from the Oxygen A-band (FRESCO+) algorithm (Wang et al., 2008) and the O_2-O_2 absorption band at 477 nm (Acarreta et al., 2004) for GOME-2 and OMI, respectively. Finally, the tropospheric SCDs are converted into TVC NO_2 by applying air mass factors (AMFs), which are derived using the IUP Bremen radiative transfer model SCIATRAN (Rozanov et al., 2005) by taking into account the viewing geometry and scattering, absorption, and reflection within the atmosphere and Earth's surface. The calculation of AMFs used for this study is based on a priori information of the parameters albedo, ground level, NO_2 vertical profile, and aerosol (optical) properties. The albedo and ground level information is derived from the GOME albedo database (Koelemeijer et al., 2003) and the Terrain-Base Global DTM Version 1.0 (Row et al., 1994), respectively. The a priori information on the vertical distribution of NO_2 is obtained from the Model for OZone And Related Chemical Tracers (MOZARTv2). The types of aerosols are classified as urban, rural, and maritime. AMF calculations are performed on a horizontal grid of 2.8125° x 2.8125° (according to the resolution of MOZARTv2) for each month of the year 1997. The retrieval is thus using NO_2 profiles, which include the effects of biomass burning on a climatological basis but not on a case-by-case basis.

Boersma et al. (2004) have shown that the assumptions used in the AMFs are often large sources of error in satellite-based retrievals of tropospheric NO_2. For instance, errors in the CTM-derived NO_2 vertical profile (Hains et al., 2010) and errors in specified aerosol properties (Martin et al., 2003; Leitão et al., 2010) influence the accuracy of AMFs. As aerosols interact with radiation in the atmosphere, AMFs calculated by radiative transfer models are sensitive to optical properties, amount and vertical distribution of aerosols. Martin et al. (2003) found a reduction of AMFs by 10–20% when influenced by biomass burning aerosols and desert dust. Moreover, an aerosol layer located above the NO_2 concentrations can decrease the AMF by up to 70% (Leitão et al., 2010). Consequently, the selection of too high (low) AMFs results in an underestimation (overestimation) of TVC NO_2. While the column integrated extinction of aerosols on a global scale is well known (e.g. Remer et al., 2008), further research needs to be carried out to increase the knowledge of vertical profiles of aerosol properties. More information regarding the AMF calculations is found in Nüß (2005) and

details concerning the influence of the NO_2 vertical profile and aerosol properties on the AMF are given in Leitão et al. (2010).

The second, third, and fourth steps of the retrieval procedure are performed in the same way for the SCDs from GOME-2 and OMI. Monthly means of TVC NO_2 for the five consecutive years (2007–2011) are binned to a horizontal resolution of 1° x 1°.

2.2.2. Satellite measurements of fire radiative power *

The MODerate resolution Imaging Spectroradiometers (MODIS) on board NASA's Terra and Aqua satellites were launched in Sun-synchronous near-polar orbits in December 1999 and May 2002 with corresponding equatorial overpass times at 10:30 LT and 13:30 LT, respectively. The instruments were designed to improve the understanding of processes on land, in the oceans, and in the atmosphere. The instruments have 36 spectral bands ranging in wavelength from 0.4–14.4 μm. The differences in 4 and 11 μm black body radiation emitted at combustion temperatures are used to derive active fires at 1 km^2 horizontal resolution. In addition to the binary fire flag, the MOD14 (MODIS Terra) and MYD14 (MODIS Aqua) fire products offer the radiant component of energy release, the so-called *fire radiative power* (FRP) (Kaufman et al., 1998; Justice et al., 2002).

FRP is described by the Stefan–Boltzmann law, which characterizes the power radiated from a black body in terms of its temperature (see Sect. 1.1.4.4). Riggan et al. (2004) have found that more than 90% of the radiant energy released by vegetation fires was observed between 830 and 1440 K with the flaming (smoldering) temperature sometimes exceeding (undershooting) 1600 K (700 K). Although there is a lack of validation concerning the satellite-derived parameter FRP, and studies dealing with FRP are rather new, recent studies have tried to assess the uncertainties in FRP. For instance, Schroeder et al. (2010) found that the detection limits are 11 and 9 MW for MODIS on board Terra and Aqua, respectively, over the Brazilian Amazon. Coincident space-based observations of the Geostationary Operational Environmental Satellite (GOES) indicated increased detection limits of 27 and 19 MW during Terra and Aqua overpass time, respectively. Due to the larger amount of non-detected (smaller) fires,

* This subsection has been previously published as part of Schreier et al. (2014a).

SEVIRI- and GOES-derived FRP is underestimated by 40–50%, when compared to FRP from MODIS (Roberts and Wooster, 2008; Xu et al., 2010).

Giglio et al. (2006a) have indicated that the amount of burned area per fire observed increases with decreasing vegetation cover, which means that a grassland fire will move faster than a woodland fire. This has implications for small ground scenes as the chances that the satellite observes a slowly moving and rather stationary fire are much higher than capturing a fast moving fire within a specific grid cell. However, the MODIS FRP product with a 1° x 1° horizontal resolution is created by averaging the mean FRP of four individual 0.5° x 0.5° grid cells. Therefore, any severe effects of slowly and fast moving fires on the presented approach can be ruled out. In the case of FRP, the critical factor is rather the duration of the fire instead of its speed. For example, short fires may ignite and virtually extinguish between two MODIS overpasses, and thus remain undetected. However, this effect may be partially compensated by assuming a longer duration for detected fires within the selected regions. Monthly data of FRP for the consecutive five years (2007–2011) have been downloaded at a horizontal resolution of 1° x 1° from ftp://neespi.gsfc.nasa.gov/data/s4pa/Fire/.

2.2.3. Global land cover map *

The Collection 5 MODIS Global Land Cover Type product, which is generated at a horizontal resolution of 500 m, was designed to support scientific investigations (Friedl et al., 2010).

The MODIS land cover product is based on five different classification systems and freely available at https://lpdaac.usgs.gov/products/modis_products_table/mcd12q1. The map used for this study represents the 2005 land cover types and has been spatially aggregated to a 1° x 1° resolution using a majority filter, which selects the most abundant land cover type within the 1° x 1° pixel. Among the different classifications included in this product, the 14-class University of Maryland classification (UMD) has been selected, which includes, among others, the land cover types evergreen broadleaf forest, open shrublands, woody savannas, savannas, and croplands (Hansen et al., 2000).

2.2.4. Satellite measurements of aerosol optical depth *

The Collection 5 MODIS aerosol products are derived from spectral radiances between 470 and 2130 nm and provide a consistent record of aerosol characteristics (Remer et al., 2008). The column integrated extinction, commonly referred to as aerosol optical depth (AOD), is a straightforward space-based parameter for characterizing Earth's aerosol system. As aerosols can significantly influence the AMFs used for the retrieval of TVC NO_2 from satellite measurements (e.g. Martin et al., 2003; Leitão et al., 2010; Bousserez, 2013), AOD measurements at 550 nm from MODIS on board Terra and Aqua are used for investigating the temporal relationship between AOD and FRP over the selected regions. In general, it is expected that AOD is highly correlated with FRP, where biomass burning is the main aerosol source. This AOD information is needed to assess the possible impact of aerosols on the estimated FERs of NO_x (see Sect. 2.3.5). The AOD product has been downloaded at a 1° x 1° horizontal resolution from ftp://ladsweb.nascom.nasa.gov/allData/51/MOD08_M3/2005/.

2.2.5. Population density *

Population density has been inferred from the Global Rural-Urban Mapping Project (GRUMPv1) in order to separate pixels, which are largely influenced by anthropogenic emissions resulting from fuel combustion in energy production and transportation. GRUMPv1 builds on the Gridded Population World (GPW) project to construct a common geo-referenced framework of urban and rural areas by combining census data with satellite data. The actual version of GRUMP consists of three data products. One important part of GRUMPv1 is a higher resolution population data set at a 30'' x 30'' grid for the years 1990, 1995, and 2000, with the latter one being used for this study. The second component of GRUMPv1 is based on NOAA's nighttime lights data. Beyond that, GRUMPv1 allocates a point data set of all urban areas with populations of greater than 1000 persons. The population density grid data set used for this study is available at http://sedac.ciesin.columbia.edu/data/collection/gpw-v3. According to the TVC NO_2, FRP, AOD, and global land cover map, the population density map has been gridded to a 1° x 1° horizontal resolution.

---

* This subsection has been previously published as part of Schreier et al. (2014a).

2.2.6. Conversion of tropospheric NO₂ vertical columns into production rates of NOₓ *

The reason for the conversion of tropospheric NO_2 vertical columns into production rates of NO_x is twofold. Firstly, as chemical models typically require values for the amount of NO_x being released as a function of time, the monthly mean top-down production rate of NO_x from fire (P_f) has been estimated for five consecutive years of GOME-2 and OMI measurements (2007–2011), and thus P_f (in g NO_x s^{-1} pixel^{-1}) is provided for the morning and early afternoon, respectively, according to the local overpass time of the two satellites. The second reason for the conversion is to enable comparability between TVC NO_2 and values of existing bottom-up emission inventories for biomass burning, e.g. Global Fire Emissions Database (GFEDv3.1). According to the units reported in GFEDv3.1 (in g NO_x month^{-1} m^{-2}), P_f is temporally integrated over a month.

As previously stated, the tropospheric NO_2 vertical column is defined by and determined via the following formula:

$$TVC = \int [NO_2](z)dz, \qquad \text{(Eq. 2.1)}$$

where *[NO₂](z)* is the concentration of NO_2 at altitude *z* of the atmosphere, integrated from the ground to the tropopause.

The instantaneous change in NO_2 is given by

$$\frac{d[NO_2]_i}{dt} = P - L[NO_2]_i, \qquad \text{(Eq. 2.2)}$$

where *t* is the time, *P* is the production rate of NO_2 and *L* is the loss rate of NO_2. The loss rate is given by

$$L = [NO_2]_i \sum j_k \left(k_{tix} + k_{tiy} + k_b\left(X_j + NO_2\right)_j[x_i] + k_{ter}(Y_k + NO_2 + M), \qquad \text{(Eq. 2.3)}\right.$$

where k_{tx}, k_{ty} and k_{tz} are transport rate coefficients for *x*, *y*, and *z* directions, respectively, and

$$k_{tix} = {}^1/_{tix} , k_{tiy} = {}^1/_{tiy} , k_{tiz} = {}^1/_{tiz}, \qquad \text{(Eq. 2.4)}$$

53

where for altitude level i, tix, tiy, and tiz are the time constants for the transport out of the field of view in the x, y, and z directions, respectively.

While the term $k_b(X_j + NO_2)_j$ represents the rate coefficients for the bimolecular reaction of NO_2 with X_j, the term $k_{ter}(Y_k + NO_2 + M)$ is the termolecular rate coefficient for the reaction of NO_2 with Y_k and a third body.

For point sources like megacities, Beirle et al. (2011) assume that the decay of NO_2 in the outflow can be fitted by a first order decay constant. They typically found time constants for the decay of NO_2 ranging from 4–8 h during daytime, with the shortest lifetimes (τ) derived for lower latitudes. Following these findings, the above stated Eqs. 2.1–2.4 can be neglected and a constant lifetime of NO_2 of the order of $\tau = 6$ h for both the morning and early afternoon state of the troposphere is assumed. As a consequence of the still poorly understood local concentrations of VOCs, which play an important role in the removal of NO_x, and thus affect the lifetime of NO_x, this assumption is reasonable and adequate for the focus of this study. The accuracy of the lifetime of NO_x retrieved from chemical models is limited by the accuracy of the knowledge of the concentrations of VOCs over biomass burning regions.

If NO_2 columns are averaged over larger pixels, e.g. 1° x 1° pixels, the effect of advection in and out of the region can be neglected and the change of NO_2 columns is dominated by chemistry. The instantaneous stationary state of NO_2 can then be described as

$$\frac{d[NO_2]_i}{dt} = P - L[NO_2]_i = 0 \quad \rightarrow \quad P = L[NO_2]_i \qquad \text{(Eq. 2.5)}$$

In the case of fire, it is assumed that P is dominated by the fire release and that it is negligible on days where no fires occur within the pixel. Typically, chemical models require values for the amount of NO_x being released as a function of time and area. Assuming that (i) FRP is a surrogate for the fire temperature, (ii) NO or NO_x is produced instantaneously, and (iii) the NO_2/NO_x ratio in the plume is defined by the Leighton photostationary state (Leighton, 1961),

$$\frac{[NO_2]_i}{[NO]_i} = \frac{k_1[O_3]_i}{J2_i}, \qquad \text{(Eq. 2.6)}$$

P is determined for the photolysis frequency of NO_2 ($J2_i$), meaning for the time and therefore solar zenith angle of the GOME-2 (morning) and OMI (early afternoon) overpass. Instead of inferring the rate constant for the reaction of ozone with NO (k_1) and tropospheric O_3 concentrations from climatologies, findings of Alvarado and Prinn et al. (2009) are followed and a constant $[NO_2]/[NO_x]$ ratio of 0.75 is assumed. In order to convert the satellite-derived NO_2 amounts produced by fire ($TVC_f\ NO_2$) for the comparison with fire NO_x emissions from GFEDv3.1, the background levels of tropospheric NO_2 ($TVC_b\ NO_2$) are subtracted from $TVC\ NO_2$ as a first step:

$$TVC_f[NO_2] = TVC[NO_2] - TVC_b[NO_2] \qquad \text{(Eq. 2.7)}$$

The background values of NO_2, also referred to as y-intercepts, are taken from the analysis of the least-squares method for the subtraction (see Sect. 2.3.2 and Fig. 2.5).

The estimation of P_f is based on the conversion between the column number density (in molecules cm^{-2}), as retrieved from satellite instruments, into column mass concentration (in g cm^{-2}). This part of the approach requires Avogadro's number (N_A) and the molar mass (M) of NO, as the emissions of NO_x are reported as NO in state-of-the-art emission inventories. The molar mass of NO is 30 g mol^{-1}. The following equation summarizes the above stated approach for estimating P_f (in g NO_x s^{-1} $pixel^{-1}$) for a single 1° x 1° box:

$$P_f = \frac{TVC_f[NO_2] * M \left(1 + \frac{NO}{NO_2}\right) A_p}{N_A * \tau}, \qquad \text{(Eq. 2.8)}$$

where $TVC_f\ NO_2$ is the number density of NO_2 molecules produced by fires and integrated over the tropospheric vertical column (in molecules cm^{-2}), M is the molar mass of NO (in g mol^{-1}), A_p is the respective pixel area (in cm^2), and N_A determines Avogadro's number (in molecules mol^{-1}). The term $1 + NO/NO_2$ accounts for the above stated ratio (without units), and τ is the lifetime of NO_x (in seconds). According to the described conversion of TVC NO_2, the FRP values have also been multiplied by A_p. As described earlier, P_f is multiplied by the number of seconds per month for the comparison with GFEDv3.1 NO_x (in g NO_x $month^{-1}$ m^{-2}).

The approach to derive space-based FERs of NO_x is based on the relationship between the above described parameters P_f and FRP. It is important to note that the retrieval of TVC NO_2 is based on static AMFs. Consequently, biome-specific, diurnal, and regional discrepancies in FERs of NO_x could be affected by changes in the NO_2 vertical profile and aerosol properties relative to the a priori. The conversion of TVC NO_2 into P_f further assumes constant values for the lifetime of NO_x and the NO_2/NO_x ratio. Therefore, biome-specific, diurnal, and regional variations in FERs could also be influenced by changes in plume chemistry.

2.3. Results and discussion *

The aim of this study is to establish an empirical relationship between tropospheric NO_2 vertical column (TVC NO_2) and fire radiative power (FRP) as a tool to estimate fire emissions of NO_x. For this purpose, the gradient of the linear relationship between the converted TVC NO_2, here referred to as production rate of NO_x from fire (P_f), and FRP is derived over characteristic tropical and subtropical biomass burning regions. The gradients, here referred to as FERs of NO_x, for the morning (early afternoon) fires are obtained from the relationship between P_f, retrieved from GOME-2 (OMI) and converted according to Eqs. 2.7 and 2.8, and FRP, retrieved from MODIS on board Terra (Aqua). A global grid with a horizontal resolution of 1° x 1° for a total of five different types of vegetation is used and evaluated for these regions.

In a first step, monthly means of tropospheric NO_2 are analyzed for their temporal correlation with monthly means of FRP for five consecutive years from 2007 to 2011 on a 1° x 1° grid. Secondly, spatially averaged regression coefficients are determined for the selected regions. The obtained regression coefficients are then used for the prediction of tropospheric NO_2 columns by simply applying a linear regression model. Thirdly, the production rate of NO_x from fire as derived from GOME-2 and OMI measurements is compared with the GFEDv3.1 NO_x. In order to ensure comparability of the obtained FERs in this study with the fire emissions of NO_x typically found in the state-of-the-art emission inventories, the number density of the NO_2 columns is converted into mass concentrations of NO_x (see Sect. 1.4). In a fourth step, FERs for

* This subsection has been previously published as part of Schreier et al. (2014a).

different types of vegetation are derived on a 1° x 1° grid by using a global land cover map and filtering the data based on population density. Finally, possible factors that could affect the retrieval and conversion of TVC NO_2 and P_f, and thus the magnitude of the presented FERs of NO_x, are discussed.

2.3.1 Correlation between tropospheric NO_2 and fire radiative power *

The global distribution of TVC NO_2, averaged over five consecutive years (2007–2011), is shown in Fig. 2.1. It indicates that the natural sources and emissions of NO_x are much more equally distributed over Earth's surface and in the atmosphere than anthropogenic sources and emissions. It should be noted that the upper limit of TVC NO_2 is restricted to 5×10^{15} molec cm^{-2}, in order to differentiate between the NO_2 production from anthropogenic and natural sources.
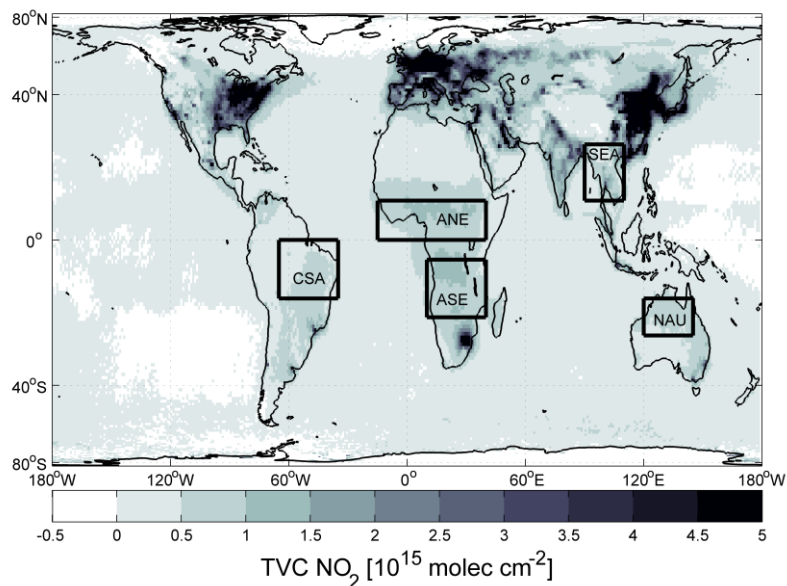
Fig. 2.1: Global mean tropospheric NO_2 vertical columns (2007-2011) retrieved from GOME-2 measurements. Africa north of Equator (ANE, 0° to 10°N and 15°W to 40°E), Africa south of Equator (ASE, 20°S to 5°S and 10°E to 40°E), central South America (CSA, 15°S to 0° and 65°W to 35°W), northern Australia (NAU, 25°S to 15°S and 120°E to 145°E), and Southeast Asia (SEA, 10°N to 25°N and 90°E to 110°E) are highlighted by black rectangles (see also Table 2.1).

The clear spatiotemporal variations of TVC NO_2 result from the inhomogeneous distribution of its sources and the relatively short lifetime of NO_x, which is estimated to be on the order of hours (e.g. Beirle et al., 2011). Moreover, it is obvious that the order of magnitude of the averaged TVC NO_2 is smaller for biomass burning regions (e.g. in Africa, north and south of the Equator) than for large agglomerations (e.g. central east China). Nevertheless, the release of NO_x emissions observed in these biomass burning regions influences the atmosphere from the local to hemispheric and global scales, and thus accurate NO_x emission estimates from vegetation fires are needed. For further analysis, five characteristic biomass burning regions, which are highlighted and defined in Fig. 2.1 and Table 2.1, have been selected

Table 2.1: Selected regions with their abbreviation, location, and absolute area.

region	abbreviation	latitudes	longitudes	area [km^2]
Africa north of Equator	ANE	0° to 10°N	15°W to 40°E	6.76 x 10^6
Africa south of Equator	ASE	20°S to 5°S	10°E to 40°E	5.41 x 10^6
central South America	CSA	15°S to 0°	65°W to 35°W	5.49 x 10^6
northern Australia	NAU	25°S to 15°S	120°E to 145°E	2.90 x 10^6
southeast Asia	SEA	10°N to 25°N	90°E to 110°E	3.53 x 10^6

A previous study by Giglio et al. (2010) showed that the total yearly area burned in these five regions accounts for about 85% of the total global area burned on average. These findings support the selection of these regions, as most of the global fire activity and its resulting emissions of trace gases and aerosols are observed within their boundaries. The selected regions are generally far away from megacities, which produce significant amounts of NO_x by high temperature combustion processes. However, the greater Bangkok area located in Southeast Asia (SEA) is an exceptional case because of its emissions from traffic.

The temporal correlation coefficients for each 1° x 1° pixel are calculated from the consecutive five year data sets of TVC NO_2 and FRP (see Fig. 2.2). The morning observations (GOME-2 TVC NO_2 vs. MODIS Terra FRP) show that the highest correlation coefficients of $r > 0.8$ are found in Africa, south of the Equator (ASE) and

Africa, north of the Equator (ANE). Moderate to high correlation coefficients are also apparent in central South America (CSA), northern Australia (NAU), and SEA. Temporal correlation between TVC NO_2 and FRP is also found beyond 30° N and 30° S, especially in boreal ecosystems, but much less strong and widespread. This is probably due to the lower signals in TVC NO_2 and FRP data sets and due to much less pronounced seasonal variations of the aforementioned parameters. The negative correlation coefficients over large agglomerations can be explained as a consequence of higher NO_2 levels being observed in the wintertime, whereas NO_x emissions from vegetation fires (mainly cropland fires) in the summertime are much lower in magnitude.
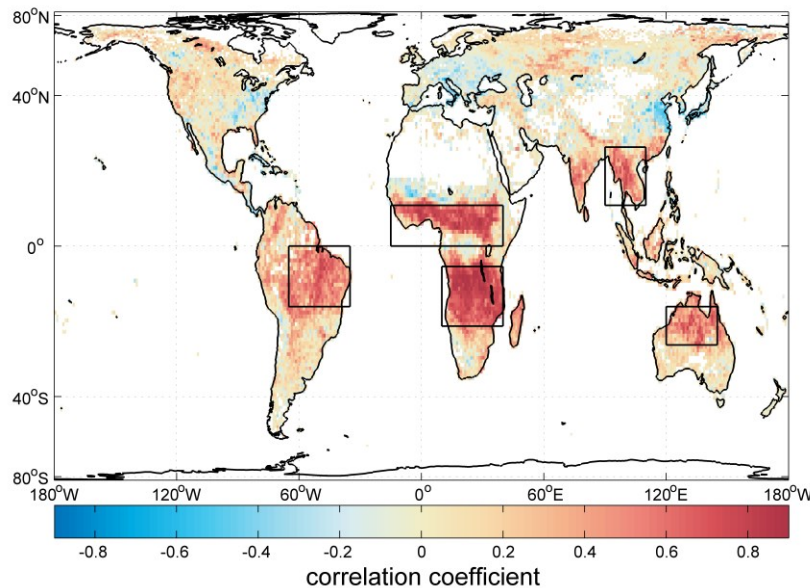
Fig. 2.2: Correlation coefficients (*r*) of the local temporal relationship between FRP and TVC NO_2 based on monthly averages from 2007-2011 on a 1° x 1° grid. Data are shown for the linear relationship observed between GOME-2 TVC NO_2 and MODIS Terra FRP.

However, these regions with negative correlation are not included for the estimation of the FERs (see below). The spatial distribution and magnitude of the correlation coefficients obtained from the relationship between TVC NO_2 and FRP for the early afternoon (OMI vs. MODIS Aqua, not shown here) is in good agreement with the morning correlations shown in Fig. 2.2, underlining the robust link between TVC NO_2 and FRP.

Figure 2.3 illustrates the time series of monthly means of TVC NO_2 and FRP, averaged over the selected regions, for the morning (GOME-2 vs. MODIS Terra) and early afternoon (OMI vs. MODIS Aqua) observations. For the TVC NO_2, 1° x 1° boxes located over the open ocean are included in the averaging procedure. While the inclusion of these pixels reduces the magnitude of the monthly mean TVC NO_2 and FRP values, especially in ANE, no deterioration of the overall seasonal variation is expected. The seasonal variability of FRP, which peaks during the dry season, is reflected by the NO_2 measurements to a high degree, especially in ANE, ASE, and CSA. The high consistency between the two seasonal cycles is a consequence of the relatively short lifetime of NO_x and the resulting small horizontal transport.
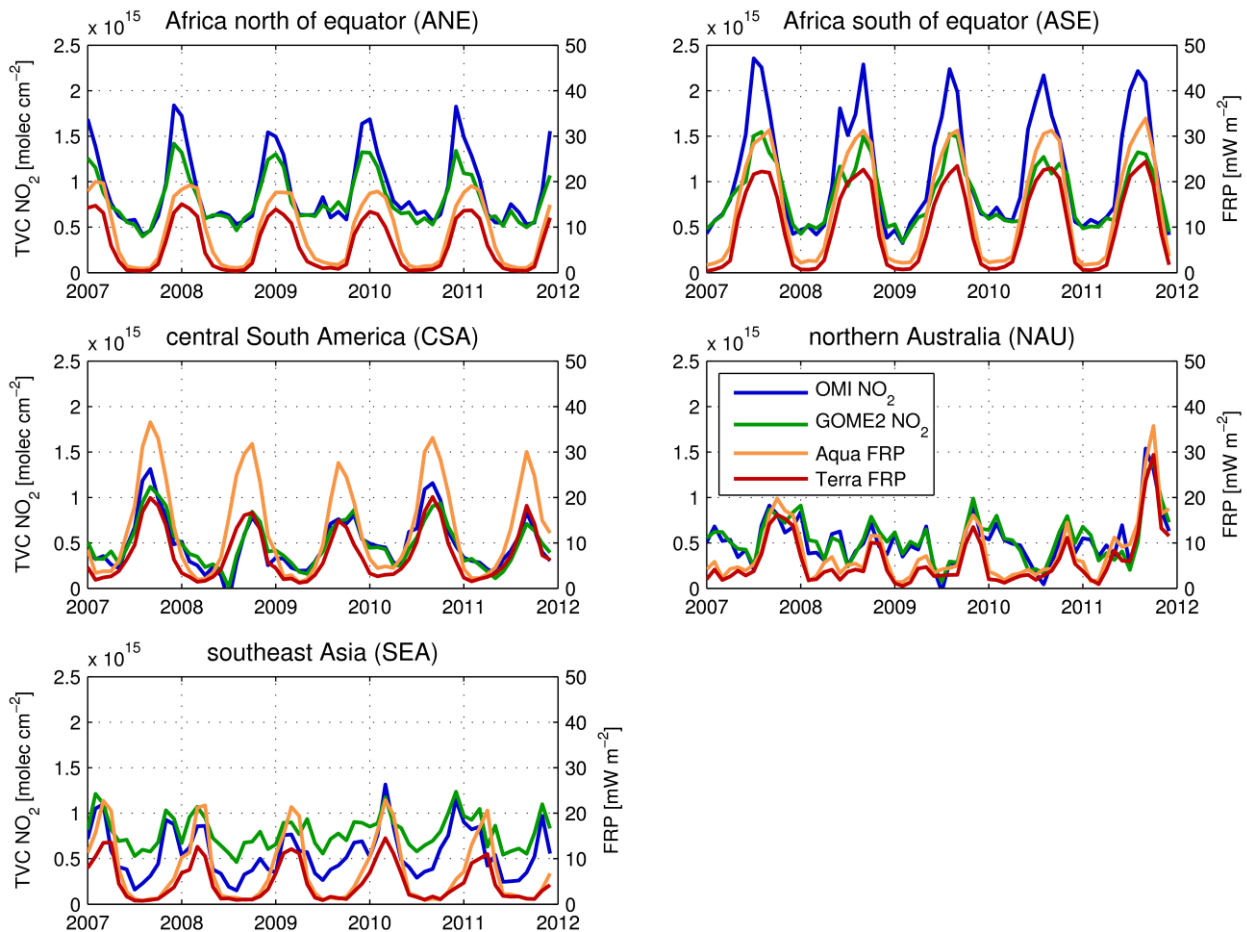
Fig. 2.3: Temporal variability of MODIS Terra (red) and MODIS Aqua (orange) derived FRP and GOME-2 (green) and OMI (blue) derived TVC NO_2 for the selected regions as highlighted in Fig. 2.1 and defined in Table 2.1.

Biomass burning as a dominant NO_x emission source in tropical regions was already mentioned by Cahoon et al. (1992). Moreover, the seasonal variation of NO_2 for African biomass burning regions, usually peaking during the dry season, was pointed out by van der A et al. (2008). They used a simple classification scheme for the identification of NO_x sources based on seasonality and showed that the movement of maximum NO_2 concentrations correlated well with fire count observations from the AVHRR and the ATSR satellite-based instruments.

In contrast to the African regions and CSA, the agreement between TVC NO_2 and FRP in the presented study is weaker over NAU and SEA. As the influence of anthropogenic sources in the selected regions remains low when spatially averaged (except for SEA), the enhanced dry season tropospheric NO_2 levels are mainly produced by active fires. In the wet season, tropospheric NO_2 levels result from soil microbial activity, lightning, and high temperature combustion processes induced by humans (e.g. Beirle et al., 2004a). Indeed, the interannual variability of TVC NO_2 over ANE and ASE is less apparent during the dry season (maxima) than during the wet season (minima). This fact indicates an overall uniform interannual pattern of fire activity in these two regions (Fig. 2.3).

In general, the early afternoon observations indicate higher intensity in fire, and thus higher values of TVC NO_2. This feature has already been found over tropical regions in a previous study by Boersma et al. (2008). They showed that column mixing ratios of NO_2, detected by OMI (13:30 LT), are typically more than 40% higher than mixing ratios detected by SCIAMACHY (10:00 LT). However, in CSA there are no significant differences between morning and early afternoon signal of TVC NO_2, although the intensity of fires is much higher during early afternoon. Possible explanations could be the differences in the detection sensitivity of fires or diurnal changes in the removal of NO_x. Another interesting feature is observed over NAU, as there are only minor differences between morning and early afternoon observations for both TVC NO_2 and FRP. In contrast to the usual diurnal cycle of fire intensity observed in other regions, which steeply increases in the early afternoon elsewhere, the fire intensity in NAU is even lower during the OMI overpass than during the GOME-2 overpass. This feature is also found in Fig. 2.3, where no obvious differences between the morning and early afternoon fire intensity are visible. In contrast, the differences of TVC NO_2 and FRP

between morning and early afternoon are more distinct in the African regions. It is suggested that the impact of accumulating NO_2 concentrations in these regions is stronger than changes in NO_x lifetime between morning and early afternoon.

The highest spatiotemporal-averaged FRP, derived from the morning observations, occurred in October 2011 in NAU, the usual observed monthly FRP being two times smaller. One explanation for these unusually high values in NAU could be the strong rainfalls in early 2011, which lead to higher amounts of fuel available for the burning later in the dry season. Overall, the early afternoon observations of FRP show that the highest spatio-temporal means are found over ASE and CSA (see Fig. 2.3).

As already mentioned before, the lower mean values of TVC NO_2 in ANE can be explained by the fact that more 1° x 1° boxes with low values of TVC NO_2 over the ocean are included in the averaging procedure. As a consequence of the higher background levels of tropospheric NO_2, the seasonal variability of TVC NO_2 is less pronounced in SEA. Moreover, the higher values of TVC NO_2 retrieved from GOME-2 most likely arise from the higher emissions of NO_x in the morning rush hours in larger agglomerations located in this region.

2.3.2 Determination of regression coefficients *

The area-averaged regression coefficients have been computed for the morning and early afternoon and the selected regions (see Fig. 2.4) for generating simple linear regression models. In general, the obtained gradients show good agreement among the regions with the highest gradients being observed in the early afternoon over the African regions. While the morning and early afternoon gradients over NAU and SEA show a similar rise, obvious differences in gradients are observed in CSA. The computed y-intercepts show some degree of disagreement among the regions, especially between those calculated for the African regions and CSA.

The higher background levels in ANE and ASE (compared to CSA) may arise from the higher wet season emission rates of savanna soils dominating in these regions. This is in good agreement with the findings of Yienger and Levy (1995), as they suggest much

* This subsection has been previously published as part of Schreier et al. (2014a).

lower emission rates of NO$_x$ from soil microbial activity in tropical rain forests covering large areas in CSA. Meyer-Arnek et al. (2005) have shown that a significant amount of TVC NO$_2$ could also be attributed to NO$_2$ production from lightning, as the lifetime of NO$_2$ is longer in the upper troposphere. In comparison to the dry season peak values of TVC NO$_2$ and FRP, the wet season values within ANE, ASE, CSA, and NAU are about two thirds smaller in magnitude.
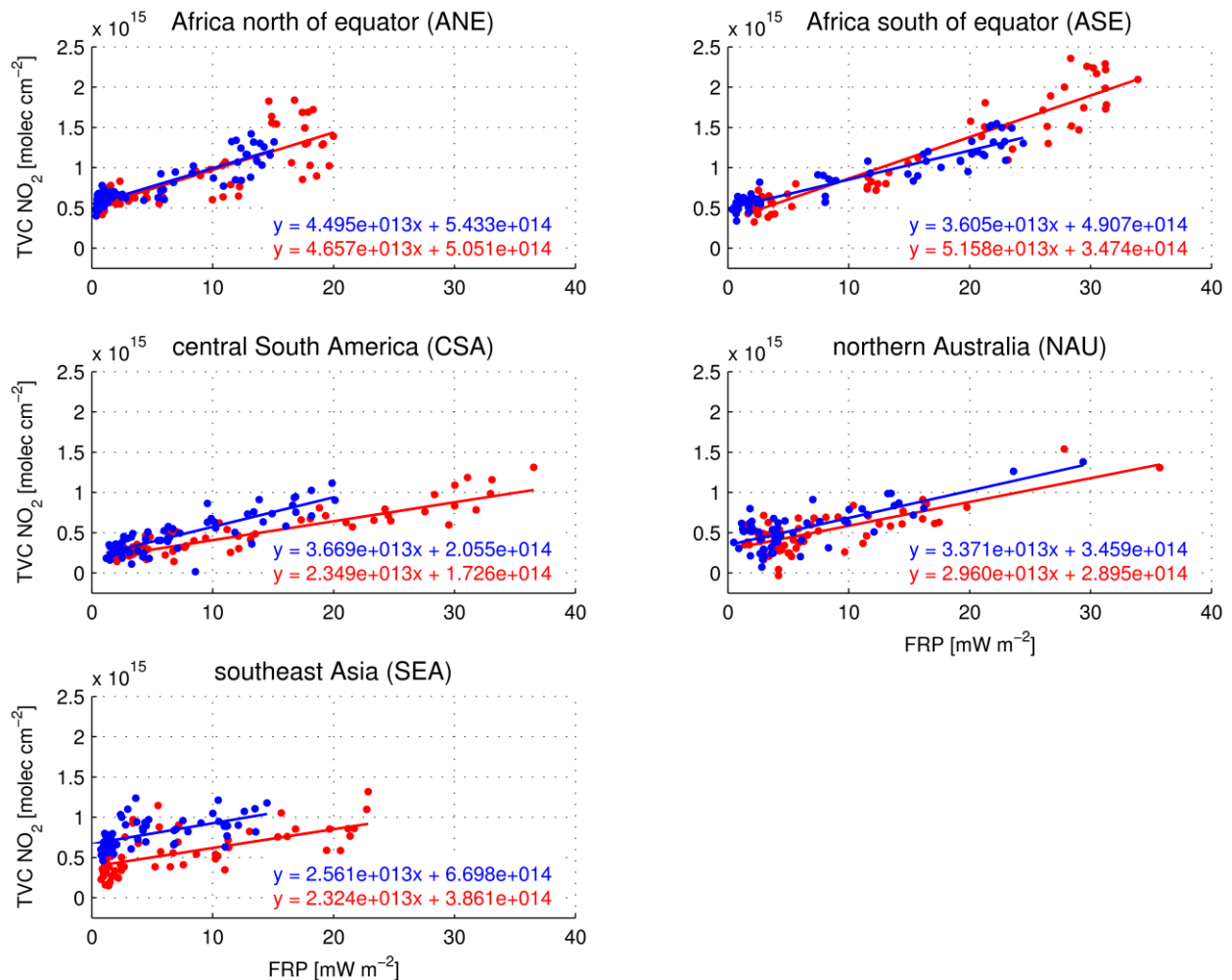
Fig. 2.4: Scatter plots with their associated regression coefficients for the selected regions, illustrating the linear relationship of GOME-2 TVC NO$_2$ vs. MODIS Terra FRP (blue) as well as OMI TVC NO$_2$ vs. MODIS Aqua FRP (red). Each dot represents a monthly average over the respective region.

The spatial distribution of the y-intercepts (Fig. 2.5) and gradients (Fig. 2.6) is generally smooth and shows some regional variation, indicating that a robust link exists between TVC NO_2 and FRP. The higher (lower) gradients indicate that lower (higher) values of FRP are necessary for reaching a specific NO_2 level. There are few pixels with unexpected high gradients, which, however, will not affect the presented analysis as the relative number of these outliers is very low.
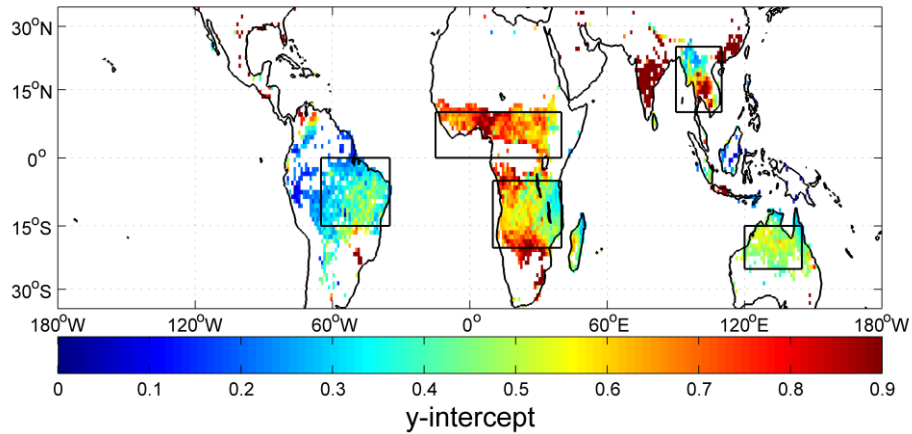
Fig. 2.5: Mean y-intercepts [in units of 10^{15} molecules cm^{-2}] of the best fitting least-squares regression lines (2007-2011) for pixels with $r > 0.3$, based on a 1° x 1° grid. Data are shown for the regression lines between GOME-2 TVC NO_2 and MODIS Terra FRP.
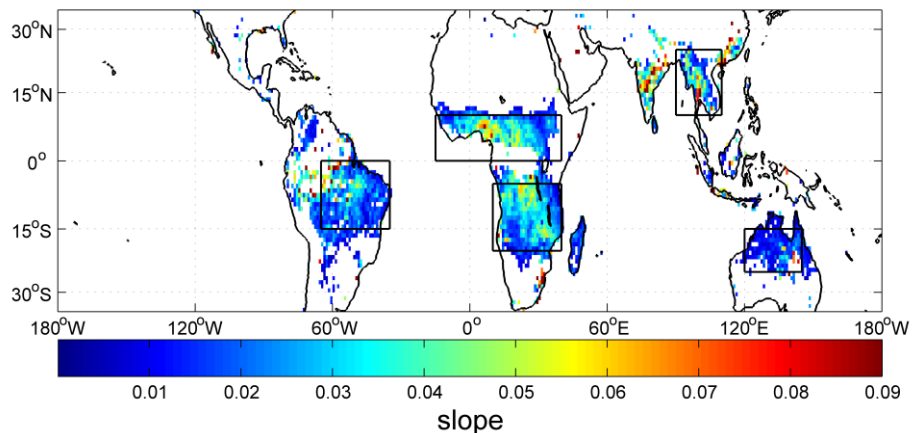
Fig. 2.6: Mean gradients [in units of 10^{15} molecules cm^{-2} (mW m^{-2})$^{-1}$] of the best fitting least-squares regression lines (2007-2011) for pixels with $r > 0.3$, based on a 1° x 1° grid. Data are shown for GOME-2 TVC NO_2 vs. MODIS Terra FRP linear relationships.

For instance, high y-intercepts in ANE are found in the coastal region of Nigeria, which is one of the world's most densely populated regions with many well-known emission sources from oil mining and gas flares (e.g. Marais et al., 2012). The greater Bangkok area in SEA, which is influenced by many emission sources, such as high-traffic roads, is also characterized by high y-intercepts. The emissions from public and private cars in Bangkok are estimated to contribute up to 80% of NO_x (Sahu et al., 2011). Both cases can be interpreted as a clear signal of anthropogenic sources increasing the tropospheric NO_2 columns.

On the other hand, low y-intercepts represent rather remote areas without any anthropogenic influence, as observed over northern parts of Australia (see Fig. 2.5).
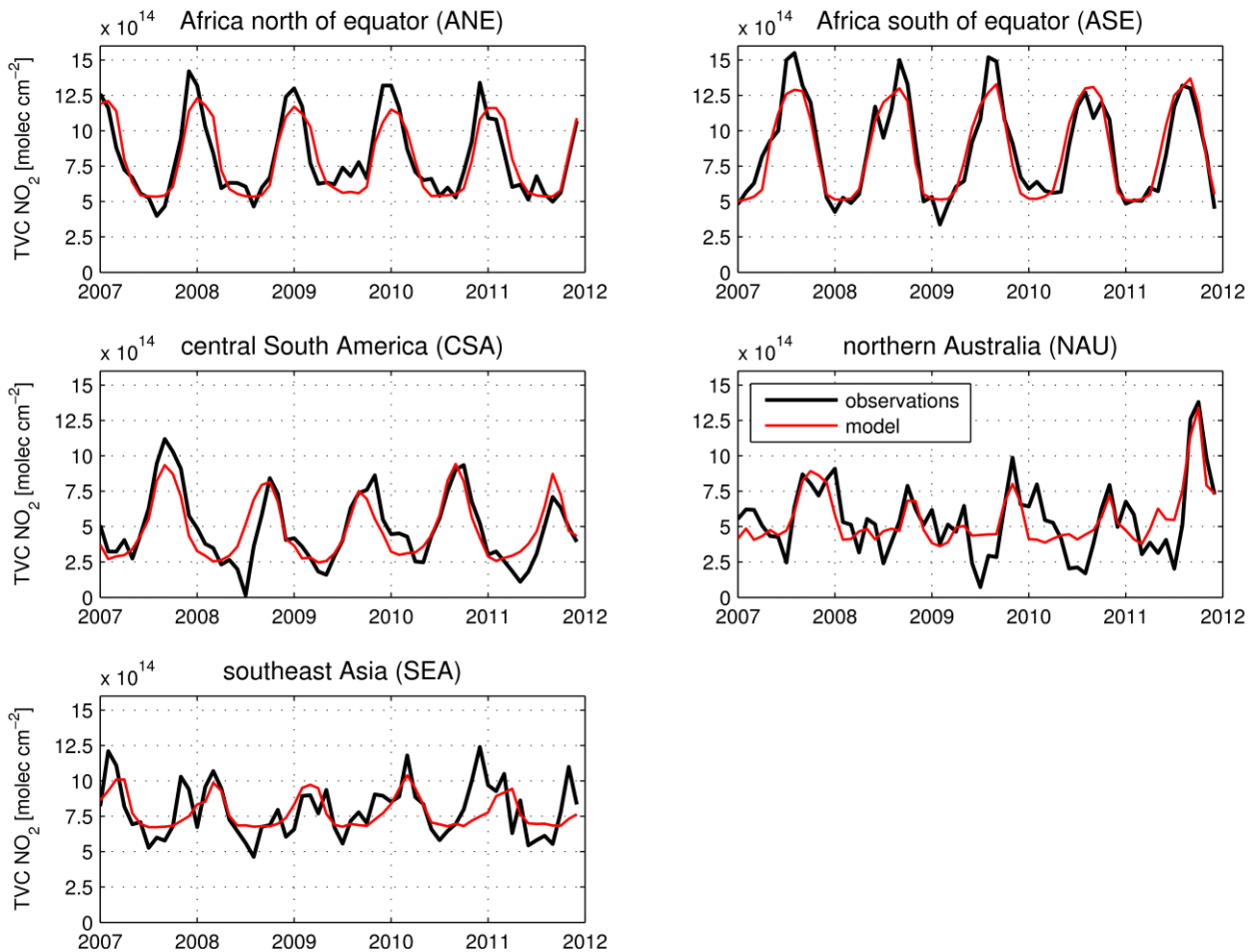
Fig. 2.7: Monthly means of TVC NO_2 from GOME-2 measurements (black line) and TVC NO_2 as calculated from the simple linear model (red line) for the selected regions.

As a test of how good the assumption is that the observed TVC NO_2 is dominated by biomass burning emissions, monthly area-averaged regression coefficients calculated for the individual regions are used in a simple linear model to predict satellite NO_2 columns using FRP (see Fig. 2.7).

As was expected from the high temporal correlation indicated in Figs. 2.2 and 2.3, the tropospheric NO_2 columns can be reproduced by simply applying regression coefficients and monthly means of FRP. The agreement between observed and estimated NO_2 columns is best for ANE ($\pm40\%$) and ASE ($\pm40\%$). Larger differences on the order of 100% are observed for CSA, NAU, and SEA. However, it is clear that large fractions of the NO_2 signal are explained by the seasonal variation of FRP. The overall agreement between the observed and calculated TVC NO_2 for the early afternoon is similar (not shown here).

2.3.3 Comparison between P_f and GFEDv3.1 NO_x *

The estimates of NO_x emissions found in biomass burning emission inventories, based on the bottom-up approach, such as GFEDv3.1 (van der Werf et al., 2010), are usually given as g NO_x m^{-2} $month^{-1}$. In order to compare the values from the emission inventory with TVC NO_2 retrieved from GOME-2 and OMI measurements, the production rate of NO_x from fire (P_f) has to be determined (see Sect. 2.2.6). According to the units reported in GFEDv3.1, the column number density of NO_2 (in molecules cm^{-2}), as retrieved from GOME-2 and OMI measurements, are converted into mass concentrations of NO_x produced by fires (in g NO_x m^{-2} $month^{-1}$).

The scatter plots of P_f obtained in this study versus GFEDv3.1 are shown in Fig. 2.8 for the selected regions. While the blue line represents the correlation between P_f obtained from GOME-2 measurements and GFEDv3.1 NO_x, the red line shows P_f obtained from OMI against GFEDv3.1 NO_x.
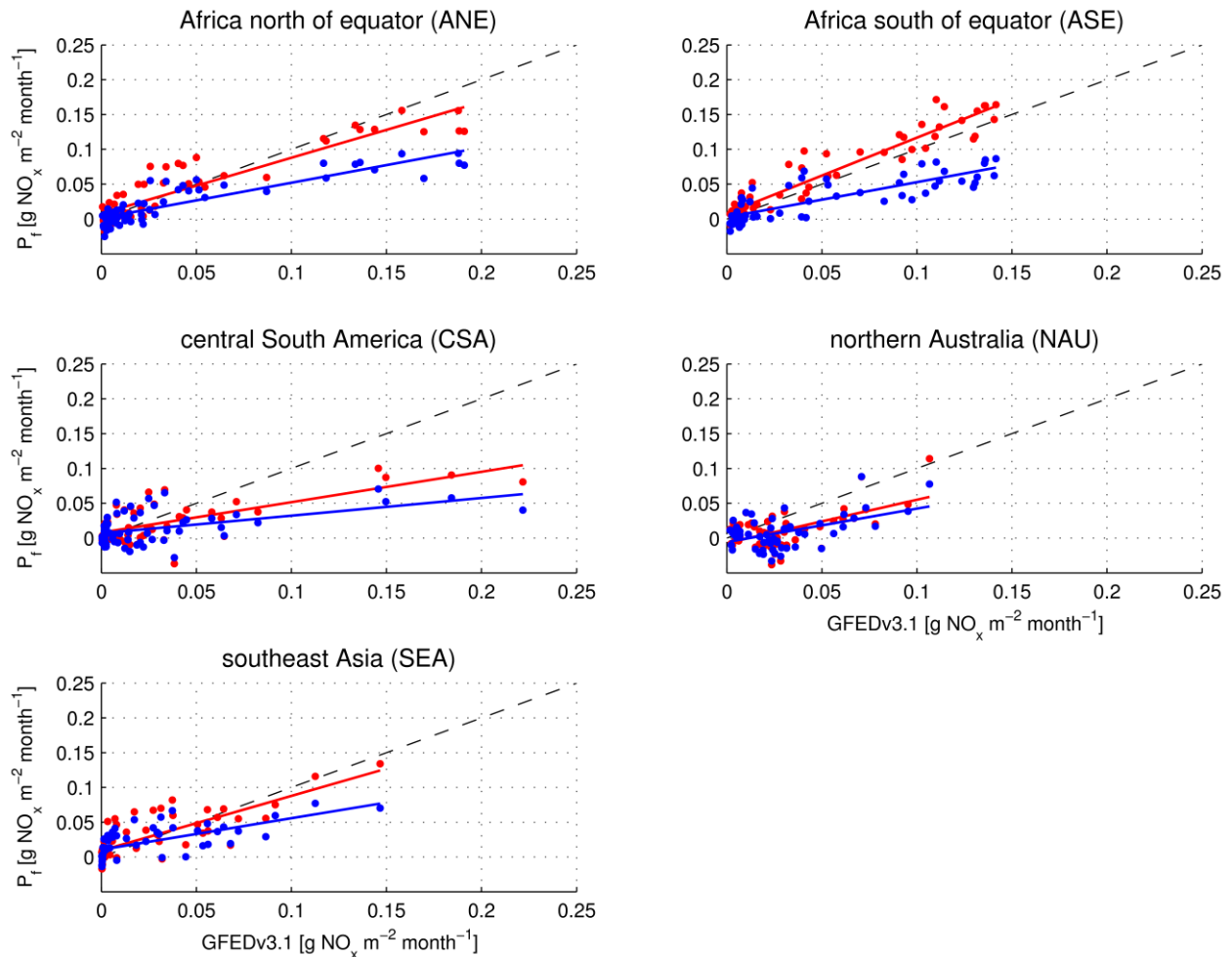
Fig. 2.8: Scatter plots of the estimated monthly production rates of NO_x from fires (P_f), retrieved from the GOME-2 (blue) and OMI (red) TVC NO_2 observations, against GFED3.1 NO_x emission fields. The 1:1 line is shown by the dashed black line.

There is a clear correlation between the two parameters, with the best agreement found for the African regions. In these regions, a stronger gradient is found for the early afternoon observations, which is related to the fact that the fire intensity in the early afternoon is higher (see Figs. 2.3 and 2.4). Consequently, higher fire intensity increases the release of NO_x emissions. A similar pattern is also found for CSA and SEA, where P_f calculated from GOME-2 is lower than P_f calculated from OMI. However, the observed differences are smallest for NAU, possibly due to the small differences in fire intensity between morning and early afternoon, as addressed in Sect. 2.3.1. Giglio (2007) found a bimodal diurnal cycle in fire activity in northern Australia, peaking around 11:00 LT and

16:00 LT. The decrease in fire activity between 11:00 LT and 13:30 LT (OMI equatorial overpass time) could explain these low observed discrepancies. By estimating the time expressing the average of daily fire activity from the findings of Giglio (2007) and Roberts et al. (2009), it is found that generally occurs between 09:30 LT and 13:30 LT. According to this estimation, the blue (red) lines are expected to have a lower (higher) slope than the 1:1 lines. However, in most of the regions, both slopes are lower than the 1:1 lines, suggesting that either GFEDv3.1 NO_x is overestimated or P_f from GOME-2 and OMI is underestimated.

2.3.4 Fire emission rates of NO_x for selected biomes and regions *

As there is some indication of heterogeneity in the global map of mean gradients, as shown in Fig. 2.6, the inclusion of a global land cover map (Fig. 2.9) and a population density data set (not shown here) is a next step towards understanding these differences and estimating the FERs of NO_x.
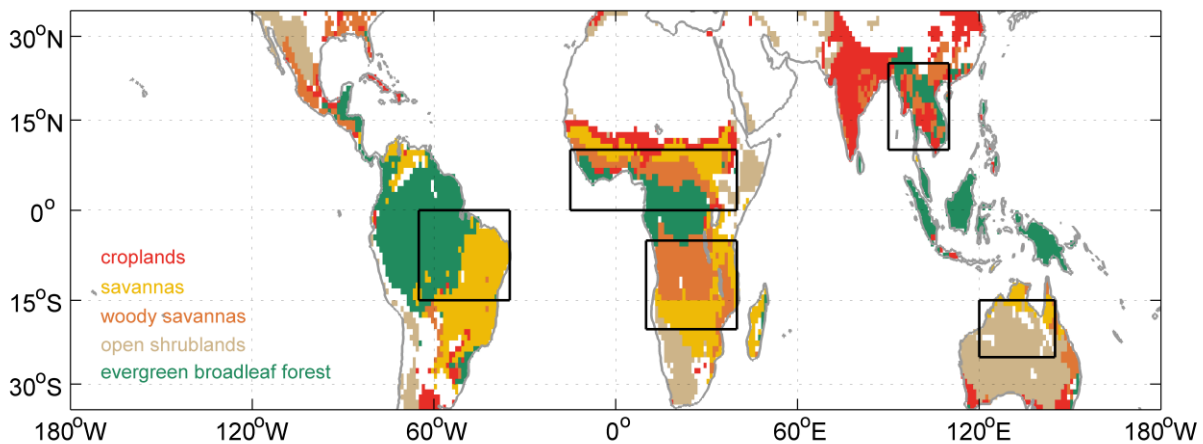
Fig. 2.9: Global land cover map used for the distinction of the different biomes (see also Sect. 2.2.3 and Table 2.2). The selected land cover types are evergreen broadleaf forest (green), open shrublands (beige), woody savannas (orange), savannas (yellow), and croplands (red).

A 1° x 1° gridded global land cover map with a total of five types of vegetation (see Fig. 2.9) is used to compute the FERs for the dominating biomes within the five selected regions. For deriving the FERs, the best fitting least-squares regression lines between P_f

and FRP are computed for each land cover type using all 1° x 1° pixels having $r > 0.3$ (see Fig. 2.2). Additionally, the population density of GRUMPv1 is used in the algorithm for the exclusion of strongly anthropogenically influenced (mainly by the residential and industrial sectors) 1° x 1° boxes, using a threshold value of 100 persons km^{-2}. The calculations have been performed for the GOME-2 vs. MODIS Terra (morning) and OMI vs. MODIS Aqua (early afternoon) observations.

Table 2.2: Absolute numbers of 1° x 1° boxes included in the analysis for the estimation of fire emission rates (FERs) of NO_x for the selected regions and different types of vegetation extracted from the Collection 5 MODIS Land Cover Type product. Absolute numbers obtained from the morning (early afternoon) observations are shown left (right).

land cover type	region				
	ANE	ASE	CSA	NAU	SEA
evergreen broadleaf forest	2258 / 4129	286 / 294	9999 / 9509	- / -	2484 / 3322
open shrublands	- / 60	240 / 300	- / -	7080 / 6780	- / -
woody savannas	6365 / 6462	12608 / 12708	60 / 60	240 / 180	1860 / 2154
savannas	5028 / 5039	8797 / 8758	9964 / 9470	1800 / 1679	- / -
croplands	1136 / 980	- / -	- / 117	- / -	950 / 893

Table 2.2 lists the land cover types with their region-specific absolute numbers of 1° x 1° boxes included in the analysis, where morning and early afternoon numbers are shown on the left and right, respectively. The FERs have then been obtained for each land cover type, when the absolute number is higher than 500. Due to the large number of P_f and FRP values, derived from the consecutive five years data sets, a binning method for averaging these values over a successive FRP-interval of 15 MW $pixel^{-1}$ is used. To ensure the quality, the averaging procedure only includes intervals, where the number of values exceeds 25 within the interval. It should be noted that this averaging procedure is also intended to reduce the deterioration of the linear relationship by the influence of a few very large fire events which, however, produce unexpected low levels of tropospheric NO_x. For example, there is a clear signal of a nonlinear relationship between P_f and FRP for savannas beyond 800 MW $pixel^{-1}$ in ANE (see Fig. 2.10). However, it is also clear that these single fire events are rather few when compared to the overall fire activity in this region.
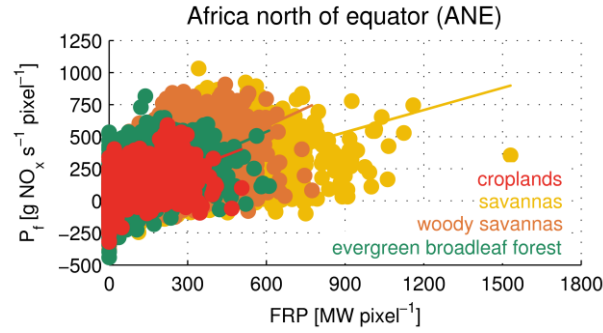
Fig. 2.10: Biome-specific FERs of NO_x for ANE. Here, the best fitting least-squares regression lines of the morning observations (GOME-2 vs. MODIS Terra) are shown for evergreen broadleaf forest (green), woody savannas (orange), savannas (yellow), and croplands (red).
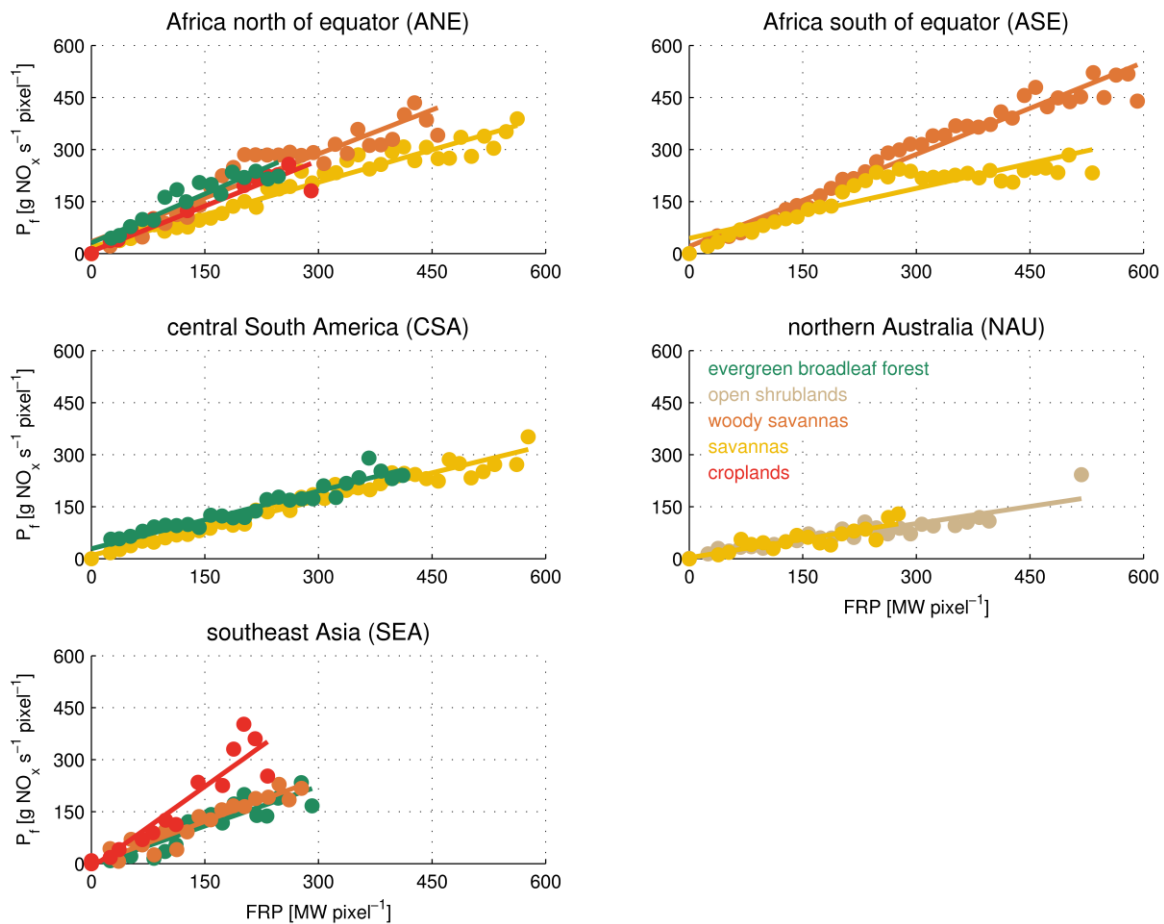
Fig. 2.11: Biome-specific FERs of NO_x, averaged via the binning method, for the selected regions. Here, the best fitting least-squares regression lines of the morning observations (GOME-2 vs. MODIS Terra) are shown for evergreen broadleaf forest (green), open shrublands (beige), woody savannas (orange), savannas (yellow), and croplands (red). The binning method used for the averaging is described in the text.

A summary of the derived biome-specific FERs for the selected regions ANE, ASE, CSA, NAU, and SEA is given in Fig. 2.11 and Table 2.3.

As already mentioned above, a threshold value of 500 for the absolute number of pixels included has been implemented after filtering the data according to population density and correlation coefficient. Therefore, the calculations of FERs within the boundaries of the selected regions have also been restricted to the rather frequently burned land cover types, such as evergreen broadleaf forest, open shrublands, woody savannas, savannas, and croplands. The estimated FERs of NO_x for the dominating types of vegetation burned are lowest for open shrublands (0.33–0.34 g NO_x s^{-1} MW^{-1}) and savannas (0.28–1.03 g NO_x s^{-1} MW^{-1}) and highest for croplands (0.87–1.56 g NO_x s^{-1} MW^{-1}) and woody savannas (0.82–1.54 g NO_x s^{-1} MW^{-1}). The FERs of NO_x are generally larger in the African regions than elsewhere, except for croplands where highest values are found in SEA.

Table 2.3: Mean gradients (FERs), in g NO_x s^{-1} MW^{-1}, derived from the best fitting least-squares regression lines for each land cover type and the selected regions, applying the morning (left) and early afternoon (right) linear relationships between P_f and FRP.

land cover type	region				
	ANE	ASE	CSA	NAU	SEA
evergreen broadleaf forest	0.94 / 0.77	- / -	0.55 / 0.43	- / -	0.76 / 0.60
open shrublands	- / -	- / -	- / -	0.33 / 0.34	- / -
woody savannas	0.84 / 1.41	0.88 / 1.54	- / -	- / -	0.82 / 1.18
savannas	0.62 / 1.03	0.48 / 0.84	0.53 / 0.49	0.35 / 0.28	- / -
croplands	0.87 / 1.19	- / -	- / -	- / -	1.56 / 1.22

In a recent study by Mebust et al. (2011), OMI NO_2 data for a smaller region in California and Nevada (USA) were used together with detailed meteorological information and a high resolution (500 m x 500 m) land classification to estimate biomass burning emission coefficients (ECs). Concerning the geographical location, vegetation, and climate, their selected region is in best agreement with NAU investigated in this study. The results of Mebust et al. (2011), which are based on a similar approach, show higher values for open shrublands (shrubs). For the other two land cover types (forests and grasslands), a

comparison is difficult, as grasslands and extratropical forests are not included in the presented analysis. In a more recent study by Mebust and Cohen (2014), smaller modifications were made to the approach and ECs were calculated for different biomes on a global scale. In general, they found the highest values for grasslands (including savannas and woody savannas), which is in good agreement with the values derived in the presented study. However, the magnitude of the ECs in their study is about two times smaller than the magnitude of FERs obtained in this study.

A regional comparison shows that the FERs for woody savannas and savannas in ANE, ASE, CSA, and SEA are similar, whereas the FERs are significantly lower in NAU than elsewhere. One explanation could be the differences in plant characteristics in various regions or even on different continents. For instance, the N content in the fuel of savannas could be higher in the African regions than in Australia, and thus higher amounts of TVC NO_2 are reached by the same intensity of FRP. Mebust and Cohen (2013) argue that the fuel moisture could also play a significant role, as they found a significant cycle in fire emission rates of NO_x for the African woody savannas. From their point of view, this means that the African regions experience an overall drier season, and thus the FERs are higher due to the fact that the N content in the fuel is likely more efficiently converted into NO_x.

2.3.5 Possible factors affecting the magnitude of FERs of NO_x *

As discussed in the previous sections, there are interesting differences and patterns in the FERs calculated in this study. However, there are also uncertainties in the approach taken, which could affect some of the results. These are discussed in the following.

First of all, tropospheric NO_2 columns over tropical and subtropical biomass burning regions have uncertainties of up to 30%, as discussed in the extensive error analysis for satellite-based retrievals of TVC NO_2 by Boersma et al. (2004). In a more recent study by Bousserez (2013), it was pointed out that the uncertainties might even be larger (up to 60%) as the influence of an elevated aerosol layer developing during Harmattan fronts can have a negative aerosol impact on the AMF. The use of spatiotemporal averages of TVC NO_2, as performed in this study, probably leads to a decrease in uncertainties

reported above. Using the y-intercept of the regression between TVC NO_2 and FRP for determining the background TVC_b assumes that NO_x emissions from other sources do not have a seasonality, which is not correct and can introduce uncertainties of up to 20%, depending on the region. In addition to the uncertainties arising during the satellite-based retrieval procedure, the conversion of TVC NO_2 into production rates of NO_x from fires contributes to the uncertainty in the estimated FERs. This includes the assumption of a constant lifetime of NO_x (τ = 6 h) as well as a constant NO_2/NO_x ratio (0.75) for estimating the production rate of NO_x, where both quantities depend on altitude, atmospheric composition, time of day, and probably also on the type of fire. This uncertainty is difficult to assess but could be as large as 30%. However, the estimated production rates of NO_x are consistent to some degree with the emission fields of NO_x from GFEDv3.1, and thus the rough assumptions made for the NO_2/NO_x ratio and the lifetime of NO_x seem to work well for the given approach. Retrieving the sum of FRP by applying the typical calculation can also introduce a negative bias on the order of 30% (Freeborn et al., 2011). Due to the fact that the errors in both TVC NO_2 and FRP have a rather negative direction, the overall uncertainties of FERs are reduced.

As outlined above, static AMFs as well as constant values for the NO_x lifetime and the NO_2/NO_x ratio for the retrieval of TVC NO_2 and the conversion into P_f are used. Therefore, the FERs and EFs derived in this study could be affected by errors arising from biome-specific, diurnal, and regional changes in AMFs, NO_x lifetime, and NO_2/NO ratio.

One possible source of errors is unaccounted for diurnal changes in the boundary layer height, which has a tendency to increase between GOME-2 and OMI overpasses. The effect of an overestimated boundary layer height is twofold: first, the measurement sensitivity, which is smaller close to the surface, is underestimated, and consequently the AMF is overestimated (Leitão et al., 2010). Second, the lifetime of NO_x, which during daytime is mainly a function of the altitude, could be overestimated. Other possible sources of errors are related to diurnal changes in aerosol properties. For instance, a decrease in the single scattering albedo (SSA) due to an increase of the combustion efficiency between morning and early afternoon can result in a general decrease of the

AMF. This effect is especially pronounced in more polluted atmospheres with an increased AOD.

In the presented analysis, the NO_x lifetime is assumed to be constant. However, a decrease or increase in NO_x lifetime between GOME-2 and OMI overpasses could also contribute to the overall error. It should be noted that all of these possible error sources could also partially affect the observed regional differences in FERs.
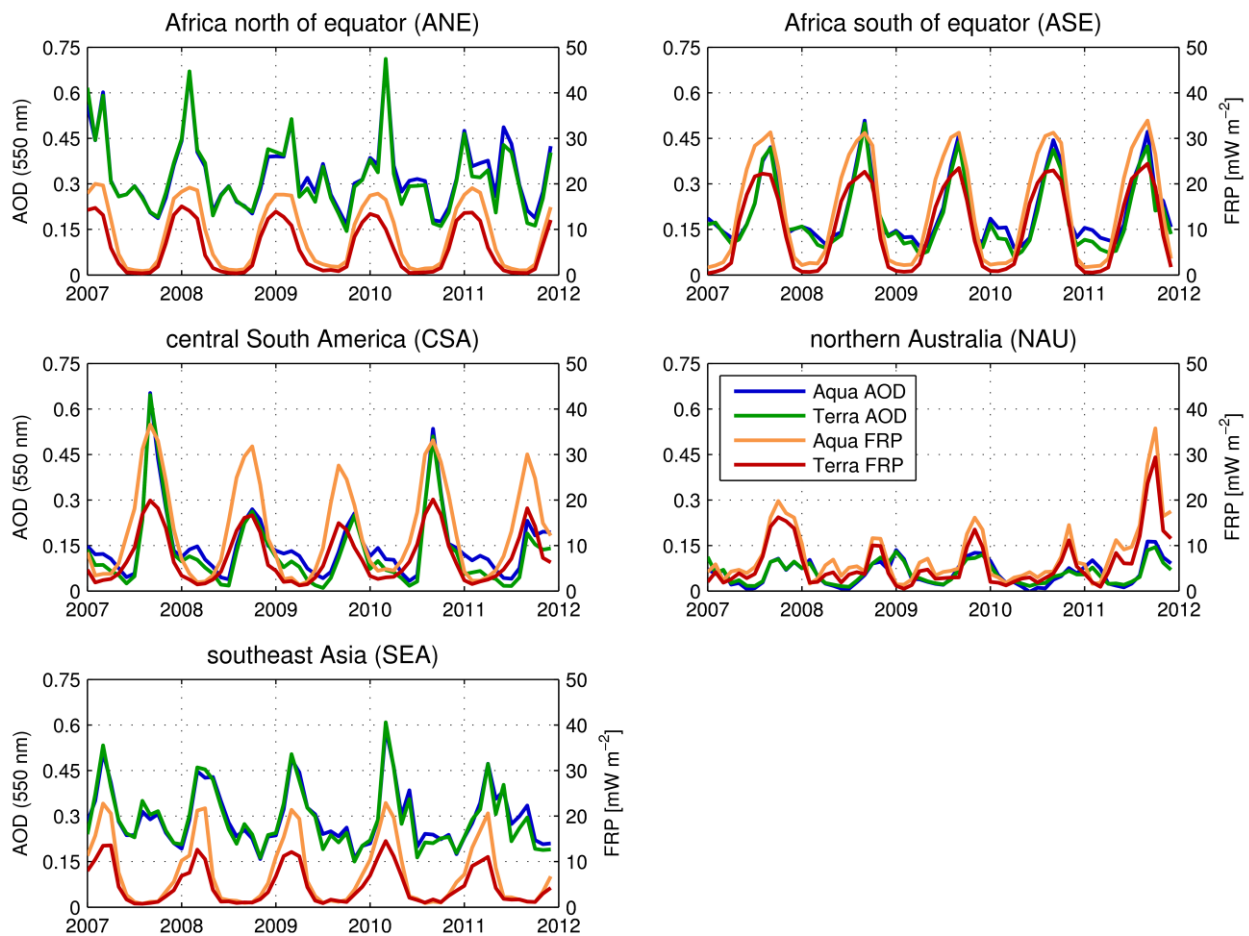
Fig. 2.12: Temporal variability of MODIS Terra (red) and MODIS Aqua (orange) derived FRP and MODIS Terra (green) and MODIS Aqua (blue) derived AOD for ANE, ASE, CSA, NAU, and SEA.

Concerning the diurnal discrepancies in FERs of NO_x (by comparing morning and early afternoon FERs), it is found that FERs for evergreen broadleaf forest are about 20% lower in the early afternoon in ANE, CSA, and SEA (see Table 2.3). In general, diurnal

variations in the boundary layer height, which influence the NO_2 vertical profile, are much lower over forested areas than, for instance, over savannas (Marion et al., 2001). Moreover, the boundary layer height usually increases during the day, which would lead to an overestimation of FERs, and thus higher values in the early afternoon. The diurnal changes in AOD are negligibly small (see Fig. 2.12), and consequently the effect of an increasing or decreasing AOD can be ruled out.

However, one possible impact of aerosols could result from changes in SSA throughout the day. The observations of FRP are higher in the early afternoon (see Fig. 2.3), which also increases the flaming phase consumption resulting in higher NO_x emissions compared to the morning hours. A more complete combustion further modifies the SSA (Eck et al., 2003) and potentially decreases the measurement sensitivity in polluted atmospheres, resulting in a decreased AMF (Leitão et al., 2010). Therefore, a possible explanation of the lower FERs observed for the early afternoon could be the overestimation of AMFs. However, a decrease in NO_x lifetime between morning and early afternoon could also contribute to an underestimation of early afternoon FERs for the evergreen broadleaf forest.

For the other land cover types, an increase in FERs between the morning and early afternoon is observed. Obvious discrepancies in the diurnal cycle are especially found for woody savannas and savannas located in ANE, ASE, and SEA. As the boundary layer height over woody savannas tends to be larger in the afternoon, the AMFs could be underestimated, and thus the early afternoon FERs of NO_x could be too high. Consequently, the differences between estimated morning and early afternoon FERs could at least in part be related to the underestimation of AMFs in the OMI retrieval performed for this study.

Considering the differences in morning and early afternoon FERs observed for croplands, the most plausible reason for the lower morning value in ANE is a change in the boundary layer height, as was discussed before for savannas and woody savannas. However, the higher morning value in SEA might also be related to the urban/industrial released aerosols in the morning rush hours. Usually, urban/industrial aerosols have a larger SSA (Giles et al., 2012), and thus lead to an increased measurement sensitivity.

Whether the negligible small differences in FERs for open shrublands in NAU are related to stable conditions or caused by counteracting effects is not clear.

In this study, some differences are also found among the selected regions for the same vegetation types. For example, the lower values of FERs observed over NAU could be a consequence of the relatively low boundary layer heights (Labonne et al., 2007).

The influence of desert dust aerosols in ANE (see Fig. 2.12), which affect the retrieval of TVC NO_2, could explain the discrepancies in FERs for savanna fires between ANE and ASE. A very recent study by Bousserez (2013) shows that the Harmattan, which are prevailing surface winds bringing dry dusty air from the Sahara to the south, can decrease the AMF over savanna fires by 10–30%. Bousserez (2013) explains the negative aerosol effect by the uplifted biomass burning aerosols that shield the NO_2 concentrations below, and thus decrease the measurement sensitivity. According to these findings, the AMFs calculated for this study would be too high over fires in ANE (compared to ASE), and consequently, TVC NO_2 could be underestimated. The observed FERs for woody savannas are 5–10% lower in ANE, which could be an indication of the use of too high AMFs. However, the FERs for savannas are higher in ANE than in ASE. One possible explanation for the higher values of FERs observed for savannas in ANE lies in the unexpected decreased slope beyond 300 MW pixel^{-1}, which is a unique feature among all derived FERs (see Fig. 2.11) and is also observed for the early afternoon (not shown). A decreased SSA resulting from an increase in both fire intensity and flaming phase consumption under highly polluted cases might be the most meaningful explanation (Leitão et al., 2010). The decrease in SSA could be lower in ANE because of the larger influence of desert dust. Therefore, the measurement sensitivity increases to a larger degree and could lead to the underestimation of TVC NO_2 and P_f. By assuming the slope between 0 and 300 MW pixel^{-1} only, the FERs would be higher for savannas, even higher than observed for ANE, thus confirming the findings of Bousserez (2013).

Interestingly, there are large regional discrepancies of up to 40% observed for evergreen broadleaf forest. By assuming that the regional variations in the boundary layer height and the aerosol properties are negligibly small, and the plant characteristics are

identical, it turns out that the only reasonable explanation for these differences in FERs would be a region-specific NO_x lifetime. The lower lifetime of NO_x over CSA could be the result of relatively high isoprene emissions over the Amazon rainforest (Barkley et al., 2011).

2.4. Summary and conclusions *

In this study, a simple statistical approach has been developed to estimate NO_x emission rates from fires using the strong correlation between the two independent geophysical parameters tropospheric NO_2 vertical column (TVC NO_2) and fire radiative power (FRP). For this, monthly average data retrieved from the measurements of four instruments (GOME-2 and OMI for TVC NO_2, MODIS Aqua and Terra for FRP), on board four different satellites, have been investigated. In general, the seasonal cycles of TVC NO_2 and FRP are strongly correlated over the biomass burning regions. In African regions, high correlation coefficients ($r > 0.8$) for both the morning and early afternoon state of the troposphere are found. Using this correlation yielded an accurate prediction of tropospheric NO_2 columns over biomass burning regions by using a simple linear regression model and FRP values. After the conversion of the TVC NO_2 into production rates of NO_x from fire (P_f), by assuming constant values for the NO_2/NO_x ratio (0.75) and lifetime of NO_x (τ = 6 h), good agreement was found between the satellite-derived fire emissions and GFEDv3.1 NO_x emission fields. The use of a global land cover map enabled the estimation of fire emission rates (FERs) of NO_x for different types of vegetation on a 1° x 1° grid. The FERs have been derived for the morning and early afternoon by making use of the linear relationship between P_f, estimated from the GOME-2 and OMI measurements, and FRP, observed by MODIS Terra and Aqua, respectively. The horizontal resolution of 1° x 1° has been selected in order to overcome the effects of horizontal transport of NO_2 in the troposphere, and also to improve the signal-to-noise ratio.

The results show that there are biome-specific, diurnal, and regional discrepancies in FERs. The estimated FERs of NO_x for the dominating types of vegetation burned are lowest for open shrublands (0.33–0.34 g NO_x s^{-1} MW^{-1}) and savannas (0.28–1.03 g NO_x

s^{-1} MW^{-1}) and highest for croplands (0.87–1.56 g NO_x s^{-1} MW^{-1}) and woody savannas (0.82–1.54 g NO_x s^{-1} MW^{-1}). The FERs of NO_x are generally larger in the African regions than elsewhere, except for croplands where the highest values are found in Southeast Asia. The application of the obtained values in bottom-up emission inventories only requires a conversion factor for deriving emission factors (EFs) of NO_x. To the authors' knowledge, there exist both constant and biome-specific conversion factors in the literature (Vermote et al., 2009; Kaiser et al., 2012).

It should be noted that the numerical values of FERs could be affected by uncertainties in both P_f and FRP, and thus the absolute values might have considerable uncertainties. Moreover, the uncertainties in the air mass factors (AMFs) and NO_x lifetime could cover the variability range of FERs derived in this study. By assuming that the uncertainties in FRP observations are systematic and consistent throughout the tropical and subtropical regions selected for this study, it is suggested that the diurnal discrepancies in FERs could be affected by changes in the NO_2 vertical profile and plume chemistry, whereas the regional discrepancies in estimated FERs of NO_x could at least in part be explained by differences in aerosol properties and plume chemistry.

Future efforts directed toward improving NO_2 AMFs for the satellite-based retrieval of TVC NO_2 and a better knowledge of the NO_x lifetime over biomass burning regions will improve the accuracy of FERs considerably.

In conclusion, the FERs of NO_x derived for different types of vegetation form the foundation of future efforts aimed at a new top-down based method for estimating global NO_x emissions from vegetation fires. As discussed above, the FERs are a valuable supplement to the universal EFs, which currently do not account for spatiotemporal variations of moisture content and weather conditions. In presented approach, these variations are included and averaged over the entire season.

The results of this study show that the temporal relationship found between TVC NO_2 and FRP can be used for the partitioning between NO_x emissions from fire and NO_x released from other sources. Nevertheless, the approach should be repeated for the data from SEVIRI instrument on board the geostationary Meteosat Second Generation

(MSG) satellite, as the obtained results are valid only for the data from the MODIS instruments.

Future work will include an improved TVC NO_2 product for biomass burning, the extension to other regions (e.g. boreal regions), and an attempt to produce a global estimation of NO_x emissions from vegetation fires, based on the approach developed in this study. In general, this estimation only requires the FRP integrated over time by including the diurnal cycle of fires and the FERs of NO_x.

Chapter 3

Differences in satellite-derived NO_x emission factors between Eurasian and North American boreal forest fires *

3.1. Introduction *

As outlined in Sect. 2.4, the estimation of fire emission rates of NO_x should be extended to the boreal regions, as large forest fires can produce significant amounts of NO_x emissions. However, this requires a modified approach for the retrieval of NO_2, in particular in terms of an improved stratospheric correction (see Sect. 3.2.1).

Boreal forest, commonly referred to as *taiga*, is one of the largest terrestrial biomes and covers about 30% of the total global forest area (Pan et al., 2011). The taiga is dominated by evergreen (coniferous) and deciduous forests storing large amounts of nitrogen (*N*), which is an essential nutrient for all living organisms. However, wildfires across these ecosystems release large masses of *N* in form of nitrogen oxides (NO_x = $NO + NO_2$) and ammonia (NH_3) by flaming and smoldering fires, respectively, and affect the biosphere and atmosphere.

In general, the total amount of emissions released from boreal forest fires is relatively low compared to tropical and subtropical vegetation fires (Lobert et al., 1999). However, during exceptional climatic years such boreal forest fires can spread over large areas. Interestingly, Wooster and Zhang (2004) found that the intensity of fires is generally lower in Russian boreal forests than in North American boreal forests, and relate this difference to the respective dominance of surface fires in Russia and crown fires in North America.

Current model estimates of future fire regimes in the boreal zone predict a doubling of the number of wildfires by the end of the 21st century, an increase in the occurrence of catastrophic fires and fires that escape from control, a substantial increase of the burning severity, and changes in the intensity and gas composition of fire emissions

caused by increased soil burning (Flannigan et al., 2009). Moreover, Shvidenko et al. (2011) suggested a linkage between catastrophic fires and large scale atmospheric anomalies for recent exceptionally large wildfires (e.g. fires in the Russian Far East vs. flooding in China in 2003; fires in European Russia vs. flooding in Pakistan and India in 2010). Thawing permafrost and the following drying up of typical landscapes in higher latitudes could lead to a dramatic loss of forested areas (Shvidenko and Schepaschenko, 2013). The increasing occurrence of catastrophic boreal wildfires in the future is likely to have an impact on air pollution and atmospheric chemistry. Therefore, accurate estimates of current fire emissions are needed to better understand the increasing future role of boreal forest fires. This can only be achieved by reducing uncertainties in fire emission estimates.

During the burning process, the nitrogen bound in the fuel is converted in part into oxides and N present in amino acids is converted to NO (see Sect. 1.3.2). However, NO_x may also result from the reaction of molecular nitrogen (N_2) with O_2 from the atmosphere at very high temperatures (Andreae and Merlet, 2001). While the higher thermal energy during the flaming stage leads to the break-up of plant materials into simpler N molecules enabling a full oxidation to NO_x, smoldering fires are rather incomplete. Chen et al. (2010) have examined the combustion efficiency by laboratory-controlled combustion experiments. Their results show that the fuel moisture content decreases the combustion efficiency and prolongs the smoldering phase before flames start. Emission factors (EFs) of NO_x, which are used in bottom-up emission inventories for the translation of biomass burned into trace gas emissions, can consequently change as a function of the fuel moisture content.

The amount of NO_x emissions being released from forest fires also depends on the N content in plant tissues. For boreal forest plants, this content varies substantially and depends on species, plant part burned, site productivity, geographical location, and other factors. For instance, in Siberian dark coniferous forests (dominated by *Pinus sibirica*, *Abies sibirica*, *Picea excelsa* and *Picea obovata*) of the southern taiga zone, the N content varies in the range of 0.1-0.45% (of dry matter mass) in stem wood, 0.5-1.0% in branches, 0.8-1.8% in needles, 0.3-0.9% in bark, and 0.4-1.2% in roots (Protopopov, 1975). Similar relative amounts are found for light coniferous forests (Rodin and

Bazilevich, 1965; Bazilevich and Rodin, 1971). In the taiga of West Siberia, lichens contain 0.5%, mosses 0.9%, and grasses 1.1-2.0% of N (Bakhnov, 2001). The results of a study in northern Alberta suggest that deciduous forests (mainly trembling aspen) have a higher N content than coniferous (mainly white spruce) and mixed forests (Jerabkova et al., 2006). Although the differences in total litter mass and total N content in the canopy are negligible between the three forest types, the input of leaves and/or needles in terms of mass and N content is higher in deciduous stands. Moreover, it was shown that the nitrogen fraction in the observed smoke plume differs considerably among various fuel types burned in laboratory-controlled combustion experiments. While the concentration ratio of NO_x to grand total carbon (including C in CO_2, CO, and $PM_{2.5}$) is higher than 20% for litter, it is less than 10% for other fuel types such as leaves and stems (Chen et al., 2010). The results described above clearly indicate that the amounts of fuel nitrogen in the vegetation are rather heterogeneous throughout the taiga. Consequently, the EF of NO_x can vary within the boreal forest due to a changing N content in different tree species and fuel types that are burned.

There has been much discussion about the leading cause of NO_x emissions from wildfires. Andreae and Merlet (2001) suggest that temperatures in typical wildfires are not high enough to produce large amounts of NO_x via the oxidation of N_2. Nevertheless, the production of NO_x is more efficient during the flaming combustion. The fraction of reactive nitrogen in volatilized fuel nitrogen emitted accounts for 25-50%, with NO_x and NH_3 being the dominant reactive nitrogen species during flaming and smoldering combustion, respectively (Goode et al., 2000; Yokelson et al., 2008). In comparison, up to 50% of the fuel nitrogen might be converted into N_2 (Lobert et al., 1990). However, the exact mechanism of N_2 formation remains unclear as the detection of N_2 from open fires is influenced by the large N_2 fraction of the ambient air. For example, Mebust and Cohen (2013) found a seasonal cycle in NO_x emissions from African woody savanna fires, but could only speculate about the exact mechanisms.

The composition of total reactive nitrogen oxides (NO_y) in the continental troposphere mainly consists of nitric acid (HNO_3) and peroxyacyl nitrates (PANs), whereas NO_x constitutes only 15% (Singh et al., 2007). Smaller NO_x/NO_y fractions of 5% (spring) and 10% (summer) were derived from in-situ measurements taken during the ARCTAS

(Arctic Research of the Composition of the Troposphere from Aircraft and Satellites) airborne campaigns in the high northern latitudes (Singh et al., 2010). Nevertheless, it was shown that the relatively small amount of NO_x can be transported into remote areas where it leads to a significant increase of O_3 (Singh et al., 2007). This can be explained by the efficient ozone production at low NO_x levels (Jacob, 1993). Val Martin et al. (2008) have shown that boreal wildfire emissions were responsible for higher levels of NO_x in remote areas downwind from the boreal region. They further concluded that the NO_x background levels during such fires were increased, and thus, the tropospheric O_3 budget was affected over large parts of the northern hemisphere.

Recent fire emission inventories are based on the translation of estimated biomass burned into trace gas emissions by applying uniform EFs for a relatively small number of biomes (e.g. van der Werf et al., 2010; Kaiser et al., 2012). However, more recent satellite-based studies have indicated substantial spatio-temporal variations of NO_x EFs within a specific biome and between different regions (Mebust and Cohen, 2013; Castellanos et al., 2014). As the bulk of these results are confined to tropical and subtropical regions, the focus is directed towards higher latitudes and the estimation of fire emission rates (FERs) and EFs of NO_x is performed for boreal forests in this study.

The following Sect. 3.2 gives a description of satellite measurements used in this study and outlines the approach to estimate FERs and EFs of NO_x from these measurements. The results are presented and discussed in Sect. 3.3. An overview on possible uncertainties in the approach is given in Sect. 3.4, followed by a summary and conclusions in Sect. 3.5.

3.2. Data retrieval and data analysis *

3.2.1. Satellite measurements of NO_2 *

Measurements from the GOME-2 instrument on board the MetOp-A satellite (Callies et al., 2004) are used for the retrieval of tropospheric NO_2. The retrieval is based on the Differential Optical Absorption Spectroscopy (DOAS) method, which is described in Sect. 1.5.1. Here, the retrieval approach as described in Sect. 2.2.1 and in Richter et al.

* This subsection has been previously published as part of Schreier et al. (2014b).

(2011) used, but slightly modified. Briefly, the slant column densities (SCDs) are retrieved from the GOME-2 spectral measurements by fitting the absorption cross section of NO_2 and other trace gases in the spectral window between 425 and 497 nm. Instead of applying the reference sector method (Richter and Burrows, 2002), the stratospheric influence on the total column measurements has been estimated using stratospheric NO_2 fields simulated by the Bremen 3d CTM (B3dCTM) and scaled to observations over the Pacific.

The B3dCTM is a combined model approach based on the 'Bremen transport model' (Sinnhuber et al., 2003a) and the chemistry code of the 'Bremen two-dimensional model of the stratosphere and mesosphere' (Sinnhuber et al., 2003b; Winkler et al., 2008), which evolved from SLIMCAT (Chipperfield, 1999). B3dCTM is driven by ECMWF ERA Interim meteorological reanalysis fields (Dee et al., 2011). The detailed model setup is described in Hilboll et al. (2013b). The simulated stratospheric profiles are interpolated in space and time for each satellite measurement to yield stratospheric vertical columns and airmass factors (AMFs) (Hilboll et al., 2013a).

The impact of clouds on the retrieval of NO_2 is accounted for by removing measurements with a cloud fraction larger than 20%, based on the FRESCO+ retrieval (Wang et al., 2008). Finally, the SCDs are converted into vertical column densities (VCDs) by dividing through an AMF, which corrects for the different sensitivity of the measurements in different altitudes. A detailed description of the AMFs used in this study can be found in Nüß (2005) and Richter et al. (2005). The final retrieved tropospheric NO_2 vertical columns (TVC NO_2) are binned to a horizontal resolution of 1° x 1° in order to reduce the effect of horizontal transport of NO_2 (see Sect. 2.4).

Uncertainties in tropospheric NO_2 slant columns originating from the stratospheric correction are usually up to 5×10^{14} molec cm^{-2}, but can be as large as 2.5×10^{15} molec cm^{-2} at high latitudes in winter (Hilboll et al., 2013a). Due to the absence of fires in winter, however, these larger uncertainties are not of relevance for this study. The satellite-based retrieval of TVC NO_2 is affected by uncertainties, which are mainly caused by the conversion of SCDs into VCDs by applying AMFs (Boersma et al., 2004). A priori information used for the calculation of AMFs introduces the bulk of these

uncertainties into the retrieval of TVC NO_2. For instance, inaccurate a priori information on aerosols can have a substantial influence on the accuracy of the AMFs, and thus, on the precision of TVC NO_2. The vertical position of the aerosol layer relative to the NO_2 layer is of particular interest. While the measurement sensitivity of the instrument is reduced when the aerosol layer is located above the NO_2 plume, it is increased when aerosols are located within or below the NO_2 plume (Leitão et al., 2010). A decrease (increase) in the measurement sensitivity by not correctly accounting for the aerosol information would lead to an overestimation (underestimation) of the AMFs, and thus, to an underestimation (overestimation) of TVC NO_2. Besides the location of the aerosol layer, uncertainties in aerosol amounts and optical properties can also deteriorate the accuracy of TVC NO_2. Leitão et al. (2010) have shown that the effect of a varying single scattering albedo (SSA) on the AMF can be larger than 70% for polluted atmospheres.

3.2.2. Satellite measurements of fire radiative power *

MODIS observations on board the near-polar orbiting satellites Terra (10:30 LT) and Aqua (13:30 LT) are available since 1999 and 2002, respectively. Amongst other parameters, FRP is retrieved from these measurements at a 1 km^2 horizontal resolution (see Sect 2.2.2). According to the equatorial overpass time of the GOME-2 instrument (9:30 LT), the MOD14CM FRP product from the Terra satellite (10:30 LT), provided at a 1° x 1° horizontal resolution, is used for this study. (ftp://neespi.gsfc.nasa.gov/data/s4pa/Fire/MOD14CM1.005/).

3.2.3. Global land cover map *

The Collection 5 MODIS Global Land Cover Type product (Friedl et al., 2010), which is available at https://lpdaac.usgs.gov/products/modis_products_table/mcd12q1, is used for the definition of boreal forests. According to the horizontal resolution selected for TVC NO_2 and FRP, the land cover product is spatially aggregated to 1° x 1° by applying a majority filter (see Sect. 2.3). The 14-class University of Maryland classification (UMD) is used to define boreal forest pixels (Hansen et al., 2000).

* This subsection has been previously published as part of Schreier et al. (2014b).
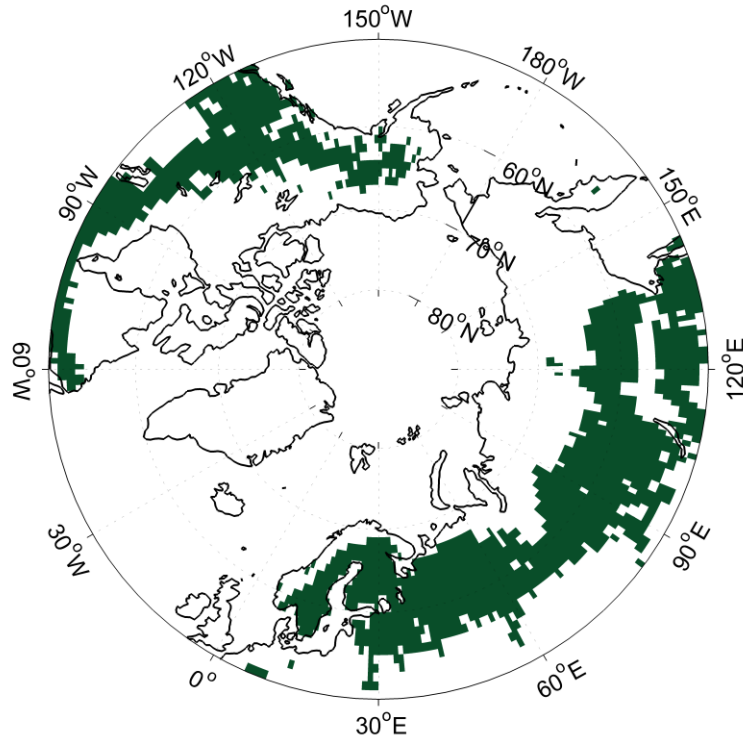
Fig. 3.1: Boreal forests in Eurasia and North America as defined by the aggregation of evergreen needleleaf forest, deciduous needleleaf forest, mixed forest, and woody savannas on a grid of 1° x 1° horizontal resolution (see Table 3.1) using the UMD classification scheme (Hansen et al., 2000; Friedl et al., 2010).

The aggregation of 1° x 1° pixels covered by coniferous forests, deciduous forests, or a mixture of both form the basis of the estimation of FERs and EFs of NO_x for boreal forests in Eurasia and North America. In the UMD classification, woody savanna is defined as a mixture of trees (40-60%) and grassland. As woody savannas cover considerable areas in Alaska, Russia, and Scandinavia, and in order to increase the data points used for the estimation of FERs of NO_x, woody savannas are included in the definition of boreal forest pixels. The aggregation of the four land cover types (evergreen needleleaf forest, deciduous needleleaf forest, mixed forest, and woody savannas) between 50° N and 80° N is shown in Fig. 3.1 and the definition of the regions Eurasia and North America is highlighted in Table 3.1.

Table 3.1: Selected regions and land cover types with their respective share of the total boreal forest area. The land cover types are used to define boreal forests in Eurasia and North America.

Region	latitudes	longitudes	land cover types[a]	share of total area[b]	share of total area[c]
Eurasia	50° to 80°N	0° to 180°E	evergreen needleleaf forest	7.1%	0.5%
			deciduous needleleaf forest	17.6%	31.2%
			mixed forest	53.7%	39.8%
			woody savannas	21.6%	28.5%
North America	50° to 80°N	170° to 35°W	evergreen needleleaf forest	57.6%	59.3%
			mixed forest	12.2%	9.3%
			woody savannas	30.2%	31.4%

[a] based on the Collection 5 MODIS Global Land Cover Type product (UMD classification)

[b] percentages represent share of total boreal forest area as defined in this study and shown in Fig. 3.1

[c] percentages represent share of total boreal forest area remaining after data filtering (see Fig. 3.3)

3.2.4. Satellite measurements of aerosol optical depth *

In order to assess the possible influence of aerosols on the retrieval of TVC NO_2, and thus, on the magnitude of the estimated FERs and EFs of NO_x for boreal forests in Eurasia and North America, the aerosol optical depth (AOD) and vertical profiles of wildfire emissions are analyzed for these regions. The AOD is a parameter describing the column integrated extinction over the entire atmosphere and is derived from MODIS spectral measurements between 470 and 2130 nm (Remer et al., 2008). The aerosol product from MODIS on board Terra at 550 nm is used to evaluate the possible relative influence of the AOD on the retrieval of TVC NO_2 between the Eurasian and North American boreal forest pixels. The AOD product has been downloaded from ftp://ladsweb.nascom.nasa.gov/allData/51/MOD08_M3/2005/.

3.2.5. Vertical profiles of wildfire emissions *

A 4-dimensional data set of fire smoke with a resolution of 1° x 1° x 500 m has been recently calculated by Sofiev et al. (2013). The estimated vertical profiles are based on a semi-empirical formula for the plume-top height, satellite observations of active fires, and meteorological conditions derived from a numerical weather prediction model. The

* This subsection has been previously published as part of Schreier et al. (2014b).

vertical profiles are available for the entire globe and cover the whole time period analyzed in this study (2007-2012). These data are used to deduce the possible role of a variable mean injection height on the retrieval of TVC NO_2 between the two regions.

3.2.6. An adapted approach for the boreal region *

In general, fire emission inventories (e.g. GFEDv3.1 and GFASv1.0) estimate the total amount of NO_x (usually reported as NO) released by fires. As satellite instruments, such as GOME-2, measure NO_2, the conversion of TVC NO_2 into production rates of NO_x from fire (P_f) is a further step to prepare the data for the analysis (see Sect. 2.2.6).

The aim of this study is the satellite-based estimation of FERs and EFs of NO_x for the Eurasian and North American boreal forests. As recent satellite-based studies have indicated substantial spatiotemporal variations in EFs for African (Mebust and Cohen, 2013) and South American (Castellanos et al., 2014) biomes, it is hypothesized that EFs could also fluctuate among the large taiga forests.

The approach as described in Sect. 2.2.6 is applied to estimate linear gradients between P_f and FRP, here referred to as FERs of NO_x. The assumption made for the following approach is that the fire radiative power is mainly related to the amount of fuel burned and not to the temperature of the individual fire. The amount of NO_x emitted in turn is assumed to be linearly related to the amount of fuel burned.

The analysis starts with evaluating the temporal correlation between the gridded monthly mean TVC NO_2 and FRP for the boreal forest pixels. As outlined in Sect. 2.3.1, a strong correlation exists for larger regions located in the tropics and subtropics. However, they also pointed out the comparatively weak correlation between the two parameters for higher latitudes. One possible reason for the weaker correlation is related to the fact that the bulk of boreal forest fires are generally smaller in size (e.g. Stocks et al., 2003) when compared to the rather extensive slash and burn activities in Africa and South America. As a result, the measurement sensitivity of the satellite instrument might be too low for the detection of NO_2 produced from such smaller fires. Another possible explanation for the weak correlations could be the larger uncertainty in tropospheric NO_2 vertical

---

columns in higher latitudes, which are introduced by the stratospheric correction method used (see Sect. 2.2.1). Basically, the applied reference sector method assumes that there are no tropospheric sources of NO_x over a specific and rather remote region over the Pacific and that the stratospheric NO_2 column varies only with latitude, but not with longitude. However, these assumptions can introduce negative NO_2 columns by overestimating the stratospheric NO_2, especially in higher latitudes mainly during winter and spring. Hilboll et al. (2013a) suggest that these negative NO_2 columns could be related to the polar vortex and the resulting zonal inhomogeneity. In order to improve the quality of TVC NO_2 over the boreal regions, stratospheric NO_2 columns as calculated by the B3dCTM simulations are used in this study (see Sect. 3.2.1).

Using the linear relationship between TVC NO_2 and FRP (see Eq. 3.1), the y-intercepts are subtracted from the TVC NO_2 (see Eq. 3.2). This step is performed to isolate the tropospheric NO_2 column contribution produced by fire (TVC_f NO_2), assuming that y-intercepts represent the NO_2 background (TVC_b NO_2) and that there is no or a negligible small seasonal cycle in NO_2 background (see Sect. 2.3.5).

$$TVC[NO_2] = slope * FRP + TVC_b[NO_2] \qquad \text{(Eq. 3.1)}$$

$$TVC_f[NO_2] = TVC[NO_2] - TVC_b[NO_2] \qquad \text{(Eq. 3.2)}$$

In a second step, the obtained monthly gridded values of TVC_f NO_2 (in units of 10^{15} molec cm^{-2}) are then converted into monthly gridded values of NO_x production rates P_f (in units of g NO_x s^{-1}) (see Eq. 3.3).

$$P_f = \frac{TVC_f[NO_2] * M \left(1 + \frac{NO}{NO_2}\right) A_p}{N_A * \tau}, \qquad \text{(Eq. 3.3)}$$

where TVC_f NO_2 is the number density of NO_2 molecules produced by fires integrated over the tropospheric vertical column (in molecules cm^{-2}) and M is the molar mass of NO (in g mol^{-1}). The term $1 + NO/NO_2$ accounts for the NO_2/NO_x ratio (without units) as derived from the MACC reanalysis data set (see below) and A_p is the respective pixel area (in cm^2). N_A denotes Avogadro's number (in molecules mol^{-1}) and τ is the assumed lifetime of NO_x (in seconds). A constant value of 6 h is used for τ, which is based on the findings of Beirle et al. (2011) for the megacity Moscow and Takegawa et al. (2003) for

biomass burning plumes over northern Australia. According to the described conversion of TVC NO_2, the FRP values have also been multiplied by A_p. Further details about the conversion are given in Sect. 2.2.6.

A detailed description of the MACC data assimilation system for chemically reactive gases, which is based on ECMWF IFS and MOZART-3 CTM simulations, can be found in Inness et al. (2013). Daily weighted averages of the NO_2/NO_x ratio has been calculated for the 8 given UT hours (3, 6, 9,12,15,18, 21, and 0 UT) by including 29 hybrid sigma-pressure levels between the surface and ~10 km altitude to reflect tropospheric values. These values were interpolated between these UT hours by including daily gridded maps of the geographical location of the GOME-2 overpass time (UT) to construct daily values of the NO_2/NO_x ratio. Finally, monthly means of the NO_2/NO_x ratio with a horizontal resolution of 1° x 1° was computed for the entire period (2007-2012). These values are included in the formula (Eq. 3.3) for the conversion of TVC NO_2 into P_f, instead of assuming a constant value for the NO_2/NO_x ratio as done in the former study focusing on tropical and subtropical regions (see Sect. 2.2.6). Although there is no systematic difference in the results when using the gridded values of NO_2/NO_x ratio obtained from the MACC reanalysis data instead of a constant value of 0.75 (not shown), these values were used as they account for the seasonal variability. An additional description about the computation of the tropospheric NO_2/NO_x ratio is given in Sect. 5.3, but for the OMI overpass time.

A linear regression model is used for the calculation of gradients between P_f and FRP for all boreal forest pixels with a correlation coefficient (r) between TVC NO_2 and FRP higher than 0.3. As the major parts of boreal forests examined in this study are located in rather remote areas, it was tested tested whether the population density filter as applied in the former study (see Sect. 2.3.4) is crucial for this study. It was found that this filter has no significant effect on the obtained results (not shown) and have therefore not applied such filtering.

In short, the approach to estimate FERs of NO_x is similar to the approach used for the tropical and subtropical regions (see Sects. 2.2.6 and 2.3.4), but three parameters have been modified for the boreal regions. Firstly, TVC NO_2 is based on a stratospheric

correction using model simulations to reduce the uncertainty from stratospheric NO_2. Secondly, monthly gridded maps of the NO_2/NO_x ratio derived from the MACC reanalysis data are used to account for seasonality and spatial variation of this ratio. Thirdly, filtering by population density data has been omitted as it proved to be not necessary.

3.3. Results and discussion *

3.3.1. Statistical evaluation of regression coefficients *

The correlation coefficients as calculated from the pixel-wise linear relationship between monthly means of TVC NO_2 and FRP are shown in Fig. 3.2 for the entire boreal forest (as defined in Fig. 3.1).

---

* This subsection has been previously published as part of Schreier et al. (2014b).
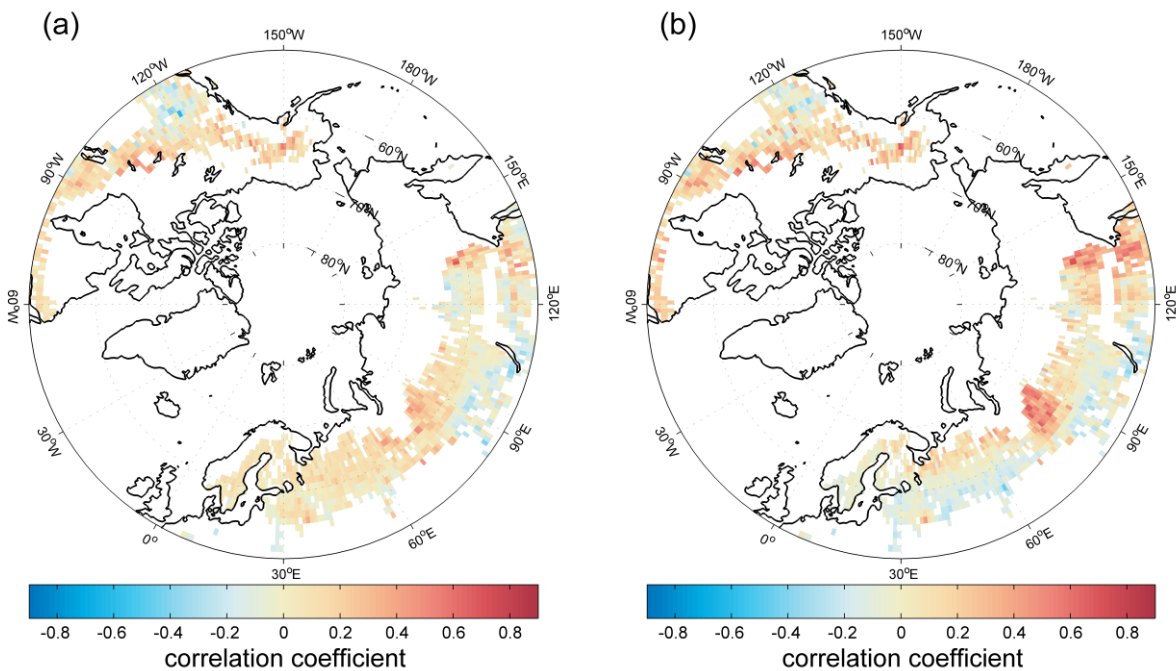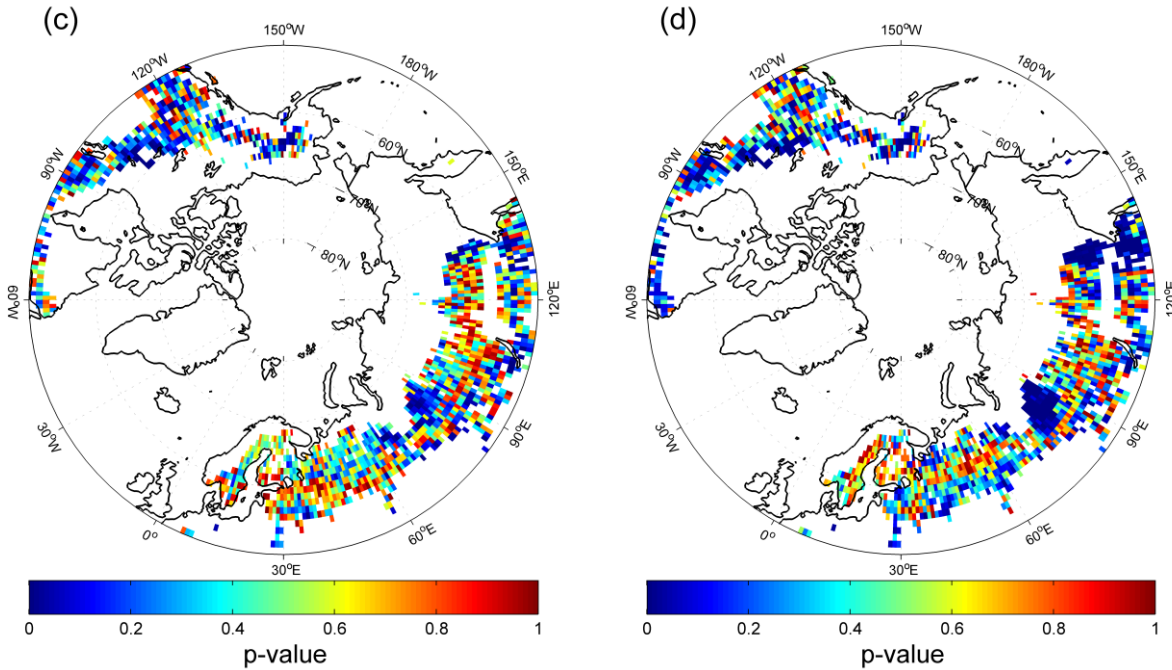
Fig. 3.2: Correlation coefficients (r) of the linear regression (see Eq. 3.1) of TVC NO$_2$ against FRP (upper) and statistical significance (lower) for the period 2007-2012. A p-value smaller than 0.05 means that the correlation is statistically significant within a 95% confidence level. The retrieval of TVC NO$_2$ is based on the removal of stratospheric NO$_2$ applying the reference sector (a) and (c) as well as using B3dCTM simulations (b) and (d). All colored 1° x 1° pixels are defined as boreal forest (see Fig. 3.1 and Table 3.1).

The correlation coefficients as computed for the tropical and subtropical regions in the former study (see Sect. 2.3.1) by applying the reference sector method for the retrieval of TVC NO$_2$ (a) are compared with the correlation coefficients based on the new TVC NO$_2$ as computed by subtracting the B3dCTM simulated stratospheric NO$_2$ (b). There is some degree of improvement, especially in the Far East Russia and parts of Siberia, due to the improved stratospheric correction of the NO$_2$ satellite measurements. Negative correlation coefficients indicate the influence of anthropogenic emissions, which are higher during winter months despite the absence of fires. As already stated in Sect. 2.3.1, negative values are not included in the approach to derive FERs of NO$_x$. In order to give evidence about the statistical significance, p-values have been computed for the linear relationship between TVC NO$_2$ (based on the reference sector method (c) and simulated stratospheric NO$_2$ (d)) and FRP (see Eq. 3.1). The adapted approach used in this study for the evaluation of FERs and EFs of NO$_x$ in the boreal region clearly

increases the number of pixels with p-values < 0.05 (statistical significance within a 95% confidence level). There are fewer pixels having correlation coefficients > 0.3 in the boreal region when compared to tropical and subtropical regions (see Sect. 2.3.1). This might be related to the fact that there are many smaller fires with NO_2 signals falling below the detection limit of GOME-2. Although large fires account for over 85% of the total area burned in the Canadian boreal forest, they account for less than 5% of the fires (Stocks et al., 2003). Therefore, it is anticipated that the estimation of FERs and EFs of NO_x is based on rather larger forest fires in this study.
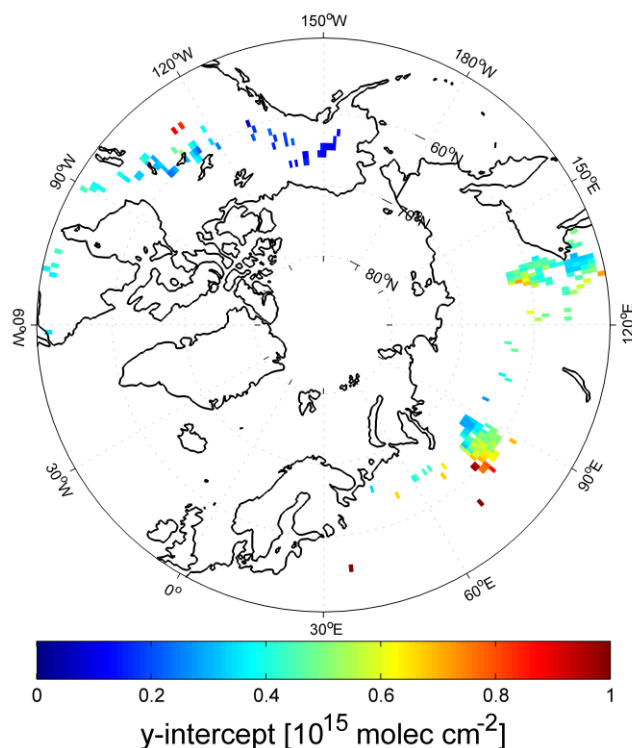
Fig. 3.3: Y-intercepts of the linear regression of TVC NO_2 against FRP for the six-year period (2007-2012). The y-intercepts representing the background levels in NO_2 columns are subtracted from the total tropospheric NO_2 columns (see Sect. 3.2.6). All pixels with a p-value < 0.05 and r > 0.3 are shown in the figure and used as a selection criterion for the estimation of FERs and EFs of NO_x.

The gradients of the linear regression model used for estimating fire emission rates are calculated for those 1° x 1° pixels having p-values < 0.05 and correlation coefficients r > 0.3. By this data selection, the focus is directed at areas where there is a clear link between satellite-observed fires and satellite retrieved NO_2 columns.

As shown in Fig. 3.3, the number of boreal forest pixels used for the estimation of FERs of NO_x is reduced by these thresholds to 141 and 63 for Eurasia and North America, respectively. Although a correlation coefficient of 0.3 is not high, it is statistically significant in the presented study, even for the relatively low amount of data points available in the selected time series. The use of a higher threshold value (e.g. $r > 0.4$) would lead to an even smaller data set, which would not be beneficial for the analysis. Therefore, confidence exists to use the above mentioned threshold values ($r > 0.3$ and p-values < 0.05) for this study.

In Fig. 3.3, the y-intercepts of the linear regressions (see Eq. 3.1) are shown for the selected boreal forest pixels, based on the filter criteria (p-value < 0.05 and $r > 0.3$). These values reveal useful information about the background level of tropospheric NO_2 in the selected areas as they reflect levels of tropospheric NO_2 produced from other NO_x sources than fire. The y-intercept values are subtracted from the TVC NO_2 grid cells to obtain the tropospheric NO_2 produced from fire ($TVC_f\ NO_2$), which is used for the conversion of TVC NO_2 into P_f (see Eq. 3.3 and Sect. 3.2.6). The subtraction of these values is performed under the assumption that there is no seasonal cycle in background tropospheric NO_2.

3.3.2. Determination of fire emission rates of NO_x *

Scatter plots for the relationship between P_f and FRP are shown in Fig. 3.4 for Eurasia (red) and North America (blue). All boreal forest pixels with a p-value < 0.05 and $r > 0.3$ are plotted in the graph. The total number of data points, i.e., TVC NO_2 averaged over one grid cell and one month, included in this plot is 6791 and 3298 for Eurasia and North America, respectively (see Table 3.2). A maximum number of 72 data points would result for a single boreal forest pixel if the satellite instruments would have detected a signal for each month of the selected time period (2007-2012) for both TVC NO_2 and FRP. As boreal wildfires mainly occur in summer and to a lesser extent in spring and fall, the maximum number of data points for the individual pixels is reduced due to the absence of fires in winter. A division of the total number of data points (6791 and 3298) by the number of boreal forest pixels remaining after data filtering (141 and 63) results in

---

* This subsection has been previously published as part of Schreier et al. (2014b).   95

average numbers (or months containing signals of both TVC NO_2 and FRP) of 48 and 52 for an individual pixel located in Eurasia and North America, respectively.

In general, a large spread of data is expected because of measurement uncertainties, the simplifications made in the conversion of NO_2 columns to NO_x production rates and from the horizontal and vertical changes of N and moisture contents in the vegetation (Fig. 3.4). For instance, a dry deciduous forest with increased N content will release more NO_x per unit FRP than a rather humid coniferous forest. There is a clear indication that single fire events can be more intensive in North America than in Russia. Wooster and Zhang (2004) suggest that the higher fire intensity in North American boreal forests is linked to more intensive crown fires.
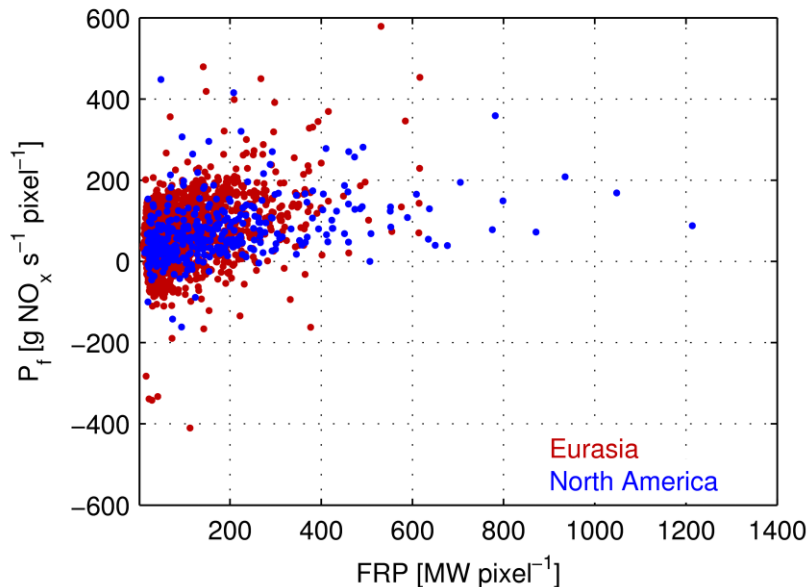
Fig. 3.4: Estimated productions rates of NO_x from fire (P_f) plotted against associated FRP values over boreal forests Eurasia (red) and North America (blue). All 1° x 1° pixels with a p-value < 0.05 and $r > 0.3$ are included in the plot (see Sect. 3.3.1).

In order to reduce the spread of data and exclude outliers, data points are averaged within consecutive FRP-intervals of 15 MW pixel^{-1}. The application of the binning method moreover leads to a result that represents spatio-temporally averaged FERs of NO_x for the respective region. Due to the larger amount of data available for Eurasia, the

threshold criterion for the binning could be set to ≥ 10 data points available within the interval, whereas for North America it is set to ≥ 5.

After binning, clear linear relationships are visible for both regions, albeit with different slopes. This result shows that there are differences in FERs of NO_x between the two selected regions with higher values observed for the Eurasian boreal forest fires (Fig. 3.5).
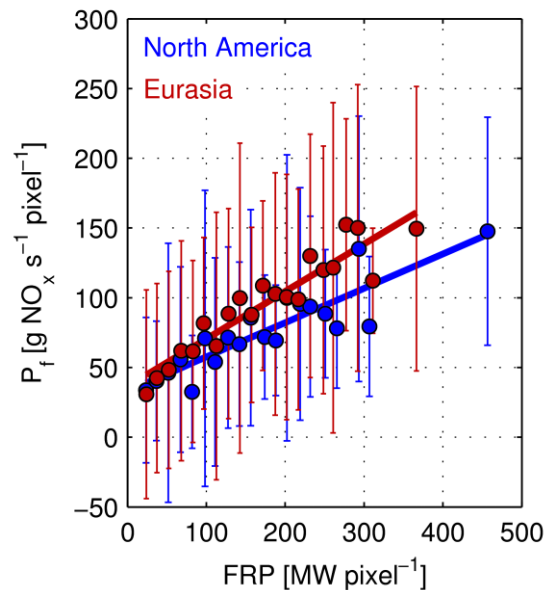
Fig. 3.5: Spatio-temporally averaged fire emission rates (FERs) of NO_x for boreal forest in Eurasia (red) and North America (blue) derived by applying a binning procedure as explained in Sect. 3.3.2. The gradients, here referred to as FERs, are calculated by applying a linear regression of monthly means of P_f against monthly means of FRP by including all pixels with a p-value < 0.05 and $r > 0.3$. The error bars show one standard deviation of P_f values within the consecutive FRP-intervals. A summary of the statistics is given in Table 3.2.

In other words, the emissions of NO_x per unit of FRP are lower on average for forest fires in North America. One possible explanation could be the lower N content in evergreen (coniferous) species dominating large parts of the North American region (see Table 3.1 and Jerabkova et al., 2006). Moreover, Chen et al. (2010) have reported that the concentration ratio of NO_x over the grand total carbon is highest for litter combustion, which is more likely in deciduous forests dominating the Eurasian region analyzed in the presented study. Wooster and Zhang (2004) found an overall higher-temperature

flaming combustion in North American boreal forests. Assuming that the production of NO_x via the oxidation of N_2 would be the dominant source of NO_x from boreal wildfires, higher FERs of NO_x would be expected for boreal forest fires in North America. As this is not the case in this study, it can only be speculated that the observed differences in FERs of NO_x between Eurasian and North American boreal forests are rather related to the variable *N* content in plant tissues. It is argued here that the higher FERs of NO_x derived for the Eurasian boreal forests are likely attributed to the larger proportion of deciduous stands such as larch forests (Schepaschenko et al., 2011) and/or to the non-existence of such forests in North America. Large differences in the *N* content are especially found in the canopy litter, with ~30% larger amounts reported for deciduous forests (Jerabkova et al., 2006). In addition the *N* content in grasses is higher than in other plant tissues (Bakhnov, 2001). Consequently, the dominance of surface fires in deciduous forests in Eurasia (see Wooster and Zhang, 2004) could explain the larger emissions of NO_x per unit of FRP.

3.3.3. Conversion into emission factors of NO_x *

In order to compare the obtained values with the values found in literature (see Table 1.1), the FERs are translated into EFs of NO_x by applying a conversion factor of 0.41 kg MJ^{-1} as suggested by Vermote et al. (2009). The values for the spatio-temporally averaged FERs and EFs of NO_x, the total number of data points included in the analysis (*N*), and the coefficient of determination (r^2) are summarized in Table 3.2.

A comparison of the obtained EFs with the EF provided by Akagi et al. (2011) indicates very good agreement, as their reported value of 0.9 g kg^{-1} for the whole boreal forest biome is in good agreement with the value derived for the Eurasian boreal forest (0.83 g kg^{-1}) in this study. However, the EF estimated for the North American boreal forest (0.61 g kg^{-1}) is about 30% lower than the average value reported by Akagi et al. (2011).

* This subsection has been previously published as part of Schreier et al. (2014b).

Table 3.2: Spatio-temporally averaged fire emission rates (FERs) of NO_x in [g s^{-1} MW^{-1}] and emission factors (EFs) of NO_x in [g kg^{-1}] for the Eurasian and North American boreal forest fires analyzed in this study. FERs and EFs of NO_x are reported as NO.

Region	N	FER[a]	r^2	EF[b]
Eurasia	6791	0.34±0.03	0.87	0.83±0.07
North America	3298	0.25±0.03	0.79	0.61±0.07

Uncertainty of FERs and EFs is given as the standard error of the slope as shown in Fig. 3.5

[a] derived by applying a binning procedure as described in the text.

[b] based on the conversion factor of 0.41 kg MJ^{-1} as suggested by Vermote et al. (2011)

Wiedinmyer et al. (2006) have estimated fire emissions for North America by assigning EFs for each land cover type in the Global Land Cover (GLC2000) classification. The EFs of NO_x used in that study are in the range of 2.1-2.7 g kg^{-1} for sub-polar needleleaved and broadleaved forests and thus, around three times larger than the EFs obtained in this study. Van der Werf et al. (2010) and Kaiser et al. (2012) applied constant values of 3.41 and 3.4 g NO_x kg^{-1}, respectively, for the entire extratropical forest biome. When compared to the values derived in this study, their values are five times larger. As about 80% of global burned area is found in the tropics and subtropics (e.g. van der Werf et al., 2010), the given difference in EFs of NO_x for the boreal forest is less important for fire emission inventories on a global scale. However, this difference would affect the magnitude of fire emissions considerably on the regional level.

3.4. Possible uncertainties in the approach *

In order to make sure that the observed differences in FERs and EFs of NO_x between the two regions are related to characteristics of the vegetation and fire type, possible factors that could affect the retrieval of TVC NO_2 and the conversion into P_f are analyzed. The bulk of uncertainties in the retrieval of TVC NO_2 results from the conversion of SCDs into VCDs by the use of AMFs (see Sect. 2.2.1). Here, the focus is directed at the impact of aerosol amounts and properties as well as on injection profiles of fire smoke that could affect the magnitude of FERs of NO_x between Eurasia and North

* This subsection has been previously published as part of Schreier et al. (2014b).

America differently. Additionally, the lifetime of NO_x and the NO_2/NO_x ratio are discussed in terms of possible relative influences on the conversion of TVC NO_2 into P_f between the two selected regions.

3.4.1. Impact of aerosol amounts and properties *

First, the AOD retrieved from MODIS on board Terra (in accordance to the overpass time of GOME-2 on board MetOp-A) is analyzed over the Eurasian and North American boreal forests. In Fig. 3.6, the AOD is plotted against FRP for boreal forest pixels with a p-value < 0.05 and r > 0.3 in Eurasia (red) and North America (blue). Clearly, the AOD is lower over North American forests when the FRP value of the respective pixel is lower than 500 MW. This might be an indication that aerosol amounts are largely dominated by fires in this region. In comparison, aerosols could be transported from anthropogenic emission sources (from coal, gas, and oil burning) into the Eurasian boreal forest pixels, as a certain proportion of data points indicate higher AOD values in Eurasia.
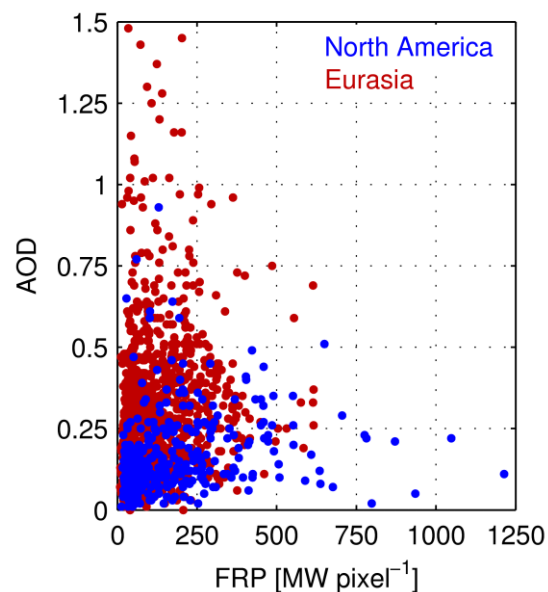

Fig. 3.6: Scatterplot between AOD and FRP for Eurasia (red) and North America (blue). The data points represent all boreal forest pixels (2007-2012) with a p-value < 0.05 and r > 0.3.

In terms of AMF calculations, an increase in AOD generally results in higher measurement sensitivity when the aerosols are below or mixed with the NO_2 molecules, and thus, increase the AMF. A decreased AMF comes along with a reduced sensitivity due to the location of aerosols above the NO_2 plume (shielding effect). Stohl et al. (2013) highlighted the important role of black carbon emissions from gas flaring in the Arctic. According to their findings, black carbon emissions from gas flaring, especially in Russia, are transported into boreal forest pixels analyzed in the presented study. Black carbon is considered as a fine black fluffy particle with highly absorbing properties. Highly absorbing aerosols, either located above or mixed with the NO_2 molecules, can only reduce the measurement sensitivity, and thus, decrease the AMF. In order to assess the influence of the increased AOD over the Eurasian boreal forest pixels on the magnitude of TVC NO_2, it is important to know the relative location and the properties of the additional aerosol load in the troposphere. However, this information is still highly unknown as no accurate data sets for the selected regions are currently available. Thus, it can only be speculated that the effect of an increased AOD could lead to an underestimation of the FERs and EFs of NO_x over Eurasia due to an overestimation of the AMF.

Secondly, the single scattering albedo (SSA) of aerosols and its possible impact on the retrieval of TVC NO_2 shall be discussed. The SSA describes the scattering and absorbing properties of aerosols and is simply defined as the ratio between scattering and extinction (scattering + absorption). While highly absorbing aerosols are characterized by a lower SSA, the SSA of highly scattering aerosols tends towards one. In general, a less complete combustion (smoldering fire) leads to a larger fine mode fraction of aerosols, which increases scattering, and thus, the SSA (Eck et al., 2009). Giles et al. (2012) have reported an average SSA of 0.95 at 440 nm for Bonanza Creek in Alaska. In contrast, the SSA in Western Siberia is estimated at 0.92-0.93 at 440 nm in an altitude between 500 and 2000 m, which is in good agreement with a measurement site at Tomsk (Panchenko et al., 2012). Both locations match with parts of the boreal forest pixels that are analyzed in this study. The lower SSA in Russia could be related to the influence of anthropogenic emissions sources in the vicinity of boreal forest pixels included in the analysis. However, a larger fraction of grasses burned could also

contribute to the lower value. By assuming that the two reported SSA values are representative for the two selected regions, it is concluded that the FERs of NO_x in Eurasia are rather underestimated than overestimated.

3.4.2. Impact of injection heights *

The mean seasonal daytime injection profiles of the plumes from fires are shown in Fig. 3.7 over boreal forest fires in Eurasia (left) and North America (right). As for the analysis of AOD, all boreal forest pixels with a p-value < 0.05 and $r > 0.3$ are included in the computation of injection profiles as presented in Fig. 3.7. In general, the seasonal distribution of the injection profiles is similar in both regions with the highest injection heights observed in April, May, June, July, and August (see Sofiev et al., 2013), which is the main forest fire season. As the differences are very small, the relative effects on the retrieval of TVC NO_2 between the two regions are assumed to be negligibly small.
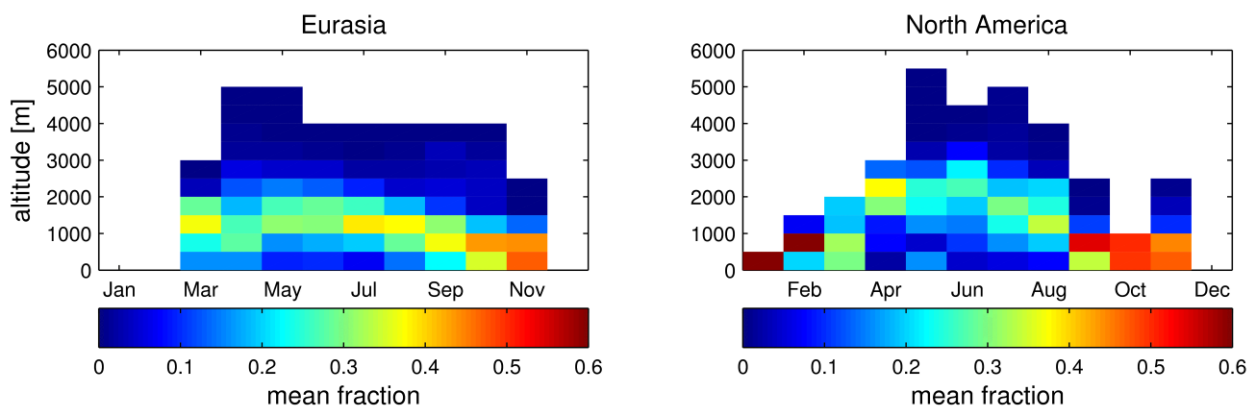
Fig. 3.7: Mean seasonal daytime injection profiles (Sofiev et al., 2013) over boreal forest fires in Eurasia (left) and North America (right). All boreal forest pixels (2007-2012) with a p-value < 0.05 and $r > 0.3$ are included in the averaging of injection profiles.

Val Martin et al. (2010) found a quantitative link between median injection heights and FRP in North America. The slightly higher injection heights in North America could thus be related to the increased FRP values observed in this region when compared with maximum FRP values in Eurasia (see Fig. 3.6). Nevertheless, the higher injection heights observed over North American boreal forest fires could potentially result in an

overestimation of the AMF. This can be explained by the fact that the measurement sensitivity, which is smallest close to the Earth's surface, is overestimated if the NO_2 plume is higher in the atmosphere than assumed (see Leitão et al., 2010). Therefore, FERs and EFs of NO_x in North America could potentially be overestimated relative to those in Eurasia.

3.4.3. Impact of NO_x lifetime and NO_2/NO_x ratio *

With respect to the lifetime of NO_x and the NO_2/NO_x ratio, the influence of an increased NO_2 layer is twofold. While the lifetime of NO_x is slightly increased towards higher altitudes, the NO_2/NO_x ratio is decreased as the relative proportion of NO_2 decreases with increasing altitude. However, the changes are too small to expect a significant relative influence on the magnitude of FERs of NO_x between the two regions.

3.5. Summary and conclusion *

In this study, the fire emission rates (FERs) and emission factors (EFs) of NO_x are estimated for boreal forest fires in Eurasia and North America, based on the empirical relationship between satellite-derived tropospheric NO_2 vertical columns (TVC NO_2) and fire radiative power (FRP). The retrieval of TVC NO_2 is based on a model-based correction of the stratosphere instead of the previously used reference sector method, which clearly improves the empirical relationship between TVC NO_2 and FRP at mid and high latitudes. As the GOME-2 retrievals provide NO_2 columns, a simplified formula including the lifetime of NO_x and the NO_2/NO_x ratio is used to convert tropospheric NO_2 column densities into production rates of NO_x from fire (P_f) in terms of mass concentrations. Instead of assuming a constant value of 0.75 for the NO_2/NO_x ratio (see Sect. 2.2.6), gridded values obtained from the MACC reanalysis data set are applied in this study. Although these monthly means account for the seasonal variability, no improvement was found for the empirical relationship.

The boreal forest pixels are defined according to the collection 5 MODIS global land cover product and confined between 50° and 80° N. The approach used to estimate FERs of NO_x only includes boreal forest pixels that exceed a value of 0.3 for the temporal correlation coefficient between TVC NO_2 and FRP and are statistically significant within a 95% confidence. This criterion has been chosen to exclude regions with an even weaker link between observed NO_2 columns and FRP, which are not beneficial for the analysis. On the other hand, a higher threshold value applied for the correlation coefficient (e.g. $r > 0.4$) decreases the available data points.

The spatio-temporally averaged FERs of NO_x are estimated at 0.34 and 0.25 g s^{-1} MW^{-1} for Eurasian and North American boreal forest fires, respectively. It is speculated that the observed difference is related to changes in the N content and moisture conditions of the fuel types burned. Moreover, the type of fire (surface fires vs. crown fires) and the linked combustion of dead material on the ground and tops of trees could affect the magnitude of FERs.

For a better comparison with values found in the literature, the FERs are translated into EFs of NO_x by simply applying a conversion factor of 0.41 kg MJ^{-1}, assuming the findings by Vermote et al. (2009). The satellite-based values are estimated at 0.83 and 0.61 g kg^{-1} for Eurasian and North American boreal forests, respectively. A comparison with the emission factor reported by Akagi et al. (2011) for the entire boreal forest (0.9 g kg^{-1}) indicates good agreement. However, recent fire emission inventories have used EFs of NO_x that are 3-5 times larger. The findings of the presented study have possible implications for future estimates of fire emissions, especially on the regional scale where the results indicate less fire related NO_x emissions.

Possible factors that could affect the observed differences in FERs and EFs of NO_x between North America and Eurasia were discussed and it was suggested that when considering possible systematic biases in the NO_2 retrievals, the real differences of NO_x EFs between the two regions could even be larger. Therefore, it is concluded that the observed differences of FERs and EFs of NO_x between Eurasia and North America are real and should be investigated by other, more direct methods in the future.

Chapter 4

Estimates of NO$_x$ emission factors from GOME-2 measurements for the major types of open biomass burning *

4.1. Introduction *

In order to complement the satellite-based estimation of emission factors (EFs) of NO$_x$, fire emission rates (FERs) of NO$_x$ are also converted for tropical and subtropical biomes and regions. The translation into EFs of NO$_x$ is performed by applying a conversion factor of 0.41 kg MJ^{-1} (see Sect. 3.3.3) as suggested by Vermote et al. (2009), following the findings of Wooster et al. (2005).

4.2. Conversion into emission factors of NO$_x$ *

The summarized correlation coefficients as obtained from the linear regression between tropospheric NO$_2$ vertical columns (TVC NO$_2$) and FRP are shown in Fig. 4.1. Here, the correlation coefficients in the tropical/subtropical and boreal regions are based on the retrieval of TVC NO$_2$ as described in Sects. 2.2.1 and 3.2.1, respectively. The global map is quite revealing in several ways. First, a very strong relationship between the two time series is found for the major biomass burning regions. Hence, the seasonal variation of TVC NO$_2$ is explained by the seasonal cycle of fire radiative power (FRP) to a large degree. Second, the empirical relationship forms the basis of the approach to estimate FERs of NO$_x$ as it is a reasonable tool to separate between different NO$_x$ sources (see Sect. 2.3).

The fits of the linear regression for the different types of open biomass burning are summarized in Fig. 4.2. The calculated FERs of NO$_x$ and their possible uncertainties are discussed in detail in the previous Sects. 2.3.5 and 3.4.
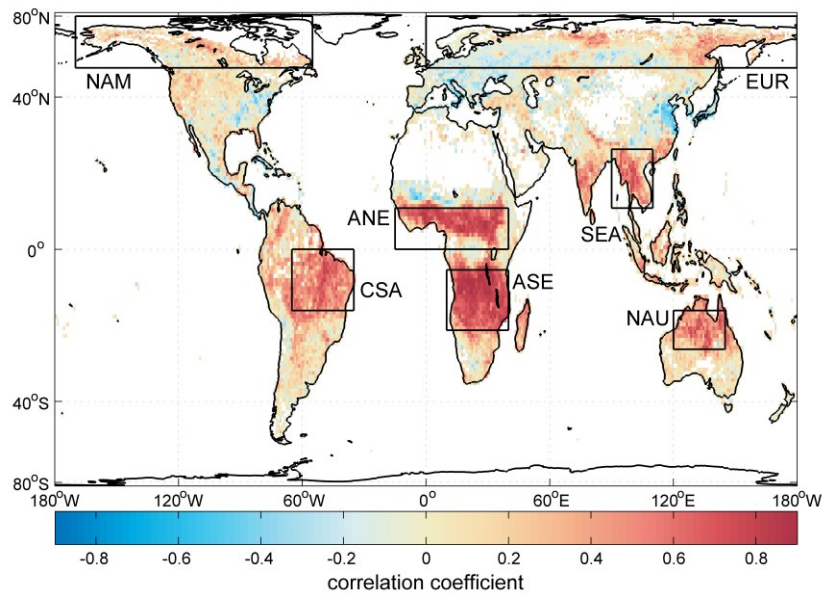
Fig. 4.1: Correlation coefficients (*r*) of the temporal relationship between TVC NO_2 and FRP based on monthly averages from 2007-2012 on a 1° x 1 grid. FERs of NO_x are derived for the tropical and subtropical regions Africa north of Equator (ANE), Africa south of Equator (ASE), central South America (CSA), northern Australia (NAU), and Southeast Asia (SEA) (see Table 2.1). The boreal regions Eurasia (EUR) and North America (NAM) are defined in Table 3.1.

The EFs of NO_x are derived for tropical forest (evergreen broadleaf forest), savanna and grassland (open shrublands, woody savannas, and savannas), crop residue (croplands), and boreal forest (evergreen needleleaf forest, deciduous needleleaf forest, mixed forest, and woody savannas). Here, the land cover types listed in brackets are the labels from the UMD classification scheme, which are used for the estimation of FERs in the earlier Sects. 2.3.4 and 3.3.2.

Figure 4.3 provides the arithmetic means of EFs as obtained from satellite data as well as arithmetic means of EFs reported by Andreae and Merlet (2001) and Akagi et al. (2011). While the error bars denote one standard deviation of the arithmetic mean in the two latter studies, they indicate the minimum and maximum values obtained for the different regions as highlighted in Fig. 4.2. The satellite-based EFs of NO_x are estimated at 1.83, 1.48, 2.96, and 0.72 g kg^{-1} for tropical forest, savanna and grassland, crop residue, and boreal forest, respectively.
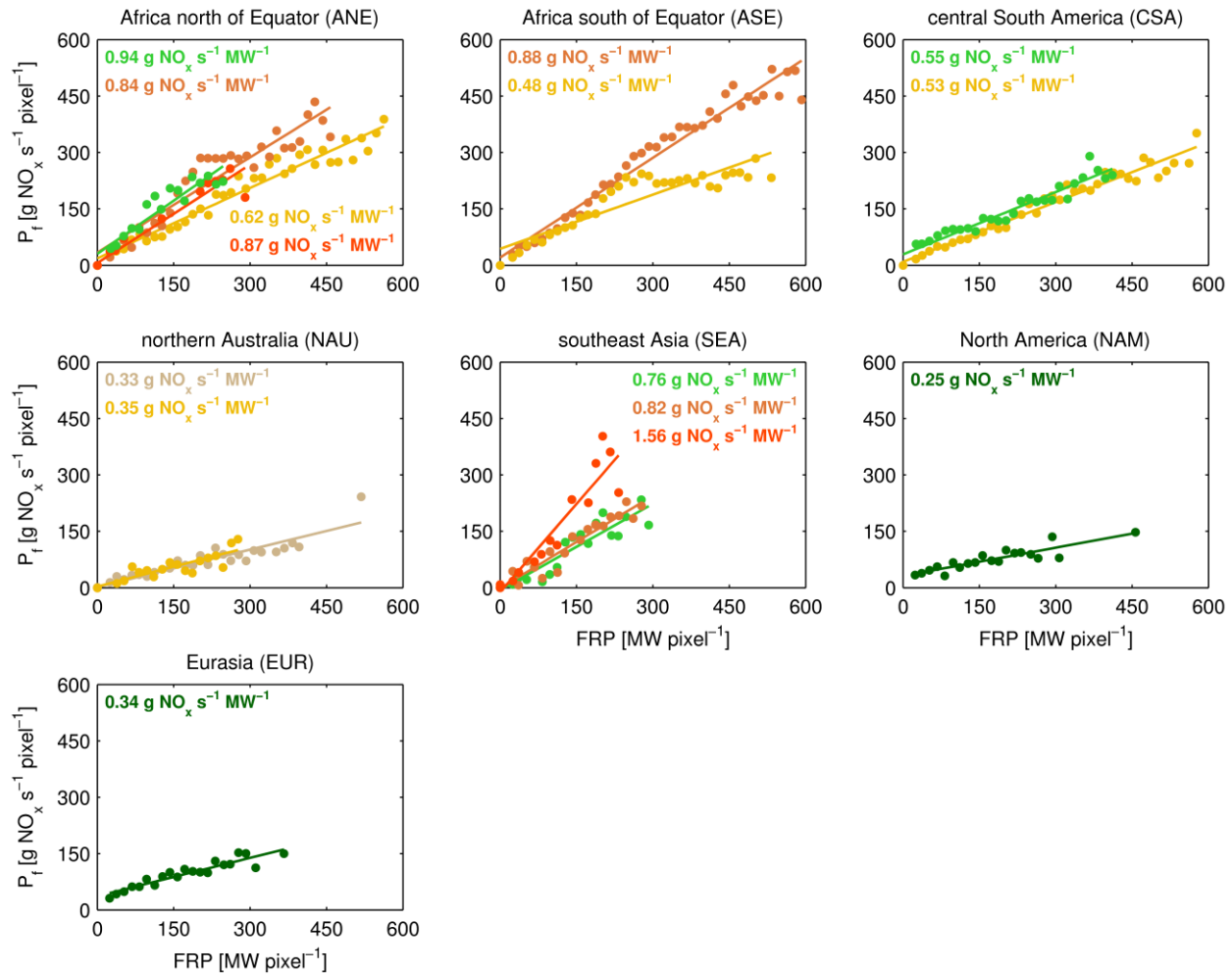
Fig. 4.2: Best fitting least-squares regression lines for evergreen broadleaf forest (light green), open shrublands (beige), woody savannas (orange), savannas (yellow), croplands (red), and boreal forest (dark green) as defined in Table 2.2 and 3.1.

From the data in Fig. 4.3 it is apparent that the arithmetic means of satellite-based EFs for tropical forest, crop residue, and boreal forest fall within one standard deviation of means reported by Andreae and Merlet (2001) and/or Akagi et al. (2011). However, the EFs for savanna and grassland obtained in this study are lower by a factor of 2.5 when compared to the other two values.
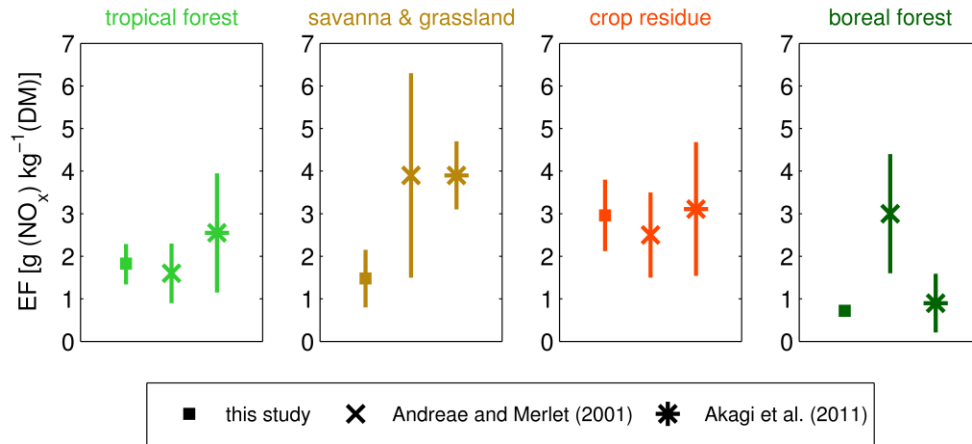
Fig. 4.3: Emission factors (EFs) of NO_x (g kg^{-1}) for tropical forest (light green), savanna and grassland (ochre), crop residue (red), and boreal forest (dark green). Satellite-based EFs are represented by squares, reported values from Andreae and Merlet (2001) are indicated by a cross, and the asterisk denotes EFs from Akagi et al. (2011).

A possible explanation for this might be the seasonal cycle in NO_x emissions rates (Mebust and Cohen 2013). It is possible that the fuel for laboratory-controlled combustion experiments has been mainly taken during that part of the fire season, where the highest emission rates are expected. In contrast, the satellite-derived EFs are based on the entire fire season, and thus, represent rather average values. Another reason could be the difference of the overpass times of GOME-2 on board MetOp-A (09:30 LT) and MODIS on board Terra (10:30 LT). Tropospheric NO_2 amounts and thus, production rates of NO_x from fire (P_f) could be underestimated for the actual Terra overpass due to the diurnal fire cycle (e.g. Giglio, 2007) with its sharp increase in the morning, in particular in African woody savannas and savannas. As a consequence, slope values of the best fitting least-squares regression lines could be too low for the morning measurements (GOME-2 vs. MODIS Terra).

One of the issues that emerge from these findings is that recent fire emission inventories might have overestimated NO_x emissions from savanna and grassland fires by a factor of 2.5.

Note that the results obtained in this study might be affected by errors in the satellite-based retrieval of TVC NO_2 and FRP as well as in the few assumptions made. A detailed discussion on the possible errors can be found in Sects. 2.3.5 and 3.4.

4.3. Summary and conclusions *

The EFs of NO_x are estimated at 1.83, 1.48, 2.96, and 0.72 g kg^{-1} for tropical forest, savanna and grassland, crop residue, and boreal forest, respectively. The EFs presented here fall within one standard deviation of the mean EFs as reported by Andreae and Merlet (2001) and/or Akagi et al. (2011). While there is overall agreement between the EFs and the comparable values presented in the literature for tropical forest, crop residue, and boreal forest, substantial differences for savanna and grassland are found.

Consequently, recent fire emission inventories could have overestimated NO_x emissions from savanna and grassland fires by a factor of 2.5. As savanna and grassland is one of the major land cover types burned on Earth, this would have a significant effect on the estimation of open biomass burning emissions of NO_x on the global scale.

---

* This subsection has been previously published as part of Schreier et al. (2014b).

Chapter 5

Two-parameter approach for estimating biomass burning emissions of NO_x for the African continent

5.1. Introduction

As outlined in Sect. 2.4, the fire emission rates (FERs) of NO_x can be applied for estimating total NO_x emissions from open biomass burning. This approach only requires one more parameter – the fire radiative energy (FRE). FRE is calculated by temporally integrating fire radiative power (FRP) and accounting for the diurnal fire cycle. The advantage of using FRE is that this parameter substitutes burned area, fuel load, and combustion completeness (see Sect. 1.1.4.4).

The two MODIS instruments on board the polar-orbiting Terra and Aqua platforms cover the entire globe within one day. On the other hand, the temporal resolution of the observations is restricted as each of the satellites overpasses the same location only twice within 24 hours. Nevertheless, the method behind GFASv1.0 is to assimilate these four daytime and nighttime measurements by using an optimal interpolation in order to produce a gridded global product of FRE (Kaiser et al., 2012).

Another satellite instrument used for the retrieval of FRE is SEVIRI on board the geostationary Meteosat Second Generation (MSG) satellites (e.g. Roberts et al., 2011). While the geostationary orbit enables high temporal resolution (repeat cycle of 15 minutes), only a part of the Earth is being covered. In the case of the MSG satellites, detailed imagery of Europe, the North Atlantic, and Africa are continually produced. As the African continent is fully covered by the SEVIRI instrument, the study to estimate total NO_x emissions for the African continent as described in the following Sects. 5.2 and 5.3 is based on FRE from SEVIRI.

5.2. Determination of parameter 1 - fire radiative energy

The current Meteosat SEVIRI sensor, which was launched in December 2005, performs measurements at 12 spectral channels in the visible and thermal infrared. The 4 visible and NIR channels cover the spectral range of 0.4-1.6 µm and the spectral range of the 8 IR channels reaches from 3.9 to 13.4 µm. Among other products, FRP is retrieved from these spectral measurements. One image of the full Earth's disc is obtained within 12 minutes (Aminou, 2002).

Table 5.1: Selected regions with their abbreviation and location.

region	abbreviation	latitudes	longitudes
Africa north	AfN	0° to 40°N	20°W to 55°E
Africa south	AfS	40°S to 0°S	20°W to 55°E

Hourly FRP observations from SEVIRI as used for this study have been provided by the Monitoring of Atmospheric Composition & Climate (MACC) project (https://www.gmes-atmosphere.eu/). In a first step, these hourly gridded maps of FRP at a horizontal resolution of 0.5° x 0.5° are averaged to daily gridded means of FRP for the entire year 2010. In Fig. 5.1, an exemplary daily cycle of FRP is shown for the 1st January 2010 for the region Africa north (AfN) as defined in Table 5.1.
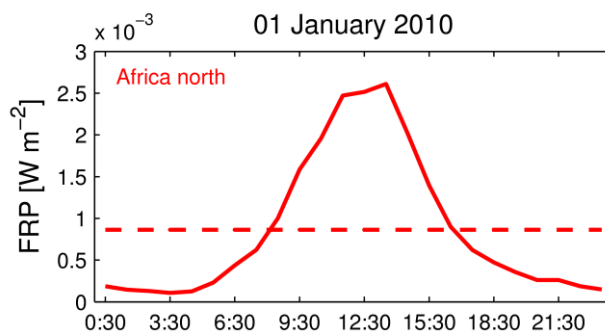
Fig. 5.1: Daily cycle of SEVIRI satellite-derived FRP for AfN as defined in Table 5.1. The solid and dashed lines represent the spatially averaged hourly and daily mean FRP, respectively.

While the solid line depicts the spatially averaged hourly FRP observations, the dotted line represents the spatially averaged daily mean of FRP as calculated from the 24 observations for AfN. Obviously, there is a clear diurnal fire cycle with a peak value in the afternoon. The characteristic diurnal fire cycles are discussed for different tropical regions and various biomes elsewhere (e.g. Giglio, 2007; Roberts et al., 2009). Besides the diurnal cycle, time series of the spatially averaged monthly means of FRP indicate a pronounced seasonal cycle for the two regions with peak values in December (AfN) and August in Africa south (AfS) (see Fig. 5.2).
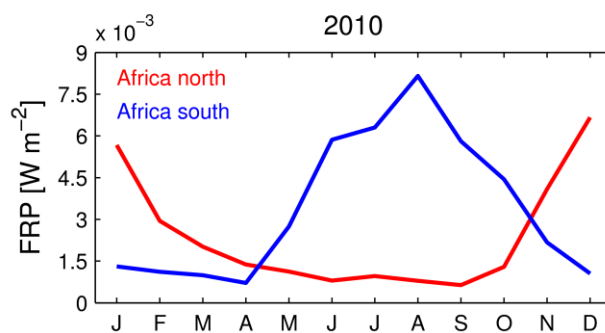
Fig. 5.2: Seasonal cycle of SEVIRI satellite-derived FRP for AfN (red) and AfS (blue) as defined in Table 5.1.
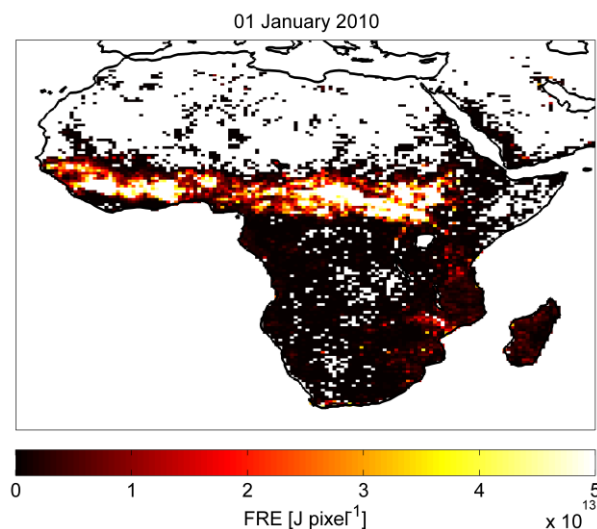
Fig. 5.3: Gridded monthly FRE for January 2010.

The seasonal pattern of fires on the African continent is largely driven by the position of the ITCZ (see also Sect. 1.4.1). In a next step, the daily gridded means of FRP are multiplied by the area of the respective grid cells. Finally, monthly means of FRP fields are temporally integrated to yield gridded monthly FRE data. An exemplary gridded map of the monthly FRE for January 2010 is shown in Fig. 5.3 for the African continent.

Due to the position of the ITCZ in Africa south of the Equator, the dry season with associated higher values of FRE prevails in Africa north of the Equator during this part of the season. The gridded maps of monthly FRE build the basis for the approach to estimate fire emissions of NO_x for the African continent.

5.3. Determination of parameter 2 - fire emission rates of NO_x

The second parameter applied for the described estimation of NO_x emissions from open biomass burning is the fire emission rates of NO_x. This parameter is largely based on the approach as described in Sects. 2.3.4 and 3.3.2. Briefly, tropospheric NO_2 vertical columns (TVC NO_2) are retrieved from OMI (see Sect. 2.2.1) and converted into production rates of NO_x from fire (P_f), based on Eq. 2.8 (see Sect. 2.2.6). The reason for the use of OMI for this study is twofold: Firstly, OMI has a higher spatial coverage than GOME-2, resulting in more data points included in the statistics. Secondly, the overpass times of Aura (OMI) and Aqua (FRP from MODIS) satellites match better than the overpass times of MetOp-A (GOME-2) and Terra (FRP from MODIS).

The gridded monthly averaged tropospheric NO_2/NO_x ratio as applied in Eq. 2.8 is calculated as described in Sect. 3.2.6. Here, the computation is based on daily gridded maps of the OMI overpass time (UT) for the year 2010. A horizontal resolution of 1.125° x 1.125° has been chosen in accordance to the horizontal resolution of the NO and NO_2 reanalysis data sets as provided by MACC. Daily weighted averages of the NO_2/NO_x ratio are calculated for the 8 given UT hours by including 29 hybrid sigma-pressure levels between the surface and ~10 km (see Sect. 3.2.6). These values are interpolated to the gridded maps of the OMI overpass time to construct daily gridded maps of the tropospheric NO_2/NO_x ratio. Exemplary gridded maps of the OMI overpass time (left)

and the interpolated tropospheric NO_2/NO_x ratio (right) are shown in Fig. 5.4 for 1st January 2010.
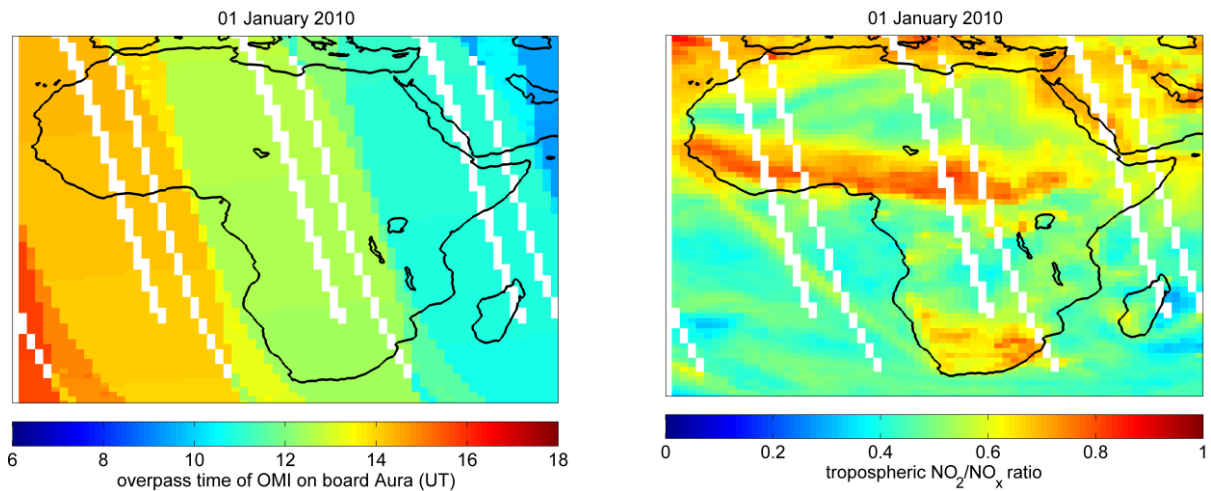
Fig. 5.4: Gridded monthly maps of the overpass time of OMI (UT) and the interpolated tropospheric NO_2/NO_x ratio for 1st of January 2010.

In a next step, monthly means of the tropospheric NO_2/NO_x ratio are generated and interpolated to a 0.5° x 0.5° resolution. These data sets are used for the estimation of P_f for the time period 2007-2012. In comparison to the determination of FERs of NO_x as described in Sect. 2.3.4 and 3.3.2, the horizontal grid resolution used for this study is set to 0.5° x 0.5°. The intention of using a higher spatial resolution was to increase the number of data points, which is a prerequisite for additionally estimating monthly resolved FERs of NO_x.

As a test of how reliable the use of a higher spatial resolution is for the described approach, the approach as described in Sect. 2.3.4 was repeated exactly in the same way for 0.5° x 0.5°. In Figure 5.5, the FERs of NO_x as derived from the original approach at a 1° x 1° resolution are plotted against the FERs of NO_x as derived at a 0.5° x 0.5° resolution. FERs of NO_x for the five regions and the selected biomes (see Table 2.3) are included in the plot.
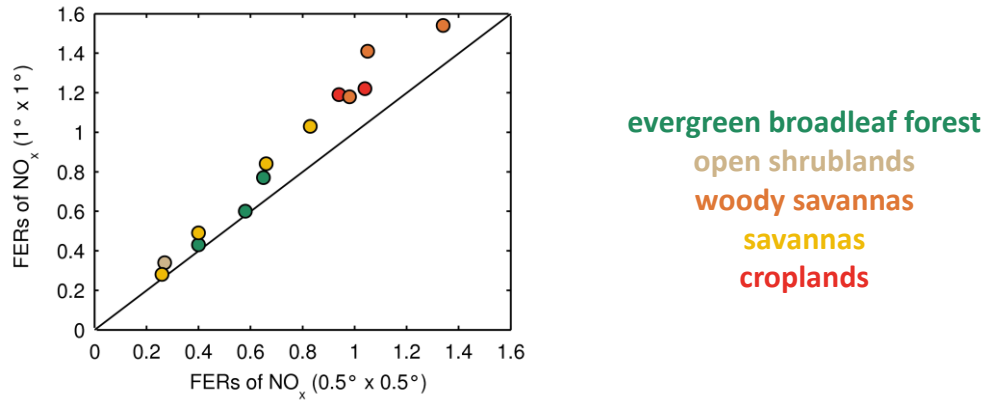
Fig. 5.5: Color-coded FERs of NO_x using the original 1° x 1° resolution plotted against the FERs of NO_x as derived at a 0.5° x 0.5° grid resolution. Here, the FERs of NO_x (OMI vs. MODIS Aqua) are shown for evergreen broadleaf forest (green), woody savannas (orange), savannas (yellow), open shrublands (beige), and croplands (red).

Interestingly, the FERs of NO_x as estimated by using the 0.5° x 0.5° grid resolution are underestimated by about 20%. One explanation for the lower FERs of NO_x could be related to transport of tropospheric NO_2 out of the pixels where no fires are observed. While such transport of NO_2 could be shifted into adjacent pixels, which are then included in the averaging to create TVC NO_2 at 1° x 1° grid resolution, the NO_2 signal might be lost more easily when calculating the best fitting least-squares regression lines at 0.5° x 0.5°. Although there are some differences between the FERs of NO_x derived from the individual grid resolution, these differences are still small enough to use the higher resolution for the following study.

Due to the limited spatial coverage of FRE as derived from SEVIRI, the approach to estimate total NO_x emissions from open biomass burning is restricted to the African continent. Therefore, the computation of the best fitting least-squares regression lines for obtaining seasonally averaged and monthly resolved FERs of NO_x has been restricted to the two African regions as defined in Table 5.1. Another modification in the approach is the omission of population density as a filter criterion, which was found to influence the results only to a negligibly small degree (see Sect. 3.2.6).

The computed seasonally averaged and monthly resolved FERs of NO_x are shown in Fig. 5.6 for the two African regions and the five different biomes.
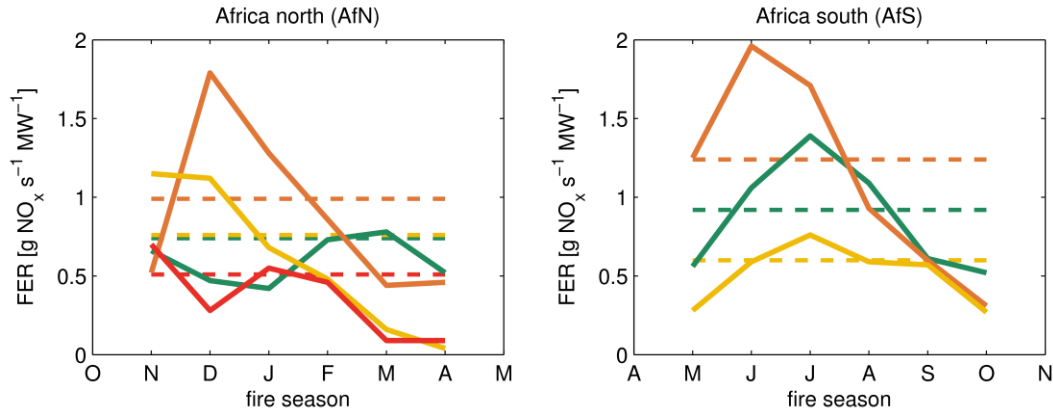
Fig. 5.6: FERs of NO$_x$ for AfN (left) and AfS (right) and selected biomes as shown in Fig. 2.9. The solid and dashed lines represent the monthly resolved and seasonally averaged FERs of NO$_x$, respectively. Here, the FERs of NO$_x$ (OMI vs. MODIS Aqua) are shown for evergreen broadleaf forest (green), woody savannas (orange), savannas (yellow), and croplands (red).

Clearly, there is a seasonal cycle observed for the FERs of NO$_x$ as estimated for the different biomes and regions. A seasonal cycle in NO$_x$ emissions from African woody savannas was already found by Mebust and Cohen (2013). They have discussed possible reasons for the observed cycles including the modified combustion efficiency and seasonal differences in the fuel N content. Here, less pronounced seasonal cycles are also observed for the other biomes. In addition to the monthly resolved FERs of NO$_x$ (solid line), the seasonally averaged FERs of NO$_x$ (dashed line) are shown in the plots.

5.4. Total fire emissions of NO$_x$ in Africa

As outlined in Sect. 5.1, the aim of this study is to develop an approach for estimating total NO$_x$ emissions from open biomass burning for the African continent. Due to the observed seasonal cycle in FERs of NO$_x$ and in order to infer the influence of not accounting for such seasonal changes, the approach to estimate total NO$_x$ emissions is based on both seasonally averaged and monthly resolved FERs of NO$_x$. The NO$_x$ emissions for the African continent are calculated from the product of monthly FRE and associated region- and biome-specific fire emission rates of NO$_x$. Note that monthly resolved FERs of NO$_x$ are only applied for the respective fire season of the two regions

(see Fig. 5.6) as the number of data points for obtaining FERs of NO_x during the wet season is not large enough for the statistics. During the wet season, seasonally averaged FERs of NO_x are used instead. Moreover, NO_x from open shrublands and grasslands are based on seasonally averaged FERs of NO_x for savannas. In both cases, however, the relative contribution of such fires is negligibly small and thus, no noticeable errors are expected for the total amounts of NO_x emissions
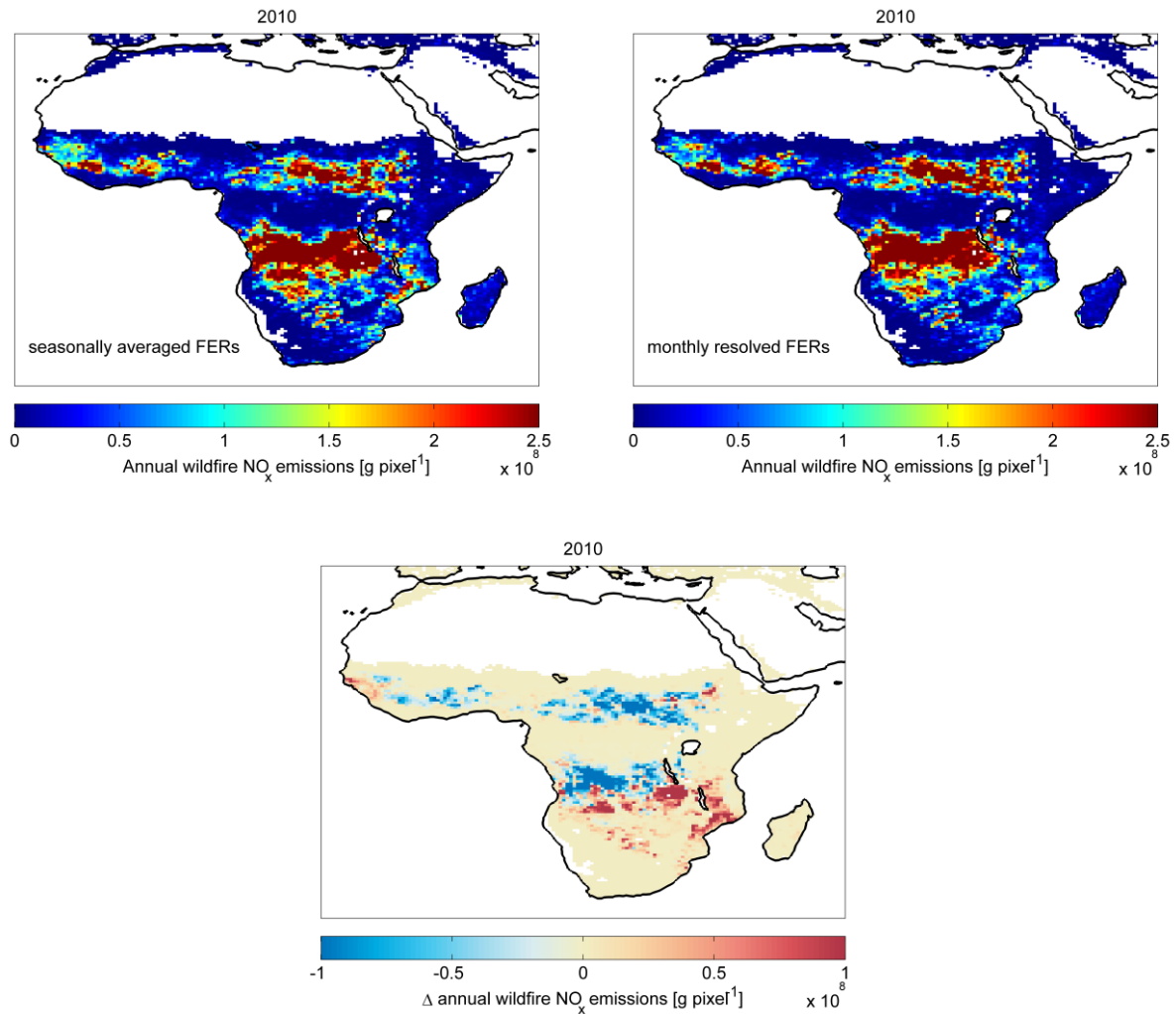
Fig. 5.7: Estimates of total NO_x emissions from open biomass burning by applying seasonally averaged (left) and monthly resolved (right) FERs of NO_x. The differences between the two approaches (seasonally averaged minus monthly resolved FERs of NO_x) are presented in the bottom.

The total emissions of NO_x for the year 2010 by applying seasonally averaged (left) and monthly resolved (right) FERs of NO_x as well as differences between the two approaches (bottom) are shown in Fig. 5.7. In general, the patterns appear quite similar at first sight. When inspecting the differences between the two approaches in more detail, however, clear differences are visible (up to 50%). For example, large parts of woody savannas in AfS are either lower or higher when applying monthly resolved FERs of NO_x. In contrast, large areas covered by woody savannas or savannas in AfN are clearly lower when applying seasonally averaged FERs of NO_x.

The calculations of NO_x from open biomass burning based on monthly resolved FERs of NO_x yield a total amount of 0.568×10^{12} g NO_x for the African continent in the year 2010. In comparison to recently reported averaged annual emissions of NO_x (van der Werf et al., 2010; Kaiser et al., 2012), the estimate derived from the two-parameter approach is about eight times smaller. Possible explanations for these large differences could be the underestimation of FRE from SEVIRI (> 50%) and/or the underestimation of FERs of NO_x using the $0.5° \times 0.5°$ resolution (~20%). Roberts et al. (2011) have highlighted that the raw FRE-based methods are underestimates because of the non-detection of small fires. Moreover, cloud cover can influence the calculation of FRE to a larger degree than the retrieval of burned area (e.g. van der Werf et al., 2010).
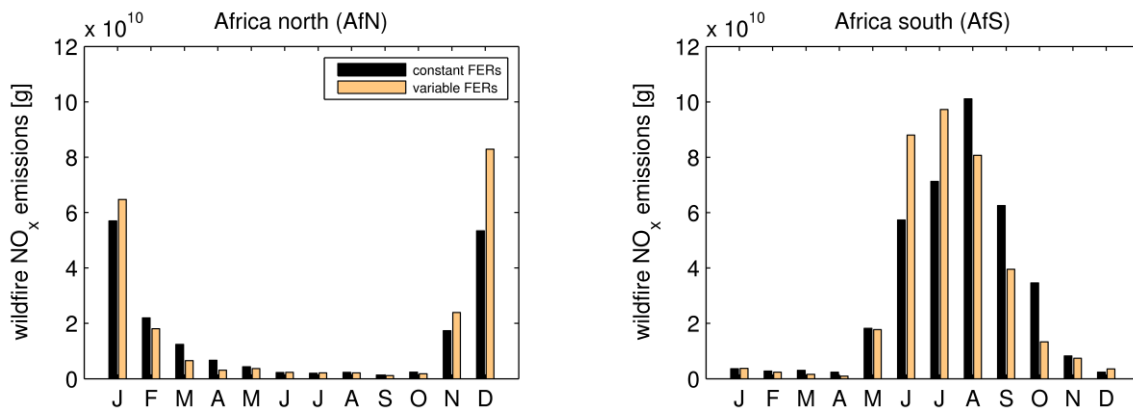
Fig. 5.8: Bar plots of monthly sums of NO_x emissions for AfN (left) and AfS (right). The dark (bright) bars represent total NO_x as estimated by applying seasonally averaged (monthly resolved) FERs of NO_x.

However, the reason for the large differences between FRE as estimated in this study and FRE as computed for the GFASv1.0 approach (Kaiser et al., 2012) still remains unclear. One possible explanation is that the optimal interpolation applied for estimating FRE in GFASv1.0 could lead to an overestimation of FRE. However, comparisons between total NO_x from GFASv1.0 and from GFEDv3 show hardly any differences.

Finally, NO_x emissions as derived from the two approaches developed in this study are compared with each other on the monthly basis for AfN and AfS. The comparison reveals up to 90% differences between the two approaches (see Fig. 5.8). In particular during the peak of the respective fire season, NO_x emissions as estimated applying monthly resolved FERs of NO_x are significantly higher.

5.5. Summary and conclusions

A two-parameter approach for estimating wildfire emissions of NO_x in Africa has been developed. In comparison to recent bottom-up emission inventories (e.g. GFED), burned area, fuel load, and combustion completeness are substituted by fire radiative energy (FRE). Moreover, emission factors and associated conversion factors are substituted by fire emission rates of NO_x (FERs).

The conversion of tropospheric NO_2 vertical columns from the OMI instrument into production rates of NO_x from fire (P_f) is based on monthly means of the tropospheric NO_2/NO_x ratio as derived from model data from MACC. The best fitting least-squares regression lines as derived from the linear relationship between P_f and FRP from MODIS (on board Aqua) are used to determine FERs of NO_x for different biomes.

Fire radiative power from SEVIRI is temporally integrated to yield monthly gridded values of FRE.

Seasonally averaged and monthly resolved FERs of NO_x are applied together with FRE to estimate fire emissions of NO_x for the African continent. The two different approaches have been tested in order to obtain the degree of uncertainties arising from ignoring such seasonal cycles in FERs of NO_x.

The results show that differences between the two estimation approaches are up to 90% on a monthly basis. Moreover, the total NO_x from open biomass burning for the year 2010 is about eight times smaller when compared with estimates reported in Kaiser et al. (2012). One explanation for this large difference could be related to the underestimation of FRE from SEVIRI caused by increased detection limits (see Sect. 2.2.2).

Future efforts directed towards improved satellite products of tropospheric NO_2 vertical columns (TVC NO_2) and FRE could substantially reduce the uncertainties of the tested approach to estimate total NO_x from open biomass burning.

Chapter 6

Ship-based MAX-DOAS measurements of tropospheric NO$_2$ and SO$_2$ in the South China and Sulu Sea *

6.1. Introduction *

Nitrogen oxides (NO$_x$ = NO + NO$_2$) are well known and significant pollutants in the troposphere (see Sect. 1.2.2).

Sulfur dioxide (SO$_2$) is a main constituent in the tropospheric sulfur cycle. Besides the natural emissions of dimethylsulfide (DMS), the anthropogenic emissions of SO$_2$ are quantitatively the most important emissions in the sulfur cycle (Berglen et al., 2004).

The amounts and distributions of NO$_2$ and SO$_2$ can be retrieved from active and passive remote sensing techniques in the ultraviolet (UV) and visible regions of the electromagnetic spectrum (see Sect. 1.5).

After successful application of the zenith scattered light DOAS method, which mainly yields stratospheric trace gas amounts (Noxon, 1975; Solomon et al., 1987; Richter et al., 1999; Wittrock et al., 2000), the development of Multi-Axis (MAX) DOAS allowed for the extension of the technique to tropospheric trace gases and aerosols by observing scattered sunlight at different viewing directions (Hönninger et al., 2004; Wagner et al., 2004; Wittrock et al., 2004).

Although MAX-DOAS is relatively simple to operate, the interpretation of the data requires detailed information about the radiation transport in the atmosphere, especially in terms of aerosol scattering (Mie scattering). For example, Wagner et al. (2004) developed a method for deriving atmospheric aerosol profiles by using MAX-DOAS measurements of the oxygen dimer (O$_4$) under clear sky conditions. They demonstrated that the O$_4$ measurements are sensitive to the aerosol extinction close to the ground and suggested the potential to retrieve aerosol profiles by the use of radiative transfer models such as SCIATRAN (Rozanov et al., 2005) and McArtim (Deutschmann et al., 2011).

Ship-based MAX-DOAS measurements of NO_2 amounts have so far been focused on both remote and coastal marine environments in the Indian and Pacific Ocean to obtain boundary layer background conditions. Peters et al. (2012) reported NO_2 background conditions < 50 pptv in the remote Western Pacific boundary layer, with tropospheric NO_2 columns rarely exceeding the detection limit of the instrument. Higher values of up to 200 pptv were estimated from MAX-DOAS observations on board the Japanese research vessel Kaiyo in the western Pacific and Indian Ocean boundary layer (Takashima et al., 2012), presumably being influenced by anthropogenic sources. However, during the NASA Pacific Exploratory Mission (PEM) Tropics B field experiment, aircraft in-situ measurements of NO_2 over the clean Pacific yielded values < 10 pptv in the boundary layer (Browell et al., 2001). Consequently, the detection limit of the MAX-DOAS instrument (30-50 pptv) may be too large for actual measurements of NO_2 background values in the boundary layer. Nevertheless, the MAX-DOAS technique has an important benefit in retrieving tropospheric profile information of trace gases (see Sect. 6.5.4). While the focus of these previous studies was on NO_2 amounts, SO_2 has received much less attention. However, SO_2 emissions in the open sea are high because of the high sulfur contents in heavy fuels often used by ships in international waters (Endresen et al., 2005).

The Southeast Asian region experiences rapid environmental changes with some of the highest rates of deforestation in humid tropical forests as observed within the last two decades (Achard et al., 2002; Miettinen et al., 2011). Large areas of natural forest have been replaced by agricultural land, especially oil palm plantations. Miettinen et al. (2011) estimated the loss of the total forest area in insular Southeast Asia to be in the order of 10% between 2000 and 2010 and emphasize the continuing deforestation in this region.

In recent years, there has been an increasing interest on studying the effect of land use changes on tropospheric chemistry in tropical regions. MacKenzie et al. (2011) observed tropospheric trace gases over a rainforest and an oil palm site on Borneo Island. The results show that NO_x mixing ratios over the oil palm plantation were higher by a factor of 1.5 resulting from nitrogen fertilizer application and on-site palm oil processing. Rising concentrations of NO_x and volatile organic compounds (VOCs) over these plantations have increased the concentrations of some photochemical pollutants and could

eventually increase tropospheric O_3 levels due to further industrialization and economic development (Hewitt et al., 2009). In addition to land use changes, international shipping emissions in the South China Sea are strongly driven by the increasing Asian trade volume (de Ruyter de Wildt et al., 2012).

The purpose of this study is to report on daytime tropospheric NO_2 vertical columns (TVC NO_2) and profiles as well as SO_2 slant columns measured by a ship-based MAX-DOAS instrument in the coastal and open waters of the South China and Sulu Sea in November 2011. TVC NO_2 is retrieved by the profile inversion method BREAM (Bremian advanced MAX-DOAS retrieval algorithm) and compared to TVC NO_2 as obtained from a geometric approach and from satellite instruments.

The MAX-DOAS measurements have been performed as part of the SHIVA ship-based campaign, which is briefly introduced and described in Sect. 6.2. The MAX-DOAS instrument, the retrieval of tropospheric NO_2 columns and profiles, as well as satellite-based instruments and data products are introduced in Sect. 6.3. The HYbrid Single-Particle Lagrangian Integrated Trajectory (HYSPLIT) model, which is used for determining the origin of elevated NO_x levels in the study area, is summarized in Sect. 6.4. The results of this study for NO_2 and SO_2 are presented in Sect. 6.5 and summarized in Sect. 6.6.

6.2. Ship cruise within SHIVA *

The aim of SHIVA (Stratospheric ozone: Halogen Impacts in a Varying Atmosphere) was to better predict the rate, timing and climate-sensitivity of ozone-layer recovery, and to identify potential risks from the recovery. For this purpose, several land-based, ship-based, aircraft-based, and space-based measurements in the insular region of Southeast Asia were combined with sophisticated numerical models (Pfeilsticker et al., 2012).

The ship cruise was carried out with the German research vessel (RV) Sonne as a part of the SHIVA campaign between 15th November (departure: Singapore) and 29th November (arrival: Manila, Philippines) 2011 in the South China and Sulu Sea. The

measurements made during the ship cruise aimed at (i) investigating the emissions of halogenated trace gases from coastal waters of the Western Pacific and upwelling waters, (ii) characterizing the marine biota causing these emissions of halogenated very short-lived substances, and (iii) studying the atmospheric transport and transformation of halogenated gases and their transport to the stratosphere (Pfeilsticker et al., 2012). Indeed, the concentrations of NO_x and VOCs in insular Southeast Asia have risen due to land use changes and increased shipping emissions and thus, could affect the concentrations of ground-level ozone (Hewitt et al., 2009; de Ruyter de Wildt et al., 2012).

The IUP Bremen MAX-DOAS instrument was part of the RV Sonne instrumentation during SHIVA to measure atmospheric trace gases. The entire ship track and daytime stages indicating the period between the first and last MAX-DOAS measurements are highlighted in Fig. 6.1.
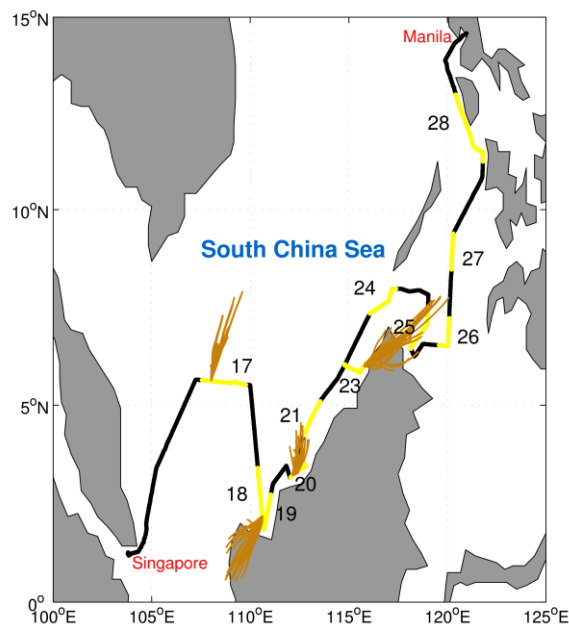
Fig. 6.1: Cruise track of the RV Sonne during SHIVA (black line), departing from Singapore on 15th November 2011 and arriving in Manila, Philippines on 29th November 2011. The sections of the cruise track highlighted in yellow indicate the distances traveled by the ship between the first and last daytime MAX-DOAS measurements presented in this study. The brown lines show ensembles of computed 12 hour backward trajectories for selected case studies with TVC NO_2 > 2 x 10^{15} molec cm^{-2} (see Sect. 6.5.3).

After installing and testing the instrument at the beginning of the campaign, continuous operation started in the morning of 17th November. Instrumental problems occurred in the middle of the campaign on 22nd November and therefore, no measurements are presented for this day. Overall, spectral measurements have been performed on eleven days during SHIVA, which provides a good basis for the analysis of NO_2 and SO_2 observations in the coastal and open waters of South China and Sulu Sea.

6.3. Instruments and data analysis *

The DOAS technique is a widely-used remote sensing method to retrieve trace gases with narrow band absorption structures in the ultraviolet and visible part of the electromagnetic spectrum. Based on Lambert-Beer's law, this spectroscopic technique makes use of the absorption of electromagnetic radiation by matter. The DOAS principle can be applied to various ground-based, ship-based, aircraft-based, and satellite-based platforms (e.g. Platt and Stutz, 2008).

6.3.1. MAX-DOAS instrument and data retrieval *

6.3.1.1. MAX-DOAS instrument *

The principle of the IUP-Bremen MAX-DOAS is briefly described in Sect. 1.5.2 and more detailed information can be found in Peters (2013).

The telescope unit of the MAX-DOAS instrument assembled on board the RV Sonne includes a video camera (for weather and event detection) and was installed on a pan/tilt head. For measurements in the UV and visible range, grating spectrometers (Andor Shamrock 303i and Acton500, respectively) with a wavelength range of 305-373 and 392-563 nm and a spectral resolution of 0.4 and 0.8 nm, respectively, were used in combination with a CCD (Andor Newton DU940N and Roper Scientific Princeton NTE/CCD, respectively) with 512 x 2048 and 100 x 1340 pixels, respectively. Further characteristics of the MAX-DOAS system used within SHIVA can be found in Peters (2013).

During the recent CINDI (Cabauw Intercomparison campaign for Nitrogen Dioxide measuring Instruments) and TransBrom campaigns, the IUP-Bremen MAX-DOAS system was used to retrieved NO_2, formaldehyde (HCHO), and iodine monoxide (IO) (Roscoe et al., 2010; Peters et al., 2012; Piters et al., 2012; Großmann et al., 2013; Pinardi et al., 2013).

6.3.1.2. Set-up on the ship *

During the SHIVA ship cruise, the azimuthal angle of the telescope unit was kept at 90° relative to the heading direction of the RV Sonne (Fig. 6.2) and elevation angles (α) of 1°, 2°, 3°, 4°, 5°, 6°, 7°, 8°, 9°, 10°, 15°, 30°, and 90° were included in the scanning sequence designed for the NO_2 retrieval. Each scanning sequence took about 15 minutes. In order to avoid the influence of twilight on the spectral measurements, the MAX-DOAS instrument was set to record off-axis spectra for solar zenith angles < 85° (17th and 18th November) and < 75° (19th to 28th November).
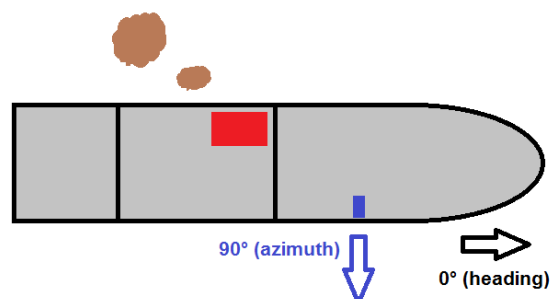
Fig. 6.2: Schematic illustration of the MAX-DOAS instrument set-up on board RV Sonne. The red rectangle indicates the ship's smoke stack and the blue rectangle depicts the position of the MAX-DOAS instrument, measuring in 90° azimuthal direction (blue arrow) relative to the ship's heading (black arrow).

6.3.1.3. Data preparation and filtering *

The ship's movements (heading, pitch, and roll) have been measured by the high accuracy (0.02°) Seatex MRU 5 instrumentation and downloaded from the ship's database at a time resolution of 50 ms after the campaign. The actual azimuthal direction and elevation angles of the scanning sequence have been corrected by the heading, pitch, and roll measurements afterward.

Due to the ship's movements in the sea, the elevation angles of the telescope, which are relative to the ship, are not the actual viewing directions. In order to overcome this effect, spectra were recorded with exposure times of 100 ms and ship's movements within this period were considered to be negligible. For each vertical scanning sequence, the individual 100 ms measurements were then corrected in terms of the roll angle and sorted according to the real viewing direction with a tolerance of ±0.5. As this tolerance together with the instrument's field of view of ~1° could affect the quality of measurements at the 1° elevation angle (due to pointing into the water), the lowest viewing direction of the scanning sequence for the retrieval of tropospheric NO_2 was selected to be 2°.

Finally, all of the individual measured spectra performed for each elevation angle of the scanning sequence (e.g. all 100 ms spectra obtained between 1.5° and 2.5° for α = 2°) have been averaged. As a result, one average spectrum is achieved for each elevation angle of the individual scanning sequences.

Under unfavorable wind conditions, the ship's exhaust plume was potentially contaminating the measurements. As the instrument was installed in front of the ship's smoke stack (see Fig. 6.2), this was not a problem for most of the time when the ship was running at full speed. In order to exclude occasional influences of the ship's exhaust plume on the MAX-DOAS measurements, individual measurements taken under unfavorable wind directions (between 90° and 280°) have been discarded. The relative wind direction (blue dots) and the ship's speed (red line) are presented in Figs. 6.5a-6.7a for the individual days. In general, the ship's speed was higher than 20 km h^{-1} when it was running at full speed. In most such cases, the recorded relative wind direction was between 90° and 280°, which rules out any influence of the ship's smoke stack on the

---

spectral measurements. It is apparent that unfavorable relative wind directions are more frequent when the ship slowed down. The bulk of data removed by data filtering occurred when the ship was slower than 5 km h^{-1}. However, the amount of spectral measurements after data filtering is still large enough for a reasonable analysis (> 500 measured spectra per day on average). All spectral measurements within the two thresholds (90° and 280°, marked by the gray shaded area) are not included in the retrieval procedure, which is described in the following Sect. 6.3.1.4.

6.3.1.4. DOAS retrieval *

The filtered MAX-DOAS spectral measurements are analyzed using the DOAS technique applying a nonlinear least-squares fitting algorithm.

Following recommendations developed during the CINDI and TransBrom campaigns (Piters et al., 2012; Peters et al., 2012), a fitting window between 425 and 490 nm has been selected for the NO_2 fit. The high resolution absorption cross-sections of O_3 (Bogumil et al., 2003) at 223 K, NO_2 (Vandaele et al., 1996) at 298 K, O_4 (Greenblatt et al., 1990), H_2O (Rothmann et al., 2003) at 273 K, and a pseudo-cross section accounting for rotational Raman scattering as computed with SCIATRAN (Rozanov et al., 2005) have been included in the retrieval. In order to account for the influence of liquid water on the fit, the liquid water absorption coefficient as measured in the laboratory by Pope and Fry (1997) was added. Moreover, an empirical correction spectrum by Peters et al. (2014) accounting for the effects of liquid water and vibrational Raman scattering (VRS) has been included in the adapted NO_2 fit (see Table 6.1). For the retrieval of differential slant column densities (DSCDs), the zenith observation of the same measurement sequence was used as Fraunhofer reference spectrum (FRS). For simplicity, the term SCD is used instead of DSCD throughout this thesis.

Table 6.1: Summary of the "standard" settings used for the visible spectra to produce NO_2 SCDs, including a cross section for liquid water and an empirical correction spectrum (italic) for the "adapted" fit (see Sect. 6.5.1). The set up for fitting in the UV to produce SO_2 SCDs is also listed (right).

	NO₂ settings	SO₂ settings
fitting window [nm]	425-490	307.5-328
polynomial degree	5	3
O₃	Bogumil et al. (2003)	Gorshelev et al. (2014)
NO₂	Vandaele et al. (1996)	Vandaele et al. (1996)
O₄	Greenblatt et al. (1990)	-
H₂O	Rothmann et al. (2003)[a]	-
SO₂	-	Bogumil et al. (2003)
Ring	SCIATRAN (VIS)	SCIATRAN (UV)
H₂O_liq.	*Pope and Fry (1997)*	-
empirical correction	*Peters et al. (2014)*	-

[a] but using HITRAN 2009

As the RV Sonne left a dense shipping lane on the 17th November, interesting insights into sulfur dioxide (SO_2) emissions from shipping are expected. Therefore, SO_2 from the MAX-DOAS UV measurements is also retrieved and the spatial distribution SO_2 columns and their relation to NO_2 is investigated. However, the main focus of this study is on the tropospheric amounts and distributions of NO_2.

The SO_2 fit includes high resolution absorption cross-sections of O_3 (Gorshelev et al., 2014; Serdyuchenko et al., 2014) at 223 and 243 K, NO_2 (Vandaele et al., 1996) at 298 K, SO_2 (Bogumil et al., 2003) at 293 K, and a pseudo-cross section accounting for rotational Raman scattering as computed with SCIATRAN (Rozanov et al., 2005). The SO_2 fit was performed in the spectral window between 307.5 and 328 nm (see Table 6.1). As the UV spectrometer covers a wavelength range of 305-373 nm, the start wavelength was restricted. In order to cover the strongly structured SO_2 absorption spectrum around 300 nm (e.g. Richter, 2006), we have selected a wavelength range as close to the start wavelength as possible. The end wavelength of the interval was set to 328 nm because SO_2 fitting errors and RMS were small and reasonable values for the SO_2 SCDs were obtained, compared to other tested end wavelengths (not shown). In general, the SO_2 settings used in our study are comparable with those used in a recent

study by Wang et al. (2014). They have retrieved SO_2 in the spectral range of 308-325 nm by including cross sections of SO_2, O_3, NO_2, and a synthetic ring spectrum. The SO_2 retrieval presented in Irie et al. (2011) is performed in a slightly smaller spectral window (310-320 nm) and includes an additional cross section for HCHO.

Due to some problems with the zenith SO_2 measurements (e.g. unexpected high values around noon causing a strong daily cycle), 30° measurements have been used as FRS. As mentioned in Peters (2013), similar problems also occurred during TransBrom in the tropics at small SZAs for NO_2 and HCHO. One possible explanation could be that direct sunlight entering the system around noon in spite of light baffles leads to saturation effects on the CCD.

6.3.1.5. Conversion to tropospheric NO_2 vertical columns *

In this study, the conversion of SCDs into TVCs is based on two different approaches:

The first approach uses the geometrical approximation by simply estimating a tropospheric airmass factor (AMF) via the $1/\sin(\alpha)$ relation (Hönninger et al., 2004), where α denotes the elevation angle of the telescope unit. TVC NO_2 for different is computed elevation angles and compared with TVC NO_2 as retrieved with the second approach.

The second approach is based on the Bremian advanced MAX-DOAS Retrieval Algorithm (BREAM), which was developed by Wittrock (2006) in order to retrieve tropospheric vertical columns and profiles of trace gases. The retrieval algorithm is motivated by the study of Wagner et al. (2004). Briefly, the measured slant columns of O_4 are used to retrieve aerosol information by comparing them with O_4 slant columns simulated with the radiative transfer model SCIATRAN (Rozanov et al., 2005). This information is essential to obtain accurate box air mass factors (BAMFs) for trace gases, such as NO_2. The box air mass factors are then used to retrieve the vertical profile of the trace gas from the measured slant column densities (SCDs) at different elevation angels. As the measurements provide only limited information on the vertical trace gas column, an optimal estimation method (Rodgers et al., 2000) is performed using an a

priori profile. Further details about BREAM and the required a priori information can be found in Wittrock (2006) and Peters et al. (2012). A similar profiling technique, which is also based on the optimal estimation method, can be found in Frieß et al. (2011).

In this study, the BREAM computations of TVC NO_2 and NO_2 profiles are performed using all observations between 2° and 30° elevation angles within time intervals of 15 min each. The ocean surface spectral reflectance in the selected spectral window is assumed to be 0.05, and an appropriate a priori profile is used for the optimal estimation. Volume mixing ratios decreasing linearly with altitude are assumed for the a priori vertical NO_2 profile initially. The a priori profile is then scaled various times with scaling factors to yield a trace gas profile. The total retrieval height is 4 km with a retrieval grid size of 50 m, resulting in 80 layers. More details about the settings used for BREAM can be found in Peters et al. (2012).

As a quality criterion of TVC NO_2 and profiles as retrieved from BREAM, computations are only performed when the correlation coefficient between the measured and simulated O_4 slant columns is higher than 0.6 and when the number of elevation angles of one scanning sequence is larger than 10. The former threshold value has been selected to exclude measurements that are affected by the own ship's plume (e.g. resulting in negative SCDs). Even if the SCDs affected by an elevated exhaust plume are not negative, but obtained by using such an influenced zenith sky measurement as reference spectrum, they are not included in the retrieval of TVC NO_2 and vertical profiles from BREAM, as the correlation criterion will not be fulfilled. As we here focus on the comparison between the two described approaches, the values obtained from the geometrical approximation are shown using the same quality criteria as for BREAM.

6.3.2. Satellite instruments and data sets

6.3.2.1. GOME-2 and OMI

Since the launch of the Global Ozone Monitoring Experiment (GOME) on board ESA's European Remote Sensing (ERS)-2 satellite (Burrows et al., 1999), the scattered light DOAS technique has also been applied to space-based measured spectra.

In this study, monthly means of TVC NO_2 from GOME's successor GOME-2 on board MetOp-A satellite (Callies et al., 2004) and from the Ozone Monitoring Instrument (OMI) on board NASA'S (Levelt et al., 2006) are used for the spatio-temporal interpretation of NO_2 in the coastal environment of the South China and Sulu sea. One of the main differences between GOME-2 and OMI is the local overpass time of the satellite platforms MetOp-A and Aura, respectively. While GOME-2 observes around 9:30 LT in the morning, the equatorial overpass time of OMI is around 13:30 LT in the early afternoon.

6.3.2.2. Satellite data retrieval

The satellite-based retrieval of TVC NO_2 is achieved in four main steps. First, the SCDs are retrieved from the instruments' spectral measurements by fitting the absorption cross section of NO_2 and other trace gases. In this study, the recommendations of Richter et al. (2011) are applied and the spectral window between 425 and 497 nm is used. Secondly, the reference sector method (Richter and Burrows, 2002) is applied for the subtraction of the stratospheric part, which is a good approximation in the tropics. Thirdly, the Fast REtrieval Scheme for Clouds from the Oxygen A-band (FRESCO+) retrieval (Wang et al., 2008) and the O_2-O_2 absorption band at 477 nm (Acarreta et al., 2004) are used for removing measurements with a cloud fraction larger than 20% for GOME-2 and OMI, respectively. In the last step, the SCDs are converted to TVC NO_2 by dividing through an AMF, which corrects for the different sensitivity of the measurements in different altitudes (e.g. Richter et al., 2005). Here, the monthly means of TVC NO_2 are binned to a horizontal resolution of 0.5° x 0.5°.

A more detailed description of the NO_2 retrieval for the two instruments is given in Sect. 2.2.1.

6.4. Backward trajectories calculations

The web-based version of the HYbrid Single-Particle Lagrangian Integrated Trajectory (HYSPLIT) model (Draxler and Rolph et al., 2013, Rolph, 2013) from the National Oceanic and Atmospheric Administration (NOAA) is used for the calculation of air mass backward trajectories. HYSPLIT is a system for the computation of simple air parcel trajectories by applying meteorological databases. The back trajectory calculations as performed for this study are based on the Global Data Assimilation System (GDAS).

Here, backward trajectories at an altitude of 500 m above sea level are computed for selected case studies with elevated NO_2 levels (TVC NO_2 > 2 x 10^{15} molec cm^{-2}). The ensemble tracks of air masses, starting 12 hours prior to the observations of elevated NO_2 amounts, are highlighted in Fig. 6.1 by brown lines for the individual case studies on 17th, 19th, 20th, and 23rd November 2011.

6.5. Results and discussion *

6.5.1. Tropospheric NO_2 slant column densities *

The "standard" set up for fitting as applied during the CINDI campaign (Roscoe et al., 2010) is compared with a fit including the absorption of liquid water (Pope and Fry, 1997) and the correction spectrum accounting for liquid water and effects of VRS (Peters et al., 2014), here referred to as "adapted" settings (see Fig. 6.3 and Table 1). In Fig. 6.3, the differential optical density of the NO_2 fit is plotted against the differential optical density of the NO_2 reference for an unpolluted (top) and polluted case (bottom) as a function of wavelength. Here, the reference is defined as the scaled cross section (with the slant column as scaling factor) and the fit is defined as the scaled cross section including the fit residuals. For the unpolluted case, all measurements at α = 2° taken on the 18th November are included in the scatter plot. The polluted case has been selected on 17th November and includes all measurements at α = 2° that exceed a value for the NO_2 SCD of 1 x 10^{16} molec cm^{-2}. The left plots in the figure represent the results using "standard" settings, whereas the right plots show the results using the "adapted" settings. There is some degree of improvement (higher r^2 values) in the NO_2 fit quality

---

* This subsection has been previously published as part of Schreier et al. (2014c). 135

when including the absorption of liquid water and the empirical correction spectrum for an elevation angle of 2°. This is in good agreement with the recent study by Peters et al. (2014).
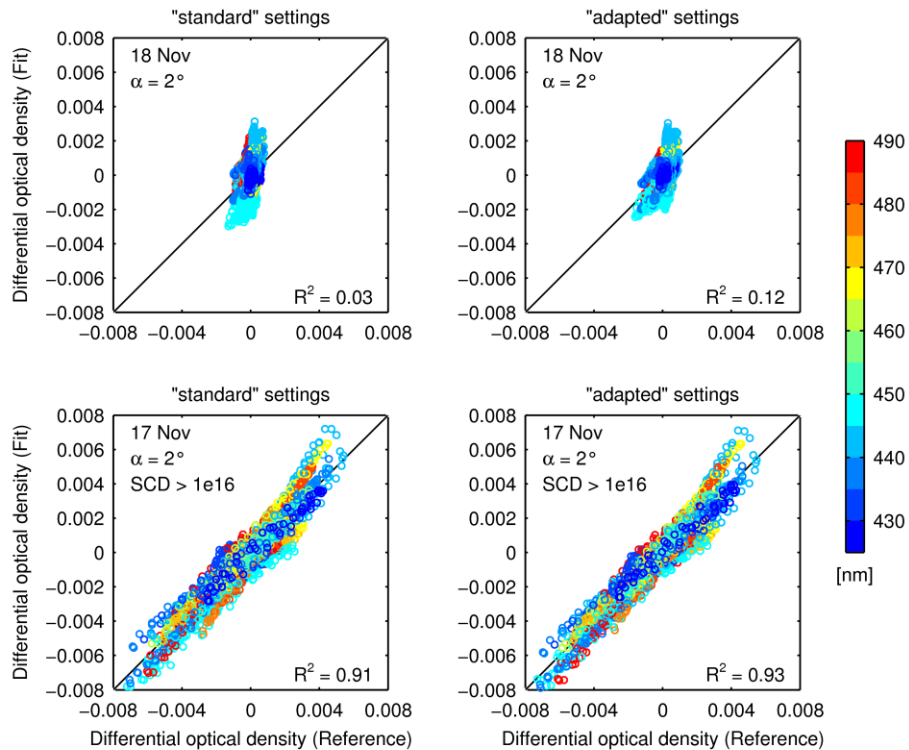
Fig. 6.3: Scatter plots of differential optical density (Fit) vs. differential optical density (Reference) for the NO₂ "standard" settings (left) and "adapted" settings including the absorption of liquid water and an empirical correction spectrum for liquid water and VRS (right). Here, the scatter plots are shown for the NO₂ fits including only α = 2° measurements for an unpolluted (top) and polluted case (bottom). Further explanations and definitions are given in the text.

While all measurements α = 2° from 17th November are included in Fig. 6.3 (bottom), only one exemplary measurement at α = 2° is shown in Fig. 6.4 for the morning of 17th November, when the RV Sonne left the dense shipping lane connecting Singapore and East China. The measurement was taken at a solar zenith angle of 78.13° and the obtained SCD is 3.75×10^{16} molec cm^{-2} with an RMS of 7.5×10^{-4}. There is good correlation between the reference (black line) and the fit (green line). Compared to the standard settings, however, there is only minor improvement, which is not directly visible in the fit result (not shown).

The results of Figs. 6.3 and 6.4 suggest that the overall fit quality for cases with elevated NO_2 levels is good enough to retrieve NO_2 SCDs and subsequently estimate TVC NO_2 via the geometric approach and BREAM.
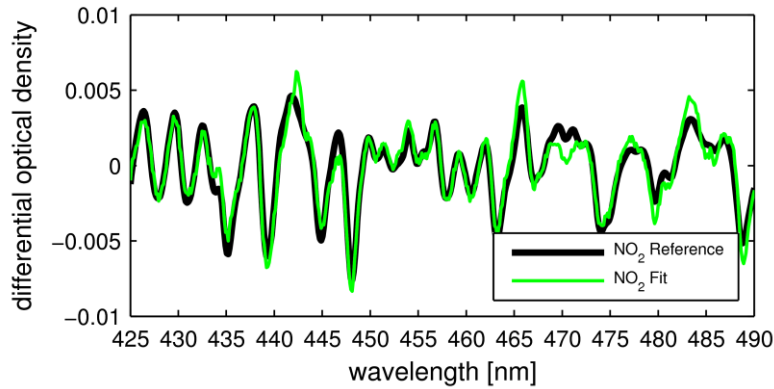
Fig. 6.4: Fit results of the NO_2 fit using the "adapted" settings for the morning of 17th November 2011 (23:32 UT) under elevated NO_2 pollution (SCD = 3.75 x 10^{16} molec cm^{-2}). The RMS of the residuals is 7.5 x 10^{-4}. Here, the optical density of the reference (differential absorption cross-section, scaled by the retrieved SCD, black line) and fit (reference + residual, green line) are retrieved at 2° elevation angle and at 78.13° solar zenith angle. Further explanations and definitions are given in the text.

A detection limit for NO_2 slant columns from MAX-DOAS measurements in the open ocean has recently been estimated by Peters et al. (2012). RMS values from the best NO_2 fits in the order of 1 x 10^{-4} were used to derive an upper detection limit of 2 x 10^{15} molec cm^{-2}. As similar RMS values are found for the best fits in this study, their detection limit can also be assumed here.

The color-coded time series of the obtained NO_2 SCDs are shown in Figs. 6.5b-6.7b for the individual days. Obviously, the highest values are observed at the lowest elevation angles, whereas the lowest values are found at the highest elevation angles, indicating that largest amounts of tropospheric NO_2 are located close to the ground. The lowest NO_2 SCDs are observed when the ship was far away from the coast and in a sufficiently large distance to other ships. For instance, the low values in the afternoon of 17th November and during almost the entire day of 18th November have been observed while the ship left the dense traffic lane and headed towards the coast of Borneo (see Fig. 6.1). On all other days, there was at least one peak in the time series of NO_2 SCDs.
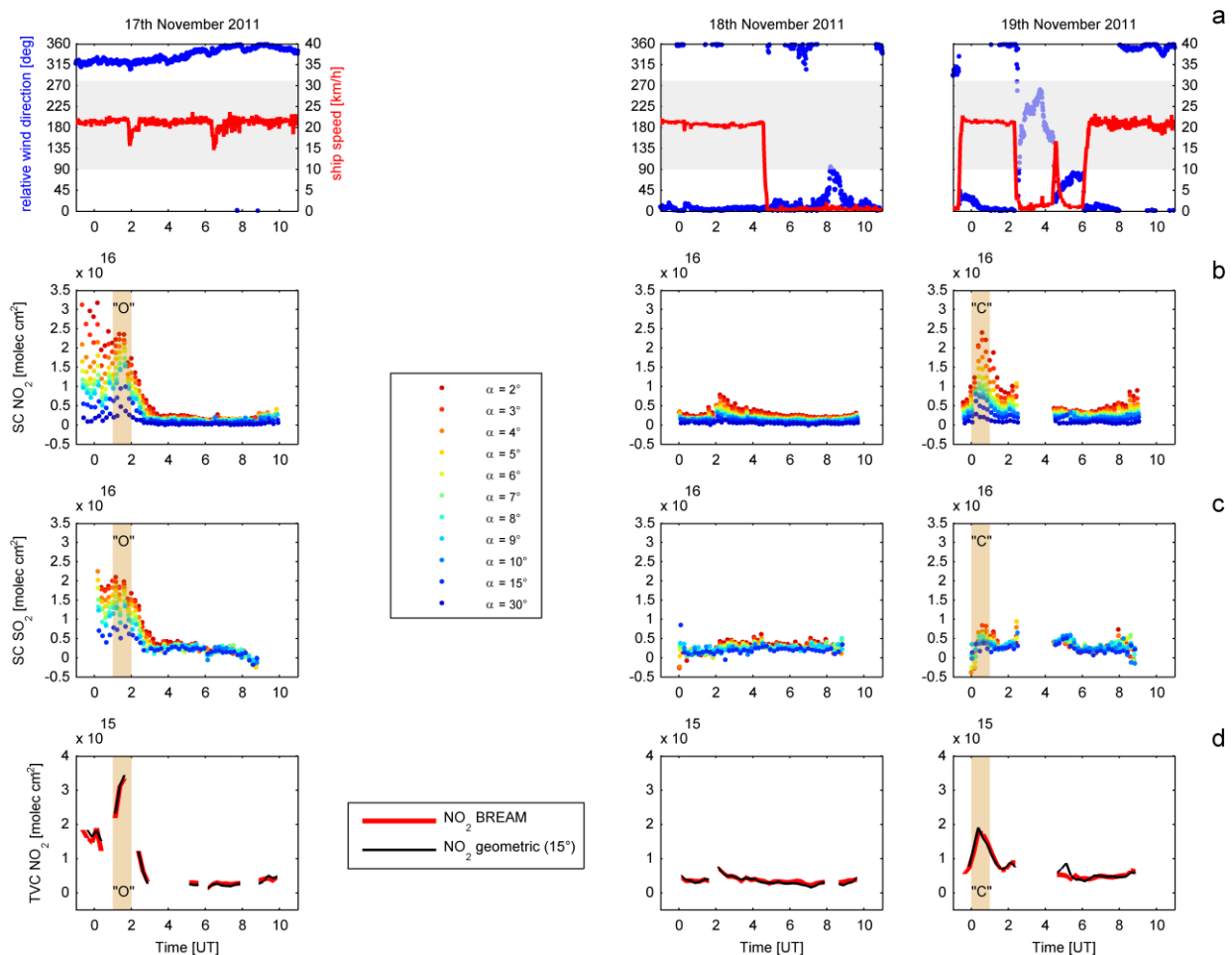
Fig. 6.5: Time series of ship's data and tropospheric NO_2 and SO_2 amounts for the days 17th, 18th, and 19th November 2011. Relative wind direction (blue dots) and ship speed (red line) as downloaded from the ship's database (a). The transparent gray area highlights the range of relative wind directions between 90° and 280°, which was used for data screening of the measured MAX-DOAS spectra. Tropospheric NO_2 (b) and SO_2 (c) SCDs as retrieved from the MAX-DOAS measurements at different elevation angles. NO_2 tropospheric vertical columns (TVC NO_2) as obtained from BREAM (red) and from the geometric approach using α = 15° (black) (d). The brown shaded areas in panels (b), (c), and (d) indicate the time of backward trajectory calculations (±30 minutes) as indicated in Fig. 6.1, where "O" and "C" denote the origin of air masses from the ocean and coast, respectively.

For most of the time when higher values of NO_2 SCDs are found, the ship was either in proximity to the coast or close to other vessels. Interestingly, the highest values exceeding 2 x 10^{16} molec cm^{-2} at α = 2° were observed in the morning hours of 19th, 20th, and 23rd November. This is in good agreement with Takashima et al. (2012), as

they have also highlighted a diurnal variation close to the coast with higher values in the morning.
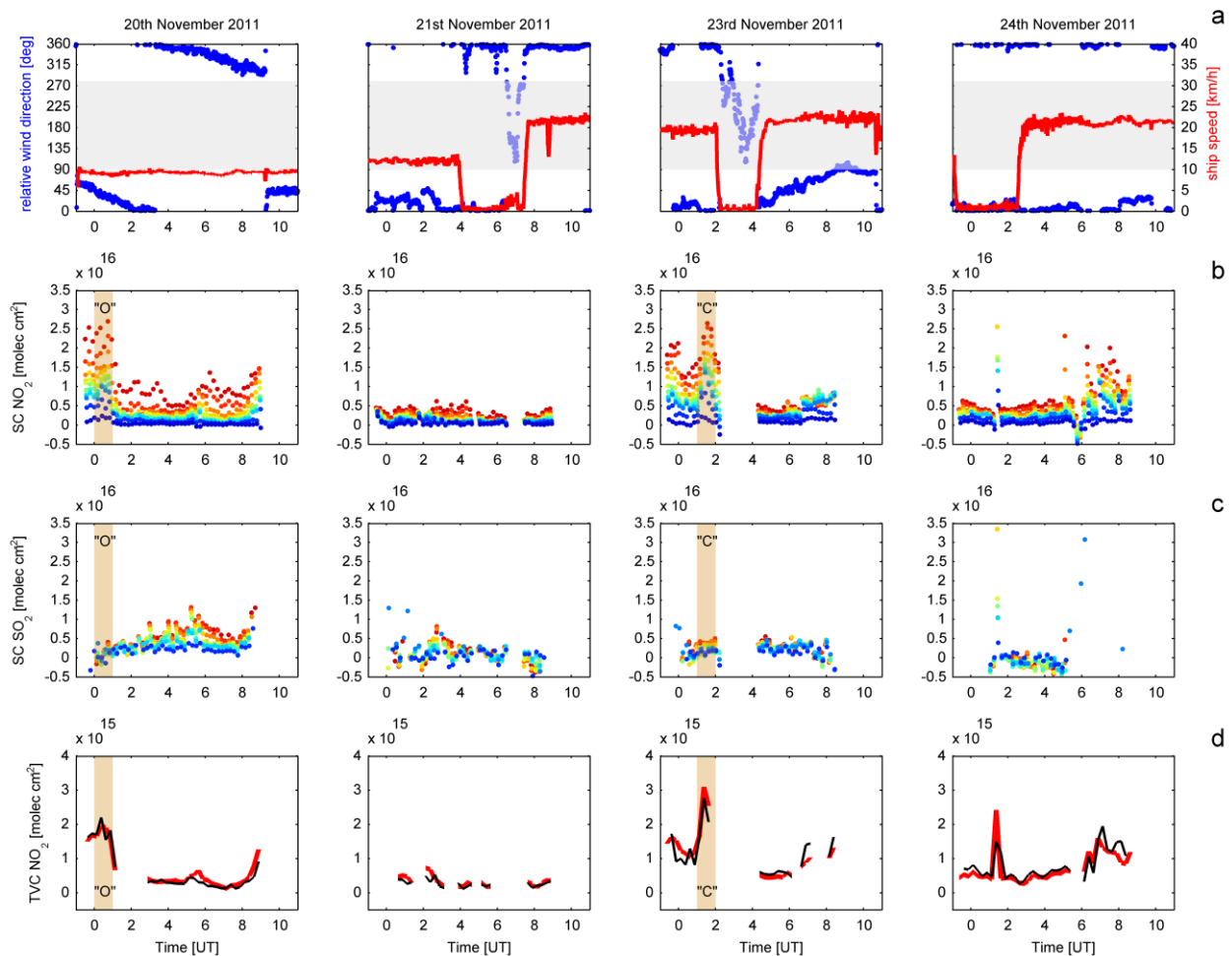
Fig. 6.6: Same as Fig. 6.5, but for the days 20th, 21st, 23rd, and 24th November 2011.

Whether these elevated levels of NO_2 are released by anthropogenic emission sources or produced by microbial activity of soils is difficult to judge. However, the sharp drop throughout the day leads to the assumption that the emission strength undergoes a daily cycle. On the other hand, photolysis of NO_2 with increasing solar UV radiation could also determine the sharp drop of NO_2 amounts. The fast photolysis of NO_2, which largely controls tropospheric O_3 formation, is important for the production of hydroxyl (OH) radicals (Crutzen and Lelieveld, 2001). These secondary products of ozone photolysis

could additionally influence the removal of tropospheric NO$_x$ and thus, explain the sharp decrease in the morning.
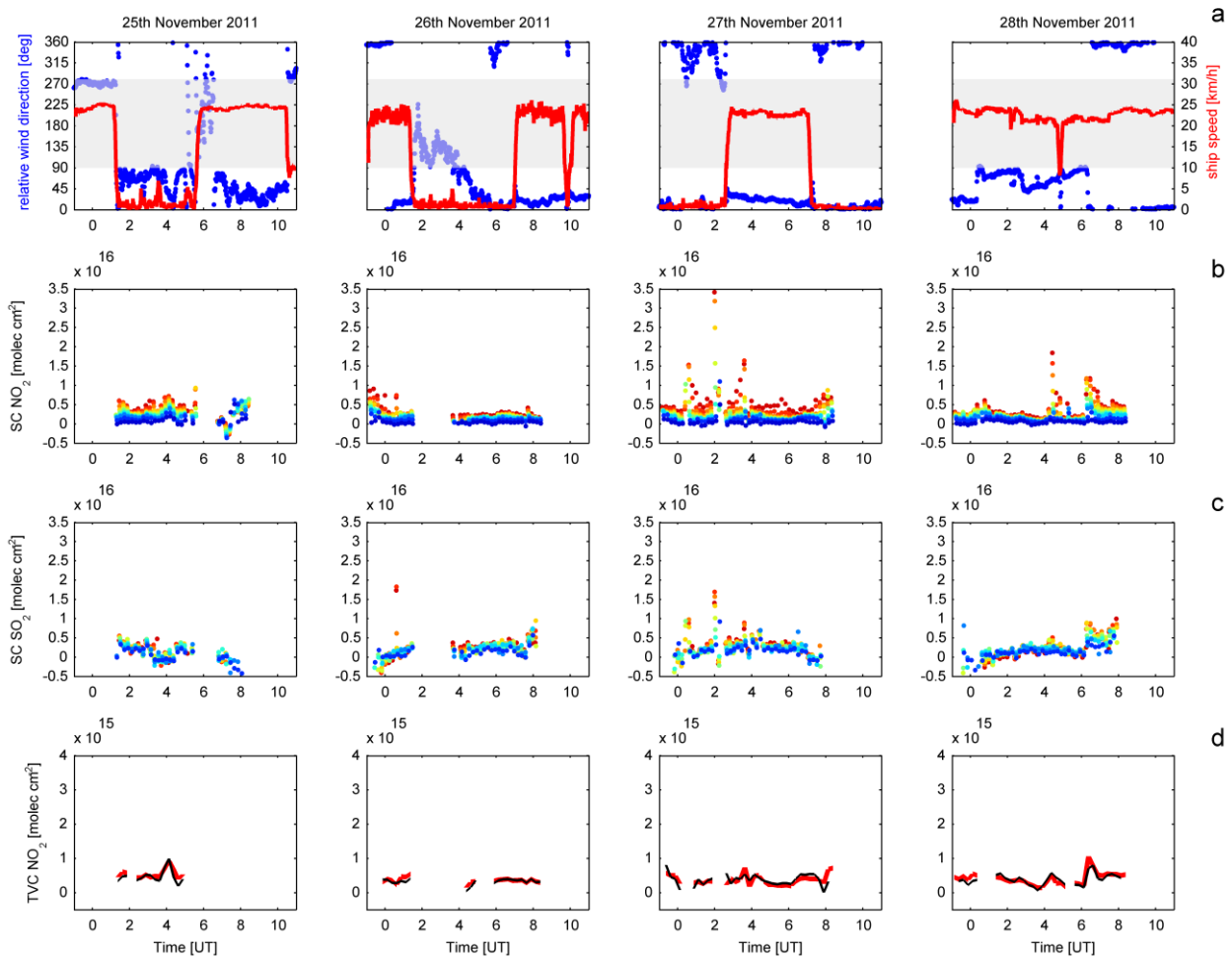
Fig. 6.7: Same as Fig. 6.5, but for the days 25th, 26th, 27th, and 28th November 2011.

It is noted that the negative SCDs which are occasionally observed, especially for larger elevation angles, could be attributed to unfavorable zenith measurements (influence of NO$_2$ from an elevated plume or from the ship's smoke stack), which are used for the retrieval of the differential SCDs. However, for the computation of vertical columns and profiles with BREAM, these measurements are not included.

The ship-based MAX-DOAS measurements indicate increased tropospheric amounts of NO$_2$ in the morning of 17th November, when the ship was leaving a busy shipping lane (see Fig. 6.5b). As no other sources than from international shipping can be expected in

this area, these elevated NO_2 levels can be clearly attributed to shipping emissions released by other vessels moving in the dense shipping lane. Moreover, air masses originating from the north brought air passing over the ship track into the instrument's field of view. When the RV Sonne left the shipping lane and moved towards the coast of Borneo, these increased NO_2 amounts disappeared and concentrations in the boundary layer reached low values.

6.5.2. Tropospheric SO$_2$ slant column densities *

In order to compare the daily cycle of NO_2 with another trace gas emitted from ship stacks, we have also retrieved SO_2 from the MAX-DOAS measurements. As NO_2 and SO_2 both have a relatively short lifetime in the tropical boundary layer of < 10 h (e.g. Beirle et al., 2011) and > 10 h (Lee et al., 2011), respectively, one would expect high temporal correlation between the two time series of NO_2 and SO_2 for 17th November 2011. Exemplary fit results of the SO_2 fit are shown in Fig. 6.8. The spectral measurement was taken on 17th November at 2° elevation angle and 53.33° solar zenith angle. In general, there is a good agreement between the reference (black line) and the fit (red line).
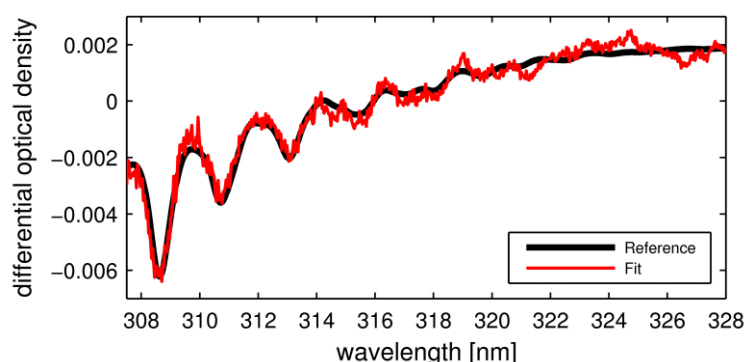
Fig. 6.8: Fit results of the SO_2 fit for a single measured spectrum taken in the morning of 17th November 2011 (01:20 UT) under elevated SO_2 pollution (SCD = 1.84 x 10^{16} molec cm^{-2}). The RMS of the residuals is 5 x 10^{-4}. Here, the optical density of the reference (black line) and fit (red line) are retrieved at 2° elevation angle and at 53.33° solar zenith angle. Further explanations and definitions are given in the text.

141

The agreement is best for the lower wavelengths where the differential optical depth is larger. However, differences are larger for cases with lower tropospheric SO_2 amounts (not shown).

For the case of SO_2, we found that RMS values for the best fits are 2×10^{-4} and thus, the best detection limit of 4×10^{15} molec cm^{-2} is two times as large as for NO_2, which might be related to both reduced light path length and sensitivity in the UV fitting window.

The time series of tropospheric SO_2 SCDs are shown in Figs. 6.5c-6.7c for all days when ship-based MAX-DOAS measurements were performed. In general, the values are rather low on most days as no larger sources are expected in this region. However, elevated values of SO_2 SCDs exceeding 2×10^{16} molec cm^{-2} at $\alpha = 2°$ are found in the morning of 17th November, when the ship was moving in proximity to the dense shipping lane. The values of SO_2 SCDs in the lowest elevation angles are slightly lower but in general consistent with NO_2 SCDs. This is in good agreement with the findings by Eyring et al. (2010) as they also report higher NO_2 than SO_2 from shipping emissions. DOAS measurements from an airborne platform in the Baltic Sea indicated slightly higher amounts of SO_2 than NO_2 from shipping emissions (Berg et al., 2012). However, these measurements were performed in the proximity to the individual ships and thus, reflected rather fresh smoke plumes having larger NO/NO_x ratio. Indeed, the NO_2/SO_2 ratio could also be influenced by differences in the sulfur content of the shipping fuels.

The sharp decrease of SO_2 on 17th November around 02:00 UT is also consistent with the decline in NO_2 and might be related to the separation of RV Sonne from the shipping lane (see Fig. 6.5b and c). In the afternoon and when the ship was moving towards the coast of Borneo, the SO_2 SCDs reached very low levels, which was also found for NO_2.

Shipping emissions from a single large vessel on 24th November are also visible from the SO_2 data. As shown in Fig. 6.6b for NO_2, there is an increased short-term signal of SO_2 at the same time and of similar magnitude. Such short-term signals are also found on 27th November, which might be released from other vessel moving in proximity to the RV Sonne. However, we could not identify larger ships from the video camera's records on that day and thus, these elevated values could also originate from the own ship's

plume in spite of the wind direction filtering applied to the data. Another explanation for these elevated values could be the transport of SO_2 from ships that were out of sight.

On 20th November, elevated SO_2 values in the afternoon could originate from flaring at offshore oil production sites that are found in this region (e.g. Nara et al., 2014). As discussed above, NO_2 observations have also indicated elevated values on that day. However, the increased NO_2 levels, which unlike SO_2 are also found in the morning, are higher in magnitude than SO_2 amounts. On 19th and 23rd November, elevated NO_2 amounts in the morning could have originated from the nearby cities of Kuching and Kota Kinabalu, respectively. This speculation is supported by slightly elevated SO_2 values. For example, high NO_2 together with low SO_2 could arise from traffic rather than from soil microbial activity.
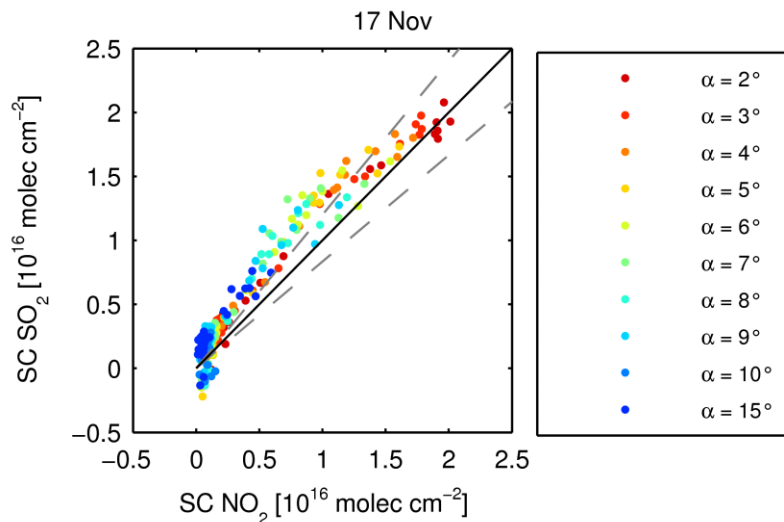
Fig. 6.9: Color-coded scatter plot of tropospheric SO_2 SCDs vs. NO_2 SCDs on 17th November.

In Fig. 6.9, a color-coded scatter plot of SO_2 SCDs vs. NO_2 SCDs for the different elevation angles is shown for all measurements taken on 17th November, when the RV Sonne left the busy shipping lane in the South China Sea. For a better comparison, we have used the 30° measurements as FRS also for NO_2. The solid black line is the 1:1 line and the dashed gray lines indicate the ±20% bounds. As already discussed above, the higher values at lower elevation angles are linked to shipping emissions. Berg et al.

(2012) found that SO_2 amounts are higher than NO_2 amounts in fresh plumes released from vessels in the Baltic Sea. The fact that increased NO_2 and SO_2 amounts observed in our study are in good agreement could be related to transport of polluted air masses from the North and the consequent increasing formation of NO_2 within the plume. However, we also observed cases where SO_2 SCDs were higher than NO_2 SCDs, which could be linked to rather fresh shipping emissions from vessels moving in proximity to RV Sonne. The scatter between NO_2 and SO_2 is larger for smaller trace gas amounts, which is linked to the fact that concentrations are below the estimated detection limits of 2 and 4×10^{15} molec cm^{-2}, respectively.

6.5.3. Tropospheric NO_2 vertical columns *

In order to make the two approaches (geometric approach vs. BREAM, see Sect. 6.3.1.5) comparable, the TVC NO_2 values obtained from the geometric approach have been interpolated to the selected BREAM time interval (15 min).

The tropospheric NO_2 vertical columns as obtained from the geometrical approximation using the 15° (blue), 10° (green), 5° (red), and 2° (cyan) measurements are compared with TVC NO_2 as computed with BREAM for all days (Fig. 6.10, bottom). There is a clear indication that both 15° and 10° measurements can be applied for the geometric approach when TVC NO_2 exceeds 1.5×10^{15} molec cm^{-2}. For cases when the NO_2 amounts are rather low ($< 1 \times 10^{15}$ molec cm^{-2}), the agreement between the geometric approach and BREAM is less strong and differences can be larger than ±20%. The decreasing match towards cases with lower NO_2 concentrations might be an artifact of the lower fit quality (see Fig. 6.3), which impacts less on BREAM which is using information from all viewing angles. We found that TVC NO_2 is underestimated when the 5° (red) and 2° (cyan) measurements are used for the geometric approach. This can be explained by the fact that the tropospheric light path is shorter than assumed in the geometric approximation when the last scattering point is located within the NO_2 layer.

---

* This subsection has been previously published as part of Schreier et al. (2014c).
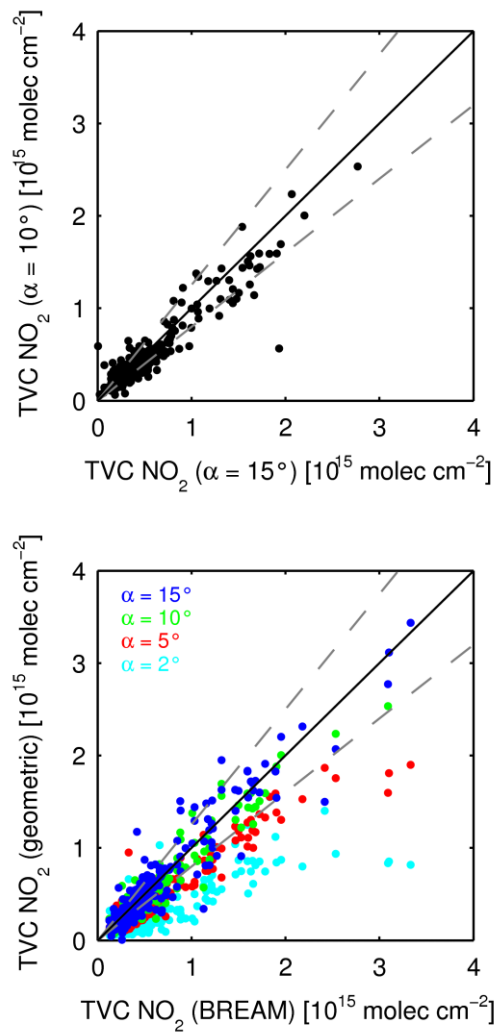
Fig. 6.10: Scatter plots of TVC NO_2 as obtained from the geometric approach using α = 10° against α = 15° (upper) and TVC NO_2 retrieved by the geometric approach against TVC NO_2 computed by BREAM, where α = 2°, α = 5°, α = 10°, and α = 15° are shown in cyan, red, green, and blue, respectively (lower). The solid black line is the 1:1 line and the dashed gray lines denote the ±20% difference.

In the upper panel of Fig. 6.10, the comparison between the geometric approach using the 15° and 10° measurements is shown. Clearly, TVC NO_2 as computed from both elevation angles are in good agreement, suggesting that in these viewing directions, the last scattering point is generally above the NO_2 layer. Recent land-based MAX-DOAS campaigns have shown that 30° elevation angles are the most appropriate measurements for the geometric approach (Brinksma et al., 2008; Halla et al., 2011).

However, due to the lower boundary layer height over the sea and thus, less vertical extent of NO_2, both 15° and 10° measurements seem to work well for the conversion of SCDs into TVC NO_2 in our data. Results from the radiosonde measurements performed during the SHIVA ship cruise indicate that the marine boundary layer height was lower than 500 m during daytime (Fuhlbrügge et al., 2014). There is a clear preference in using these measurements as the sensitivity for tropospheric NO_2 is much larger compared to 30° as a result of the longer light path through the boundary layer.

The time series of TVC NO_2 as obtained from the geometric approach using the 15° (red) measurements and from BREAM calculations are shown in Figs. 6.5d-6.7d. There is overall good agreement between the two time series found for most of the days. For the TVC NO_2 values from BREAM, there are some data gaps, which result from the selected time interval (15 min), threshold value for the correlation between measured and simulated O_4 slant columns (r > 0.6), and a minimum value for the number of elevation angles (10) within one time interval. We note that these data gaps indicate unfavorable conditions (e.g. clouds or pollution from the smoke stack in the field of view) and the TVC NO_2 obtained from the geometric approach yield unexpected high and negative values for some of these cases.

On 17th, 19th, 20th, and 23rd November, TVC NO_2 amounts of up to 3.5 x 10^{15} molec cm^{-2} were observed in the morning hours by both approaches (geometric vs. BREAM). During the previous TransBrom campaign (Peters et al., 2012), the highest values of TVC NO_2 (up to 2 x 10^{15} molec cm^{-2}) were also observed close to the coast and are in good agreement with the values observed during SHIVA. In order to investigate the origin of these elevated levels, backward trajectories were calculated for the time of peak values. The backward trajectories for these cases are shown in Fig. 6.1 and indicate the origin of air masses.

For instance, air masses coming from the north crossed the track of RV Sonne in the morning of 17th November. These air masses moved through the dense shipping lane connecting Singapore and coastal cities of eastern China, which bring elevated NO_2 levels from shipping emissions to the proximity of RV Sonne.

Significant NO_2 signals from international shipping have recently been identified by the evaluation of SCIAMACHY and GOME-2 satellite measurements (Beirle et al., 2004b; Richter et al., 2004, 2011). Among other shipping lanes, the dense one in the South China Sea can be clearly seen from the long-term mean tropospheric NO_2 fields. De Ruyter De Wild et al. (2012) retrieved NO_2 column densities from the GOME, SCIAMACHY, OMI, and GOME-2 instruments to analyze trends over international shipping lanes. They found increasing trends of NO_2 between 2003 and 2008 over the major shipping lanes with annual running means of TVC NO_2 reaching up to 0.7×10^{15} molec cm^{-2} in the South China Sea. The trend reversed in 2008 as a consequence of the economic crisis and the linked decreased trade volume. In comparison to our MAX-DOAS results, the lower values obtained from satellite instruments are probably related to the averaging over large pixels.

Backward trajectories on the 19th and 23rd November reveal that air masses originated from the coast of Borneo. In the case of 19th November, the emissions of NO_x could be related to anthropogenic emissions from Kuching, which is the largest city on Borneo Island. The same is true for 23rd November, when air masses again originated from the coast and the city Kota Kinabalu.

The diurnal variation in TVC NO_2 shows a decrease during daytime. In addition to the enhanced photolysis of NO_2 with increasing solar UV radiation and faster removal of NO_x due to the reaction with OH, this could also be a consequence of the increased stomata uptake of NO_2 by plants throughout the day. Ganguly et al. (2009) suggested an increased NO_x uptake with increasing solar radiation in a tropical mangrove forest. During the night, the leaf stomata close and reduce NO_x uptake. Hence, the enhanced levels in observed TVC NO_2 in the morning hours could emerge due to the inactive nighttime stomata. The removal of NO_2 within the first few hours after sunrise could thus at least in part be attributed to the stomatal activity of plants during day.

The diurnal cycle in TVC NO_2 can also be seen from satellite observations. Five-year averages (2007-2011) of TVC NO_2 retrieved from the GOME-2 (9:30 LT) and OMI (13:30 LT) instruments for November 2011 are shown in Fig. 6.11. The difference GOME-2 minus OMI TVC NO_2 underlines the fact that higher values are observed in the

morning hours close to the coast, whereas no significant pattern is observed for the remote regions of the South China and Sulu Sea. In regions where the MAX-DOAS instrument on board RV Sonne observed the distinct daily NO_2 cycle, the differences between the two satellite data are larger than 0.5 x 10^{15} molec cm^{-2}.
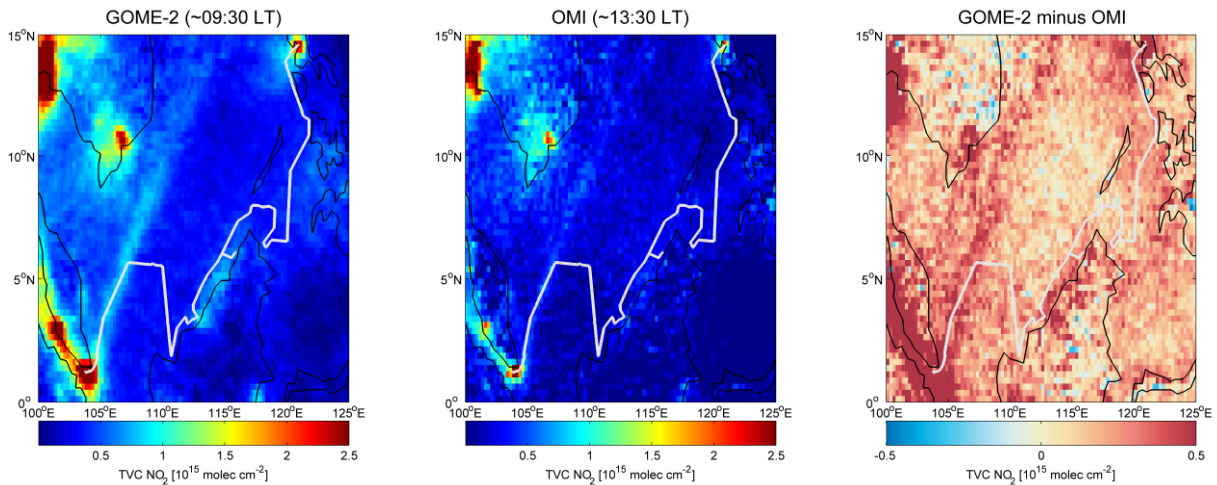
Fig. 6.11: Monthly gridded (0.5° x 0.5°) means of TVC NO_2 as retrieved from GOME-2 (left) and OMI (middle) for November (2007-2011). The right panel displays the differences between TVC NO_2 from GOME-2 minus TVC NO_2 from OMI.

Differences in satellite-derived tropospheric NO_2 over shipping lanes between morning and afternoon have previously been discussed in Franke et al. (2009). They also found higher NO_2 amounts in the morning observed from SCIAMACHY and relate these to the diurnal cycle of NO_2, which is consistent with model simulations.

It is noted that the differences observed in the proximity of the coast are representative for this time of the season, where no significant sources of NO_x other than anthropogenic and soil are found close to the ground. However, higher values of TVC NO_2 in the afternoon are expected during the biomass burning season.

In addition to the elevated TVC NO_2 originating from the coast, the MAX-DOAS measurements include some observations of sharp peaks in the open sea. The most striking temporary increase in TVC NO_2 far away from any coast was observed in the

148

morning of 24th November (see Fig. 6.6d). The video camera recordings revealed that this was a large vessel in the proximity to RV Sonne (not shown).
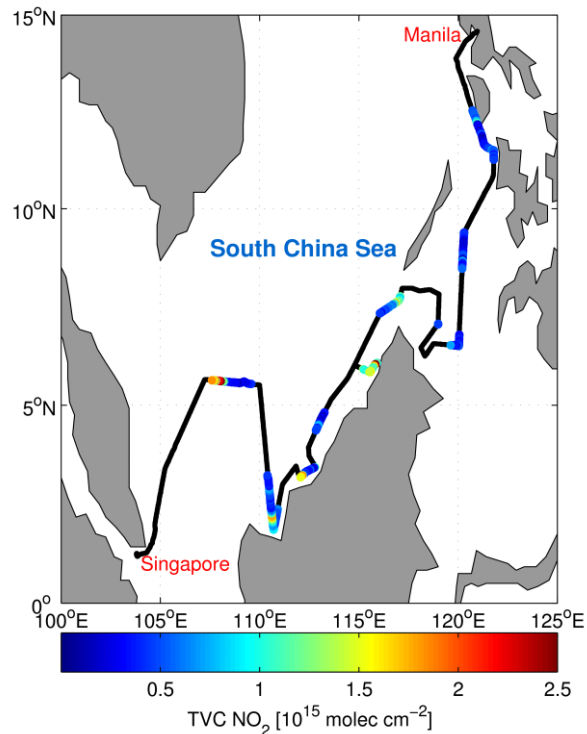
Fig. 6.12: Geographical map of color-coded TVC NO$_2$ as obtained from BREAM.

In Fig. 6.12, color-coded TVC NO$_2$ values as computed with BREAM are plotted along the ship track. Clearly, the lowest (highest) values are found in the open (coastal) waters of the South China and Sulu Sea. Increased NO$_2$ amounts in the open sea are the result of shipping emissions from other vessels observed by the MAX-DOAS instrument.

6.5.4. Tropospheric NO$_2$ profiles *

The tropospheric NO$_2$ columns do not provide information about the vertical distribution of NO$_2$ and thus, a further step towards achieving this information is the retrieval of NO$_2$ profiles with BREAM (see Sect. 6.3.1.5). As the boundary layer height is well below 4 km in the tropics (e.g. Luo et al., 2014), the profile retrieval is expected to reflect all tropospheric NO$_2$ produced from soil microbial activity and anthropogenic combustion

149

processes. However, NO$_x$ from lightning might not be included in the obtained vertical profiles, as we expect NO$_x$ from lightning to be emitted into higher altitudes where the sensitivity of the MAX-DOAS observations is small.
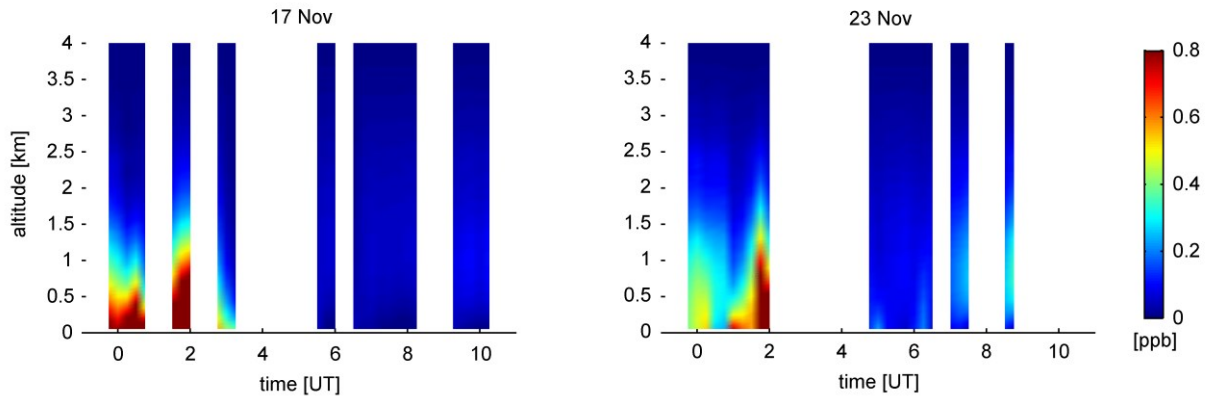
Fig. 6.13: Exemplary vertical profiles of NO$_2$ mixing ratios for 17th and 23rd November as obtained from BREAM.

The retrieved profiles are shown in Fig. 6.13 for two exemplary days (17th and 23rd November). The gaps between the single profiles are the result of the limitations as already outlined in Sect. 6.4.3. Wittrock (2006) has shown that the errors of the volume mixing ratios in the lowermost 500 m are within 25%. The highest observed NO$_2$ mixing ratios exceeding 1 ppbv are found close to the surface when the RV Sonne was moving in a dense shipping lane (17th November) or along the coast (23rd November). These elevated NO$_2$ mixing ratios are in good agreement with the highest values (~0.8 ppbv) reported by Peters et al. (2012).

The lowest NO$_2$ mixing ratios close to the ground are < 30-50 pptv and can be as high as 100 pptv, as observed on 18th November, for instance (not shown). This is in good agreement with the former ship-based studies by Peters et al. (2012) and Takashima et al. (2012), suggesting boundary layer background mixing ratios of < 50 and up to 200 pptv, respectively. The explanation of the lower background values found in our study could be related to the improvements achieved using the adapted fit, which increases the signal-to-noise ratio.

6.6. Summary and conclusions *

Ship-based Multi-Axis Differential Optical Absorption Spectroscopy (MAX-DOAS) measurements performed in the South China and Sulu Sea in November 2011 have been used to retrieve tropospheric NO_2 vertical columns (TVC NO_2) and slant column densities (SCDs) of SO_2.

For NO_2, the cross-sections and the 425-490 nm fitting window as suggested in Roscoe et al. (2012) were used, but the NO_2 fit was adapted by including a cross-section for liquid water and an empirical correction spectrum as discussed in Peters et al. (2014). As a result, the fit quality slightly improved, especially for the lowest elevation angles and when NO_2 amounts are rather low.

The time series of tropospheric NO_2 SCDs, which have been obtained by using a zenith measurement close in time as Fraunhofer reference spectrum (FRS), indicate that the highest levels of NO_2 are found at the lowest elevation angles. The conversion of SCDs into the more commonly used TVC NO_2 is based on two different approaches.

The simple geometric approach was tested for different elevation angles and compared with TVC NO_2 as computed from the vertical profiles inverted with BREAM. The comparison between TVC NO_2 as obtained from 10° to 15° measurements for SZA < 75° showed that both can be used to retrieve TVC NO_2 from MAX-DOAS measurements in the tropical marine environment with values comparable to what is derived by a full inversion. Geometric values from even lower elevations underestimate the true columns as the last scattering point moves into the layer of enhanced NO_2.

Although the NO_2 amounts in the marine environment of Southeast Asia are rather low when compared to larger cities or intensive biomass burning regions, the MAX-DOAS measurements on board the RV Sonne yielded some interesting insights in the spatio-temporal patterns of tropospheric NO_2. Very low values were expected, but increased NO_2 amounts could occasionally be identified, mostly resulting from fuel combustion and possibly also from soil microbial activity – but to a lesser proportion than from anthropogenic activities. These peaks, which predominantly occurred in the morning

---

* This subsection has been previously published as part of Schreier et al. (2014c).   151

hours, disappeared quite soon after – most probably due to fast photolysis of NO_2 with increasing solar UV radiation.

The results show that the boundary layer values of NO_2 are well below 100 pptv and < 30 pptv in the open waters of the South China and Sulu Sea. However, mixing ratios exceeded 0.8 ppbv when the RV Sonne was heading along the coast or in proximity to other vessels.

In addition to NO_2, SO_2 SCDs were retrieved in a fitting window between 307.5 and 328 nm. Increased tropospheric SO_2 SCDs are found for the lowest layers when the RV Sonne was in proximity to a dense shipping lane and thus, these values are attributed to both fresh and aged plumes released from larger vessels. The values are in general agreement with NO_2 SCDs, indicating comparable magnitudes of shipping NO_x and SO_2.

From these measurements it is clear, that ship traffic has a large impact on pollutant levels in the South China Sea, at least in the vicinity of the busy shipping lanes.

Chapter 7

Summary and conclusions

The main focus of this thesis was the analysis and interpretation of tropospheric NO_2 from biomass burning and other sources. The first and larger part dealt with the characterization of NO_x emissions from open biomass burning in tropical, subtropical, and boreal regions using satellite measurements of tropospheric NO_2. In the second part of the present thesis, tropospheric NO_2 and SO_2 amounts as retrieved from ship-based MAX-DOAS measurements conducted in a tropical marine environment were analyzed.

Satellite-derived fire emission rates of NO_x for tropical and subtropical biomes

The existing long-term data sets of satellite measurements from the GOME-2 (on board MetOp-A satellite) and OMI (on board Aura satellite) instruments have been used to retrieve tropospheric NO_2 vertical columns. While the two space-based spectrometers generally possess similar characteristics, their main difference lies in the local overpass time. Hence, both instruments, which share a common long-term period of measurements starting in 2007, provide insights into tropospheric NO_2 amounts in the morning and early afternoon. The acquisition of fire radiative power from the two MODIS instruments (on board Terra and Aqua satellites), covering the same time period, was a next step towards the characterization of biomass burning NO_x.

As the overpass times of the GOME-2 (09:30 LT) and OMI (13:30 LT) instruments match with the MODIS overpass times (10:30 and 13:30 LT) to a high degree, correlation analyses on a 1° x 1° grid could be performed for the entire globe and a multi-year period (2007-2011). The results show that the seasonal pattern of tropospheric NO_2 is largely driven by the intensity of fires in large areas, in particular in tropical and subtropical regions.

FERs of NO$_x$ (in g NO$_x$ s^{-1} MW^{-1}) for GOME-2 (left) / OMI (right)	ANE	ASE	CSA	NAU	SEA
evergreen broadleaf forest	0.94 / 0.77	- / -	0.55 / 0.43	- / -	0.76 / 0.60
open shrublands	- / -	- / -	- / -	0.33 / 0.34	- / -
woody savannas	0.84 / 1.41	0.88 / 1.54	- / -	- / -	0.82 / 1.18
savannas	0.62 / 1.03	0.48 / 0.84	0.53 / 0.49	0.35 / 0.28	- / -
croplands	0.87 / 1.19	- / -	- / -	- / -	1.56 / 1.22

The empirical relationship between the two parameters was further used to separate biomass burning from other NO$_x$ sources by subtracting the background from the total tropospheric NO$_2$ column. Under certain assumptions, the number density of NO$_2$ produced from fire could be converted into mass concentrations of NO$_x$ – a more frequently used term for estimating fire emissions. By separating monthly gridded means of both fire radiative power and calculated production rates of NO$_x$ from fire according to land cover type, fire emission rates of NO$_x$ (in g NO$_x$ s^{-1} MW^{-1}) as derived from the best fitting least-squares regression lines could be derived – for various tropical and subtropical biomes and regions (see Table). The results indicate differences in fire emission rates of NO$_x$ between the selected biomes and regions, which call into question the application of constant emission factors for large biomes in recent fire emission inventories.

Satellite-derived emission factors of NO$_x$ for boreal forests

While the temporal variability of tropospheric NO$_2$ and fire radiative power was in good agreement in tropical and subtropical biomass burning regions, the relationship was weaker over boreal forest fires.

In order to also provide fire emission rates of NO$_x$ for boreal forests, which cover large parts of the world, the retrieval of tropospheric NO$_2$ from GOME-2 and the subsequent conversion into production rates of NO$_x$ from fire was modified. More specifically, the stratospheric correction was based on stratospheric NO$_2$ from B3dCTM model simulations, which substantially reduced the number of unphysical negative tropospheric NO$_2$ values and improved the correlation between tropospheric NO$_2$ and FRP. The

conversion of NO_2 number densities was improved by using reanalysis data of the tropospheric NO_2/NO_x ratio from MACC.
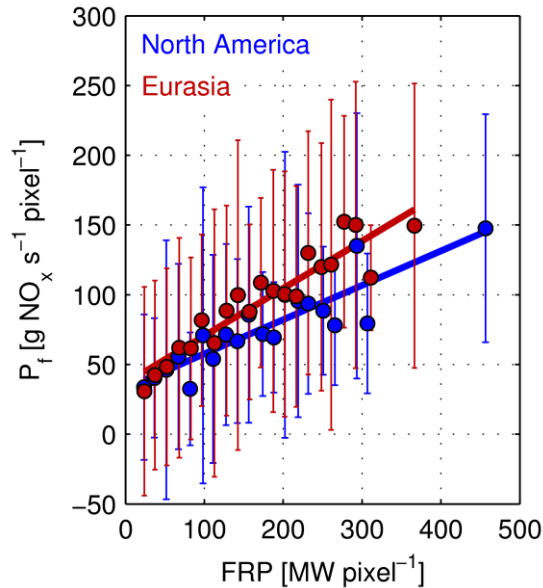
The results indicate small – but statistically significant – differences in fire emission rates of NO_x between the two selected boreal regions (see Figure). For a better comparison of values estimated by the new developed approach with values found in the literature, fire emission rates of NO_x were converted into emission factors of NO_x. The satellite-derived emission factors are in good agreement with values reported in a recent emission factor compilation. However, recent fire emission inventories have applied emission factors of NO_x for boreal forest that are 3-5 times larger than the values presented in this thesis.

Emission factors of NO_x for the major types of open biomass burning

The computation of NO_x emission factors for boreal forests using satellite measurements of tropospheric NO_2 was promising, as the comparison with literature values has shown.

Further analysis was motivated by this finding and aimed at expanding the provision of satellite-derived emission factors of NO_x for other major types of biomass burning including tropical forest, savanna and grassland, and crop residue.

The results show that arithmetic means of satellite-based emission factors for tropical forest and crop residues fall within one standard deviation of means reported by emission factor compilations (see Figure). However, the emission factors for savanna and grassland presented in this thesis are lower by a factor of 2.5 when compared to the literature. As savanna and grassland is the most frequently burned land cover type on Earth, however, these findings could have possible implications for future fire emission inventories.

Two-parameter approach towards estimating fire NO_x for the African continent

As recent satellite-based studies have indicated spatial and seasonal changes in NO_x emission factors within various regions, another study was conducted for evaluating the uncertainties that could arise when such spatio-temporal differences are not being considered.

The study was focused on the estimation of annual NO_x emissions from open biomass burning for the African continent by combining several satellite products. Besides the use of tropospheric NO_2 from OMI and fire radiative power from MODIS (on board Aqua) for the estimation of seasonally averaged and monthly resolved fire emission rates of NO_x, fire radiative energy from the geostationary SEVIRI sensor has been calculated on a monthly basis at a 0.5° x 0.5° resolution. The estimation, which was based on seasonally averaged and monthly resolved fire emission rates of NO_x, was performed for the different biomes and subsequently aggregated to yield a total amount of biomass

burning NO_x for the African continent and the year 2010. It is apparent from this analysis that the differences in total NO_x as estimated from the two approaches (seasonally averaged vs. monthly resolved fire emission rates) can be as large as 90% on a monthly basis. Taken together, these results suggest that future fire emission inventories should introduce improved emission factors in terms of spatial and seasonal variability.

Ship-based MAX-DOAS measurements of NO_2 and SO_2

In November 2011, ship-based MAX-DOAS measurements were performed in a tropical marine environment within the SHIVA ship campaign. The ship track included interesting sources of NO_2 and SO_2 from international shipping, agglomerations, and soil.
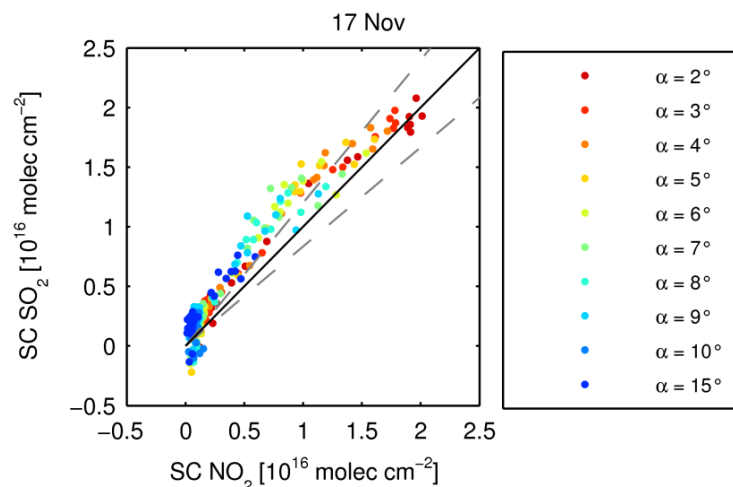
The study as presented in the second part of this thesis dealt with the retrieval of these measurements and the interpretation of tropospheric NO_2 and SO_2 amounts. The retrieval of tropospheric NO_2 and SO_2 was based on improved and novel DOAS fits, respectively. The results opened up new insights into polluted shipping lanes in the South China Sea and pollution levels close to the coast of Borneo. Interestingly, the time series and amounts of NO_2 and SO_2 were found to be in good agreement on the day, when the research vessel left a dense shipping lane (see Figure).

Chapter 8

Outlook

Further research in this field would be of great help in improving satellite-derived fire emission rates and emission factors of NO_x.

- First, improvements of the NO_2 retrieval over biomass burning regions in terms of vertically resolved aerosol a priori information for the entire globe would be necessary. To the author's knowledge, such global gridded data about aerosols is not available yet from measurements.

- Another essential aspect is the NO_x lifetime, which has so far been assumed as constant for the different biomes and regions. Although the values applied in the presented thesis are supported by the literature, slight spatial and temporal changes are expected.

- In terms of the two-parameter approach for estimating NO_x from open biomass burning as presented in this thesis, an improved and validated satellite product of fire radiative energy for the entire globe would significantly reduce existing uncertainties in this relatively new parameter and support the development of such a new estimation approach.

Future satellite missions are in progress. For example, the launch of the TROPOspheric Monitoring Instrument (TROPOMI) on board the Sentinel-5 Precursor satellite will open up new research activities in the field. The imaging spectrometer covering the ultraviolet, visible, near-infrared, and shortwave infrared spectral regions, will have an improved spatial resolution (7×7 km^2). The launch is planned in early 2016 and the projected mission lifetime is 7 years (Veefkind et al., 2012).

- In order to validate such new satellite products, ground-based measurements of tropospheric trace gas amounts (e.g. MAX-DOAS measurements) are needed in the future, in particular at places where tropospheric trace gas amounts are of special interest – in larger agglomerations or in biomass burning regions.

Bibliography

Acarreta, J. R., De Haan, J. F., and Stammes, P.: Cloud pressure retrieval using the O2-O2 absorption band at 477 nm, J. Geophys.Res.-Atmos., 109, D05204, doi:10.1029/2003JD003915, 2004.

Achard, F., Eva, H. D., Stibig, H. J., Mayaux, P., Gallego, J., Richards, T., and Malingreau, J. P.: Determination of deforestation rates of the world's humid tropical forests, Science, 297, 999-1002, 2002.

Akagi, S. K., Yokelson, R. J., Wiedinmyer, C., Alvarado, M. J., Reid, J. S., Karl, T., Crounse, J. D., and Wennberg, P. O.: Emission factors for open and domestic biomass burning for use in atmospheric models, Atmos. Chem. Phys., 11, 4039–4072, doi:10.5194/acp-11-4039-2011, 2011.

Alvarado, M. J. and Prinn, R. G.: Formation of ozone and growth of aerosols in young smoke plumes from biomass burning: 1. Lagrangian parcel studies, J. Geophys. Res.-Atmos., 114, D09306, doi:10.1029/2008JD011144, 2009.

Aminou, D. M. A.: MSG's SEVIRI Instrument, ESA Bull., 111, 15–17, 2002.

Andreae, M. O. and Merlet, P.: Emission of trace gases and aerosols from biomass burning, Global Biogeochem. Cy., 15, 955–966, 2001.

Archibald, S., Staver, C., and Levin, S. A.: Evolution of human-driven fire regimes in Africa, P. Natl. Acad. Sci. USA, 109, 847–852. 2012.

Arino, O., Rosaz, J. M., and Goloub, P.: The ATSR World Fire Atlas. A synergy with 'Polder' aerosol products, Earth Observation Quarterly, 1-6, 1999.

Arino, O. and Plummer, S.: The Along Track Scanning Radiometer World Fire Altas – Detection of night-time fire activity, IGBP-DIS Working Paper #23, Potsdam, Germany, 2001.

Atkinson, R.: Atmospheric chemistry of VOCs and NO(x), Atmospheric Environment, 34, 2063-2101, 2000.

Bakhnov, V. R.: General scheme of evolution of swampy soils and swamps of taiga belt. In Weat Siberian Peatlands and Carbon Cycle: Past and Present, edited by Vasiliev, S. V., Titlyanova, A. A., Velichko, A. A., Novosibirsk, Institute of Soil Science and Agrochemistry, Siberian Branch of RAS, p. 10-11, 2001.

Bar-Yosef, O.: The Upper Paleolithic revolution, Annual Review of Anthropology, 31, 363-393, 2002.

Barkley, M. P., Palmer, P. I., Ganzeveld, L., Arneth, A., Hagberg, D., Karl, T., Guenther, A., Paulot, F., Wennberg, P. O., Mao, J., Kurosu, T. P., Chance, K., Müller, J. F., De Smedt, I., Van Roozendael, M., Chen, D.,Wang, Y., and Yantosca, R. M.: Can a "state of the art" chemistry transport model simulate Amazonian tropospheric chemistry?, J. Geophys. Res.-Atmos., 116, D16302, doi:10.1029/2011JD015893, 2011.

Bazilevich, N. I., Rodin, L. E., eds.: Biological productivity and mineral cycling in the terrestrial plant communities. Nuka Publ., Leningrad, 313 pp., 1971. [in Russian]

Beirle, S., Platt, U.,Wenig, M., and Wagner, T.: NOx production by lightning estimated with GOME, Adv. Space Res., 34, 793–797, 2004a.

Beirle, S., Platt, U., von Glasow, R., Wenig, M., and Wagner, T.: Estimate of nitrogen oxide emissions from shipping by satellite remote sensing, Geophys. Res. Lett., 31, L18102, doi:10.1029/2004GL020312, 2004b.

Beirle, S., Boersma, K. F., Platt, U., Lawrence, M. G., and Wagner, T.: Megacity emissions and lifetimes of nitrogen oxides probed from space, Science, 333, 1737–1739, 2011.

Bell, T. and Adams, M.: Chapter 14 Smoke from Wildfires and Prescribed Burning in Australia: Effects on Human Health and Ecosystems, Developments in Environmental Science, 8, 289–316, 2008.

Berg, N., Mellqvist, J., Jalkanen, J.-P., and Balzani, J.: Ship emissions of SO2 and NO2: DOAS measurements from airborne platforms, Atmos. Meas. Tech., 5, 1085-1098, doi:10.5194/amt-5-1085-2012, 2012.

Berglen, T. F., Bernsten, T. K., Isaksen, I. S. A., and Sundet, J. K.: A global model of the coupled sulfur/oxidant chemistry in the troposphere: the sulfur cycle, J. Geophys. Res. 109, D19310, 2004.

Boersma, K. F., Eskes, H. J., and Brinksma, E. J.: Error analysis for tropospheric NO2 retrieval from space, J. Geophys. Res.-Atmos., 109, D04311, doi:10.1029/2003JD003962, 2004.

Boersma, K. F., Jacob, D. J., Eskes, H. J., Pinder, R. W., Wang, J., and van der A, R. J.: Intercomparison of SCIAMACHY and OMI tropospheric NO2 columns: observing the diurnal evolution of chemistry and emissions from space, J. Geophys. Res.-Atmos., 113, D16S26, doi:10.1029/2007JD008816, 2008.

Bogumil, K., Orphal, J., Homann, T., Voigt, S., Spietz, P., Fleischmann, O. C., Vogel, A., Hartmann, M., Kromminga, H., Bovensmann, H., Frerick, J., and Burrows, J. P.: Measurements of molecular absorption spectra with the SCIAMACHY preflight model: instrument characterization and reference data for atmospheric remote-sensing in the 230–2380 nm region, J. Photochem. Photobiol. A, 157, 167–184, 2003.

Bond, W. J. and Keeley, J. E.: Fire as a global 'herbivore': the ecology and evolution of flammable ecosystems, Trends Ecol. Evol., 20, 387–394, 2005.

Bousserez, N.: Space-based retrieval of NO2 over biomass burning regions: quantifying and reducing uncertainties, Atmos. Meas. Tech. Discuss., 6, 6645–6684, doi:10.5194/amtd-6-6645-2013, 2013.

Bovensmann, H., Burrows, J. P., Buchwitz, M., Frerick, J., Noël, S., Rozanov, V. V., Chance, K. V., and Goede, A. P. H.: SCIAMACHY: Mission objectives and measurement modes, J. Atmos. Sci., 56, 127–150, 1999.

Bowman, D. M. J. S., Balch, J. K., Artaxo, P., Bond, W. J., Carlson, J. M., Cochrane, M. A., D'Antonio, C. M., DeFries, R. S., Doyle, J. C., Harrison, S. P., Johnston, F. H., Keeley, J. E., Krawchuk, M. A., Kull, C. A., Marston, J. B., Moritz, M. A., Prentice, I. C., Roos, C. I., Scott, A. C., Swetnam, T. W., van der Werf, G. R., Pyne, S. J.: Fire in the Earth System, Science, 324(5926), 481–484, 2009.

Brewer, A. C., McElroy, C. T, and Kerr, J. B.: Nitrogen dioxide concentrations in the atmosphere, Nature, 246, 129–133, 1973.

Brinksma, E. J., Pinardi, G., Braak, R., Volten, H., Richter, A., Schoenhardt, A., Van Roozendael, M., Fayt, C., Hermans, C., Dirksen, R. J., Vlemmix, T., Berkhout, A. J. C., Swart, D. P. J., Oetjen, H., Wittrock, F., Wagner, T., Ibrahim, O. W., de Leeuw, G., Moerman, M., Curier, R. L., Celarier, E. A., Knap, W. H., Veefkind, J. P., Eskes, H. J., Allaart, M., Rothe, R., Piters, A. J. M., and Levelt, P. F.: The 2005 and 2006 DANDELIONS NO2 and aerosol intercomparison campaigns, J. Geophys. Res. 113, D16S46, 2008.

Brown, S. S., Dibb, J. E., Stark, H., Aldener, M., Vozella, M., Whitlow, S., Williams, E. J., Lerner, B. M., Jakoubek, R., Middlebrook, A. M., DeGouw, J. A., Warneke, C., Goldan, P. D., Kuster, W. C., Angevine, W. M., Sueper, D. T., Quinn, P. K., Bates, T. S., Meagher, J. F., Fehsenfeld, F. C., and Ravishankara, A. R.: Nighttime removal of NOx in the summer marine boundary layer, Geophysical Research Letters, 31, L07108 07101-07105, 2004.

Browell, E.V., Fenn, M. A., Butler, C. F., Grant, W. B., Ismail, S., Ferrare, R. A., Kooi, S. A., Brackett, V. G., Clayton, M. B., Avery, M. A., Barrick, J. D. W., Fuelberg, H. E., Maloney, J. C., Newell, R. E., Zhu, Y., Mahoney, M. J., Anderson, B. E., Blake, D. R., Brune, W. H., Heikes, B. G., Sachse, G. W., Singh, H. B., and Talbot, R. W: Large-scale air mass characteristics observed over the remote tropical Pacific Ocean during March– April 1999: Results from PEM Tropics B Field Experiment, J. Geophys. Res., 106, 32481 – 32501, 2001.

Browne, E. C. and Cohen, R. C.: Effects of biogenic nitrate chemistry on the NOx lifetime in remote continental regions, Atmos. Chem. Phys., 12, 11917–11932, doi:10.5194/acp-12- 11917-2012, 2012.

Bucsela, E. J., Celarier, E. A., Wenig, M. O., Gleason, J. F., Veefkind, J. P., Boersma, K. F., and Brinksma, E. J.: Algorithm for NO2 vertical column retrieval from the ozone monitoring instrument, IEEE T. Geosci. Remote, 44, 1245–1257, 2006.

Burrows, J. P., Hölzle, E., Goede, A. P. H., Visser, H., and Fricke, W.: SCIAMACHY-scanning imaging absorption spectrometer for atmospheric chartography, Acta Astronaut., 35, 445–451, 1995.

Burrows, J. P., Dehn, A., Deters, B., Himmelmann, S., Richter, A., Voigt, S., and Orphal, J.: Atmospheric remote-sensing reference data from GOME: part 1. Temperature-dependent absorption cross-sections of NO2 in the 231-794 nm range, Journal of Quantitative Spectroscopy and Radiative Transfer, 60, 1025-1031, 1998.

Burrows, J. P., Weber, M., Buchwitz, M., Rozanov, V., Ladstätter-Weißenmayer, A., Richter, A., Debeek, R., Hoogen, R., Bramstedt, K., Eichmann, K. U., Eisinger, M., and Perner, D.: The Global Ozone Monitoring Experiment (GOME): Mission concept and first scientific results, J. Atmos. Sci., 56, 151–175, 1999.

Burrows, J. P., Platt, U., and Borrell, P.: The Remote Sensing of Tropospheric Composition from Space, 1st Edn., Springer, Heidelberg, Germany, 2011.

Cahoon Jr, D. R., Stocks, B. J., Levine, J. S., Cofer Iii, W. R., and O'Neill, K. P.: Seasonal distribution of African savanna fires, Nature, 359, 812–815, 1992.

Callies, J., Corpaccioli, E., Eisinger, M., Lefebvre, A., Munro, R., Perez-Albinana, A., Ricciarelli, B., Calamai, L., Gironi, G., Veratti, R., Otter, G., Eschen, M., and Van Riel, L.: GOME-2 ozone instrument on-board the European METOP satellites, in: Weather and Environemental Satellites, Proceedings of SPIE - The International Society for Optical Engineering, Denver, CO, 60–70, 2004.

Cançado, J. E. D., Saldiva, P. H. N., Pereira, L. A. A., Lara, L. B. L. S., Artaxo, P., Martinelli, L. A., Arbex, M. A., Zanobetti, A., and Braga, A. L. F.: The impact of sugar cane-burning emissions on the respiratory system of children and the elderly, Environ. Health Persp., 114, 725–729, 2006.

Castellanos, P., Boersma, K. F., and van der Werf, G. R.: Satellite observations indicate substantial spatiotemporal variability in biomass burning NOx emission factors for South America, Atmos. Chem. Phys., 14, 3929-3943, doi:10.5194/acp-14-3929-2014, 2014.

Chaffey, C. J., and Grant, C. D.: Fire management implications of fuel loads and vegetation structure in rehabilitated sand mines near Newcastle, Australia, Forest Ecology and Management, 129, 269-278, 2000.

Chen, L.-W. A., Verburg, P., Shackelford, A., Zhu, D., Susfalk, R., Chow, J. C., and Watson, J. G.: Moisture effects on carbon and nitrogen emission from burning of wildland biomass, Atmos. Chem. Phys., 10, 6617-6625, doi:10.5194/acp-10-6617-2010, 2010.

Chipperfield, M. P.: Multiannual simulations with a three-dimensional chemical transport model, J. Geophys. Res., 104, 1781–1805, 1999.

Christian, T. J., Kleiss, B., Yokelson, R. J., Holzinger, R., Crutzen, P. J., Hao, W. M., Saharjo, B. H., and Ward, D. E.: Comprehensive laboratory measurements of biomass-burning emissions: 1. Emissions from Indonesian, African, and other fuels, Journal of Geophysical Research D: Atmospheres, 108, ACH 3-1 - ACH 3-13, 2003.

Clarisse, L., R'Honi, Y., Coheur, P. F., Hurtmans, D., and Clerbaux, C.: Thermal infrared nadir observations of 24 atmospheric gases, Geophysical Research Letters, 38, 2011.

Clarke, P. J., Latz, P. K., and Albrecht, D. E.: Long-term changes in semi-arid vegetation: Invasion of an exotic perennial grass has larger effects than rainfall variability, Journal of Vegetation Science, 16, 237-248, 2005.

Conrad, R.: Soil microorganisms as controllers of atmospheric trace gases (H2, CO, CH4, OCS, N2O, and NO), Microbiol. Rev., 60, 609–40, 1996.

Coquart, B., Jenouvrier, A., and Merienne, M. F.: The NO2 absorption spectrum. II. Absorption cross-sections at low temperatures in the 400-500 nm region, Journal of Atmospheric Chemistry, 21, 251-261, 1995.

Crutzen, P. J. and Lelieveld, J.: Human impacts on atmospheric chemistry, Annu. Rev. Earth Planet. Sci. 29, 17-45, 2001.

Davidson, E.: Pulses of nitric oxide and nitrous oxide flux following wetting of dry soil: an assessment of probable sources and importance relative to annual fluxes, Ecol. Bull., 42, 149–155, 1992.

Cooke, W. F., Koffi, B., and Grégoire, J.-M.: Seasonality of vegetation fires in Africa from remote sensing data and application to a global chemistry model, Journal of Geophysical Research D: Atmospheres, 101, 21051-21065, 1996.

Crutzen, P. J.: The influence of nitrogen oxides on the atmospheric ozone content, Q. J. Roy. Meteor. Soc., 96, 320–325, 1970.

Crutzen, P. J. and Andreae, M. O.: Biomass burning in the tropics: Impact on atmospheric chemistry and biogeochemical cycles, Science, 250, 1669–1678, 1990.

De Ruyter De Wildt, M., Eskes, H., and Boersma, K. F.: The global economic cycle and satellite-derived NO2 trends over shipping lanes, Geophysical Research Letters, 39, 2012.

Dee, D. P., Uppala, S. M., Simmons, A. J., Berrisford, P., Poli, P., Kobayashi, S., Andrae, U., Balmaseda, M. A., Balsamo, G., Bauer, P., Bechtold, P., Beljaars, A. C. M., van de Berg, L., Bidlot, J., Bormann, N., Delsol, C., Dragani, R., Fuentes, M., Geer, A. J., Haimberger, L., Healy, S. B., Hersbach, H., Hólm, E. V., Isaksen, L., Kållberg, P., Köhler, M., Matricardi, M., McNally, A. P., Monge-Sanz, B. M., Morcrette, J.-J., Park, B.-K., Peubey, C., de Rosnay, P., Tavolato, C., Thépaut, J.-N., and Vitart, F.: The ERA-Interim reanalysis: configuration and performance of the data assimilation system, Q. J. Roy. Meteorol. Soc., 137, 553–597, doi:10.1002/qj.828, 2011.

Dennekamp, M., and Abramson, M. J.: The effects of bushfire smoke on respiratory health, Respirology, 16, 198-209, 2011.

Deutschmann, T., Beirle, S., Frieß, U., Grzegorski, M., Kern, C., Kritten, L., Platt, U., Prados-Roman, C., Puklite, J., Wagner, T., Werner, B., and Pfeilsticker, K.: The Monte Carlo atmospheric radiative transfer model McArtim: Introduction and validation of Jacobians and 3D features, J. Quant. Spectrosc. Radiat. Trans. 112, 1119-1137, 2011.

Dozier, J.: A method for satellite identification of surface temperature fields of subpixel resolution, Remote Sensing of Environment, 11, 221-229, 1981.

Draxler, R. R., and Rolph, G. D.: HYSPLIT (HYbrid Single-Particle Lagrangian Integrated Trajectory) Model access via NOAA ARL READY Website, available at: http://www.arl.noaa.gov/HYSPLIT.php (last access: May 2014). NOAA Air Resources Laboratory, College Park, MD, 2013.

Duncan, B. N., Martin, R. V., Staudt, A. C., Yevich, R., and Logan, J. A.: Interannual and seasonal variability of biomass burning emissions constrained by satellite observations, Journal of Geophysical Research D: Atmospheres, 108, ACH 1-1 ACH 1-22, 2003.

Eck, T. F., Holben, B. N., Reid, J. S., O'Neill, N. T., Schafer, J. S., Dubovik, O., Smirnov, A., Yamasoe, M. A., and Artaxo, P.: High aerosol optical depth biomass burning events: a comparison of optical properties for different source regions, Geophys. Res. Lett., 30, 2035, doi:10.1029/2003GL017861, 2003.

Eck, T. F., Holben, B. N., Reid, J. S., Sinyuk, A., Hyer, E. J., O'Neill, N. T., Shaw, G. E., Vande Castle, J. R., Chapin, F. S., Dubovik, O., Smirnov, A., Vermote, E., Schafer, J. S., Giles, D., Slutsker, I., Sorokine, M., and Newcomb, W. W.: Optical properties of boreal region biomass burning aerosols in central Alaska and seasonal variation of aerosol optical depth at an Arctic coastal site, Journal of Geophysical Research D: Atmospheres, 114, doi:10.1029/2008JD010870, 2009.

Endresen, Ø., Bakke, J., Sørgård, E., Berglen, T. F., and Holmvang, P.: Improved modelling of ship SO2 emissions e a fuel based approach, Atmos. Environ. 39, 3621-3628, 2005.

Eyring, V., Isaksen, I.S.A., Berntsen, T., Collins, W. J., Corbett, J. J., Endresen, Ø., Grainger, R. G., Moldanova, J., Schlager, H., and Stevenson, D. S.: Transport impacts on atmosphere and climate: Shipping, Atmos. Environ., 44, 4735–4771, doi:10.1016/j.atmosenv.2009.04.059, 2010.

Farman, J. C., Gardiner, B. G., and Shanklin, J. D.: Large losses of total ozone in Antarctica reveal seasonal ClOx/NOx interaction, Nature, 315, 207-210, 1985.

Ferek, R. J., Reid, J. S., Hobbs, P. V., Blake, D. R., and Liousse, C.: Emission factors of hydrocarbons, halocarbons, trace gases and particles from biomass burning in Brazil, Journal of Geophysical Research D: Atmospheres, 103, 32107-32118, 1998.

Firestone, M. and Davidson, E.: Exchange of Trace Gases Between Terrestrial Ecosystems and the Atmosphere, John Wiley, New York, 1989.

Flannigan, M. D., Krawchuk, M. A., De Groot, W. J., Wotton, B. M., and Gowman, L. M.: Implications of changing climate for global wildland fire, International Journal of Wildland Fire, 18, 483-507, DOI: 10.1071/WF08187, 2009.

Franke, K., Richter, A., Bovensmann, H., Eyring, V., Jockel, P., Hoor, P., and Burrows, J. P.: Ship emitted NO2 in the Indian Ocean: comparison of model results with satellite data, Atmos. Chem. Phys., 9, 7289–7301, doi:10.5194/acp-9-7289-2009, 2009.

Frankenberg, E., McKee, D., and Thomas, D.: Health consequences of forest fires in Indonesia, Demography, 42, 109-129, 2005.

Franzblau, E.: Electrical discharges involving the formation of NO, NO2, HNO3, and O3, Journal of Geophysical Research, 96, 22,337-322,345, 1991.

Freeborn, P. H., Wooster, M. J., and Roberts, G.: Addressing the spatiotemporal sampling design of MODIS to provide estimates of the fire radiative energy emitted from Africa, Remote Sens. Environ., 115, 475–489, 2011.

Friedl, M. A., Sulla-Menashe, D., Tan, B., Schneider, A., Ramankutty, N., Sibley, A., and Huang, X.: MODIS Collection 5 global land cover: Algorithm refinements and characterization of new datasets, Remote Sens. Environ., 114, 168–182, 2010.

Frieß, U., Sihler, H., Sander, R., Pöhler, D., Yilmaz, S., and Platt, U.: The vertical distribution of BrO and aerosols in the Arctic: measurements by active and passive differential optical absorption spectroscopy, J. Geophys. Res., 116, D00R04, doi:10.1029/2011JD015938, 2011.

Fröhlich, C., and Lean, J.: Solar radiative output and its variability: Evidence and mechanisms, Astronomy and Astrophysics Review, 12, 273-320, 2004.

Fuhlbrügge, S., Quack, B., Krüger, K., Tegtmeier, S., Atlas, E., Raimund, R., Hepach, H., and Shi, Q.: The contribution of oceanic halocarbons to marine and free tropospheric air over the South China and Sulu Seas (in preperation)

Ganguly, D., Dey, M., Sen, S., and Jana, T. K.: Biosphere-atmosphere exchange of NOx in the tropical mangrove forest, J. Geophys. Res., 114, G04014, doi:10.1029/2008JG000852, 2009.

Giglio, L., van der Werf, G. R., Randerson, J. T., Collatz, G. J., and Kasibhatla, P.: Global estimation of burned area using MODIS active fire observations, Atmos. Chem. Phys., 6, 957– 974, doi:10.5194/acp-6-957-2006, 2006a.

Giglio, L., Csiszar, I., and Justice, C. O.: Global distribution and seasonality of active fires as observed with the Terra and Aqua Moderate Resolution Imaging Spectroradiometer (MODIS) sensors, Journal of Geophysical Research G: Biogeosciences, 111, 2006b.

Giglio, L.: Characterization of the tropical diurnal fire cycle using VIRS and MODIS observations, Remote Sens. Environ., 108, 407–421, 2007.

Giglio, L., Randerson, J. T., van der Werf, G. R., Kasibhatla, P. S., Collatz, G. J., Morton, D. C., and DeFries, R. S.: Assessing variability and long-term trends in burned area by merging multiple satellite fire products, Biogeosciences, 7, 1171–1186, doi:10.5194/bg-7-1171-2010, 2010.

Giglio, L., Randerson, J. T., and van der Werf, G. R.: Analysis of daily, monthly, and annual burned area using the fourth-generation global emissions database (GFED4), J. Geophys. Res.-Biogeo., 118, 317–328, 2013.

Giles, D. M., Holben, B. N., Eck, T. F., Sinyuk, A., Smirnov, A., Slutsker, I., Dickerson, R. R., Thompson, A. M., and Schafer, J. S.: An analysis of AERONET aerosol absorption properties and classifications representative of aerosol source regions, J. Geophys. Res.-Atmos., 117, D17203, doi:10.1029/2012JD018127, 2012.

Girardin, M. P., Ali, A., Carcaillet, C., Mudelsee, M., Drobyshev, I., Hély, C., and Bergeron, Y.: Heterogeneous response of circumboreal wildfire risk to climate change since the early 1900s, Global Change Biology, 15, 2751-2769, 2009.

Goldammer, J. G., Statheropoulos, M., and Andreae, M. O.: Chapter 1 Impacts of Vegetation Fire Emissions on the Environment, Human Health, and Security: A Global Perspective, Developments in Environmental Science, 8, 3-36, 2008.

Goldenbaum, G. C., and Dickerson, R. R.: Nitric oxide production by lightning discharges, Journal of Geophysical Research, 98, 18,333-318,338, 1993.

Goode, J. G., Yokelson, R. J., Ward, D. E., Susott, R. A., Babbitt, R. E., Davies, M. A., and Hao, W. M.: Measurements of excess O3, CO2, CO, CH4, C2H4, C2H2, HCN, NO, NH3, HCOOH, CH3COOH, HCHO, and CH3OH in 1997 Alaskan biomass burning plumes by airborne Fourier transform infrared spectroscopy (AFTIR), J. Geophys. Res., 105, 22147–22166, doi:10.1029/2000JD900287, 2000.

Gorshelev, V., Serdyuchenko, A., Weber, M., Chehade, W., and Burrows, J. P.: High spectral resolution ozone absorption cross-sections – Part 1: Measurements, data analysis and comparison with previous measurements around 293 K, Atmos. Meas. Tech., 7, 609-624, doi:10.5194/amt-7-609-2014, 2014.

Gottwald, M. and Bovensmann, H., eds.: SCIAMACHY - Exploring the Changing Earth's Atmosphere, Springer Netherlands, Dordrecht, 2011.

Govender, N., Trollope, W. S. W., and Van Wilgen, B. W.: The effect of fire season, fire frequency, rainfall and management on fire intensity in savanna vegetation in South Africa, Journal of Applied Ecology, 43, 748-758, 2006.

Granier, C., Bessagnet, B., Bond, T., D'Angiola, A., van der Gon, H. D., Frost, G. J., Heil, A., Kaiser, J. W., Kinne, S., Klimont, Z., Kloster, S., Lamarque, J. F., Liousse, C., Masui, T., Meleux, F., Mieville, A., Ohara, T., Raut, J. C., Riahi, K., Schultz, M. G., Smith, S. J., Thompson, A., van Aardenne, J., van der Werf, G. R., and van Vuuren, D. P.: Evolution of anthropogenic and biomass burning emissions of air pollutants at global and regional scales during the 1980-2010 period, Climatic Change, 109, 163-190, 2011.

Greenblatt, G. D., Orlando, J. J., Burkholder, J. B., and Ravishankara, A. R.: Absorption-measurements of oxygen between 330nm and 1140nm, J. Geophys. Res.-Atmos., 95, 18577–18582, 1990.

Großmann, K., Frieß, U., Peters, E., Wittrock, F., Lampel, J., Yilmaz, S., Tschritter, J., Sommariva, R., von Glasow, R., Quack, B., Krüger, K., Pfeilsticker, K., and Platt, U.: Iodine monoxide in the Western Pacific marine boundary layer, Atmos. Chem. Phys. 13, 3363-3378, 2013.

Guenther, A., Karl, T., Harley, P., Wiedinmyer, C., Palmer, P. I., and Geron, C.: Estimates of global terrestrial isoprene emissions using MEGAN (Model of Emissions of Gases and Aerosols from Nature), Atmos. Chem. Phys., 6, 3181–3210, doi:10.5194/acp-6- 3181-2006, 2006.

Hänninen, O., Kauhaniemi, M., Karppinen, A., Kukkonen, J., Kousa, A., and Jantunen, M.: Inter-comparison of predicted population exposure distributions during four selected episodes in Helsinki and evaluation against measured data, International Journal of Environment and Pollution, 40, 248-266, 2010.

Hains, J. C., Boersma, K. F., Mark, K., Dirksen, R. J., Cohen, R. C., Perring, A. E., Bucsela, E., Volten, H., Swart, D. P. J., Richter, A., Wittrock, F., Schoenhardt, A., Wagner, T., Ibrahim, O. W., Roozendael, M. V., Pinardi, G., Gleason, J. F., Veefkind, J. P., and Levelt, P.: Testing and improving OMI DOMINO tropospheric NO2 using observations from the DANDELIONS and INTEXB validation campaigns, J. Geophys. Res.-Atmos., 115, D05301, doi:10.1029/2009JD012399, 2010.

Halla, J. D., Wagner, T., Beirle, S., Brook, J. R., Hayden, K. L., O'Brien, J. M., Ng, A., Majonis, D., Wenig, M. O., and McLaren, R.: Determination of tropospheric vertical columns of NO2 and aerosol optical properties in a rural setting using MAX-DOAS, Atmos. Chem. Phys. 11, 12475-12498, 2011.

Hansen, M. C., Defries, R. S., Townshend, J. R. G., and Sohlberg, R.: Global land cover classification at 1 km spatial resolution using a classification tree approach, Int. J. Remote Sens., 21, 1331–1364, 2000.

Harder, J. W., Brault, J. W., Johnston, P. V., and Mount, G. H.: Temperature dependent NO2 cross sections at high spectral resolution, Journal of Geophysical Research D: Atmospheres, 102, 3861-3879, 1997.

Hessl, A. E.: Pathways for climate change effects on fire: Models, data, and uncertainties, Progress in Physical Geography, 35:393, doi:10.1177/0309133311407654, 2011.

Heue, K.-P., Richter, A., Bruns, M., Burrows, J. P., v. Friedeburg, C., Platt, U., Pundt, I.,Wang, P., and Wagner, T.: Validation of SCIAMACHY tropospheric NO2-columns with AMAXDOAS measurements, Atmos. Chem. Phys., 5, 1039–1051, doi:10.5194/acp-5-1039-2005, 2005.

Heue, K.-P., Wagner, T., Broccardo, S. P., Walter, D., Piketh, S. J., Ross, K. E., Beirle, S., and Platt, U.: Direct observation of two dimensional trace gas distributions with an airborne Imaging DOAS instrument, Atmos. Chem. Phys., 8, 6707–6717, doi:10.5194/acp-8-6707-2008, 2008.

Hewitt, C. N., MacKenzie, A. R., Di Carlo, P., Di Marco, C. F., Dorsey, J. R., Evans, M., Fowler, D., Gallagher, M. W., Hopkins, J. R., Jones, C. E., Langford, B., Lee, J. D., Lewis, A. C., Lim, S. F., McQuaid, J., Misztal, P., Moller, S. J., Monks, P. S., Nemitz, E., Oram, D. E., Owen, S. M., Phillips, G. J., Pugh, T. A. M., Pyle, J. A., Reeves, C. E., Ryder, J., Siong, J., Skiba, U., and Stewart, D. J.: Nitrogen management is essential to prevent tropical oil palm plantations from causing ground-level ozone pollution, Proceedings of the National Academy of Sciences of the United States of America, 106, 18447-18451, 2009.

Hilboll, A., Richter, A., Rozanov, A., Hodnebrog, Ø., Heckel, A., Solberg, S., Stordal, F., and Burrows, J. P.: Improvements to the retrieval of tropospheric NO2 from satellite – stratospheric correction using SCIAMACHY limb/nadir matching and comparison to Oslo CTM2 simulations, Atmos. Meas. Tech., 6, 565-584, doi:10.5194/amt-6-565-2013, 2013a.

Hilboll, A., Richter, A., and Burrows, J. P.: Long-term changes of tropospheric NO2 over megacities derived from multiple satellite instruments, Atmos. Chem. Phys., 13, 4145-4169, doi:10.5194/acp-13-4145-2013, 2013b.

Hill, R. D., Rinker, R. G., and Wilson, H. D.: Atmospheric nitrogen fixation by lightning, J. Atmos. Sci., 37, 179-192, 1980.

Hoelzemann, J. J., Schultz, M. G., Brasseur, G. P., Granier, C., and Simon, M.: Global Wildland Fire Emission Model (GWEM): Evaluating the use of global area burnt satellite data, Journal of Geophysical Research D: Atmospheres, 109, 2004.

Holloway, A. and Wayne, R.: Atmospheric Chemistry, RSC Publishing, 2010.

Hönninger, G., von Friedeburg, C., and Platt, U.: Multi axis differential optical absorption spectroscopy (MAX-DOAS), Atmos. Chem. Phys., 4, 231–254, doi:10.5194/acp-4-231-2004, 2004.

Hudman, R. C., Moore, N. E., Mebust, A. K., Martin, R. V., Russell, A. R., Valin, L. C., and Cohen, R. C.: Steps towards a mechanistic model of global soil nitric oxide emissions: implementation and space based-constraints, Atmos. Chem. Phys., 12, 7779–7795, doi:10.5194/acp-12-7779-2012, 2012.

Ichoku, C. and Kaufman, Y. J.: A method to derive smoke emission rates from MODIS fire radiative energy measurements, IEEE T. Geosci. Remote, 43, 2636–2649, 2005.

Ichoku, C., Kahn, R., and Chin, M.: Satellite contributions to the quantitative characterization of biomass burning for climate modeling, Atmos. Res., 111, 1–28, 2012.

Inness, A., Baier, F., Benedetti, A., Bouarar, I., Chabrillat, S., Clark, H., Clerbaux, C., Coheur, P., Engelen, R. J., Errera, Q., Flemming, J., George, M., Granier, C., Hadji-Lazaro, J., Huijnen, V., Hurtmans, D., Jones, L., Kaiser, J. W., Kapsomenakis, J., Lefever, K., Leitão, J., Razinger, M., Richter, A., Schultz, M. G., Simmons, A. J., Suttie, M., Stein, O., Thépaut, J.-N., Thouret, V., Vrekoussis, M., Zerefos, C., and the MACC team: The MACC reanalysis: an 8 yr data set of atmospheric composition, Atmos. Chem. Phys., 13, 4073–4109, doi:10.5194/acp-13-4073-2013, 2013.

IPCC: Climate Change 2007: The Physical Science Basis, contribution of Working Group I to the Fourth Assessment Report of the Intergovernmental Panel on Climate Change, edited by: Solomon, S., Qin, D., Manning, M., Chen, Z., Marquis, M., Averyt, K. B., Tignor, M., and Miller, H. L., Cambridge Univ. Press, Cambridge, UK and New York, USA, 2007.

IPCC: Climate Change 2013: The Physical Science Basis, contribution of Working Group I to the Fifth Assessment Report of the Intergovernmental Panel on Climate Change, edited by: Stocker, T. F., Qin, D., Plattner, G.-K., Tignor, M., Allen, S. K., Boschung, J., Nauels, A., Xia, Y., Bex, V., and Midgley, P. M., Cambridge Univ. Press, Cambridge, UK and New York, NY, USA, 2013.

Irie, H., Takashima, H., Kanaya, Y., Boersma, K. F., Gast, L., Wittrock, F., Brunner, D., Zhou, Y., and van Roozendael, M.: Eight-component retrievals from ground-based MAX-DOAS observations, Atmos. Meas. Tech. 4, 1027-1044, 2011.

Jacob, D. J.: Factors regulating ozone over the United States and its export to the global atmosphere, Journal of Geophysical Research, 98, 14817-814826, 1993.

Jacob, D. J.: Heterogeneous chemistry and tropospheric ozone, Atmospheric Environment, 34, 2131-2159, 2000.

Jacob, D. J., Crawford, J. H., Maring, H., Clarke, A. D., Dibb, J. E., Emmons, L. K., Ferrare, R. A., Hostetler, C. A., Russell, P. B., Singh, H. B., Thompson, A. M., Shaw, G. E., McCauley, E., Pederson, J. R., and Fisher, J. A.: The Arctic Research of the Composition of the Troposphere from Aircraft and Satellites (ARCTAS) mission: design, execution, and first results, Atmos. Chem. Phys., 10, 5191–5212, doi:10.5194/acp-10-5191-2010, 2010.

Jaeglé, L., Steinberger, L., Martin, R. V., and Chance, K.: Global partitioning of NOx sources using satellite observations: Relative roles of fossil fuel combustion, biomass burning and soil emissions, Faraday Discuss., 130, 407–423, 2005.

Jerabkova, L., Prescott, C. E., and Kishchuk, B. E.: Nitrogen availability in soil and forest floor of contrasting types of boreal mixedwood forests, Canadian Journal of Forest Research, 36, 112-122, DOI: 10.1139/x05-220, 2006.

Johnston, H.: Reduction of stratospheric ozone by nitrogen oxide catalysts from supersonic transport exhaust, Science, 173, 517-522, 1971.

Justice, C. O., Giglio, L., Korontzi, S., Owens, J., Morisette, J. T., Roy, D., Descloitres, J., Alleaume, S., Petitcolin, F., and Kaufman, Y.: The MODIS fire products, Remote Sens. Environ., 83, 244–262, 2002.

Kaiser, J. W., Heil, A., Andreae, M. O., Benedetti, A., Chubarova, N., Jones, L., Morcrette, J.-J., Razinger, M., Schultz, M. G., Suttie, M., and van der Werf, G. R.: Biomass burning emissions estimated with a global fire assimilation system based on observed fire radiative power, Biogeosciences, 9, 527–554, doi:10.5194/bg-9-527-2012, 2012.

Karkanas, P., Shahack-Gross, R., Ayalon, A., Bar-Matthews, M., Barkai, R., Frumkin, A., Gopher, A., and Stiner, M. C.: Evidence for habitual use of fire at the end of the Lower Paleolithic: Site-formation processes at Qesem Cave, Israel, Journal of Human Evolution, 53, 197-212, 2007.

Kaufman, Y. J., Justice, C. O., Flynn, L. P., Kendall, J. D., Prins, E. M., Giglio, L., Ward, D. E., Menzel, W. P., and Setzer, A. W.: Potential global fire monitoring from EOS-MODIS, J. Geophys. Res.-Atmos., 103, 32215–32238, 1998.

Keeley, J. E., and Rundel, P. W.: Fire and the Miocene expansion of C4 grasslands, Ecology Letters, 8, 683-690, 2005.

Kirkpatrick, J. B., Marsden-Smedley, J. B., and Leonard, S. W. J.: Influence of grazing and vegetation type on post-fire flammability, Journal of Applied Ecology, 48, 642-649, 2011.

Koelemeijer, R. B. A., de Haan, J. F., and Stammes, P.: A database of spectral surface reflectivity in the range 335–772 nm derived from 5.5 yr of GOME observations, J. Geophys. Res.-Atmos., 108, 4070, doi:10.1029/2002JD002429, 2003.

Korontzi, S., McCarty, J., Loboda, T., Kumar, S., and Justice, C.: Global distribution of agricultural fires in croplands from 3 years of Moderate Resolution Imaging Spectroradiometer (MODIS) data, Global Biogeochemical Cycles, 20, 2006.

Künzli, N., Kaiser, R., Medina, S., Studnicka, M., Chanel, O., Filliger, P., Herry, M., Horak Jr, F., Puybonnieux-Texier, V., Quénel, P., Schneider, J., Seethaler, R., Vergnaud, J. C., and Sommer, H.: Public-health impact of outdoor and traffic-related air pollution: A European assessment, Lancet, 356, 795–801, 2000.

Labonne, M., Bréon, F. M., and Chevallier, F.: Injection height of biomass burning aerosols as seen from a spaceborne lidar, Geophys. Res. Lett., 34, L11806, doi:10.1029/2007GL029311, 2007.

Lambin, E. F., Goyvaerts, K., and Petit, C.: Remotely-sensed indicators of burning efficiency of savannah and forest fires, International Journal of Remote Sensing, 24, 3105-3118, 2003.

Langmann, B., Duncan, B., Textor, C., Trentmann, J., and van der Werf, G. R.: Vegetation fire emissions and their impact on air pollution and climate, Atmos. Environ., 43, 107—116, 2009.

Le Page, Y., Pereira, J. M. C., Trigo, R., Da Camara, C., Oom, D., and Mota, B.: Global fire activity patterns (1996-2006) and climatic influence: An analysis using the World Fire Atlas, Atmospheric Chemistry and Physics, 8, 1911-1924, 2008.

Lee, D. S., Köhler, I., Grobler, E., Rohrer, F., Sausen, R., Gallardo- Klenner, L., Olivier, J. G. J., Dentener, F. J., and Bouwman, A. F.: Estimations of global NO(x) emissions and their uncertainties, Atmos. Environ., 31, 1735–1749, 1997.

Lee, C., Martin, R. V., van Donkelaar, A., Lee, H., Dickerson, R. R., Hains, J. C., Krotkov, N., Richter, A., Vinnikov, K., and Schwab, J. J.: SO2 emissions and lifetimes: estimates from inverse modeling using in situ and global, space-based (SCIAMACHY and OMI) observations, J. Geophys. Res. 116, D06304, 2011.

Leighton, P. A.: Photochemistry of Air Pollution, Academic, New York, 1961.

Leitão, J., Richter, A., Vrekoussis, M., Kokhanovsky, A., Zhang, Q. J., Beekmann, M., and Burrows, J. P.: On the improvement of NO2 satellite retrievals – aerosol impact on the airmass factors, Atmos. Meas. Tech., 3, 475–493, doi:10.5194/amt-3-475-2010, 2010.

Letnic, M., Tischler, M., and Gordon, C.: Desert small mammal responses to wildfire and predation in the aftermath of a La Niña driven resource pulse, Austral Ecology, 38, 841-849, 2013.

Levelt, P. F., Van Den Oord, G. H. J., Dobber, M. R., Mälkki, A., Visser, H., De Vries, J., Stammes, P., Lundell, J. O. V., and Saari, H.: The ozone monitoring instrument, IEEE T. Geosci. Remote, 44, 1093–1100, 2006.

Levine, J. S., Rogowski, R. S., Gregory, G. L., Howell, W. E., and Fishman, J.: Simultaneous measurements of NOx, NO and O production in a laboratory discharge: atmospheric implications (lightning-energy), Geophysical Research Letters, 8, 357-360, 1981.

Lobert, J. M., Scharffe, D. H., Hao, W. M., and Crutzen, P. J.: Importance of biomass burning in the atmospheric budgets of nitrogen-containing gases, Nature, 346, 552–554, 1990.

Lobert, J. M., Keene, W. C., Logan, J. A., and Yevich, R.: Global chlorine emissions from biomass burning: Reactive Chlorine Emissions Inventory, Journal of Geophysical Research D: Atmospheres, 104, 8373-8389, 1999.

Logan, J. A.: Tropospheric ozone: seasonal behavior, trends, and anthropogenic influence, Journal of Geophysical Research, 90, 10463-10482, 1985.

Luo, T., Yuan, R., and Wang, Z.: Lidar-based remote sensing of atmospheric boundary layer height over land and ocean, Atmos. Meas. Tech., 7, 173-182, doi:10.5194/amt-7-173-2014, 2014.

MacKenzie, A. R., Langford, B., Pugh, T. A. M., Robinson, N., Misztal, P. K., Heard, D. E., Lee, J. D., Lewis, A. C., Jones, C. E., Hopkins, J. R., Phillips, G., Monks, P. S., Karunaharan, A., Hornsby, K. E., Nicolas-Perea, V., Coe, H., Gabey, A. M., Gallagher, M. W., Whalley, L. K., Edwards, P. M., Evans, M. J., Stone, D., Ingham, T., Commane, R., Furneaux, K. L., McQuaid, J. B., Nemitz, E., Seng, Y., Fowler, D., Pyle, J. A., and Hewitt, C. N.: The atmospheric chemistry of trace gases and particulate matter emitted by different land uses in Borneo, Philosophical Transactions of the Royal Society B: Biological Sciences, 366, 3177-3195, 2011.

Marais, E. A., Jacob, D. J., Kurosu, T. P., Chance, K., Murphy, J. G., Reeves, C., Mills, G., Casadio, S., Millet, D. B., Barkley, M. P., Paulot, F., and Mao, J.: Isoprene emissions in Africa inferred from OMI observations of formaldehyde columns, Atmos. Chem. Phys., 12, 6219–6235, doi:10.5194/acp-12-6219-2012, 2012.

Marion, T., Perros, P. E., Losno, R., and Steiner, E.: Ozone production efficiency in savanna and forested areas during the EXPRESSO experiment, J. Atmos. Chem., 38, 3–30, 2001.

Martin, R. V., Jacob, D. J., Chance, K., Kurosu, T. P., Palmer, P. I., and Evans, M. J.: Global inventory of nitrogen oxide emissions constrained by space-based observations of NO_2 columns, J. Geophys. Res.-Atmos., 108, 4537, doi:10.1029/2003JD003453, 2003.

Matson, M., and Dozier, J.: Identification of subresolution high temperature sources using a thermal IR sensor, Photogrammetric Engineering and Remote Sensing, 47, 1311-1318, 1981.

Matson, M., Schneider, S. R., Aldridge, B., and Satchwell, B.: Fire detection using the NOAA (National Oceanic and Atmospheric Administration)-series satellites, 1984.

Mebust, A. K., Russell, A. R., Hudman, R. C., Valin, L. C., and Cohen, R. C.: Characterization of wildfire NOx emissions using MODIS fire radiative power and OMI tropospheric NO_2 columns, Atmos. Chem. Phys., 11, 5839–5851, doi:10.5194/acp-11-5839-2011, 2011.

Mebust, A. K. and Cohen, R. C.: Observations of a seasonal cycle in NOx emissions from fires in African woody savannas, Geophys. Res. Lett., 40, 1451–1455, 2013.

Mebust, A. K. and Cohen, R. C.: Space-based observations of fire NOx emission coefficients: a global biome-scale comparison, Atmos. Chem. Phys., 14, 2509-2524, doi:10.5194/acp-14-2509-2014, 2014.

Meland, B. R. and Boubel R. W.: A Study of Field Burning Under Varying Environmental Conditions, JAPCA J. AirWaste Ma., 16, 481–484, 1966.

Merienne, M. F., Jenouvrier, A., and Coquart, B.: The NO_2 absorption spectrum. I: Absorption cross-sections at ambient temperature in the 300-500 nm region, Journal of Atmospheric Chemistry, 20, 281-297, 1995.

Meyer-Arnek, J., Ladstätter-Weißenmayer, A., Richter, A., Wittrock, F., and Burrows, J. P.: A study of the trace gas columns of O_3, NO_2 and HCHO over Africa in September 1997, Faraday Discuss., 130, 387–405, 2005.

Miettinen, J., Shi, C., and Liew, S. C.: Deforestation rates in insular Southeast Asia between 2000 and 2010, Global Change Biology, 17, 2261-2270, 2011.

Miyazaki, K., Eskes, H. J., Sudo, K., Takigawa, M., van Weele, M., and Boersma, K. F.: Simultaneous assimilation of satellite NO_2, O_3, CO, and HNO_3 data for the analysis of tropospheric chemical composition and emissions, Atmos. Chem. Phys., 12, 9545-9579, doi:10.5194/acp-12-9545-2012, 2012.

Miyazaki, K., Eskes, H. J., Sudo, K., and Zhang, C.: Global lightning NOx production estimated by an assimilation of multiple satellite data sets, Atmos. Chem. Phys., 14, 3277-3305, doi:10.5194/acp-14-3277-2014, 2014.

Molina, L. T. and Molina, M. J.: Production of chlorine oxide (Cl_2O_2) from the self-reaction of the chlorine oxide (ClO) radical, J. Phys. Chem., 91(2), 433–436, doi:10.1021/j100286a035, 1987.

Molina, M. J., and Molina, L. T.: Megacities and atmospheric pollution, Journal of the Air and Waste Management Association, 54, 644-680, 2004.

Mollicone, D., Eva, H. D., and Achard, F.: Ecology: Human role in Russian wild fires, Nature, 440, 436-437, 2006.

Morgan, W. T., Allan, J. D., Flynn, M., Darbyshire, E., Hodgson, A., Johnson, B. T., Haywood, J. M., Freitas, S., Longo, K., Artaxo, P., and Coe, H.: Overview of the South American biomass burning analysis (SAMBBA) field experiment, AIP Conference Proceedings, 587-590, 2013.

Munro, R., Perez Albiñana, A., Callies, J., Corpaccioli, E., Eisinger, M., Lefebvre, A., and Hahne, A.: Expectations for GOME-2 on the METOP Satellites, in: ERS-Envisat Symposium 'Looking Down to Earth in the New Millennium', European Space Agency, (Special Publication) ESA SP, Gothenburg, 221–227, 2000.

Nara, H., Tanimoto, H., Tohjima, Y., Mukai, H., Nojiri, Y., and Machida, T.: Emissions of methane from offshore oil and gas platforms in Southeast Asia, Scientific Reports 4, Article number: 6503, 2014.

Noxon, J. F.: Nitrogen dioxide in the stratosphere and troposphere measured by ground based absorption spectroscopy, Science, 189, 547-549, 1975.

Nüß, J. H.: Improvements of the retrieval of tropospheric NO_2 from GOME and SCIAMACHY data, Ph.D. Thesis, University of Bremen, Bremen, Germany, 2005.

Olivier, J. G. J., Bouwman, A. F., Van der Maas, C. W. M., and Berdowski, J. M.: Emission database for global atmospheric research (EDGAR), Environ. Monit. Assess., 31, 93–106, 1994.

Olson, J. R., Baum, B. A., Cahoon, D. R., and Crawford, J. H.: Frequency and distribution of forest, savanna, and crop fires over tropical regions during PEM-Tropics A, Journal of Geophysical Research D: Atmospheres, 104, 5865-5876, 1999.

Ortiz De Zárate, I., Ezcurra, A., Lacaux, J. P., and Van Dinh, P.: Emission factor estimates of cereal waste burning in Spain, Atmospheric Environment, 34, 3183-3193, 2000.

Pan, Y., Birdsey, R. A., Fang, J., Houghton, R., Kauppi, P. E., Kurz, W. A., Phillips, O. L., Shvidenko, A., Lewis, S. L., Canadell, J. G., Ciais, P., Jackson, R. B., Pacala, S. W., McGuire, A. D., Piao, S., Rautiainen, A., Sitch, S., and Hayes, D.: A large and persistent carbon sink in the world's forests, Science, 333, 988–993, 2011.

Panchenko, M. V., Zhuravleva, T. B., Terpugova, S. A., Polkin, V. V., and Kozlov, V. S.: An empirical model of optical and radiative characteristics of the tropospheric aerosol over West Siberia in summer, Atmospheric Measurement Techniques, 5, 1513-1527, DOI: 10.5194/amt-5-1513-2012, 2012.

Pereira, J. M. C.: A comparative evaluation of NOAA/AVHRR vegetation indexes for burned surface detection and mapping, IEEE Transactions on Geoscience and Remote Sensing, 37, 217-226, 1999.

Pereira, P., and Ubeda, X.: Spatial distribution of heavy metals released from ashes after a wildfire, Journal of Environmental Engineering and Landscape Management, 18, 13-22, 2010.

Perner, D. and Platt, U.: Detection of nitrous acid in the atmosphere by differential optical absorption, Geophys. Res. Lett., 6, 917–920, 1979.

Peters, E., Wittrock, F., Großmann, K., Frieß, U., Richter, A., and Burrows, J. P.: Formaldehyde and nitrogen dioxide over the remote western Pacific Ocean: SCIAMACHY and GOME-2 validation using ship-based MAX-DOAS observations, Atmospheric Chemistry and Physics, 12, 11179-11197, 2012.

Peters, E.: Improved MAX-DOAS measurements and retrievals focused on the marine boundary layer, Ph.D., University of Bremen, Bremen, Germany, available at: http://www.doas-bremen.de/paper/diss_peters_2013.pdf (last access: May 2014), 2013.

Peters, E., Wittrock, F., Richter, A., Alvarado, L. M. A., Rozanov, V. V., and Burrows, J. P.: Liquid water absorption and scattering effects in DOAS retrievals over oceans, Atmos. Meas. Tech. Discuss., 7, 5027-5073, doi:10.5194/amtd-7-5027-2014, 2014.

Pfeilsticker, K. and the SHIVA consortium: Overview on the project SHIVA (stratospheric ozone: halogen impacts in a varying atmosphere): achievements and key results (in preparation)

Pinardi, G., Van Roozendael, M., Abuhassan, N., Adams, C., Cede, A., Clémer, K., Fayt, C., Frieß, U., Gil, M., Herman, J., Hermans, C., Hendrick, F., Irie, H., Merlaud, A., Navarro Comas, M., Peters, E., Piters, A. J. M., Puentedura, O., Richter, A., Schönhardt, A., Shaiganfar, R., Spinei, E., Strong, K., Takashima, H., Vrekoussis, M., Wagner, T., Wittrock, F., and Yilmaz, S.: MAX-DOAS formaldehyde slant column measurements during CINDI: intercomparison and analysis improvement, Atmos. Meas. Tech., 6, 167-185, doi:10.5194/amt-6-167-2013, 2013.

Piters, A. J. M., Boersma, K. F., Kroon, M., Hains, J. C., Van Roozendael, M., Wittrock, F., Abuhassan, N., Adams, C., Akrami, M., Allaart, M. A. F., Apituley, A., Beirle, S., Bergwerff, J. B., Berkhout, A. J. C., Brunner, D., Cede, A., Chong, J., Clémer, K., Fayt, C., Frieß, U., Gast, L. F. L., Gil-Ojeda, M., Goutail, F., Graves, R., Griesfeller, A., Großmann, K., Hemerijckx, G., Hendrick, F., Henzing, B., Herman, J., Hermans, C., Hoexum, M., van der Hoff, G. R., Irie, H., Johnston, P. V., Kanaya, Y., Kim, Y. J., Klein Baltink, H., Kreher, K., de Leeuw, G., Leigh, R., Merlaud, A., Moerman, M. M., Monks, P. S., Mount, G. H., Navarro-Comas, M., Oetjen, H., Pazmino, A., Perez-Camacho, M., Peters, E., du Piesanie, A., Pinardi, G., Puentedura, O., Richter, A., Roscoe, H. K., Schönhardt, A., Schwarzenbach, B., Shaiganfar, R., Sluis, W., Spinei, E., Stolk, A. P., Strong, K., Swart, D. P. J., Takashima, H., Vlemmix, T., Vrekoussis, M., Wagner, T., Whyte, C., Wilson, K. M., Yela, M., Yilmaz, S., Zieger, P., and Zhou, Y.: The Cabauw Intercomparison campaign for Nitrogen Dioxide measuring Instruments (CINDI): design, execution, and early results, Atmos. Meas. Tech., 5, 457–485, doi:10.5194/amt-5-457-2012, 2012.

Platt, U. and Hausmann, M.: Spectroscopic measurement of the free radicals NO3, BrO, IO, and OH in the troposphere, Res. Chem. Intermediat., 20, 557–578, 1994.

Platt, U. and Stutz, J.: Differential Optical Absorption Spectroscopy. Physics of Earth and Space Environments, Springer, Berlin, 2008.

Pope, R. M. and Fry, E. S.: Absorption spectrum (380–700 nm) of pure water. II. Integrating cavity measurements, Appl. Opt., 36, 8710–8723, 1997.

Prasad, V. K., Kant, Y., Gupta, P. K., Sharma, C., Mitra, A. P., and Badarinath, K. V. S.: Biomass and combustion characteristics of secondary mixed deciduous forests in Eastern Ghats of India, Atmospheric Environment, 35, 3085-3095, 2001.

Protopopov, V. V.: Sredoobrazuiushchaia rol' temnokhvoinogo lesa. Novosibirsk, 1975.

Rahlao, S. J., Milton, S. J., Esler, K. J., Van Wilgen, B. W., and Barnard, P.: Effects of invasion of fire-free arid shrublands by a fire-promoting invasive alien grass (Pennisetum setaceum) in South Africa, Austral Ecology, 34, 920-928, 2009.

Remer, L. A., Kleidman, R. G., Levy, R. C., Kaufman, Y. J., Tanré, D., Mattoo, S., Martins, J. V., Ichoku, C., Koren, I., Yu, H., and Holben, B. N.: Global aerosol climatology from the MODIS satellite sensors, J. Geophys. Res.-Atmos., 113, D14S07, doi:10.1029/2007JD009661, 2008.

Ricchiazzi, P., Yang, S. R., Gautier, C., and Sowle, D.: SBDART: A research and teaching software tool for plane-parallel radiative transfer in the Earth's atmosphere, B. Am. Meteorol. Soc., 79, 2101-2114, 1998.

Richter, A., Eisinger, M., Ladstätter-Weißenmayer, A., and Burrows, J. P.: DOAS zenith sky observations: 2. Seasonal variation of BrO over Bremen (53°N) 1994-1995, Journal of Atmospheric Chemistry, 32, 83-99, 1999.

Richter, A. and Burrows, J. P.: Tropospheric NO2 from GOME measurements, Adv. Space Res., 29, 1673–1683, 2002.

Richter, A., Eyring, V., Burrows, J. P., Bovensmann, H., Lauer, A., Sierk, B., and Crutzen, P. J.: Satellite Measurements of NO2 from International Shipping Emissions, Geophys. Res. Lett., 31, L23110, doi:10.1029/2004GL020822, 2004.

Richter, A., Burrows, J. P., Nüß, H., Granier, C., and Niemeier, U.: Increase in tropospheric nitrogen dioxide over China observed from space, Nature, 437, 129-132, DOI: 10.1038/nature04092, 2005.

Richter, A.: Differential optical absorption spectroscopy as a tool to measure pollution from space, Spectroscopy Europe, 18, 14-21, 2006.

Richter, A., Begoin, M., Hilboll, A., and Burrows, J. P.: An improved NO2 retrieval for the GOME-2 satellite instrument, Atmos. Meas. Tech., 4, 1147–1159, doi:10.5194/amt-4-1147-2011, 2011.

Riggan, P. J., Tissell, R. G., Lockwood, R. N., Brass, J. A., Pereira, J. A. R., Miranda, H. S., Miranda, A. C., Campos, T., and Higgins, R.: Remote measurement of energy and carbon flux from wildfires in Brazil, Ecol. Appl., 14, 855–872, 2004.

Roberts, G. J. and Wooster, M. J.: Fire detection and fire characterization over Africa using meteosat SEVIRI, IEEE T. Geosci. Remote, 46, 1200–1218, 2008.

Roberts, G., Wooster, M. J., and Lagoudakis, E.: Annual and diurnal african biomass burning temporal dynamics, Biogeosciences, 6, 849–866, doi:10.5194/bg-6-849-2009, 2009.

Roberts, G., Wooster, M., Freeborn, P. H., and Xu, W.,: Integration of geostationary FRP and polar-orbiter burned area datasets for an enhanced biomass burning inventory, Remote Sens. Environ., 115, 2047–2061, doi:10.1016/j.rse.2011.04.006, 2011.

Rodgers, C. D.: Inverse Methods for Atmospheric Sounding – Theory and Practice, Series on Atmospheric, Oceanic and Planetary Physics, World Scientific, Singapore, 2000.

Rodin, L. E., Bazilevich, N. I.: Dynamics of organic matter and biological turnover of ash constituents and nitrogen in major types of vegetation of the globe. Moscow-Leningrad, Academy of Sciences of the USSR, 253 pp., 1965. [in Russian]

Rolph, G. D.: Real-time Environmental Applications and Display sYstem (READY) Website, available at: http://www.ready.noaa.gov (last access: May 2014). NOAA Air Resources Laboratory, College Park, MD, 2013.

Roscoe, H. K., Van Roozendael, M., Fayt, C., du Piesanie, A., Abuhassan, N., Adams, C., Akrami, M., Cede, A., Chong, J., Clémer, K., Friess, U., Gil Ojeda, M., Goutail, F., Graves, R., Griesfeller, A., Grossmann, K., Hemerijckx, G., Hendrick, F., Herman, J., Hermans, C., Irie, H., Johnston, P. V., Kanaya, Y., Kreher, K., Leigh, R., Merlaud, A., Mount, G. H., Navarro, M., Oetjen, H., Pazmino, A., Perez-Camacho, M., Peters, E., Pinardi, G., Puentedura, O., Richter, A., Schönhardt, A., Shaiganfar, R., Spinei, E., Strong, K., Takashima, H., Vlemmix, T., Vrekoussis, M., Wagner, T., Wittrock, F., Yela, M., Yilmaz, S., Boersma, F., Hains, J., Kroon, M., Piters, A., and Kim, Y. J.: Intercomparison of slant column measurements of NO2 and O4 by MAX-DOAS and zenith-sky UV and visible spectrometers, Atmos. Meas. Tech., 3, 1629–1646, doi:10.5194/amt-3-1629-2010, 2010.

Rothman, L. S., Barbe, A., Benner, D. C., Brown, L. R., Camy-Peyret, C., Carleer, M. R., Chance, K., Clerbaux, C., Dana, V., Devi, V. M., Fayt, A., Flaud, J.-M., Gamache, R. R., Goldman, A., Jacquemart, D., Jucks, K. W., Lafferty, W. J., Mandin, J.-Y., Massie, S. T., Nemtchinov, V., Newnham, D. A., Perrin, A., Rinsland, C. P., Schroeder, J., Smith, K. M., Smith, M. A. H., Tang, K., Toth, R. A., Auwera, J. V., Varanasi, P., and Yoshino, K.: The HITRAN molecular spectroscopic database: edition of 2000 including updates through 2001, J. Quant. Spectr. Rad. Transf., 82, 5–44, 2003.

Row L. W., Hastings, D. A., and Dunbar, P. K.: Terrainbase worldwide digital terrain data. Release 1.0., National Geophysical Data Center, Boulder, 1994.

Rozanov, V. V., Diebel, D., Spurr, R. J. D., and Burrows, J. P.: GOMETRAN: A radiative transfer model for the satellite project GOME, the plane-parallel version, J. Geophys. Res., 102(D14), 16 683–16 696, doi:10.1029/96JD01535, 1997.

Rozanov, A., Rozanov, V. V., Buchwitz, M., Kokhanovsky, A. A., and Burrows, J. P.: SCIATRAN 2.0 – a new radiative transfer model for geophysical applications in the 175– 2400 nm spectral region, Adv. Space Sci., 36, 1015–1019, doi:10.1016/j.asr.2005.03.012, 2005.

Sahu, L. K., Kondo, Y., Miyazaki, Y., Pongkiatkul, P., and Kim Oanh, N. T.: Seasonal and diurnal variations of black carbon and organic carbon aerosols in Bangkok, J. Geophys. Res.-Atmos., 116, D15302, doi:10.1029/2010JD015563, 2011.

Sanders, R. W.: Visible and near-ultraviolet spectroscopy at McMurdo Station, Antarctica 9. Observations of OClO from April to October 1991, Journal of Geophysical Research, 98, 7219-7228, 1993.

Sastry, N.: Forest fires, air pollution, and mortality in Southeast Asia, Demography, 39, 1-23, 2002.

Serdyuchenko, A., Gorshelev, V., Weber, M., Chehade, W., and Burrows, J. P.: High spectral resolution ozone absorption cross-sections – Part 2: Temperature dependence, Atmos. Meas. Tech., 7, 625-636, doi:10.5194/amt-7-625-2014, 2014.

Schepaschenko, D., McCallum, I., Shvidenko, A., Fritz, S., Kraxner, F., and Obersteiner, M.: A new hybrid land cover dataset for Russia: A methodology for integrating statistics, remote sensing and in situ information, Journal of Land Use Science, 6, 245-259, DOI: 10.1080/1747423X.2010.511681, 2011.

Scholes, R. J., Kendall, J., and Justice, C. O.: The quantity of biomass burned in southern Africa, Journal of Geophysical Research D: Atmospheres, 101, 23667-23676, 1996.

Schreier, S. F., Richter, A., Kaiser, J. W., and Burrows, J. P.: The empirical relationship between satellite-derived tropospheric NO2 and fire radiative power and possible implications for fire emission rates of NOx, Atmos. Chem. Phys., 14, 2447-2466, doi:10.5194/acp-14-2447-2014, 2014.

Schroeder, W., Csiszar, I., Giglio, L., and Schmidt, C. C.: On the use of fire radiative power, area, and temperature estimates to characterize biomass burning via moderate to coarse spatial resolution remote sensing data in the Brazilian Amazon, J. Geophys. Res.-Atmos., 115, D21121, doi:10.1029/2009JD013769, 2010.

Schultz, M. G., Heil, A., Hoelzemann, J. J., Spessa, A., Thonicke, K., Goldammer, J. G., Held, A. C., Pereira, J. M. C., and van Het Bolscher, M.: Global wildland fire emissions from 1960 to 2000, Global Biogeochemical Cycles, 22, 2008.

Scott, A. C., and Glasspool, I. J.: The diversification of Paleozoic fire systems and fluctuations in atmospheric oxygen concentration, Proceedings of the National Academy of Sciences of the United States of America, 103, 10861-10865, 2006.

Ségalen, L., Lee-Thorp, J. A., Cerling, T.: Timing of C4 grass expansion across sub-Saharan Africa, Journal of Human Evolution 53, 549-559, 2007.

Seiler, W. and Crutzen, P. J.: Estimates of gross and net fluxes of carbon between the biosphere and the atmosphere from biomass burning, Clim. Change, 2, 207–247, 1980.

Seinfeld, J. H. and Pandis, S. N.: Atmospheric chemistry and physics: from air pollution to climate change, John Wiley & Sons, Hoboken, 2nd edn., 2006.

Shea, R. W., Shea, B. W., Kauffman, J. B., Ward, D. E., Haskins, C. I., and Scholes, M. C.: Fuel biomass and combustion factors associated with fires in savanna ecosystems of South Africa and Zambia, Journal of Geophysical Research D: Atmospheres, 101, 23551-23568, 1996.

Shindell, D. T., Faluvegi, G., Bell, N., and Schmidt, G. A.: An emissions-based view of climate forcing by methane and tropospheric ozone, Geophysical Research Letters, 32, 1-4, 2005.

Shvidenko, A. Z., Shchepashchenko, D. G., Vaganov, E. A., Sukhinin, A. I., Maksyutov, S. S., McCallum, I., and Lakyda, I. P.: Impact of wildfire in Russia between 1998-2010 on ecosystems and the global carbon budget, Doklady Earth Sciences, 441, 1678-1682, DOI: 10.1134/S1028334X11120075, 2011.

Shvidenko, A. Z. and Schepaschenko, D. G.: Climate change and wildfires in Russia, Lesovedenie, 5, 50-61, DOI: 10.1134/S199542551307010X, 2013.

Simon, M., Plummer, S., Fierens, F., Hoelzemann, J. J., and Arino, O.: Burnt area detection at global scale using ATSR-2: The GLOBSCAR products and their qualification, Journal of Geophysical Research D: Atmospheres, 109, 2004.

Singh, H. B., Salas, L., Herlth, D., Kolyer, R., Czech, E., Avery, M., Crawford, J. H., Pierce, R. B., Sachse, G. W., Blake, D. R., Cohen, R. C., Bertram, T. H., Perring, A., Wooldridge, P. J., Dibb, J., Huey, G., Hudman, R. C., Turquety, S., Emmons, L. K., Flocke, F., Tang, Y., Carmichael, G. R., and Horowitz, L. W.: Reactive nitrogen distribution and partitioning in the North American troposphere and lowermost stratosphere, Journal of Geophysical Research D: Atmospheres, 112, DOI: 10.1029/2006JD007664, 2007.

Singh, H. B., Anderson, B. E., Brune, W. H., Cai, C., Cohen, R. C., Crawford, J. H., Cubison, M. J., Czech, E. P., Emmons, L., Fuelberg, H. E., Huey, G., Jacob, D. J., Jimenez, J. L., Kaduwela, A., Kondo, Y., Mao, J., Olson, J. R., Sachse, G. W., Vay, S. A., Weinheimer, A., Wennberg, P. O., Wisthaler, A., and the ARCTAS Science Team.: Pollution influences on atmospheric composition and chemistry at high northern latitudes: Boreal and California forest fire emissions, Atmos. Environ., 44, 4553–4564, doi:10.1016/j.atmosenv.2010.08.026, 2010.

Sinnhuber, B.-M., Weber, M., Amankwah, A., and Burrows, J. P.: Total ozone during the unusual Antarctic winter of 2002, Geophys. Res. Lett., 30, 1580–1584, doi:10.1029/2002GL016798, 2003a.

Sinnhuber, M., Burrows, J. P., Chipperfield, M. P., Jackman, C. H., Kallenrode, M.-B., Künzi, K. F., and Quack, M.: A model study of the impact of magnetic field structure on atmospheric composition during solar proton events, Geophys. Res. Lett., 30, 1818–1821, doi:10.1029/2003GL017265, 2003b.

Smith, M. A., Grant, C. D., Loneragan, W. A., and Koch, J. M.: Fire management implications of fuel loads and vegetation structure in jarrah forest restoration on bauxite mines in Western Australia, Forest Ecology and Management, 187, 247-266, 2004.

Soares Neto, T. G., Carvalho, J. A., Cortez, E. V., Azevedo, R. G., Oliveira, R. A., Fidalgo, W. R. R., and Santos, J. C.: Laboratory evaluation of Amazon forest biomass burning emissions, Atmospheric Environment, 45, 7455-7461, 2011.

Sofiev, M., Vankevich, R., Ermakova, T., and Hakkarainen, J.: Global mapping of maximum emission heights and resulting vertical profiles of wildfire emissions, Atmos. Chem. Phys., 13, 7039-7052, doi:10.5194/acp-13-7039-2013, 2013.

Soja, A. J., Sukhinin, A. I., Cahoon Jr, D. R., Shugart, H. H., and Stackhouse Jr, P. W.: AVHRR-derived fire frequency, distribution and area burned in Siberia, International Journal of Remote Sensing, 25, 1939-1960, 2004.

Solomon, S., Schmeltekopf, A. L., and Sanders, R. W.: On the interpretation of zenith sky absorption measurements, Journal of Geophysical Research, 92, 8311-8319, 1987.

Spicer, C. W.: Nitrogen oxide reactions in the urban plume of Boston, Science, 215, 1095–1097, 1982.

Stehfest, E. and Bouwman, L.: N2O and NO emission from agricultural fields and soils under natural vegetation: summarizing available measurement data and modeling of global annual emissions, Nutr. Cycl. Agroecosys., 74, 207–228, doi:10.1007/s10705-006-9000-7, 2006.

Stocks, B. J., Mason, J. A., Todd, J. B., Bosch, E. M., Wotton, B. M., Amiro, B. D., Flannigan, M. D., Hirsch, K. G., Logan, K. A., Martell, D. L., and Skinner, W. R.: Large forest fires in Canada, 1959–1997, J. Geophy. Res., 108, 8149, doi:10.1029/2001JD000484, 2003.

Stohl, A., Klimont, Z., Eckhardt, S., Kupiainen, K., Shevchenko, V. P., Kopeikin, V. M., and Novigatsky, A. N.: Black carbon in the Arctic: The underestimated role of gas flaring and residential combustion emissions, Atmospheric Chemistry and Physics, 13, 8833-8855, DOI: 10.5194/acp-13-8833-2013, 2013.

Sundell, J.: On the history of indoor air quality and health, Indoor Air, Supplement, 14, 51-58, 2004.

Takashima, H., Irie, H., Kanaya, Y., and Syamsudin, F.: NO2 observations over the western Pacific and Indian Ocean by MAX-DOAS on Kaiyo, a Japanese research vessel, Atmospheric Measurement Techniques, 5, 2351-2360, 2012.

Takegawa, N., Kondo, Y., Koike, M., Ko, M., Kita, K., Blake, D. R., Nishi, N., Hu, W., Liley, J. B., Kawakami, S., Shirai, T., Miyazaki, Y., Ikeda, H., Russell-Smith, J., and Ogawa, T.: Removal of NOx and NOy in biomass buring plumes in the boundary layer over northern Australia, Journal of Geophysical Research D: Atmospheres, 108, ACH 2-1 - 2-14, 2003.

Tansey, K., Grégoire, J. M., Binaghi, E., Boschetti, L., Brivio, P. A., Ershov, D., Flasse, S., Fraser, R., Graetz, D., Maggi, M., Peduzzi, P., Pereira, J., Silva, J., Sousa, A., and Stroppiana, D.: A global inventory of burned areas at 1 km resolution for the year 2000 derived from spot vegetation data, Climatic Change, 67, 345-377, 2004.

Thonicke, K., Spessa, A., Prentice, I. C., Harrison, S. P., Dong, L., and Carmona-Moreno, C.: The influence of vegetation, fire spread and fire behaviour on biomass burning and trace gas emissions: Results from a process-based model, Biogeosciences, 7, 1991-2011, 2010.

Trollope, W. S. W., Trollope, L. A., Potgieter, A. L. F., and Zambatis, N.: SAFARI-92 characterization of biomass and fire behavior in the small experimental burns in the Kruger National Park, Journal of Geophysical Research D: Atmospheres, 101, 23531-23539, 1996.

Val Martin, M., Honrath, R. E., Owen, R. C., and Lapina, K.: Large-scale impacts of anthropogenic pollution and boreal wildfires on the nitrogen oxides over the central North Atlantic region, Journal of Geophysical Research D: Atmospheres, 113, DOI: 10.1029/2007JD009689, 2008.

Val Martin, M., Logan, J. A., Kahn, R. A., Leung, F.-Y., Nelson, D. L., and Diner, D. J.: Smoke injection heights from fires in North America: analysis of 5 years of satellite observations, Atmos. Chem. Phys., 10, 1491-1510, doi:10.5194/acp-10-1491-2010, 2010.

Van der A, R. J., Eskes, H. J., Boersma, K. F., van Noije, T. P. C., Van Roozendael, M., De Smedt, I., Peters, D. H. M. U., and Meijer, E. W.: Trends, seasonal variability and dominant NOx source derived from a ten year record of NO2 measured from space, J. Geophys. Res.-Atmos., 113, D04302, doi:10.1029/2007JD009021, 2008.

Van der Werf, G. R., Randerson, J. T., Giglio, L., Collatz, G. J., Mu, M., Kasibhatla, P. S., Morton, D. C., DeFries, R. S., Jin, Y., and van Leeuwen, T. T.: Global fire emissions and the contribution of deforestation, savanna, forest, agricultural, and peat fires (1997–2009), Atmos. Chem. Phys., 10, 11707–11735, doi:10.5194/acp-10-11707-2010, 2010.

Vandaele, A. C., Hermans, C., Simon, P. C., Roozendael, M. V., Guilmot, J. M., Carleer, M., and Colin, R.: Fourier transform measurement of NO2 absorption cross-section in the visible range at room temperature, J. Atmos. Chem., 25, 289–305, 1996.

Vermote, E., Ellicott, E., Dubovik, O., Lapyonok, T., Chin, M., Giglio, L., and Roberts, G. J.: An approach to estimate global biomass burning emissions of organic and black carbon from MODIS fire radiative power, J. Geophys. Res.-Atmos., 114, D18205, doi:10.1029/2008JD011188, 2009.

Wagner, T., Dix, B., Friedeburg, C. V., Frieß, U., Sanghavi, S., Sinreich, R., and Platt, U.: MAX-DOAS O4 measurements: A new technique to derive information on atmospheric aerosols - Principles and information content, Journal of Geophysical Research D: Atmospheres, 109, 1-19, 2004.

Wang, P., Richter, A., Bruns, M., Rozanov, V. V., Burrows, J. P., Heue, K.-P.,Wagner, T., Pundt, I., and Platt, U.: Measurements of tropospheric NO2 with an airborne multi-axis DOAS instrument, Atmos. Chem. Phys., 5, 337–343, doi:10.5194/acp-5-337-2005, 2005.

Wang, P., Stammes, P., van der A, R., Pinardi, G., and van Roozendael, M.: FRESCO+: an improved O2 A-band cloud retrieval algorithm for tropospheric trace gas retrievals, Atmos. Chem. Phys., 8, 6565–6576, doi:10.5194/acp-8-6565-2008, 2008.

Wang, Y., Li, A., Xie, P. H., Wagner, T., Chen, H., Liu, W. Q., and Liu, J. G.: A rapid method to derive horizontal distributions of trace gases and aerosols near the surface using multi-axis differential optical absorption spectroscopy, Atmos. Meas. Tech. 7, 1663-1680, 2014.

Wayne, R. P., Barnes, I., Biggs, P., Burrows, J. P., Canosa-Mas, C. E., Hjorth, J., Le Bras, G., Moortgat, G. K., Perner, D., Poulet, G., Restelli, G., and Sidebottom, H.: The nitrate radical: Physics, chemistry, and the atmosphere, Atmos. Environ. A-Gen., 25, 1– 203, 1991.

Werner, P. A.: Impact of feral water buffalo and fire on growth and survival of mature savanna trees: An experimental field study in Kakadu National Park, northern Australia, Austral Ecology, 30, 625-647, 2005.

Westerling, A. L., Hidalgo, H. G., Cayan, D. R., and Swetnam, T. W.: Warming and earlier spring increase Western U.S. forest wildfire activity, Science, 313, 940-943, 2006.

WHO: Health Aspects of Air Pollution with Particulate Matter, Ozone and Nitrogen Dioxide, World Health Organization, Bonn, 2003.

Wiedinmyer, C., Quayle, B., Geron, C., Belote, A., McKenzie, D., Zhang, X., O'Neill, S., and Wynne, K. K.: Estimating emissions from fires in North America for air quality modeling, Atmos. Environ., 40, 3419–3432, doi:10.1016/j.atmosenv.2006.02.010, 2006.

Winkler, H., Sinnhuber, M., Notholt, J., Kallenrode, M.-B., Steinhilber, F., Vogt, J., Zieger, B., Glassmeier, K.-H., and Stadelmann, A.: Modeling impacts of geomagnetic field variations on middle atmospheric ozone responses to solar proton events on long timescales, J. Geophys. Res., 113, 11 pp., D02302, doi:10.1029/2007JD008574, 2008.

Wittrock, F., Müller, R., Richter, A., Bovensmann, H., and Burrows, J. P.: Measurements of Iodine monoxide (IO) above Spitsbergen, Geophysical Research Letters, 27, 1471-1474, 2000.

Wittrock, F., Oetjen, H., Richter, A., Fietkau, S., Medeke, T., Rozanov, A., and Burrows, J. P.: MAX-DOAS measurements of atmospheric trace gases in Ny-Ålesund – Radiative transfer studies and their application, Atmos. Chem. Phys., 4, 955–966, doi:10.5194/acp-4-955-2004, 2004.

Wittrock, F.: The retrieval of oxygenated volatile organic compounds by remote sensing techniques, Ph.D., University of Bremen, Bremen, Germany, available at: http://www.doas-bremen.de/paper/diss_wittrock_06.pdf (last access: May 2014), 2006.

WMO: Scientific assessment of ozone depletion: 1994, Rep. 37, Global Ozone Res. And Monit. Proj., Geneva, 1995.

Wooster, M. J. and Zhang, Y. H.: Boreal forest fires burn less intensely in Russia than in North America, Geophys. Res. Lett., 31, L20505, doi:10.1029/2004GL020805, 2004.

Wooster, M. J., Roberts, G., Perry, G. L.W., and Kaufman, Y. J.: Retrieval of biomass combustion rates and totals from fire radiative power observations: FRP derivation and calibration relationships between biomass consumption and fire radiative energy release, J. Geophys. Res.-Atmos., 110, 1–24, 2005.

Wrangham, R., Jones, J., Laden, G., Pilbeam, D., and Conklin-Brittain, N.: The raw and the stolen: Cooking and the ecology of human origins. Current Anthropology, 40(5):567-594, 1999.

Xu, W., Wooster, M. J., Roberts, G., and Freeborn, P.: New GOES imager algorithms for cloud and active fire detection and fire radiative power assessment across North, South and Central America, Remote Sens. Environ., 114, 1876–1895, 2010.

Yienger, J. J. and Levy II, H.: Empirical model of global soil biogenic NOx emissions, J. Geophys. Res., 100, 11447–11464, 1995.

Yokelson, R. J., Christian, T. J., Karl, T. G., and Guenther, A.: The tropical forest and fire emissions experiment: laboratory fire measurements and synthesis of campaign data, Atmos. Chem. Phys., 8, 3509–3527, doi:10.5194/acp-8-3509-2008, 2008.

Zemp, E., Elsasser, S., Schindler, C., Künzli, N., Perruchoud, A. P., Domenighetti, G., Medici, T., Ackermann-Liebrich, U., Leuenberger, P., Monn, C., Bolognini, G., Bongard, J. P., Brändli, O., Karrer, W., Keller, R., Schöni, M. H., Tschopp, J. M., Villiger, B., and Zellweger, J. P.: Long-term ambient air pollution and respiratory symptoms in adults (SAPALDIA Study), American Journal of Respiratory and Critical Care Medicine, 159, 1257-1266, 1999.

Zhang, Y. H., Wooster, M. J., Tutubalina, O., and Perry, G. L. W.: Monthly burned area and forest fire carbon emission estimates for the Russian Federation from SPOT VGT, Remote Sensing of Environment, 87, 1-15, 2003.

Zien, A. W., Richter, A., Hilboll, A., Blechschmidt, A.-M., and Burrows, J. P.: Systematic analysis of tropospheric NO2 long-range transport events detected in GOME-2 satellite data, Atmos. Chem. Phys., 14, 7367-7396, doi:10.5194/acp-14-7367-2014, 2014.